Durham E-Theses

The distribution of cosmic ray electrons and magnetic field in the galaxy

French, David K.

THE DISTRIBUTION OF COSMIC RAY ELECTRONS
AND MAGNETIC FIELD IN THE GALAXY

by

David K. French, B. Sc.

A thesis submitted to the University of
Durham for the Degree of Doctor of Philosophy.

October, 1977.

To my parents.

ABSTRACT

An attempt is made to model the distribution of cosmic ray
electrons and magnetic field in the galaxy such that agreement is
reached with the observed continuum radiation.

A new composite map of galactic spiral structure has been obtained
by combining the model of Georgelin, based on observations of H II
regions, with the map of neutral hydrogen outside the solar circle of
Verschuur. Using models which relate the galactic magnetic field and
relativistic electron distribution to this structure, profiles of the
synchrotron radio emission along the galactic plane are predicted for
$30^{o} < \ell^{\textbf{\textit{II}}} < 330^{o}$. These are compared with the observed profile at 150 MHZ
corrected for thermal emission, local sources and extra galactic back-
ground. The way in which the spiral arm compression, produced by
density waves, falls-off with height above the plane is obtained using
magnetohydrodynamic shock theory. The fall-off in emissivity with
height above the plane is fitted to the observations of Landecker and
Wielebinski.

Detailed comparison with observation gives preference for a
uniform distribution of electrons in the disc of the galaxy. There is
evidence that the observed magnitude of the galactic magnetic field in
the neighbourhood of the sun is more typical of an interarm than an
arm region. A magnetic field which, in the galaxy as a whole, can be
decomposed into random and regular components of approximately equal
magnitude, is indicated. The observed latitude distribution of bright-
ness temperature at 150 MHZ may be understood if the emissivity
distribution with height above the plane has an equivalent half width
of 2.75 kiloparsecs, half width at half maximum of 2 kiloparsecs and
extent of about 10 kiloparsecs at the sun. This thick disc or halo
decreases in extent towards the galactic centre and increases in extent

towards the edge of the galaxy.

The two closed galaxy models proposed by Peters, Rasmussen and Westergaard are both discussed in connection with the cosmic ray electron component. Both models are found to be inconsistent with, in one case, the observed positron flux and, in the other, with the observed continuum emission.

PREFACE

The work presented in this thesis was carried out during the period 1974-77 while the author was a research student under the supervision of Dr. John L. Osborne in the Physics Department of the University of Durham.

Some of the work reported here was carried out in collaboration with Dr. J.L. Osborne, but most of the research and all calculations are of the author.

Parts of the work are published as follows:

French D.K. and Osborne J.L. 1976   Nature 260 372

French D.K. and Osborne J.L. 1976   M.N.R.A.S. 177 569-582

Brindle C. French D.K. and
            Osborne J.L. 1977   Proc. 15th Int. Cosmic
                                   Ray Conf. Vol. 2 p.386

CONTENTS

CHAPTER 1

Introduction.

The galactic continuum radiation is the meeting place of radio astronomy and cosmic ray astrophysics. Through observations of the continuum radiation important information can be obtained on the galactic magnetic field and the cosmic ray electron distribution. In recent years cosmic ray electrons have come to play an increasingly important role in cosmic ray physics by virtue of the fact that their distribution throughout the galaxy is mirrored in the continuum emission and that their site of origin is known to be the galaxy. Also of importance is the positron component which offers a unique opportunity for the application of propagation models of particles in the galaxy as the positron source spectrum is calculable as they are thought to be of entirely secondary origin.

Electrons were once thought to be the main constituent of the primary cosmic rays. In the 1930's cascade theory quantitatively developed by Bhabha and Heitler (1934) and by Carlson and Oppenheimer (1937) was able to explain the observations (just then established) that the total intensity of cosmic radiation passes through a maximum at an altitude of about 20 km. if the primary radiation was taken to be electrons with a particular energy spectrum. At about the same time the east-west asymmetry of the total radiation, Johnson and Barry (1939), indicated that the primary radiation was mainly positively charged. This led many to conclude that perhaps the primary radiation was positrons although others considered protons more likely. It was quickly realised however, following balloon experiments by Schein et al (1940, 1941), that the primary radiation was mainly protons and the electrons in the atmosphere were of secondary origin. It was not until the early sixties that electrons were positively identified in the primary radiation by Earl (1961) and Meyer and Vogt (1961).

In 1935 Jansky observed non terrestrial radio emission continuously along the galactic plane which peaked in the direction of the galactic centre and showed a minimum in the anticentre direction. This resulted in the inescapable conclusion that the Galaxy was a source of intense radiation at frequencies of of a few tens of megahertz. Following this initial discovery, the radio emission from the galaxy has been mapped at many frequencies. The most recent full-sky map is that presented by Landecker and Wißlebinski (1970) at 150 MHz. The origin of the galactic radio emission remained obscure for many years following its discovery. Jansky suggested that it was merely long-wavelength stellar emission. This was rather unsatisfactory as the sun showed no such radio emission. Whipple and Greenstein (1937) suggested that the observations referred to the Rayleigh-Jeans tail of a blackbody distribution of $30^{o}K$ dust. This was dismissed by Reber (1940a) who failed to observe the 'cosmic noise' at 3300 and 900 MHz. which on the Whipple-Greenstein model should have been very intense. Reber 1940b interpreted his fluxes as arising from thermal bremsstrahlung in a hot $T_e = 10^4$ K dense ($ne = 1$ cm^{-3}) gas. This interpretation was consistent with his measurements at 163, 900 and 3300 MHz. but was inconsistent with Jansky's earlier lower frequency measurements which required an electron temperature of 1.5×10^5 K. However, Reber (1944) interpreted secondary maxima in the distribution along the galactic plane at 163 MHz. as being the directions tangential to spiral arms and concluded that spiral arms existed in the directions of Cygnus, Cassiopeia and Canis Major. This was the first use made of the galactic continuum radiation in mapping the structure of the galaxy. Further progress could not be made in the use of the continuum radiation until its true nature had become clear. Alfven and Herlofsun (1950), to explain the possibility of the existence of a population of radio stars, suggested that the emission might originate from cosmic electrons trapped in the magnetic fields of such stars resulting in synchrotron emission.

In 1952 Shklovskii put forward the synchrotron mechanism for explaining the emission from the Crab nebula and this was quickly verified by polarisation measurements. This opened the door for a synchrotron interpretation of the galactic continuum emission. Kieperheuer in 1950 had generalised the Alfven-Herlofson idea by filling the galaxy with electrons laced by a magnetic field to explain the continuum emission but it wasn't until the confirmation of Shklovskii's ideas on the Crab nebula that this synchrotron explanation was accepted. Following Kiepenheuer's work Shklovskii 1952, through an analysis of the Bolton and Westfold (1950) 100 MHz. survey, concluded that the galaxy must possess an almost spherical, structureless halo or corona of radio emission. Over the last decade the existence of such a radio halo has been hotly debated (see chapter 7).

Mills (1959) showed that correlations existed between the radio continuum and the spiral arms of the galaxy and pointed the way to the modelling of the galaxy to obtain the observed continuum features. It is interesting that this was in fact fifteen years after it had first been suggested by Reber (1944).

The galactic continuum emission presents the observational link between the cosmic ray electrons and magnetic field in the galaxy through the synchrotron mechanism. The way in which the electrons and magnetic field are distributed in the galaxy to produce the galactic radio emission is also capable of shedding some light on the structure of the galaxy. In this thesis the distribution of cosmic ray electrons and magnetic field in the galaxy are considered in the light of recent radio continuum observations. This also involves a comprehensive discussion concerning the global structure of the galaxy.

Chapter 2 reviews the present observational situation as regards cosmic ray electrons and looks at their propagation in the galaxy. Obviously when considering various electron distributions it is important that they are physically realistic and are possible distributions resulting from our present knowledge of the primary electron source distribution.

Chapter 3 discusses the galaxy and interstellar medium concentrating on those factors that are of importance in modelling the synchrotron emission. The galactic magnetic field is discussed in considerable detail whereas a discussion of the observational and theoretical aspects of spiral structure is left until chapter 4.

Chapter 5 presents the observations of the continuum emission against which the models are compared. Also discussed in this chapter is the way in which the observed data are reduced to the correct form for the comparison.

Chapter 6 outlines the way in which the various models have been constructed and the calculations carried out whereas chapter 7 presents the results from the various models. In chapter 7 the halo problem is also discussed in the light of the present and past work.

Chapter 8 discusses the various conclusions that can be reached, in the framework of such models as those presented in chapters 6 and 7, on the structure of the galactic magnetic field and on the distribution of cosmic ray electrons.

This thesis therefore sets out to model the magnetic fields and electron intensities throughout the galaxy in the framework of the theoretically expected and observationally observed spiral structure such that agreement can be reached with the observed galactic continuum radiation.

References

Alfven H and Herlofson N. 1950. Phys. Rev. <u>78</u> 616.

Baldwin J.E. 1954. Nature <u>174</u> 320.

Bhabha H.J. and Heitler W. 1937. Proc. Roy. Soc. <u>A.159</u> 432

Bolton J.G. and Westfold K.C. 1950. Aust. J. Sci. Res. <u>3A</u> 19-33

Carlson J.F. and Oppenheimer J.R. 1937. Phys. Rev. <u>51</u> 220

Earl J.A. 1961 Phys. Rev. Letts <u>6</u> 125.

Jansky K. 1935 Proc. Inst. Rad. Eng. <u>23</u> 1158.

Johnson T.H. and Barry J.G. 1939 Phys. Rev. <u>56</u> 219.

Kiepenheuer K.O. 1950. Phys. Rev. <u>79</u> 738.

Landecker T.L. and Wielebinski R. 1970. Aust. J. Phys. Astrophys. Suppl. <u>16</u>.

Meyer P. and Vogt R. 1961. Phys. Rev. Letts <u>6</u> 193.

Mills B.Y. 1959. Proc. I.A.U. Symp. 9 431.

Reber G. 1940 a Proc. Inst. Rad. Eng. <u>28</u> 68

    ibid 1940 b Ap J. <u>91</u> 621

    ibid 1944 Ap. J. <u>100</u> 279

Schein M. Jesse W.P. and Wollam E.O. 1940 Phys. Rev. <u>57</u> 847

                                          1941 Phys. Rev. <u>59</u> 615

Shklovskii I.S. 1952. Astron Zh <u>29</u> 418

Whipple F.L. and Greenstein J.L. 1937. Proc. Nat. Acad. Sci. <u>23</u> 117

CHAPTER 2

COSMIC RAY ELECTRONS

2.1. Observations of the Cosmic Ray Electron Component.

Certainty about the presence of an electron component in the primary cosmic radiation was established by 1950 through the interpretation of the newly observed radio continuum in terms of synchrotron radiation emitted by high energy electrons radiating in a magnetic field, Kiepenheuer (1950). Cosmic electrons were not directly observed until the early 1960's when balloon flights made this possible. Observations were made almost simultaneously by Earl (1961) and Meyer and Vogt (1961). During the past decade observations of the electron spectrum have been made over the energy range of a few KeV. to almost 1000GeV. with an accuracy comparable to that of the observations of the nuclear cosmic ray components. Figure 2.1 summarises the observed electron spectrum over the full energy range in comparison with the spectrum of protons (solid line). Simultaneously, the charge composition of these primary electrons is determined by either using magnetic spectrometers or the earth's magnetic field as a magnetic analyser. Figures 2.2 and 2.3 summarise our present knowledge of the e^+/e^- ratio and the absolute flux of the e^+. The ratios of primary electrons/protons (observed to be approximately 100) and e^+/e^- give important evidence as to the way in which cosmic rays propagate within the Galaxy (see section 2.4). In this thesis the electron spectrum best fitting Figure 2.1 is used and is taken to be;

$$N(E)\,dE = 80 {+70 \atop -30}\ E^{-2.6}\ (m^2.\,s.\,sr.\,GeV.)^{-1}$$

2.2 Energy Loss processes.

Unlike the nuclear component of the cosmic rays, cosmic electrons lose energy fairly rapidly during propagation due to their interaction
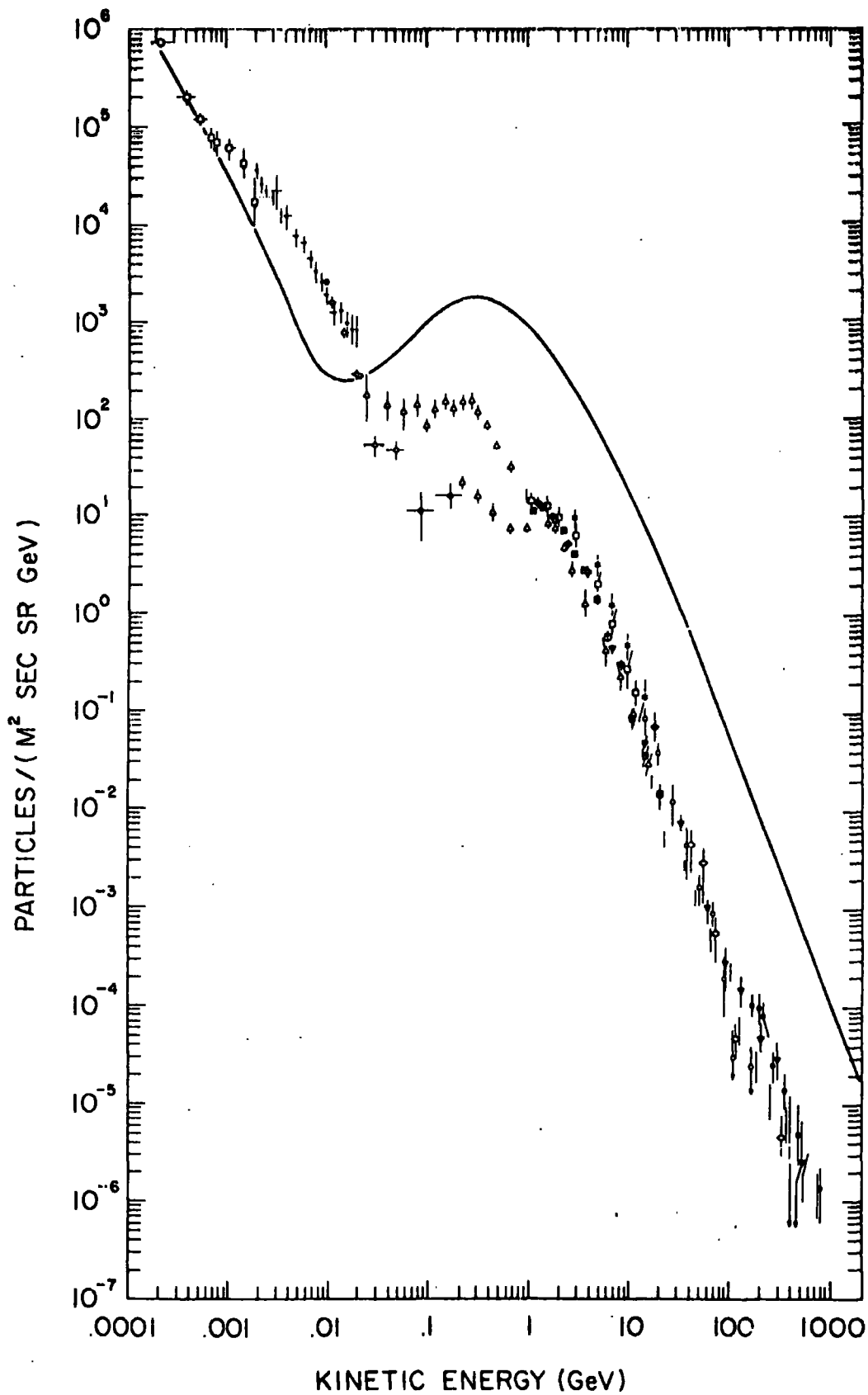
Figure 2.1: A summary of cosmic ray electron measurements. The spread of data in the 0.1 to 1GeV. interval is due to changes in solar modulation. The line represents the proton spectrum for comparison (Meyer 1974)
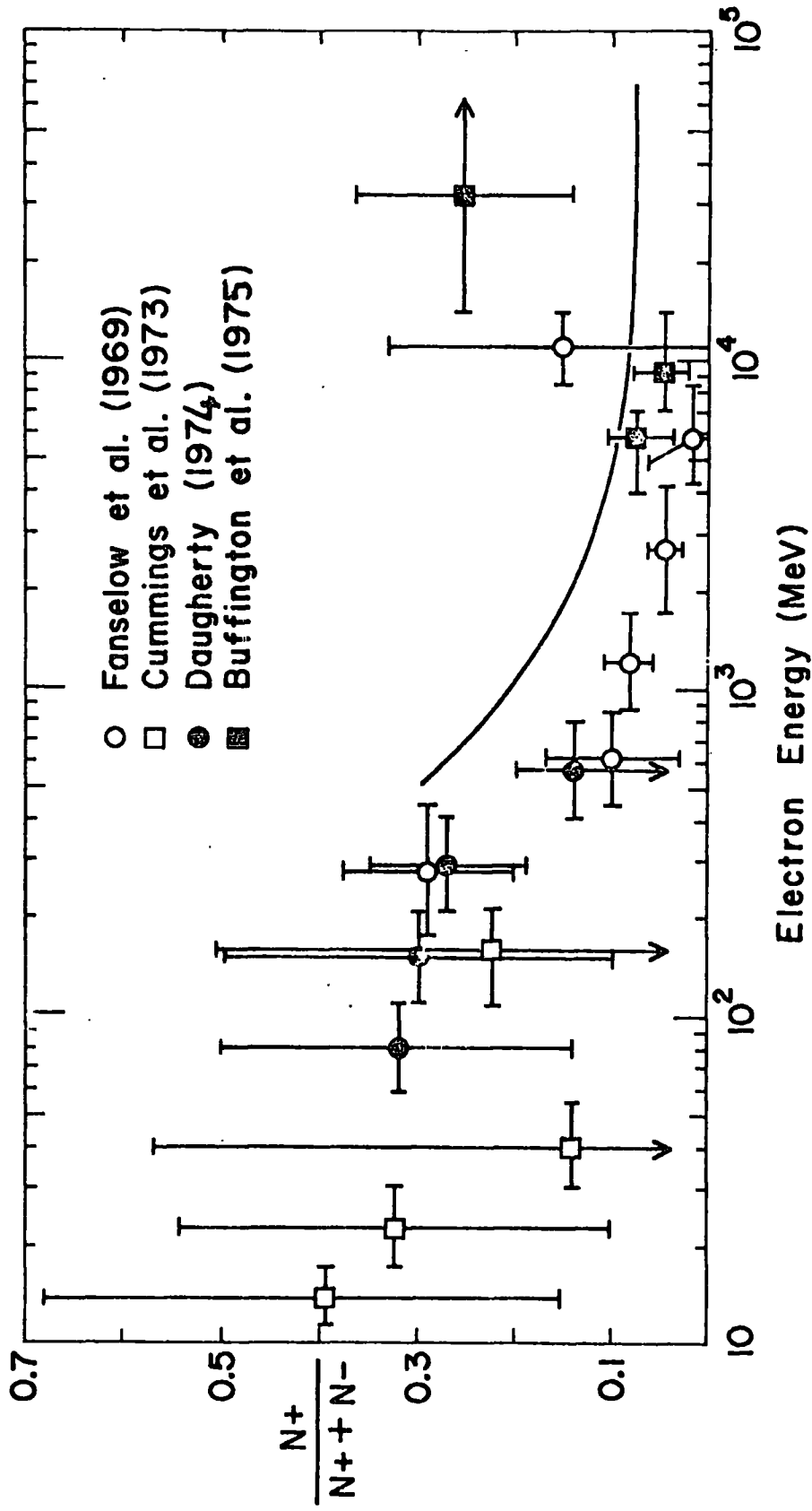
Figure 2.2: The fraction of positrons in the cosmic radiation as a function of energy as measured by several observers.

Figure 2.3: A summary of positron measurements. The line is the calculated intensity using an exponential age distribution with $T_e = 3.3 \times 10^6$ years (Ramaty 1974)

with magnetic and radiation fields as well as with matter.

2.2.1. Inverse Compton Scattering.

This is rather a misnomer as the interesting interaction is
Thomson scattering, i.e. the interaction of photons on free electrons.
In the Thomson approximation the electron loses little energy in each
collision. For electron energies $E \leqslant E_{tr} = \dfrac{(mc^2)^2}{\bar{E}}$ where $\bar{E}$ is the average
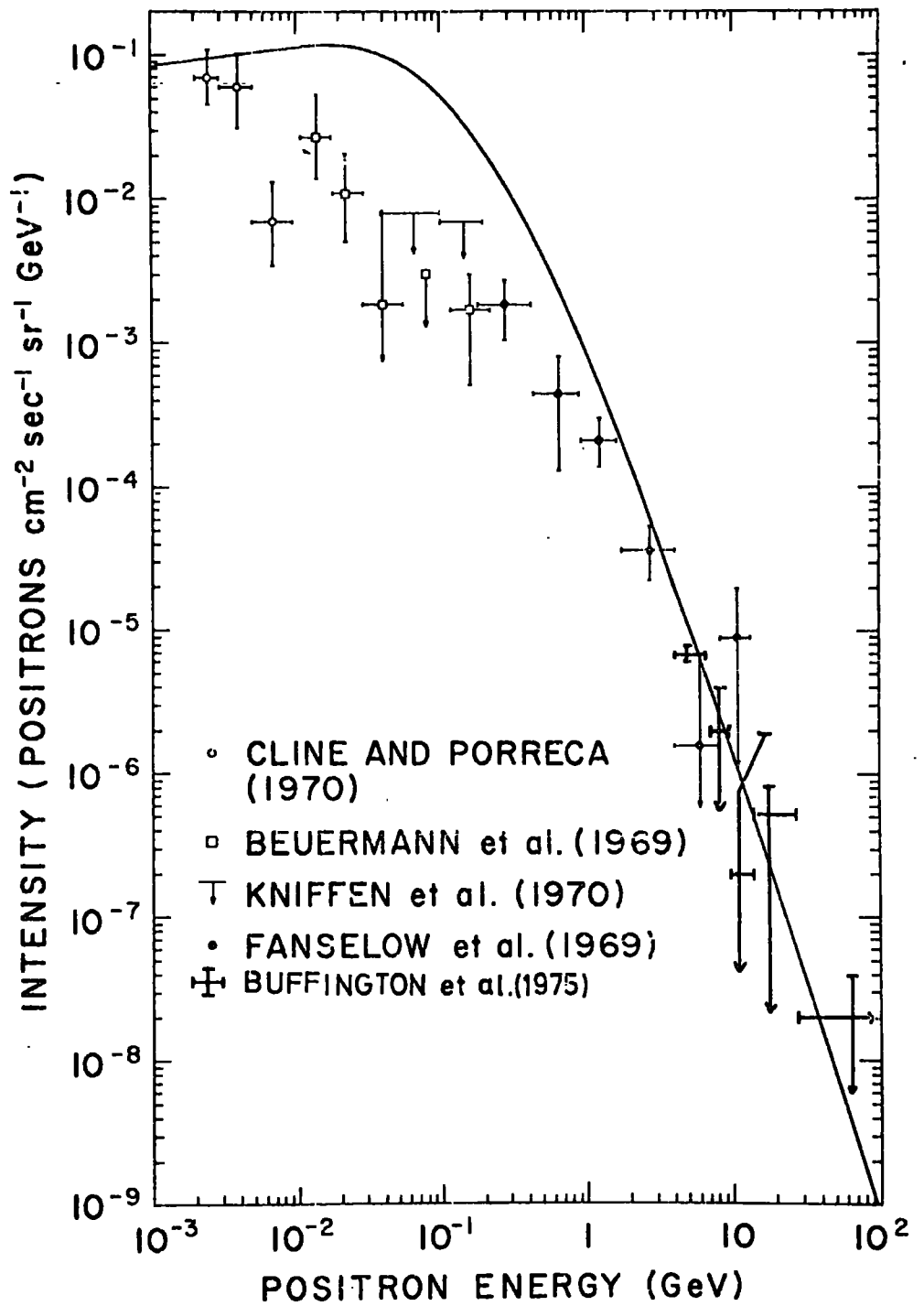energy of the photons in the frame of the Galaxy, the energy loss is
given by:

$$\left(\frac{dE}{dt}\right)_{I.C} = \frac{4}{3} c\, \sigma_{th.}\, \rho_{ph.} \left(\frac{E}{mc^2}\right)^2 \approx 10^{-16}\, \rho_{ph.}\, E^2 \;(GeV.s^{-1}) \quad 2.1$$

where $\sigma_{th.} = 6.6 \times 10^{-25} cm^2$ is the Thomson cross-section and $\rho_{ph.}$ is the
energy density of photons (in eV/cm^3). For electron energies greater
than E_{tr}. the Klein-Nishima cross-section must be used. For the
case of cosmic ray electrons there are two photon fields which need to
be considered: the photons from starlight, $\rho_{ph.} \approx 0.5\, eV/cm^3$, $\bar{E} \approx 3eV$ and those
from the universal blackbody radiation $\rho_{ph.} \approx 0.25\, eV/cm^3$, $\bar{E} \approx 10^{-3} eV$. These give
respectively values of 80GeV. and 2×10^5GeV. for the transition energy,
$E_{tr.}$, corresponding to γ's, the electron's Lorentz factor, of 10^5 and
10^8.

2.2.2. Ionisation Loss.

When a charged particle passes through matter it loses energy by
exciting and ionising atoms. For relativistic electrons the ionisation
loss is almost constant, showing only the relativistic increase of the
Bethe-Block expression:-

$$\left(\frac{dE}{dt}\right)_I \approx 7.6 \times 10^{-18}\, n_h \left(3\, \log E/mc^2 + 18.8\right) GeV.s^{-1} \quad 2.2$$

This is the expression for neutral hydrogen: the energy loss becomes
somewhat larger if Helium is present and larger by a factor of 3 or 4 in
ionised hydrogen. n_h is the number density of hydrogen atoms per cm^3.

2.2.3. Bremsstrahlung Loss.

Bremsstrahlung, which is a german word meaning 'braking radiation', is the radiation emitted by a decelerating charged particle. When a relativistic electron passes close to a nucleus it emits photons and loses energy, Bethe and Heitler (1934). This energy loss may, in a good approximation, be considered as a continuous energy loss proportional to the electron energy. In atomic hydrogen

$$\left(\frac{dE}{dt}\right)_B \approx 8 \times 10^{-16}\, n_H\; E \quad GeV.s^{-1}. \qquad 2.3$$

This is slightly modified in the case of an ionised medium, Blumenthal and Gould (1970).

2.2.4.   Synchrotron Radiative Loss.

Referring to Appendix I equation I.6;

$$P(E,\nu)\,d\nu = \frac{\sqrt{3}\,e^3}{mc^2\,4\pi}\, H_\perp \; x \int_x^\infty K_{5/3}(\eta)\,d\eta\,d\nu$$

This represents the power emitted by an electron of energy E radiating in a magnetic field with perpendicular component $H_\perp$. Integrating this equation over all frequencies results in the rate of energy loss;

$$\left(\frac{dE}{dt}\right)_S = \int_0^\infty P(E,\nu)\,d\nu = B.\,H_\perp\,\nu_c \int_0^\infty F(x)\,dx$$

where B and ν_c are defined in appendix I.

Upon integration this gives:

$$\left(\frac{dE}{dt}\right)_S = K_S\, H_\perp^2\, E^2 \quad GeV.s^{-1} \qquad 2.4$$

where $K_S^{-1} = 2.64 \times 10^7 s$. (microgauss)^2. GeV. if E is expressed in GeV. and $H_\perp$ in μG.

The time required for the electron to lose half of its energy E_o by emitting synchrotron radiation is:

$$t_{1/2} = \left(K_S\, H_\perp^2\, E_o\right)^{-1}$$

and therefore an electron with E_o= 3GeV. trapped in an effective field of 10μG will radiate half its energy in approximately 3×10^7 years.
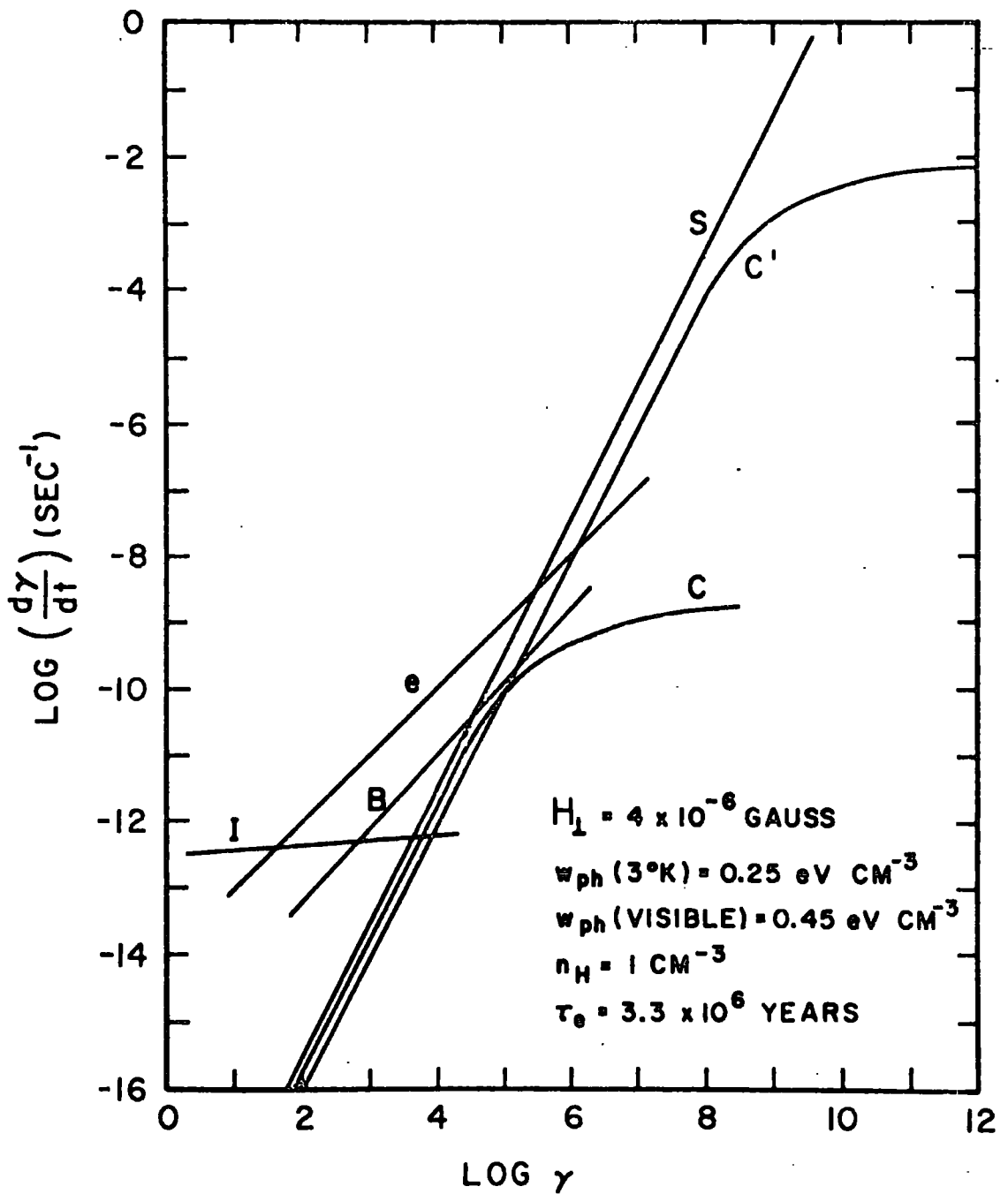
Figure 2.4: Energy loss processes for electrons in the galaxy. S- synchrotron loss, C- Compton loss (Blackbody), C' - Compton loss (starlight), B- bremsstrahlung, e- escape, I- ionisation.

Figure 2.4 shows the way in which the various energy loss mechanisms vary with energy. Also plotted is the energy loss due to 'escape' from the propagation region assuming an escape lifetime of 3.3 X 10^6 years.

2.3 Electron Sources

The sources of electrons must be galactic as the energy loss by interactions with the black-body radiation via the inverse Compton process excludes electrons from filling extragalactic space (Fazio et al. 1966).

As in the case of the nuclear components, the electron component is made up of particles directly accelerated in sources and of particles which are secondaries resulting from interactions of cosmic ray nuclei on the interstellar medium.

2.3.1. Secondary Electron Sources.

At very low energies, 0.1 to 20 MeV., the observed electron energy spectrum and flux may be entirely due to the knock-on source: the production of cosmic electrons by Coulomb interactions of cosmic rays with neutral hydrogen atoms or free ambient electrons. The spectrum of knock-on electrons was first calculated by Abraham et al. (1966) and was found to be of the form $q(\gamma_e) \approx 5(\gamma_e - 1)^{-2.76}$ electrons. $(g.s. \gamma_e)^{-1}$ in interstellar space for energies of 3 to 20 MeV. As only relativistic nuclei produce relativistic knock-on electrons, the effects of solar modulation on the knock-on source is almost negligible. Hurford et al. (1974) have extended these calculations to lower energies and conclude that the knock-on source can account for the electron flux up to 15MeV., if solar modulation does not suppress the electron flux by more than a factor of approximately 3.

The evidence for the presence of positrons below 3 MeV. is not well

established and the presently known upper limits of the positron flux

do not require any particular sources such as the radioactive decay of

nuclides, such as ^{11}C, ^{13}N, ^{14}O and ^{15}O, as discussed by Ramaty et al.

(1970) and Verma et al (1969) to be considered. It should be noted

that MeV. electrons appear to be emitted by the planet Jupiter,

Teegarten et al. (1974) and may contribute to the low energy flux of

electrons at the earth and that the observed electron spectrum may in

part be of planetary origin. The planetary particles are expected

to consist exclusively of negatrons.

As one moves towards energies above 10MeV. the π-μ-e decay

source becomes increasingly important. Here electrons are produced by

collisions of high energy protons with the interstellar gas, leading to

the production of π- mesons and subsequent π-μ-e decay of the charged

pions. The producing protons have roughly one order of magnitude higher

energy than the resulting electrons and hence calculations of the source

spectrum are not handicapped by a lack of knowledge of the proton spectrum

due to a poorly known amount of solar modulation. The requirements for

calculating the electron source spectrum are a knowledge of

(a) the proton flux and energy spectrum,

(b) the production cross-section for pions,

(c) the density of the interstellar gas.

Early calculations were carried out by Ramaty and Lingenfelter (1966) and

Perola et al. (1967) and a computer analysis has recently been carried out

by Ramaty (1974). Figure 2.5 shows the electron and positron production

spectra in interstellar space originating in the π-μ-e source as calculated

by Ramaty. It should be noted from this figure that at all energies the

fraction of positrons $\dfrac{e^+}{e^+ + e^-}$ is ≥ 0.5. Hence the observations of approx-

imately 90% of negatrons at E $>$ 500MeV. constitutes the proof for a major

primary source contribution to the electron flux.
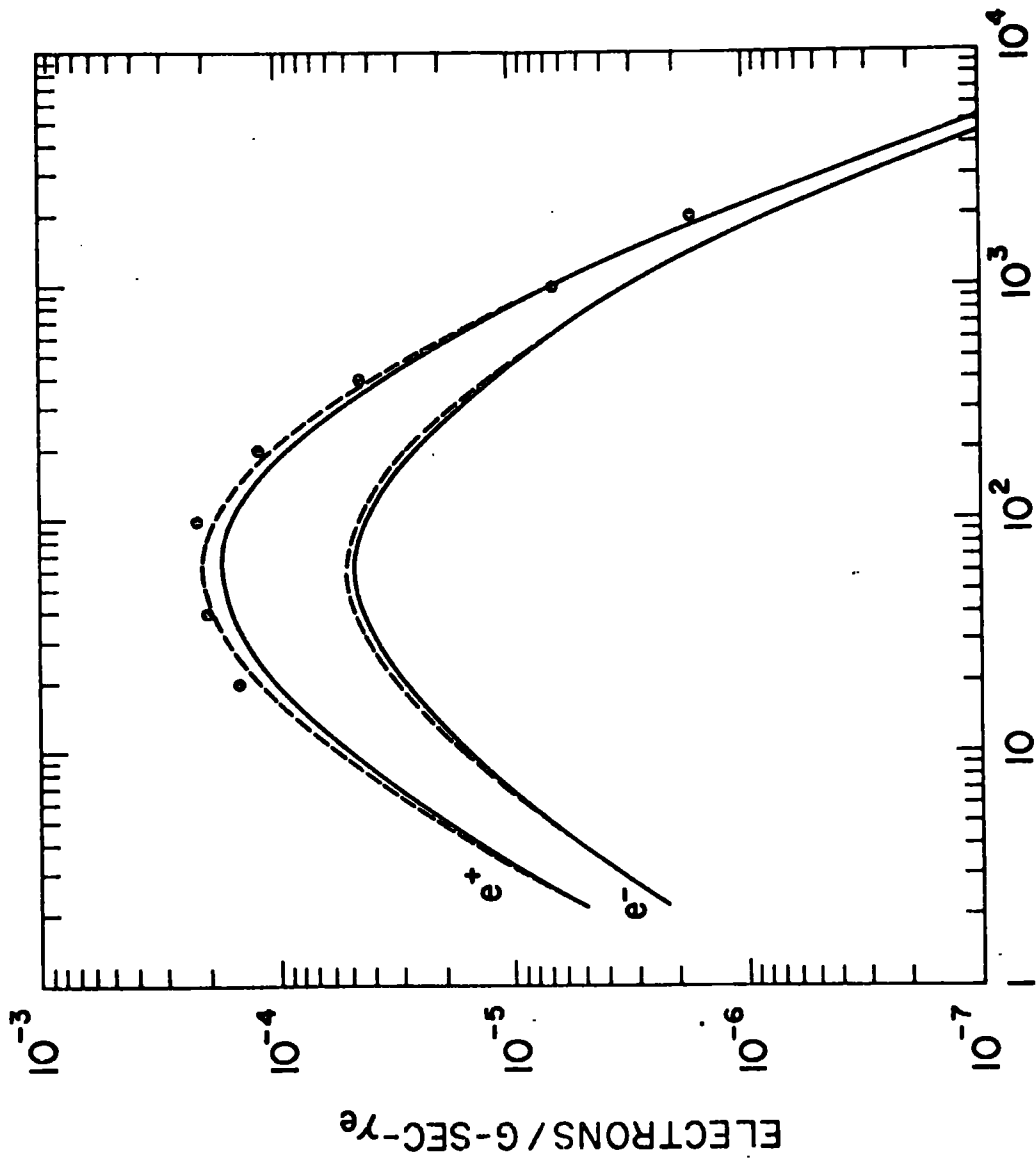
Figure 2.5: Electron and positron production spectra in interstellar space, originating in the $\pi-\mu-e$ source (Ramaty 1974). ——— are the spectra for solar minimum cosmic ray spectrum , — · — · — are the spectra for the demodulated cosmic ray spectrum. ● are from the calculations of Perola et al. (1967)

2.3.2. Primary Electron Sources

It is known that many galactic as well as extragalactic objects contain highly relativistic electrons but little is understood about the details of the acceleration process. It is generally thought that the major source of cosmic ray electrons must be supernovae, supernovae remnants and pulsars. Dickel (1974) has compared the observed integrated luminosity of the galaxy at 400MHz. with that expected from supernovae occuring 1 in every 50 years. He finds that the calculated monochromatic luminosity from all supernovae electrons is 1.4 times the apparent observed luminosity of the galaxy based on Baldwin's (1967) determination. This would indeed suggest that supernovae are a major source of primary cosmic ray electrons.

One important clue as to the acceleration mechanism for electrons may be gained from the primary electron/proton ratio. In figure 2.6 is shown the abundance ratio of protons to electrons in terms of energy, rigidity and Lorentz factor.

The observation of electrons (3-12 MeV.) and protons (15-80 MeV.) emitted in a solar flare of July 7 1966 by the I.M.P.III satellite (Cline and Macdonald 1968) indicated that these components have similar power law spectra in rigidity with a differential exponent of approximately 3 and that the electron to proton ratio is 10^{-2} for the same equivalent rigidity interval. This is similar to the situation as shown in figure 2.6 suggesting that perhaps in all explosive acceleration processes of cosmic rays the spectra of protons and electrons are similar in rigidity scale with an intensity ratio such that $n_e/n_p \approx 10^{-2}$. Several acceleration mechanisms have been considered (Ginzburg and Syrovatski 1964, Hayakawa et al. 1964). Unfortunately most encounter difficulties in explaining observations.

If both protons and electrons were accelerated by a shock wave from a supernova explosion, they should end up with about the same velocity. Therefore, at the same energy, if they have a power law spectrum, their

LORENTZ FACTOR γ

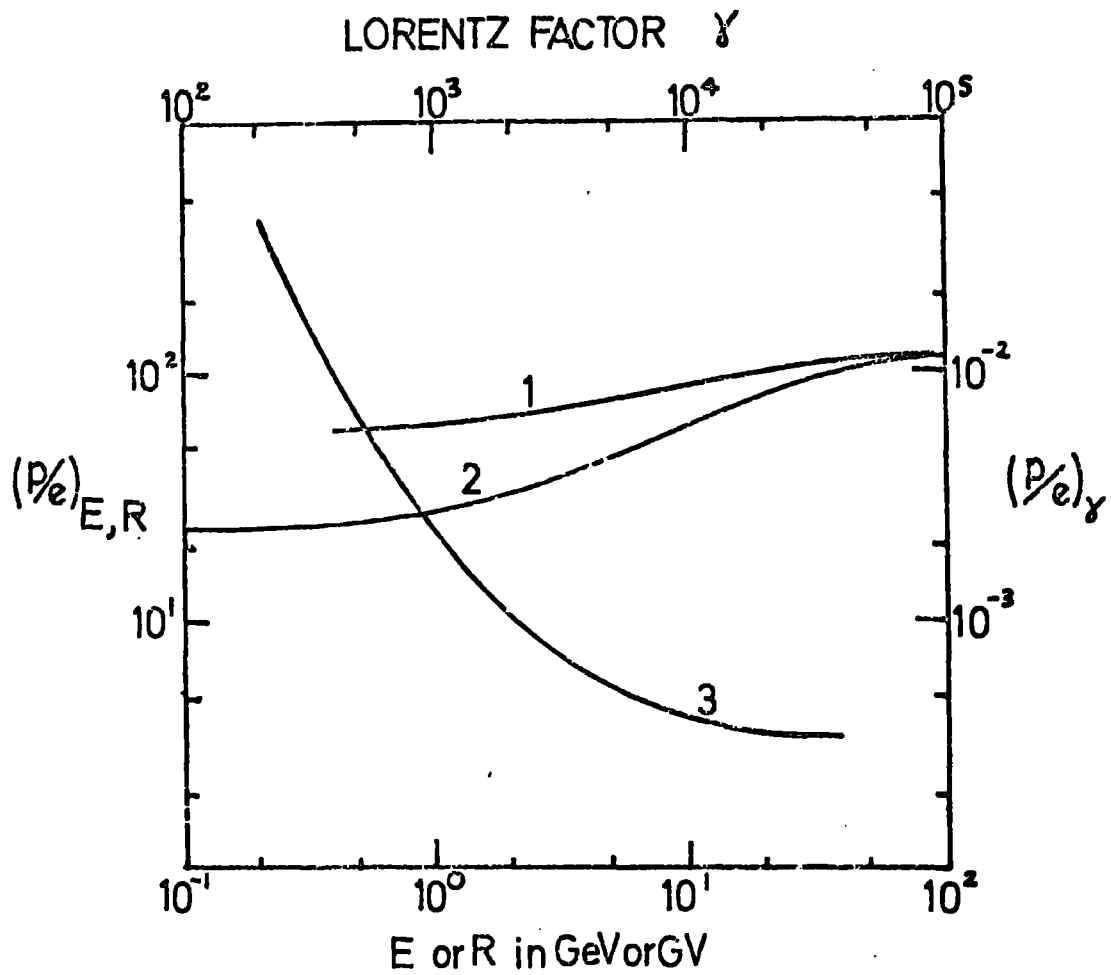$(p/e)_{E,R}$

$(p/e)_\gamma$

E or R in GeVorGV

Figure 2.6: The abundance ratio of protons to electrons as a function of rigidity (1), energy (2) and Lorentz factor (3) in interstellar space (Apparao and Daniel 1976)

intensity should be in the ratio $(m_e/mp)^{\gamma-1}$, where γ is the power law index. For $\gamma = 2.6$ this yields $e/p = 10^{-6}$ which is much lower than observed.

In pulsar models usually the same energy is imparted to protons and electrons and hence $e/p = 1$. This is much larger than the observed ratio.

Recently Apparao and Daniel (1976) have proposed that the existing observations on cosmic ray electrons and protons between a few hundred MeV. and about 1000GeV. can be well understood in a model where:-
(1) particles are accelerated in a mixed mechanism involving both betatron and Fermi acceleration processes with injection at a relatively lower temperature, (as the Fermi mechanism favours protons while the betatron mechanism favours electrons it is possible by a suitable mixing of the two to obtain the required ratio of electrons to protons).
(2) particles then escape into interstellar space from the source region in a rigidity dependent fashion and (3) the apparent excess of protons over electrons and its dependence on energy result from a combination of effects due to injection, acceleration and modulation in the source region and in the solar system.

The acceleration models required to obtain the observed primary e/p ratio are obviously fairly complex and at present not well understood.

2.4 Propagation of Electrons in the Galaxy.

The relative abundance of Li,Be and B with respect to C,N,O and F nuclei in the cosmic radiation is higher by more than five orders of magnitude than the corresponding universal abundance ratio. The general explanation for this anomalous abundance of light elements (L nuclei) is that they are produced by the nuclear fragmentation of heavier nuclei such as carbon, nitrogen, oxygen and fluorine (M nuclei), in nuclear interactions with the matter in the interstellar medium. (H,He and D nuclei) Any theory of the origin and propagation of cosmic rays should be able to

account not only for the presence of the light nuclei but also for their observed relative abundances. Figure 2.7 shows the observed L/M ratio versus energy up to nearly 100 Gev. At low energies, up to say 2Gev. the ratio appears to be fairly constant at approximately 0.23. Shapiro and Silverberg (1968) have calculated the average amount of matter traversed by cosmic rays required to create the observed abundance of light elements. Using a slab approximation, in which all the cosmic rays traverse the same amount of matter, they found that the slab thickness needed was $4.0^{+1.0}_{-0.5}$ g.cm^{-2}. The decrease of the L/M ratio at high energies may be attributed to an energy dependent leakage path length from the galaxy. In the following propagation models consistency of the inferred L/M ratio with 0.23 is demanded.

Before discussing propagation models for the galaxy as a whole, mention must be made of the effects the solar wind has on the lower energy particles (i.e. below a few GeV.) The modulation of cosmic rays is produced by the magnetic scattering of the cosmic ray particles in the many kinks and irregularities in the interplanetary magnetic field that are being convected outwards by the solar wind. The cosmic ray density is expected to approach the interstellar level at some distance from the sun greater than that of the earth. This expected variation of the modulated cosmic ray density with radial distance from the sun is known as the 'radial gradient', although it is probably a complex function of particle energy and time during the solar cycle. Calculations based on measured interplanetary magnetic field variations, Parker 1963, 1965 and Jokipii 1971, suggest that the modulation factor, by which the observed particle intensity must be multiplied, has the form exp $(-M(t)/R\beta)$ for rigidities between 0.5GV. and 5GV., where M is a time dependent constant and β is the ratio of the particle velocity to the velocity of light. Observations are best represented with a value of M = 0.4 to 1.0 GV. (Biswas et al. 1967, Gloecker and Jokipii 1967). For lower rigidities the observations suggest that the modulation is β dependent. The effects of solar modulation upon a particular model for the equilibrium electron spectrum will be considered in the last section of this chapter.
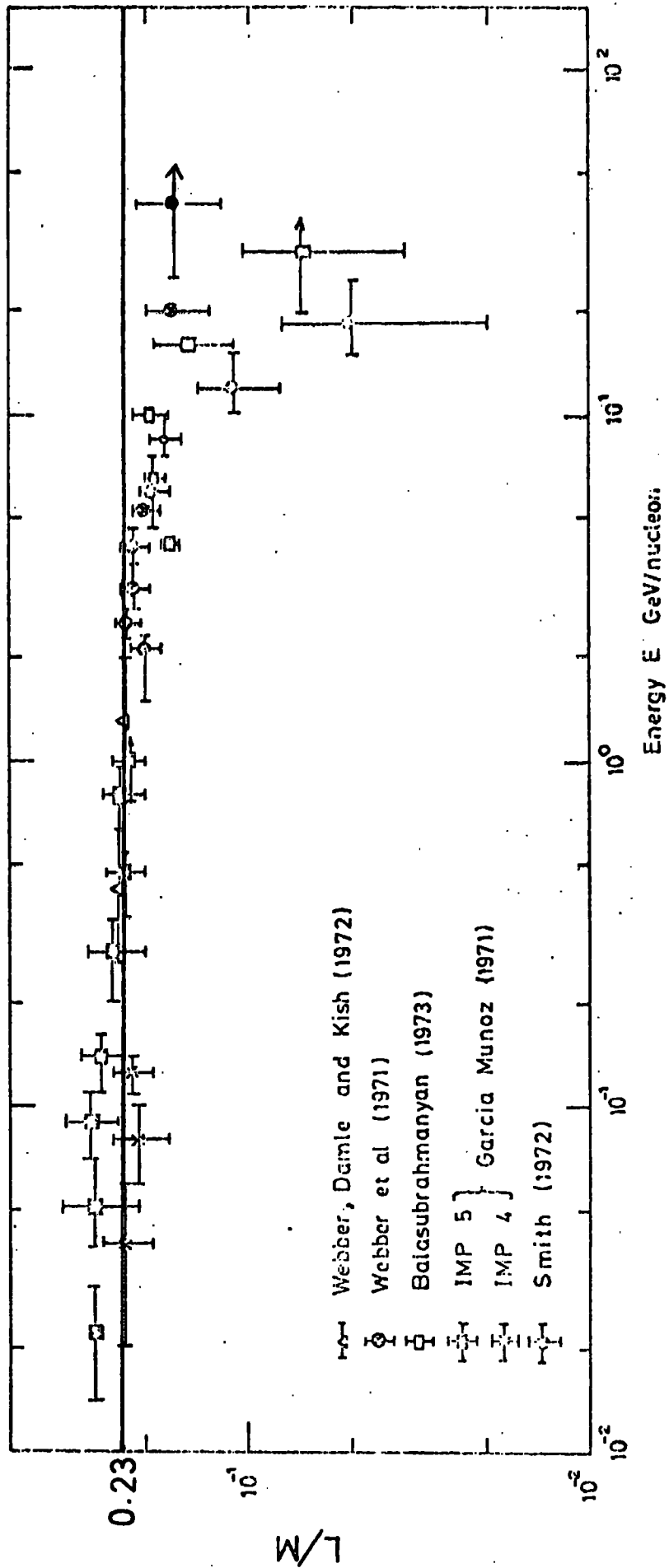
Figure 2.7: The L/M ratio against energy per nucleon. The line is at L/M=0.23 the value taken as constant up to 2GeV.

Models for the propagation of electrons must be set up to enable the equilibrium spectrum to be calculated from the source spectrum. As particle propagation on a small scale in the galaxy is obviously very complex the particles are usually treated in bulk and their propagation described in the diffusion picture.(Ginzberg and Syrovatskii 1964).

$$\frac{\partial n}{\partial t} - \nabla \cdot (D \nabla n) + \frac{\partial}{\partial E}(\dot{E}n) = q(\vec{x}, t, E) \qquad 2.5$$

represents the diffusion of electrons with sources and sinks in three dimensions. $n(\vec{r},t,E)$ is the position, time and energy dependent cosmic ray density and $q(\vec{r},t,E)$ is the source function. $D=1/3$ $lc\beta$ is the spatially and directionally independent diffusion coefficient corresponding to the mean free path, l, if the diffusion is isotropic. $\dot{E}$ is the rate of energy loss of an electron in interstellar space. For electrons the energy loss processes may be regarded as being continuous but for the case of protons catastrophic loss must be considered. This would be taken into account by introducing the extra term n/T onto the left hand side of equation 2.5, where T is a time characteristic of the catastrophic loss process.

Equation 2.5 may be simplified, in the so called homogeneous model, by replacing the diffusion term by n/T_e, where T_e is a characteristic lifetime of the electrons. For the equilibrium situation equation 2.5 reduces to:

$$q(\vec{x}, E) - n/T_e - \frac{\partial}{\partial E}(\dot{E}n) = 0 \qquad 2.6$$

which has very simple solutions for the two regions of energy where the energy loss dominates and where the escape term dominates. For a source spectrum of the form $q(E) = q_0 E^{-\Gamma}$ and energy losses of the Form $\dot{E} = kE^2$, corresponding to synchrotron and inverse Compton losses (see sections 2.2.4 and 2.2.1), one obtains the following solutions.

For $E \ll E_{cr}. = \dfrac{1}{kT_e(\Gamma - 1)}$

$n(E) = T_e\, q_0\, E^{-\Gamma}$ corresponding to

the situation where the escape term dominates and for

$E \gg E_{cr}.$

$$n(E) = q_0 \frac{E^{-(\Gamma+1)}}{k(\Gamma-1)}$$ corresponding

to the energy loss term dominating. This shows that at high energy one expects a steepening of the electron spectrum by one as compared with the spectrum at lower energies. In the above approximation since $k \gtrsim 10^{-16}$ (GeV.s.)$^{-1}$ the break in the spectrum is predicted to be at approximately 200 GeV. At present the electron observations, however, are not accurate enough to enable this break to be recognised, if present.

An n/T_e term may also be introduced into equation 2.5 for the case of a propagation region with reflecting boundaries. This term now approximates to the situation where the boundaries are partially reflecting and the electrons have a constant probability of escaping. The solution of equation 2.5, with the n/T_e term included, is approached by use of the Green's function solution leading to (Ramaty 1974)

$$n(\vec{\lambda},\,\vec{\lambda},\,E) = \int_0^{\Theta_{max}} \frac{\dot{E}(E_0)}{\dot{E}(E)} \exp\left[-\int_{E_0}^{E} \frac{dE'}{\dot{E}(E')\,T_e(E)}\right] \int d^3\lambda_0\, \varphi(\vec{\lambda},\vec{\lambda_0},\kappa)\, q(\vec{\lambda},E_0,\dot{L}-\Theta)\, d\Theta \quad 2.7$$

where the $\int d^3\lambda_0$ is taken over the spatial extent of the source distribution and where Θ, E_0 and κ are defined by:-

$$\Theta = \int_{E_0}^{E} \frac{dE'}{\dot{E}(E')} \quad 2.8 \qquad ; \qquad \kappa = \int_{E_0}^{E} \frac{dE'\, D(E')/D_0}{\dot{E}(E')} \quad 2.9$$

where D_0 is the diffusion coefficient at some fixed energy E_0.

$\varphi(\vec{\lambda},\vec{\lambda_0},\kappa)$ satisfies

$$\frac{\partial\varphi}{\partial\kappa} - \nabla^2\varphi = \frac{\dot{E}}{|\dot{E}|}\, \delta(\vec{\lambda}-\vec{\lambda_0})\, \delta(\kappa) \quad 2.10$$

Using the coordinate system and source region as shown in figure 2.8 and setting D=1c/3 for $/Z/ \lesssim a$ equation 2.10 has the solution

$$\varphi(\vec{\lambda},\,\vec{\lambda_0},\kappa) = \left(\frac{1}{4\pi D_\parallel \kappa}\right)\left(\frac{1}{4\pi D_\perp \kappa}\right)^{\frac{1}{2}} \exp\left[-\frac{(x-x_0)^2 + (y-y_0)^2}{4D_\parallel \kappa}\right]. \quad 2.11$$

$$\left\{\sum_{n=-\infty}^{n=+\infty} \exp\left[-\frac{(z-z_0-4na)^2}{4D_\perp \kappa}\right] \div \sum_{n=-\infty}^{n=+\infty} \exp\left[-\frac{(z+z_0+4na-2a)^2}{4D_\perp \kappa}\right]\right\}$$
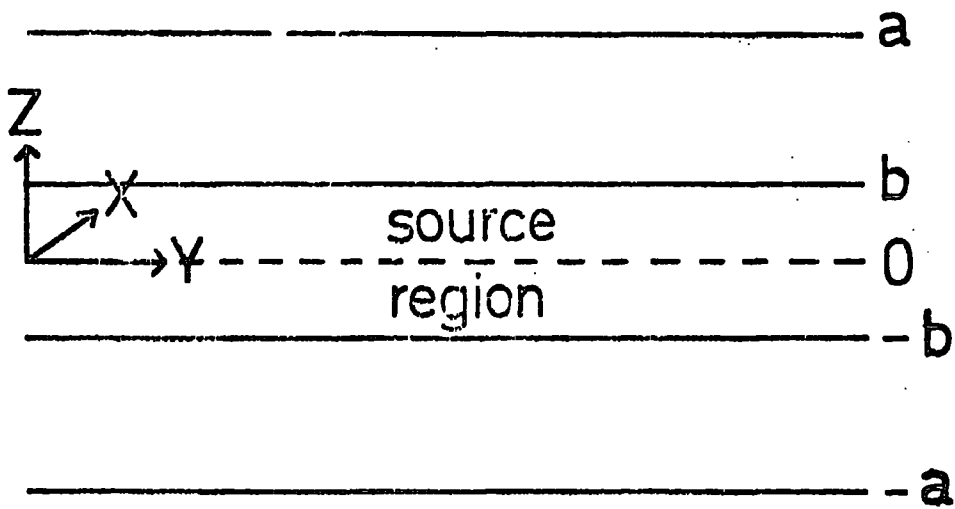
Figure 2.8: Geometry used in the various diffusion models. The source region lies within $Z = {}^{+b}_{-b}$ where $n_h = 1$ cm^{-3} and the boundaries of the propagation region are at $Z = {}^{+a}_{-a}$ within which $n_h = 0$.

where (-) or (+) correspond to absorbing or reflecting boundaries at

$z = \pm a$ and $D_{\parallel}$ and $D_{\perp}$ are the diffusion coefficients parallel and

perpendicular to the Y-axis. This form of solution is useful only

for $\frac{a^2}{D_{\perp} X} \gtrsim 1$, i.e. for times short compared with the characteristic

time for particles to reach the boundary. For longer times the

following solutions converge rapidly:

$$\varphi(\vec{\lambda}, \vec{\lambda}_0, X) = \left(\frac{1}{4\pi D_{\parallel} X}\right)\left(\frac{1}{4\pi D_{\perp} X}\right)^{1/2} \exp\left[-\frac{(x-x_0)^2 + (y-y_0)^2}{4 D_{\parallel} X}\right] \cdot$$
$$\left\{\left|\frac{1/2a}{0}\right| + \frac{1}{a}\sum \left|\frac{\cos}{\sin}\right| \frac{(n\pi(z_0+a))}{2a} \left|\frac{\cos}{\sin}\right| \left(\frac{n\pi}{2a}(z+a)\right) \exp -\left(\frac{n^2\pi^2}{4}\frac{D_{\perp} X}{a^2}\right)\right\} \quad 2.12$$

The upper terms referring to a reflecting boundary and the lower terms to

an absorbing boundary. Assuming the source function to be time

independent and a separable function of energy and position it may be

written as:

$$q(\vec{\lambda}, t, E) = q(E) \, \zeta(\vec{\lambda})$$

where q(E) depends on the production mode of the electrons and ζ (r)

is assumed in the simple case to be

$$\zeta(\lambda) = 1 \quad \text{for all X and Y and} \quad /Z/ < b$$
$$= 0 \quad \text{otherwise}$$

$D_{\perp}$ and $D_{\parallel}$ are assumed equal.

Substituting in equation 2.7 one obtains

$$n(\vec{\lambda}, E) = \int_0^{\theta_{max}} d\theta \, \frac{\dot{E}(E_0)}{\dot{E}(E)} \, q(E_0) \, \exp\left[-\int_{E_0}^{E} \frac{dE'}{\dot{E}(E')\, T_e(E')}\right] P(x) \quad 2.13$$

where $P(x) = \int d^3\lambda_0 \, \varphi(\vec{\lambda}, \vec{\lambda}_0, X) \, \zeta(\vec{\lambda}_0)$

$$\quad 2.14$$

represents the age distribution function of the electrons.

Therefore using equation 2.12 in equation of 2.14

$$P(x) = \frac{1}{2}\sum_{-\infty}^{+\infty}\left(\text{erf}\left[\frac{b-z-4na}{(4DX)^{1/2}}\right] - \text{erf}\left[\frac{-b-z-4na}{(4DX)^{1/2}}\right]\right) \quad 2.15$$

$$+ \frac{1}{2}\sum_{-\infty}^{+\infty}\left(\text{erf}\left[\frac{b+z+4na-2a}{(4DX)^{1/2}}\right] - \text{erf}\left[\frac{-b+z+4na-2a}{(4DX)^{1/2}}\right]\right)$$

Here the error function is defined to be $\text{erf}(u) = \int_0^u \exp(-x^2)dx$

The corresponding solution for longer times compared with the time for the electrons to reach the boundary is

$$P(x) = \begin{vmatrix} b/a \\ 0 \end{vmatrix} + \frac{4}{\pi} \sum_{n=1}^{\infty} \frac{1}{n} \exp\left(-\left(\frac{n\pi}{2a}\right)^2 DX\right) \begin{vmatrix} \cos \\ \sin \end{vmatrix} \quad 2.16$$

$$\left(\frac{n\pi}{2a}(z+a)\right) \cdot \begin{vmatrix} \cos \\ \sin \end{vmatrix} \left(\frac{n\pi}{2}\right) \sin\left(\frac{n\pi}{2}\frac{b}{a}\right)$$

From section 2.2 and figure 2.4 it is apparent that for electrons of a few GeV. the dominant energy loss mechanisms are Compton losses, in the Thomson regime, and synchrotron losses and therefore $\dot{E} = -kE^2$

where $k = 4 \times 10^{-6}H_{\perp}^2 + 10^{-16}(\rho_{ph.}(\text{starlight}) + \rho_{ph.}(\text{black body}))_{(\text{GeV.s.})^{-1}}$

2.17

where $H_{\perp}$ is in Gauss and $\rho_{ph.}$ is in eV/cm^3.

Applying 2.17 to equation 2.8 leads to

$$\theta = \frac{E_0 - E}{kEE_0}$$

and if the source is assumed to be a power law given by $q(E) = AE^{-\Gamma}$ equation 2.13 may be written in the form

$$n(E,z) = AE^{-\Gamma} \int_0^{1/kE} d\theta (1-kE\theta)^{\Gamma-2} \exp\left[-\int_E^{E_0} \frac{dE}{kE'^2 T_e(E')}\right] P(\theta,z) \quad 2.18$$

Here D has been taken as energy independent making $\gamma = \theta$ from equations 2.8 and 2.9. If T_e is also energy independent

$$n(E,z) = AE^{-\Gamma} \int_0^{1/kE} d\theta (1-kE\theta)^{\Gamma-2} \exp\left(-\theta/T_e\right) P(\theta,z) \quad 2.19$$

This equation enables the equilibrium spectrum for electrons to be determined once the source spectrum and $P(\theta)$ have been decided upon. For the absorbing boundary case $T_e = \infty$ but for the case of an exponential age distribution, i.e. $P(\theta) = 1$, which corresponds to the situation discussed following equation 2.6, and for the reflecting boundary case, T_e needs to be determined such that the models reproduce the observed L/M ratio. For the absorbing boundary case the situation for reproducing the

L/M ratio is more complex and will be discussed later.

Therefore considering the production of L nuclei in more detail (Lingenfelter 1971): the equilibrium density n_j of isotope j resulting from the fragmentation of isotope i with equilibrium density n_i can be written as

$$n_j(E) = \sum_{i=j+1}^{N} n_h\, c\, \sigma_{ij}\, n_i(E) \int_0^\infty d\theta\, \exp\left(-n_h^* c\, \sigma_{jj}\theta\right) \exp\left(-\theta/T_e\right) \quad 2.20$$
$$\int d^3\lambda_o\, \varphi(\vec{\lambda},\vec{\lambda_o},\theta)\, f(\vec{\lambda_o})$$

where σ_{ij} and σ_{jj} are the fragmentation cross sections of isotope i into isotope j and the total breakup of isotope j respectively. The first n_h term is the hydrogen density in the production region taken to be constant at $n_h = 1$ cm^{-3} in this work. The n_h^* term occurs, however, in the expression $n_h^* c\, \sigma_{jj}$ which gives the rate of attenuation of isotope j per unit time and here one should use an effective value for n_h which takes into account the fact that the nuclei will have spent a fraction of the time outside the production region. In general n_h^* will be a function of θ and $n_h^* = (n_h(\theta))$ effective will be less than n_h. One can see the effect of this on the relation between the L/M ratio and the equilibrium electron spectrum by rewriting equation 2.20 in the form

$$n_L(E) = n_h\, c\, \sigma_{LM}\, n_H(E) \int_0^\infty d\theta\, \exp\left(-\frac{(n_h(\theta))_{eff.}}{T_L}\cdot\theta\right) \exp\left(-\theta/T_e\right) P(\theta) \quad 2.21$$

where σ_{LM} is the effective cross-section for the production of a light nucleus by a heavy nucleus and T_L is the fragmentation lifetime of light nuclei in a medium with $n_h = 1$cm^{-3} (for a mean free path against fragmentation of 10g.cm^{-2} corresponding to $\sigma_L = 160$ m barns, $T_L \approx 6.4 \times 10^6$ years). Equation 2.19 can be written in a similar way to equation 2.21.

$$n_e(E) = n_h\, c\, \sigma_{p-e}\, n_{cA}(E) \int_0^{1/kE} d\theta\, (1-kE\theta)^{\Gamma-2}\, \exp\left(-\theta/T_e\right) P(\theta) \quad 2.22$$

where the source function $AE^{-\Gamma}$ has been written as $n_h c\, \sigma_{p-e}\, n_{cr}(E)$ where σ_{p-e} is some effective cross-section for the production of electrons of energy E per cosmic ray nucleus of the same energy. For the exponential age distribution $P(\theta) = 1$ and $(n_h(\theta))$ eff. $= n_h$ and therefore 2.21 becomes

$$\frac{n_L}{n_M} = c\,\sigma_{LM} \int_0^\infty d\Theta \exp -\left(\frac{\Theta}{T_L} + \frac{\Theta}{T_e}\right)$$

$$= c\,\sigma_{LM} \left(\frac{1}{T_L} + \frac{1}{T_e}\right)^{-1}$$

<div align="right">2.23</div>

For the reflecting boundary situation the electrons will be distributed uniformly throughout the confinement region and, except for very small values of Θ , i.e. about the time for diffusion to the boundary, $(n_h(\Theta))$ eff. $= \frac{b}{a}\,n_h$ and from equation 2.16 $P(\Theta) = b/a$ and therefore the integral in equation 2.21 becomes

$$\int_0^\infty \frac{b}{a}\, \exp\left(-\left(\frac{b}{a}\frac{\Theta}{T_L} + \frac{\Theta}{T_{eA}}\right)\right) = \frac{b}{a}\left(\frac{b}{a}\frac{1}{T_L} + \frac{1}{T_{eA}}\right)^{-1}$$

where T_{er}^0 is the escape lifetime appropriate for a reflecting boundary. Because the L/M ratio is fixed

$$\left(\frac{1}{T_L} + \frac{1}{T_e}\right)^{-1} = \frac{b}{a}\left(\frac{b}{a}\frac{1}{T_L} + \frac{1}{T_{eA}}\right)^{-1} \qquad T_{eA} = \frac{a}{b}\,T_e$$

At low energies the effective age of cosmic ray electrons for the exponential case is T_e while for the reflecting case it is $b/a\ T_{er}$ which is equal to T_e. Thus at low energies the two cases predict exactly the same secondary equilibrium electron spectrum. T_e for the exponential age distribution may be determined from equation 2.23 using effective values for σ_{LM} and T_L obtained from cross-section measurements. (Ramaty 1974) For $n_h = 1\mathrm{cm}^{-3}$ and fixing $n_L/n_M = 0.23$ $T_e = 3.3 \times 10^6$ years. Figure 2.9 shows a graph of equilibrium density/source function against energy for the exponential age distribution with $T_e = 3.3 \times 10^6$ years. and for the reflecting boundary case for a=200 pc..and b=100 pc. with $T_{er}=6.6 \times 10^6$ years. As discussed above both these models are consistent with the observed L/M ratio of 0.23.

The treatment of the exponential age distribution and the reflecting boundary case given above is similar to that appearing in Ramaty (1974). Several errors appearing in his treatment have been corrected particularly those in connection with the agreement with the observed L/M ratio. Solutions to the equations for the age distributions have also been expressed in more convenient forms.
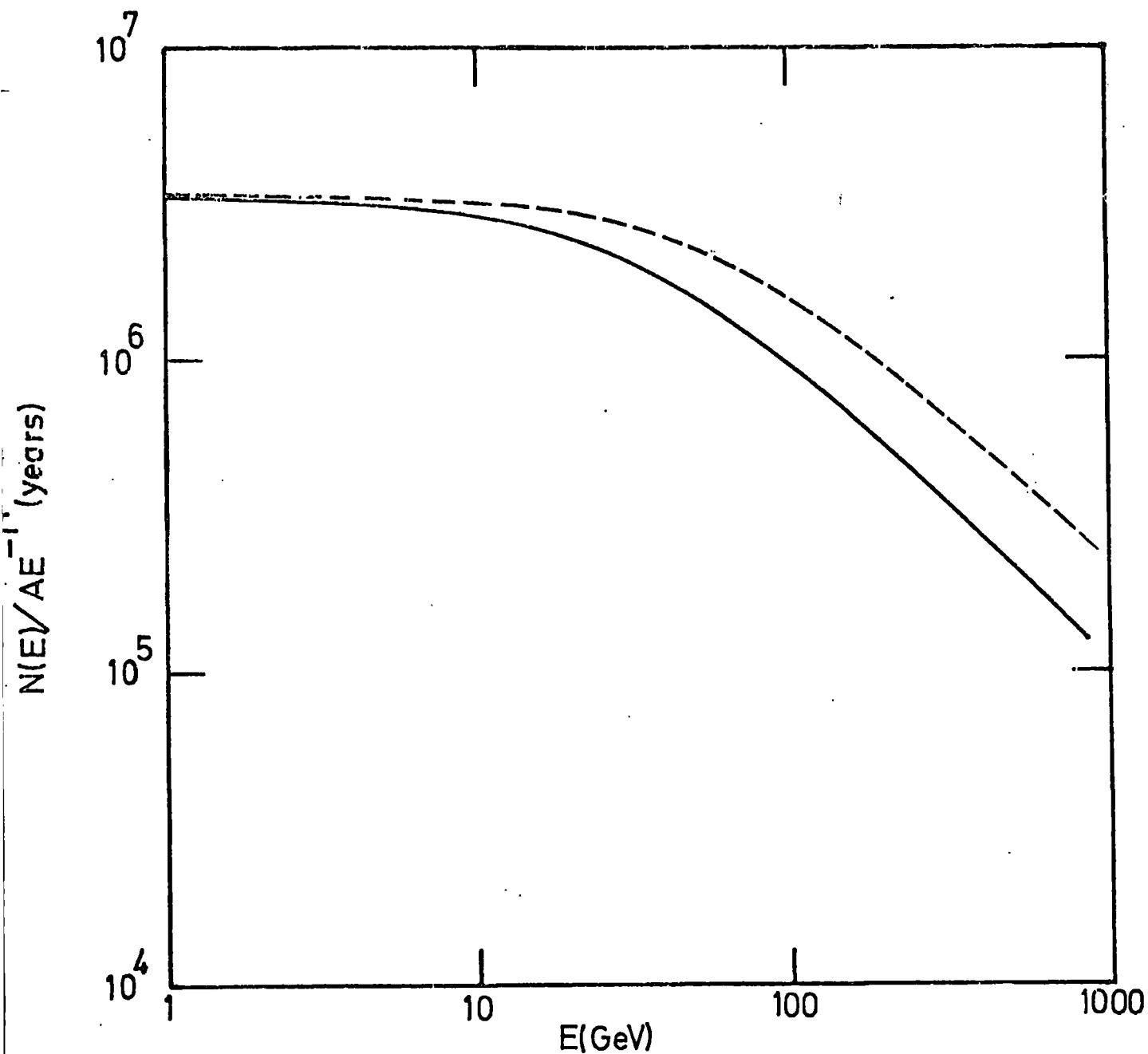
Figure 2.9: Equilibrium density/source function versus energy for an exponential age distribution with T_e = 3.3 X 10^6 yrs. (———) and for a reflecting boundary (————) with a/b = 2 and T_{er} = 6.6 X 10^6 yrs. Both these models are consistent with the observed L/M ratio of 0.23.

Before continuing with the absorbing boundary case it is worth

considering the effects of an energy dependent lifetime as inferred

from the gradual decrease of the L/M ratio with increasing energy

(figure 2.7).

If the escape lifetime is expressed as $T_e(E) = T_1(E_1/E)^{-\delta}$

equation 2.18 reduces to

$$ n(E) = AE^{-\Gamma} \int_0^{1/kE} d\theta (1-kE\theta)^{\Gamma-2} \exp\left[\frac{-E^\delta(1-(1-kE\theta)^{\delta-1})}{EkT_1 E_1^\delta(\delta-1)(1-kE\theta)^{\delta-1}}\right] P(\theta) \quad 2.24 $$

rather than equation 2.19.

Using $q(E)_e+ = 1.266 \times 10^{-17} E^{-2.9} \, cm^{-2}.s^{-1}.sr^{-1}.GeV^{-1}$;

(Ramaty 1974) as the source spectrum for secondary positrons and using

equation 2.24 it is possible to see the effects of an energy dependent

lifetime on the equilibrium spectrum of positrons. Figure 2.10 shows

the equilibrium spectrum for positrons in the case of an exponential

age distribution for various values of δ . In all cases $E_1 = 2GeV$.

and $T_1 = 3.3 \times 10^6$ yrs. From the observations in figure 2.7 it is

thought that $\delta \approx 0.3$. As can be seen from figure 2.10 such a value of δ

has very little effect on the equilibrium spectrum in the region of

present measurements.

Returning to the case of an absorbing boundary: it is necessary

to calculate the mean free path, l, that satisfies the observed L/M ratio

so that this can be substituted in equation 2.15 or 2.16 and the equilibrium

spectrum determined using equation 2.19. To obtain the correct value for

l one can use a treatment due to Ptuskin (1972). Figure 2.8 shows the

situation under consideration. As before the source region is confined

to a region with half width of b= 100 pc. with gas density $n_h = 1cm^{-3}$.

The absorbing boundary is placed at a distance of 5kpc. from the plane.

From work by Baldwin (1976) this is thought to be the sort of height

above the plane at which the emissivity has fallen to zero (see later
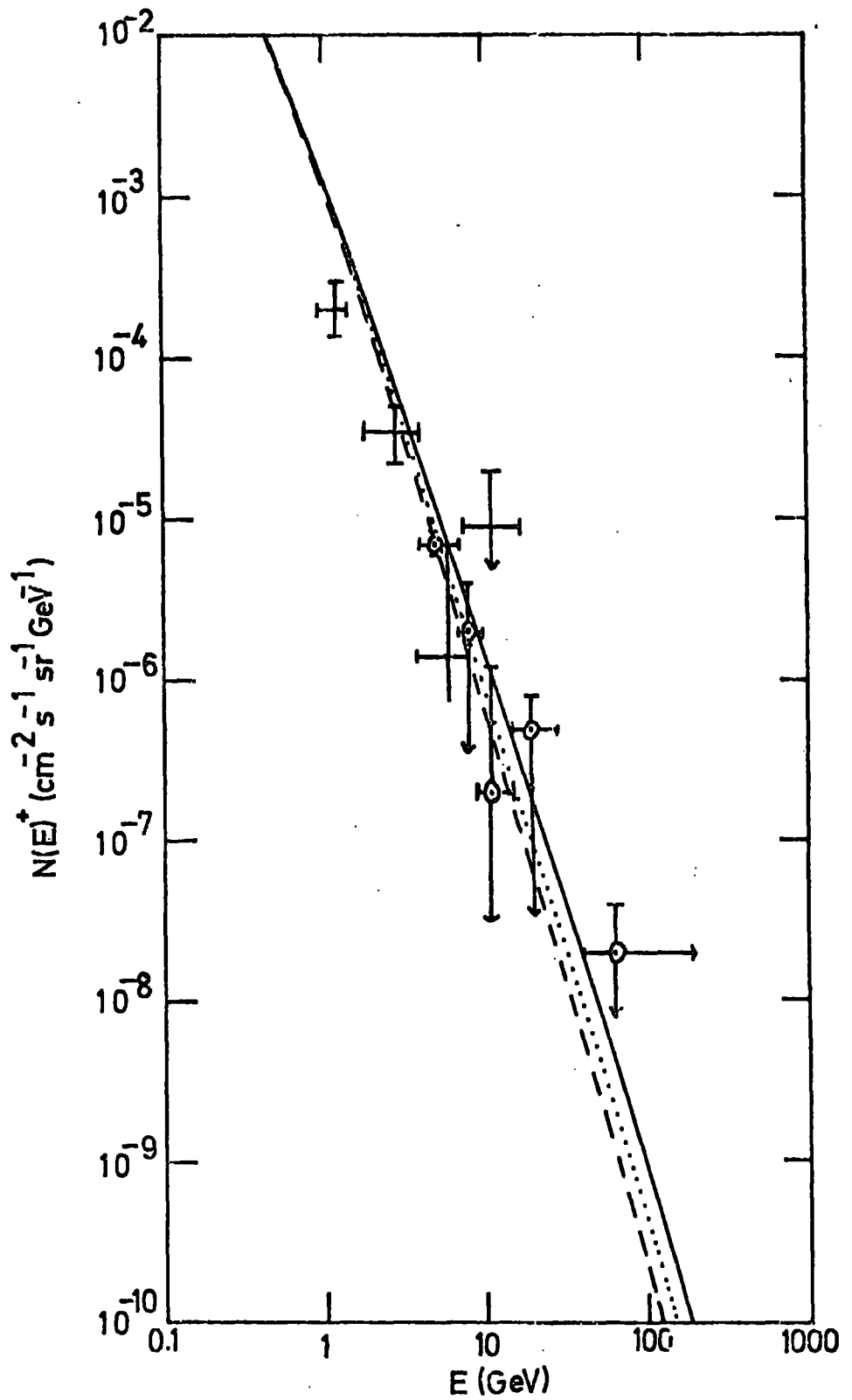
chapters for further discussion).

Figure 2.10: Equilibrium positron spectra for an exponential age distribution for various values of δ as defined in the text. —— $\delta = 0$, ······ $\delta = 0.3$, ———— $\delta = 0.5$. The observations are ⊙ Buffington et al. (1975) and ⊢⊤⊣ Fanselow et al. (1969).

Following Ptuskin (1972), the propagation of nuclei may be considered to satisfy a one-dimensional steady state diffusion equation with allowance for fragmentation:

$$-\frac{D\,\partial^2 N_i}{\partial z^2} = -n_h\, c\, \sigma_i\, N_i + \sum_{k>i} n_h\, c\, \sigma_{ik}\, N_k + q_i \qquad 2.25$$

where σ_i is the total inelastic cross-section for a nucleus i,

σ_{ik} is the cross-section for the production of a nucleus i from a nucleus k, q_i is the source density of nuclei i and the summation is over all nuclei heavier than type i. Equation 2.25 has a solution of the form

$$N_i = \sum_{k \geq i} a_{ik}\, F_k \qquad 2.26$$

where the coefficients a_{ik} are determined by recurrance formulae and are linear combinations, q_k. These coefficients appear in the solution of a system of the type.

$$\frac{\partial y_i(t)}{\partial t} + \sigma_i\, y_i(t) = \sum_{k>i} \sigma_{ik}\, y_k(t) \qquad 2.27$$

$$\text{with } y_i(0) = q_i$$

and the solution has the form

$$y_i(t) = \sum_{k=i}^{\infty} a_{ik}\, \exp(-\sigma_k t)$$

$F_k(z)$ is determined from

$$-D\frac{d^2 F_k}{dz^2} = -n_h\, c\, \sigma_k\, F_k + \Theta(b-|z|)$$

where the last term expresses the situation of the sources being within b of the galactic plane. From the conditions of continuity of F_k and $\frac{dF_k}{dz}$ at b and $F_k = 0$ at the boundary (i.e. at $Z=a=5$kpc.)

$$F_k(z=0) = \frac{1}{n_h c \sigma_k}\left[1 - \left[ch\left((n_h c\sigma_k/D)^{1/2} b\right) + sh\left((n_h c\sigma_k/D)^{1/2} b\right)(n_h c\sigma_k/D)^{1/2}(a-b)\right]^{-1}\right] \qquad 2.28$$

By considering the two groups of nuclei, L and M, rather than the individual nuclei Ptuskin obtains approximate values for the cross-sections $\sigma_M = 190$ mb., $\sigma_L = 132$ mb. and $\sigma_{LM} = 80$mb.

With $q_L = 0$ and using equations 2.26 and 2.27

$$O = q_L = \frac{1}{F_L}\left(N_L + \frac{\sigma_{LM}}{\sigma_M - \sigma_L}\; N_M\right) - \frac{N_M}{F_M}\; \frac{\sigma_{LM}}{\sigma_M - \sigma_L}$$

and therefore
$$\frac{F_L}{F_M} = 1 + \left(\frac{\sigma_M - \sigma_L}{\sigma_{LM}}\right)\frac{N_L}{N_M} \qquad 2.29$$

substituting $X = \frac{b^2 n_h c}{D}$ and combining equations 2.28, 2.29

gives

$$1 + \frac{\sigma_M - \sigma_L}{\sigma_{LM}}\; \frac{N_L}{N_M} =$$

$$\frac{\sigma_M}{\sigma_L}\; \frac{\left[1 - \left[ch\,(X\sigma_L)^{1/2} + sh\left(X\sigma_L\right)^{1/2}(X\sigma_L)^{1/2}\,\frac{a-b}{b}\right]^{-1}\right]}{\left[1 - \left[ch\,(X\sigma_M)^{1/2} + sh\,(X\sigma_M)^{1/2}(X\sigma_M)^{1/2}\,\frac{a-b}{b}\right]^{-1}\right]}$$

Using the values for the cross-sections given above, a = 5000 pc., b= 100 pc. and with N_L/N_M = 0.23, X = 9.74 x 10^{-5} mb^{-1} corresponding to a diffusion coefficient D = 2.92 X 10^{28} $cm^2 s^{-1}$ and a mean free path l = 0.95 pc. Figure 2.11 shows the way in which l varies with a. Therefore to obtain the equilibrium spectrum for an absorbing boundary at 5kpc. from the plane with l=0.95 pc. equation 2.15 or 2.16 needs to be solved for P(θ) and then equation 2.19 evaluated with $T_e = \mathcal{O}$ and $k = 1/300$ $My^{-1}GeV.^{-1}$ if we assume H = 3μG. Figure 2.12 shows the variation of equilibrium density/source function with energy for various values of Z, height above the plane. For Z=0 the graph shows two changes in slope of a half; one at approximately 1GeV. and the other at about 3000GeV. For E<E_1=D/a^2k≈1.2 GeV. the particles are lost by escape through the boundary at a, for E>E_1 and E<E_2=D/b^2k≈2900GeV. the particles are lost due to energy losses before reaching the boundary at a and for E>E_2 the particles are lost due to energy losses before reaching the boundary at b, i.e. they are confined to the source region. For Z>b a continuous increase in slope is seen once the energy is greater than E_1. Figure 2.13 shows the rate of fall-off of the electron density at various energies
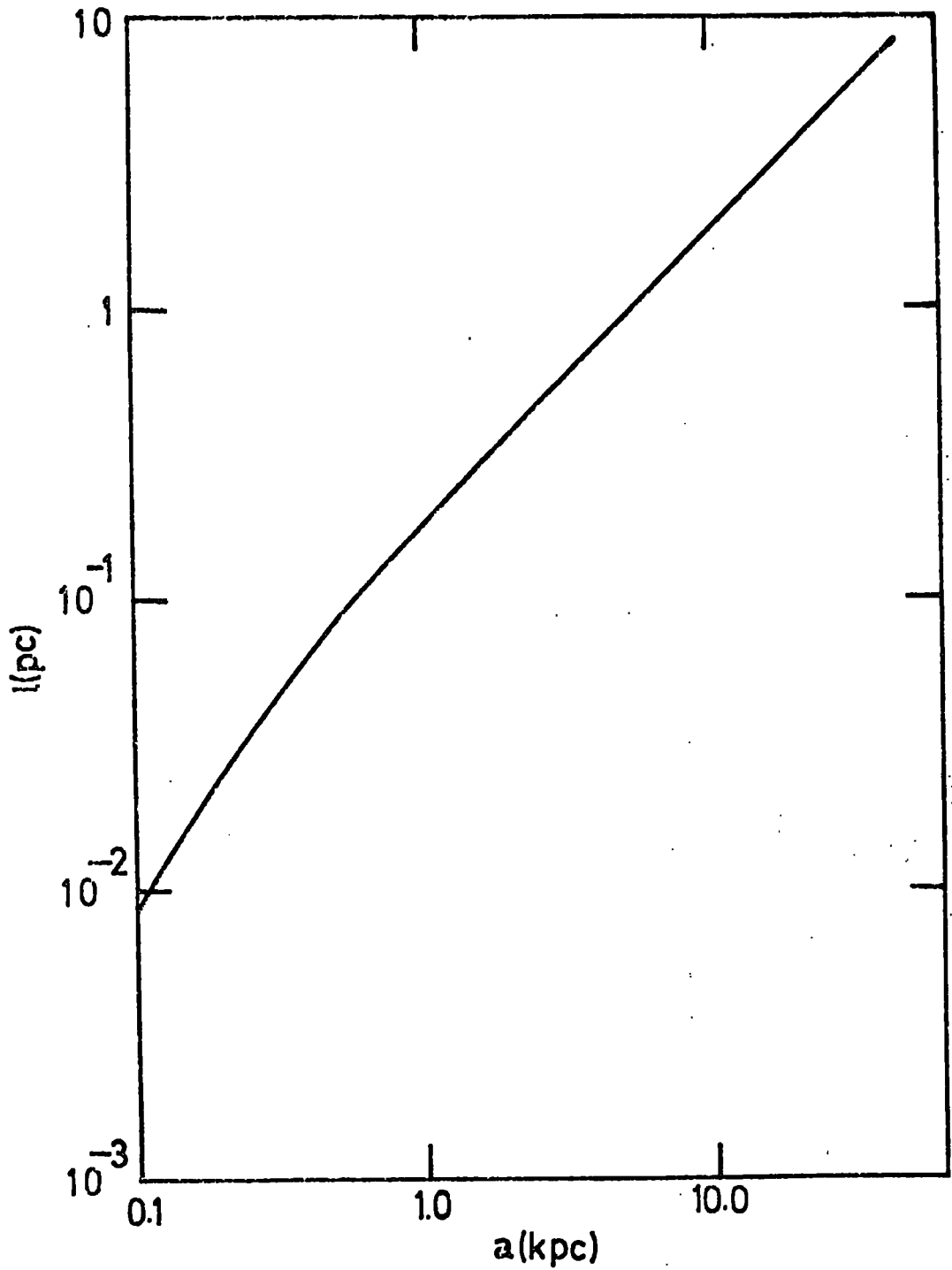
Figure 2.11: The mean free path, l, as a function of the height of the absorbing boundary above the plane.

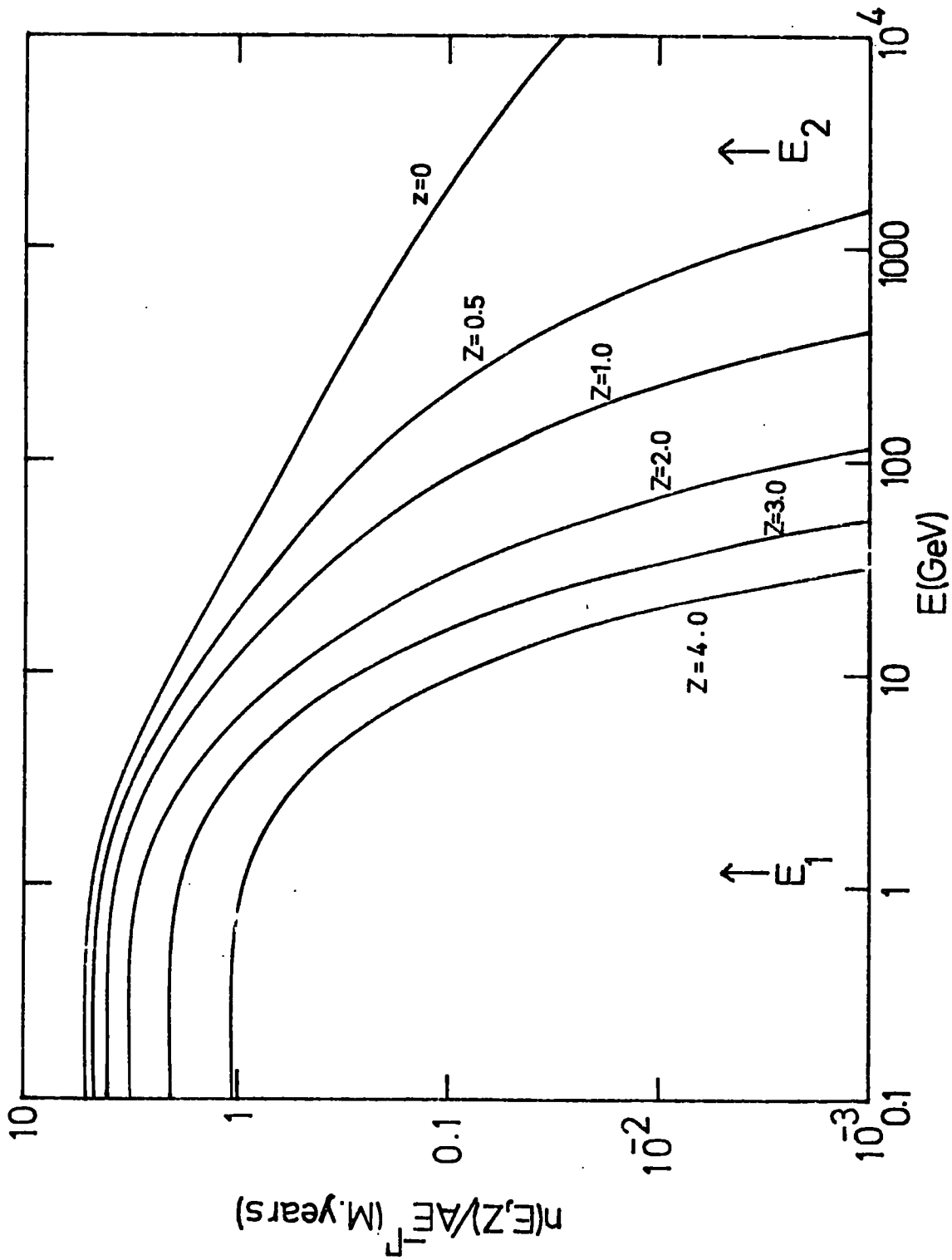**Figure 2.12:** The variation of equilibrium density/source function with energy for various heights Z (kpc) above the plane. E_1 and E_2 are the energies at which the spectral index changes for Z=0.
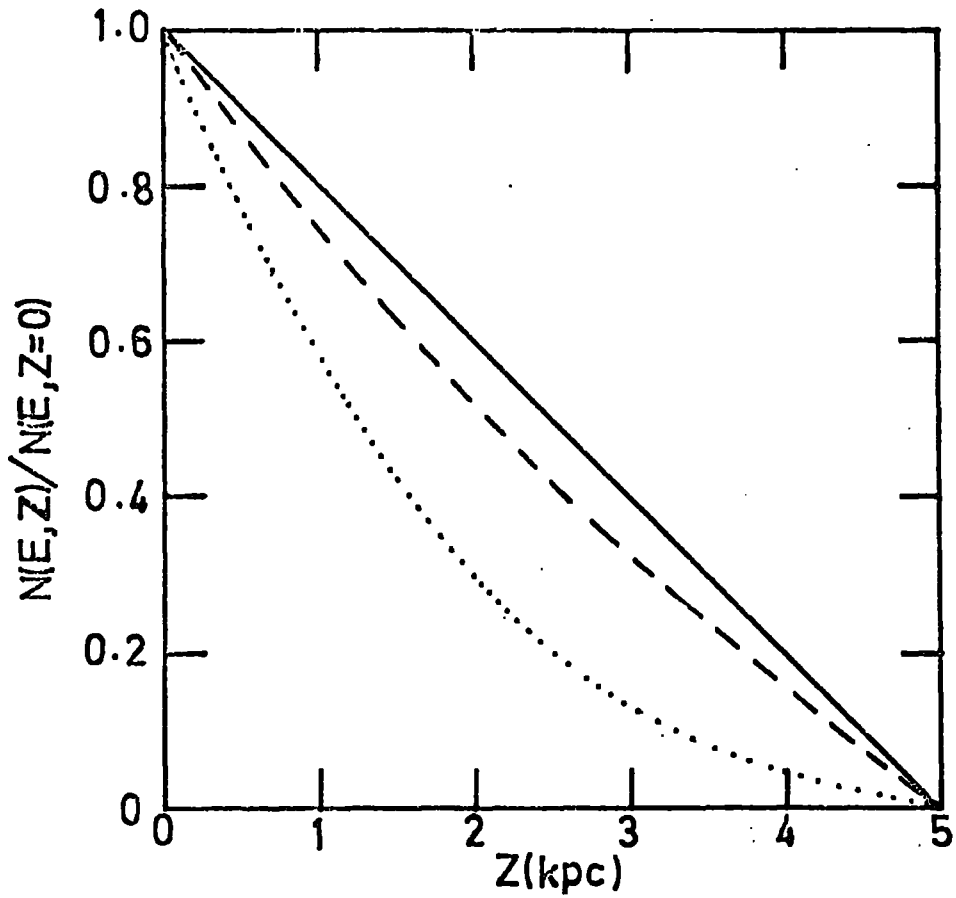
Figure 2.13: The rate of fall-off of electron density with height above the plane for the case of an absorbing boundary at 5 kpc. for various energies; ———— 1 GeV, ———— 3 GeV, ... 10 GeV.

with height above the plane. For electrons of a few GeV. it can be seen that this fall-off is approximately linear implying that the energy losses are relatively unimportant and that the electrons are lost mainly by escape through the boundary at **a** . Recently Owens and Jokipii (1977) have described a one-dimensional diffusion model for the galactic halo in which they include the possible convection of particles out of the plane by a galactic wind, Ipavich 1975. For an absorbing boundary at 5kpc. they find that the convection has very little effect on electrons with energies of a few GeV. Therefore the density of electrons in this energy range, to a good approximation, may be considered to fall linearly with height above the plane. Propagation of electrons away from the plane in a model such as this will be applied in chapters 6 and 7 to a three dimensional model for the continuum radiation.

Bulanov and Dogel (1974) have considered the situation of diffusion with absorbing boundaries but with an energy dependent diffusion coefficient. For $D(E)=D_0(E/Eo)^\mu$ with $\mu < 1$ they find that the spectrum also shows two breaks, with index changing from $\Gamma + \mu \rightarrow \Gamma + \frac{1}{2}\mu + \frac{1}{2} \rightarrow \Gamma + 1$. The breaks now occur at

$$E_1 = \left[\frac{D_0}{a^2 (1-\mu) E_0^\mu k} \right]^{1/(1-\mu)} \qquad E_2 = \left[\frac{D_0}{b^2 (1-\mu) E_0^\mu k} \right]^{1/(1-\mu)}$$

corresponding to the same regions of propagation as previously discussed in the case of constant diffusion coefficient.

2.5 Comments on a Closed Galaxy Model for Cosmic Ray Propagation.

(French and Osborne 1976)

In contrast to the models of cosmic ray propagation already presented, Rasmussen and Peters (1975) have presented a model accounting for the observed elemental composition of cosmic rays in which the particles do not escape from the confinement region but are eventually absorbed by meson producing interactions with the interstellar gas (the closed galaxy

model). All protons result from the spellation of heavy nuclei and the observed light element abundance is accounted for by invoking a local source which contributes about 15% of the incident nucleons. A flux of positrons is produced from the decay of mesons generated by the interactions of the cosmic ray nuclei with the interstellar gas. Figure 2.14, which is adapted from a figure of Orth and Buffington (1975) shows the positron intensity calculated by them for a diffusion model with an exponential age distribution with $T_e = 3 \times 10^6$ years and $X_o = \langle \rho \rangle c \, T_e = 4g./cm^2$ (the leaky box model). For the case of no escape from the Galaxy, as is appropriate to the closed galaxy model, the calculation of the positron equilibrium intensity is simple. From the observed equilibrium flux of nucleons Orth and Buffington obtain

$$Q(E) = 8.48 \times 10^{-14} E^{-2.65} n_h \quad (m^{-2}.sr^{-1}.s^{-1}.GeV^{-1})/s$$

as the rate of production of positrons of energy E GeV. where n_h is the effective mean density of the interstellar gas traversed by the cosmic rays in nucleons cm^{-3}. For the steady state, when the positron intensity has reached its equilibrium value N(E), the diffusion equation, with no escape term, is

$$Q(E) = q_0 E^{-\Gamma} = \frac{d}{dE} (\dot{E} N(E))$$

where $\dot{E} = bE^2 + aE$ is the rate of energy loss, the first term corresponding to synchrotron and inverse Compton losses and the second to bremsstralung. The solution of this equation is $N(E) = q_0 E^{-\Gamma} (\Gamma - 1)^{-1} (Eb+a)^{-1}$. Using $b = 1.0 \times 10^{-16} \ GeV.s^{-1}$ and $a = 8 \times 10^{-16} n_h \ GeV.s^{-1}$.

$$N(E) = 514 \ E^{-2.65} \frac{n_h}{(E + 8n_h)} \quad m^{-2}.sr^{-1}.s^{-1}.GeV^{-1}$$

To compare this with observations the modulation of the intensity by the interplanetary magnetic field has to be included. The form of the modulation, as discussed in the previous section, for E>1GeV. is thought to have the form $exp(-E_{mod}/E)$. The value of the modulation parameter, E_{mod}, has been obtained in a number of ways. The form of the interstellar electron spectrum can be deduced from the non-thermal radio background spectrum (Goldstein et al. 1970). This spectrum can then be normalised
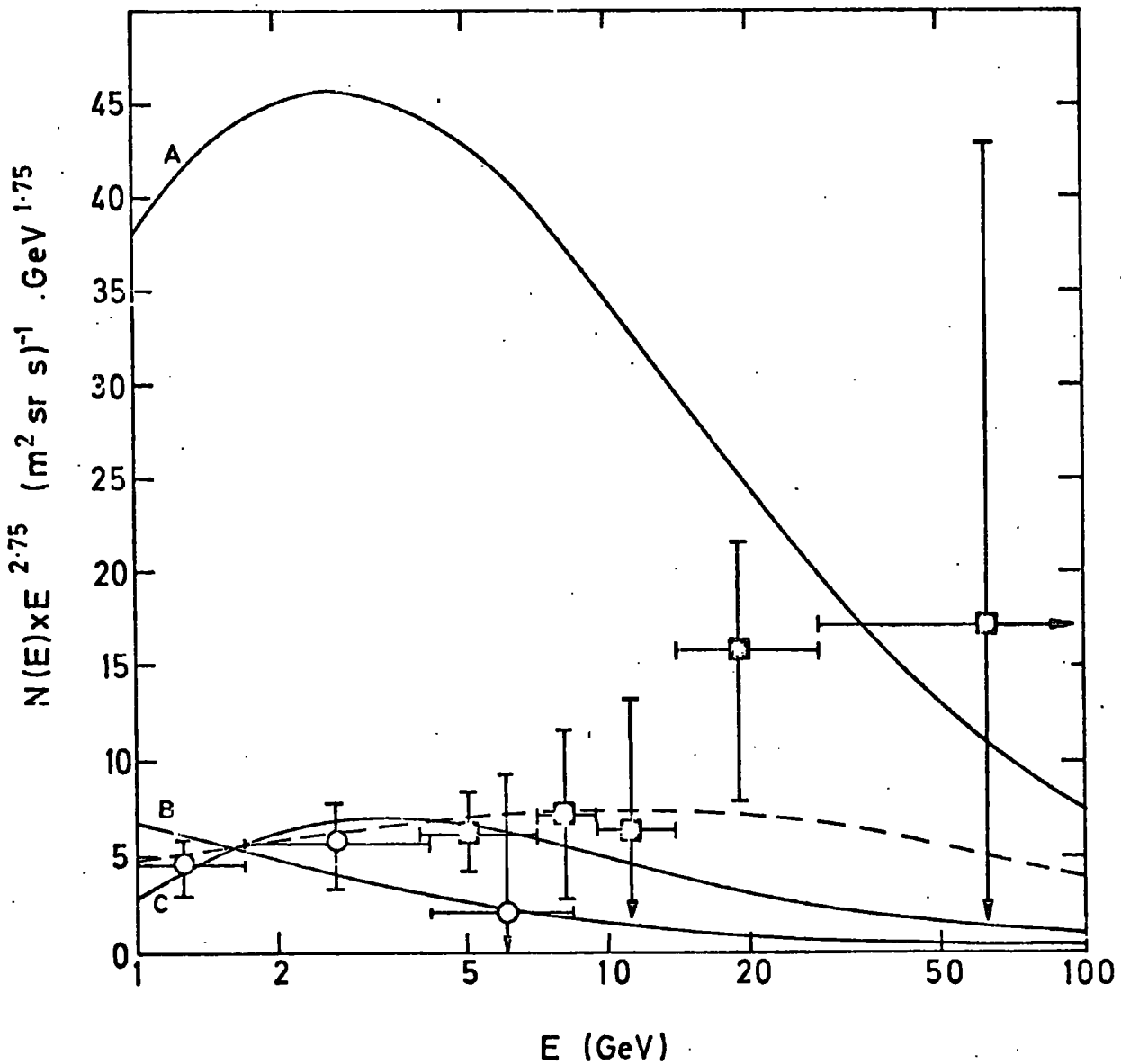
Figure 2.14:   Positron intensities above 1 GeV. — — — — — Leaky - Box
model with average matter traversal of 4g cm^{-2} and
$E_{mod.}$ = 0.4GeV; ————— closed galaxy model with various
values of $E_{mod.}$ and n_h (see text). O Fanselow et al. (1969), ▣
Buffington et al. (1975).

to the observed electron intensity above 10GeV. where modulation can be assumed to be negligible. Alternatively, the modulation can be deduced from comparison of the observed and predicted interstellar energy spectra of nuclei of secondary origin such as helium-3 and deuterium (Ramaty and Lingenfelter 1968). Care must be taken, however, to avoid circular arguments in which the secondary spectra are predicted assuming that the leaky box model is correct.

The leaky box model spectrum in figure 2.14 was obtained using $E_{mod.} = 0.4$ GeV. and $n_h = 1cm^{-3}$. Curve A is the calculated positron spectrum for the closed galaxy model for the same values of these parameters. The observations fit the former curve but show that either a lower value of n_h or a higher value of $E_{mod.}$ is required by the closed galaxy model. It is not unreasonable to reduce n_h as a value near unity would imply that cosmic rays are confined close to the plane of the galaxy while a much larger confinement volume is natural for the closed galaxy model. Curve B is obtained by fixing $E_{mod.} = 0.4$ GeV. and varying n_h to give a weighted best fit to the observations. The optimum value is $n_h = 0.027$ cm^{-3}. implying that the confinement volume extends to about twenty times the scale height of the gas above the plane and that the lifetime of cosmic rays in the galaxy is about 5×10^9 years. There is some uncertainty in the value of E_{mod}. If we take an extreme view and regard it as a free parameter we can obtain the joint optimum values for n_h and E_{mod}. The best fit is curve C which has $n_h = 0.1cm^{-3}$. and $E_{mod.} = 2.3$ GeV. It is not possible to rule out a modulation as large as this, at least down to 1GeV, although the non-thermal radio background would favour a smaller value.

Independent evidence is provided by the galactic gamma ray emission above 100MeV from around the anticentre direction. Dodds et al. (1975) have shown that if nuclear cosmic rays filled the disk with their local interstellar density out to the edge of the galaxy (at a distance from the galactic centre, R, of 20 to 30 kpc.) their interactions with the observed neutral hydrogen would produce twice as many gamma-rays as observed. Agreement with

observations is obtained if, for instance, the cosmic ray intensity decreases with R as exp-((R-10)/2.44kpc.), in proportion to the mass density, or if the intensity remains constant out to a boundary at R=/2kpc. and is zero beyond it.. This type of behaviour is unlikely for the closed galaxy model, which favours a large confinement volume with a uniform cosmic ray intensity. The gamma-rays are produced by cosmic ray nuclei in the 1-10GeV. energy range. E_{mod}=0.4GeV was assumed in deriving the local interstellar intensities of nuclei used by Dodds et al from those observed at the earth. If the larger modulation of Curve C were applied, the intensity would be greater and the discrepancy in the gamma-ray flux would be increased by a further factor of two. As pointed out by Ramaty and Westergaard (1976) the increase in the interstellar electron density would result in an increase in the observed gamma-rays through electron bremsstralung. It would result in about 50% of the galactic gamma-ray emission at photon energies greater than 100 MeV. being due to Bremsstralung interactions.

It therefore seems that although the closed galaxy model can be reconciled with the observed positron flux as shown in figure 2.14 there are difficulties in making it agree at the same time with the observed gamma-ray flux.

References

Abraham, P.B., Brunstein, K.A. and Cline, T.L., 1966, Phys. Rev. 150 1088.

Apparao, K.M.V., and Daniel, R.R., 1976 Preprint.

Balasubrahmanyan, V.K., and Ormes, J.F., 1973, Ap. J. 186, 109

Baldwin, J.E., 1967, I.A.U. Symp. 31 337

Baldwin, J.E., 1976 in The Structure and Content of the Galaxy and Galactic Gamma Rays, ed. Stecker, F.W., (NASA Goddard space flight centre, preprint) 206

Bethe, H.A., and Heitler, W., 1934 Proc. Roy. Soc. A146 83.

Beuermann, K.P., Rice, C.J., Stone, E.C., and Vogt, R.E., 1969 Phys. Rev. Letts. 22 412

Biswas, S., Ramadurai, S., and Sreenivasan, N., 1967 Phys. Rev. 159 1063

Blumenthal, G.R., and Gould, R.J., 1970 Rev. Mod. Phys. 42 237.

Buffington, A., Orth, C.D., and Smoot, G.F., 1975 Ap. J. 199 669-79.

Bulanov, S.V., and Dogel, V.A., 1974 Astrophys. and Space Sci. 29 305-318

Cline, T.L., and McDonald, F.B. 1968 Canadian J. Phys. 46 S761

Cline, T.L., and Porreca G., 1970 Acta Physica Academiae Scientarium Hungaricae 29 suppl. 1 145

Cummings, A.C., Stone, E.C., and Vogt, R.E., 1973 13th. Int. Conf. Cosmic Rays, Denver 1 340.

Daugherty, J.K. 1974 Goddard Space Flight Centre preprint X-660-74-16.

Dickel, J.R., 1974 Ap. J. 193 755-757

Dodds, D., Strong, A.W., and Wolfendale, A.W., 1975, M.N.R.A.S., 1971 569-577

Earl, J.A., 1961, Phys. Rev. Letts. 6 125

Fanselow, J.L., Hartman, R.C., Hildebrand, R.H., and Meyer, P., 1969, Ap. J. 158 771-780.

Fazio G.G, Stecker, F.W., and Wright, J.P., 1966, Ap. J. 144 611

French, D.K., and Osborne, J.L., 1976 Nature 260 372.

Ginzberg V., and Syrovatski, S.I., 1964, Origin of Cosmic Rays Pergamon Press, New York

Gloeker, G., and Jokipii, J.R., 1967 Ap. J. 148 141

Goldstein, M.L., Ramaty, R., and Fisk, L.A., 1970 Phys. Rev. Letts. 24 1193-1196

Hayakawa, S., Nishimura, J., Obayashi, H., and Sato, H., 1964 Suppl. Prog. Theor. Phys. 30 86

Hurford, G.S., Mewaldt, R.A., Stone, E.C., and Vogt, R.E., 1973 Pric. 13th. Int. Conf. Cosmic Rays, Denver 1 324.

Ipavitch, F.M., 1975, Ap. J. 196 107.

Jokipii, J.R., 1971 Rev. Geophys. Space Phys. 9 27.

Kiepenheuer, K.O., 1950, Phys. Rev. 79 738

Kniffen, D.A., Cline, J.L. and Fichtel, C.E., 1970 Acta Physica Academiae Scientarium Hungaricae 29, Suppl. 1 187-194

Lingenfelter, R.E., 1971 Proc. 12th. Int. Conf. Cosmic Rays, Hobart OG106

Meyer, P. and Vogt, R., 1961 Phys. Rev. Letts. 6 193.

Meyer, P. in Origin of Cosmic Rays, N.A.T.O. Advanced Study Inst. eds. Osborne, J.L., and Wolfendale, A.W., ch.3

Orth, C.D., and Buffington, A., 1975 Proc. 14th. Int. Cosmic Ray Conf., Munich 1 411

Owens, A.J. and Jokipii, J.R., 1977 Ap. J. 215 677-689

Parker, E.N. 1963 Interplanetary Dynamical Processes, John Wiley, New York

Parker, E.N. 1965 Planet. Space Sci. 13 9

Perola, G.C., Scarsi L., and Sironi G., 1967, II Nuovo Cimento LIIB 455-471

Ptuskin, V.S., 1972 Kosmicheskie Issledovaniya 10 351-357

Ramaty, R., and Lingenfelter, R.E., 1968 Phys. Rev. Letts. 20 120-124

Ramaty, R., Stecker, F.W., and Misra, D., 1970 Acta Physica Academiae Scientaiarum Hungaricae, Suppl. 1 165

Ramaty R., 1974 in High Energy Particles and Quanta in Astrophysics eds. McDonald, F.B., and Fichtel, C.E. Ch.3.

Ramaty, R., and Westergaard, N.J. 1976 Astrophys. Space Sci.

Rasmussen, I.L., and Peters, B., 1975, Nature 256, 412.

Shapiro, M.M., and Silverberg, R., 1968 Can J. Phys. 46 S561

Smith, L.H., Buffington, A., Smoot, G.F., Alvarez, L., and Wahlig, M.A., 1973 Ap. J. 180 987.

Teegarten, B.J., McDonald, F.B., Trainor, J.H., Webber, W.R., and Roelof, E.C., Goddard Space Flight Centre, preprint X-660-74-197, 1974.

Verma, S.D., 1969, Ap. J. 156 479

Webber, W.R., Damle, S.V., and Kish, J. 1972 Astrophys. Space Sci. 15, 245

Webber, W.R., Damle, S.V., and Kish, J. 1971 Ap. J. Letts. 9 125

CHAPTER 3

THE GALAXY AND THE INTERSTELLAR MEDIUM

3.1 Introduction

This chapter introduces some properties of the galaxy and the interstellar medium that are pertinent to the discussions in future chapters. Discussion of spiral structure is left until the next chapter as this requires a more in depth treatment as it is the basis for the synchrotron models developed in chapters six and seven.

3.2 Structure of the Galaxy

3.2.1 Mass

The matter of the Galaxy is in the form of stars, dust and gas distributed mainly in a flat disc. The total mass of the Galaxy is 2×10^{11} $M_\odot$ (solar masses). The greatest fraction of the matter is in its approximately 10^{11} stars. The total mass of gas in the form of atomic hydrogen, estimated from the 21 cm. emission, is about 5×10^9 $M_\odot$. In addition there is molecular hydrogen, helium and heavier elements, which may bring the mass of gas up to 10% of the total mass of the Galaxy.

3.2.2. Position of the Sun

The sun lies within 12pc. of the galactic plane. The centre of the galaxy is in the constellation Sagittarius at 265.6° R.A., -28.9° dec. Its distance can be found by estimating the distance of RR lyrae variable stars in the central condensation (Arp 1965). The usually accepted value of 10 kpc will be used throughout this thesis. It should be noted, however, that recently Oort and Plaut (1975) have obtained the value 8.7 $\pm$ 0.6 kpc from RR lyrae stars and Crampton and Georgelin 1975 have obtained 9 kpc from the observation of distant H II regions at 90° from the galactic centre. In fact the models developed in later chapters are not very sensitive to the value taken as most of the parameters scale with it.

The position of the sun relative to the galactic spiral structure will

be discussed in great detail in the next chapter and in the chapters

describing the various models. It is obviously of great importance

as to whether our local environment is typical of an arm or interarm

region.

3.2.3 The Distribution of Stars

Figure 3.1 displays a cross-section of the galaxy showing contours

of mass density in stars in units of the smoothed density near the sun.

The diameter of the disc is about 30 kpc. and the sun is thus at 2/3 of the

radius from the centre. The black dots on the figure indicate positions

of globular star clusters projected onto the plane through the sun and the

galactic centre. These, the oldest stellar systems, form a roughly spherical

halo of radius 15 kpc. The surface density of all stars projected onto

the galactic plane is strongly peaked towards the galactic centre. (For

clarity the central contours have been omitted from the figure). Beyond

about 1 kpc from the galactic centre the surface density falls approximately

as exp (-R/4kpc).

The Z (height above the plane) distribution of stars is of importance

as will be discussed later in connection with the height to which spiral

structure might extend. Results of the measurement of the Z-distributions

of various spectral classes of stars have been summarised by Elvius (1965).

The distributions may be represented by

$$D_S(z) = D_S(0) \exp(-z/\beta)$$ 3.1

where $D_s(0)$ is the density of a particular class, S, of star at the plane

and β represents a scale factor or effective z thickness of that class.

Table 3.1 lists β for various classes of star. It should be noted that

for an exponential distribution, as given above, $z_{1/2} = 0.94\beta$ where $2z_{1/2}$

is the distance between half density points on either side of the galactic

plane. Also listed in table 3.1 are several other population I objects
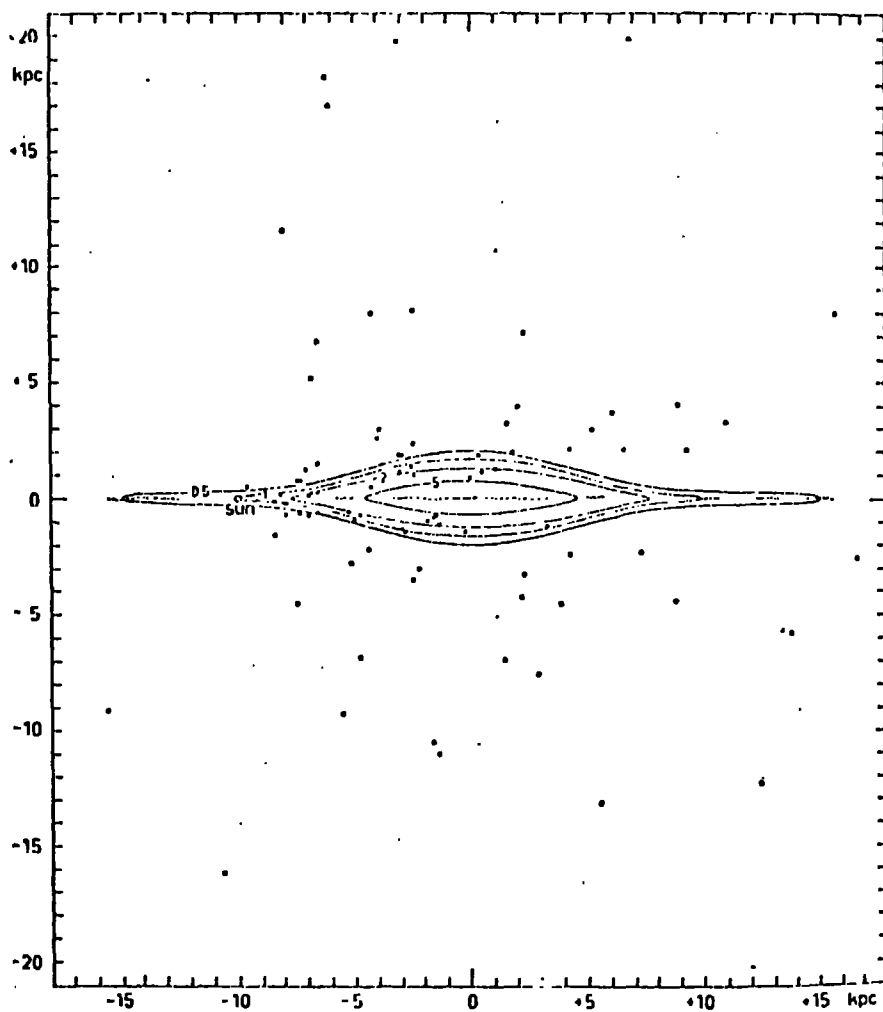
for comparison.

Figure 3.1: Distribution of Globular Clusters projected

on a plane perpendicular to the galactic plane through

the sun and centre,and lines of equal mass density. The

steep increase in density in the inner parts is not indicated.

Shaded parts give a schematic representation of the distri-

bution of interstellar gas and extreme population I.

(J. H. Oort in "Galactic Structure", Chicago, 1965).

Table 3.1 (Allen 1963)

Object	$\beta(pc)$	Characteristic Population
O	50	I
B	60	I
A	115	I
G,K,M	340	Mixed
Interstellar dust and gas	125	I
Cepheid Variables	45	I
Galactic clusters	80	I

3.2.4 Galactic Rotation

Since the mass in the galaxy is centrally concentrated, the stars travel, very roughly, in Keplerian-like orbits about the galactic centre. Hence, the smaller the orbit, the shorter is the star's period of revolution and the greater is its orbital velocity. This is referred to as the differential galactic rotation first studied in detail by Oort 1927.

A determination of the linear rotation velocity $\Theta(r)$ as a function of distance from the galactic centre is of considerable interest when discussing models of spiral structure such as density wave theory. The value of Θ at the sun, Θ_0 may be estimated from the local group of galaxies or from globular clusters and is found to be $250 \pm 30 \; km \; s^{-1}$ in the direction $\ell \approx 70^\circ, b \approx 0$, implying a period of rotation for the sun about the galactic centre of 2.5×10^8 years. When requiring information on the variation of Θ with galactic radius a radio technique is required to avoid the problem of interstellar absorption.

Neutral hydrogen possesses a hyperfine transition in its ground state which gives rise to a spectral line lying in the radio region of the spectrum at approximately 21cm.

Observations of this line enable the distribution of neutral hydrogen in the galaxy to be determined as well as $\Theta(r)$. Results on the distribution of neutral hydrogen will be presented in the next chapter but the method will be described here as it differs very little from the technique for measuring $\Theta(r)$.

The splitting of the ground state of neutral hydrogen is caused by the proton and electron having spin which give rise to magnetic moments that interact. This interaction causes the substate in which the spins are aligned to lie at a slightly higher energy than the substate in which the spins are opposed. The energy difference between these two substates corresponds to 1420.406 MHz, 21.105 cm. As the interstellar medium is

not at absolute zero the upper substate may become populated due to collisions

between the atoms.   Once in the upper substate an atom may de-excite to the

lower state either by a further collision or by a radiative transition emitting

a photon of frequency 1420.406 MHz.   As this radiative transition is strongly

forbidden its transition probability is very low;   it occurs once in 3.5×10^{14}

seconds or about 10^7 years.   The line at 21 cm. is observed due to the fact that

a vast number of atoms are observed along any line of sight.   The profile

observed is complex.   It is spread out in frequency due to different atoms

along the line of sight having different velocities due to galactic rotation

causing the transition frequency to be doppler shifted by different amounts.

The intensity of the radiation (the area under the complete profile) is

proportional to the total number of hydrogen atoms along the line of

sight.   The observed profiles can be interpreted to give information on

both $\Theta(r)$ and on the distribution of HI.   The radial velocity (i.e. velocity

away from the sun) at distance r from the galactic centre may be written as

$$ V_R \;=\; R_o \left(\Omega(r) - \Omega_o \right) \, \sin \left(\ell^{I\!I} \right) \qquad\qquad 3.2 $$

where $\Omega(r)$ and Ω_o are the angular velocity of rotation at r and R_o respectively

and $\Omega_o = \Theta_o / R_o$ with Θ_o and R_o known.   The radial velocity V_R attains a

maximum from regions where $r = r_{min} = R_o \sin 1^{I\!I}$ and therefore by determin-

ing the maximum radial velocity for varying $\ell^{I\!I}$ between 0 and 90° (from

the northern hemisphere) and between 270° and 360° (from the southern

hemisphere) it is possible to construct the rotation curve $\Omega(r)$ or $\Theta(r)$

versus r for $r \lessgtr R_o$.   This was first done by Kwee et al. 1954.   This

technique assumes that the HI gas is undergoing true circular motion.   For

r>10kpc the optical measurement of Cepheid variables is required to obtain

$\Theta(r)$ (Kraft and Schmidt 1963). Figure 3.2a gives the general rotation

curve for the galaxy as presented by Contopolus and Stromgren (1965).   They

have derived an interpolation polynomial for $\Theta(r)$ for $3 \leqslant r \leqslant 13$ kpc.

$$ \Theta(r) \;=\; 67.76 + 50.06\,r - 4.0448\,r^2 + 0.0861\,r^3 \; km\,s^{-1} $$
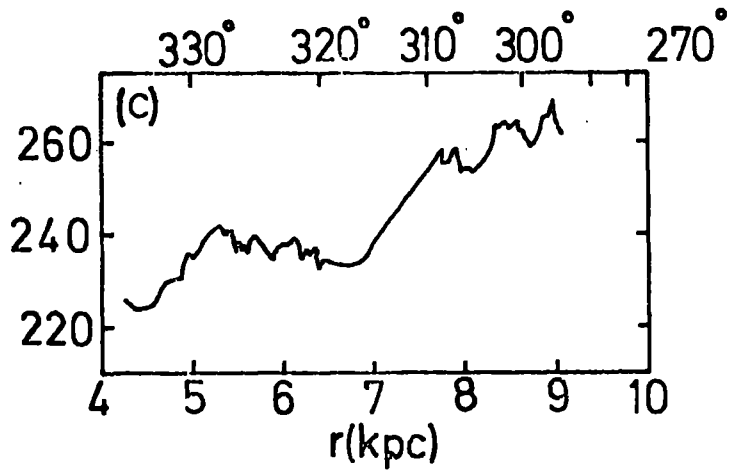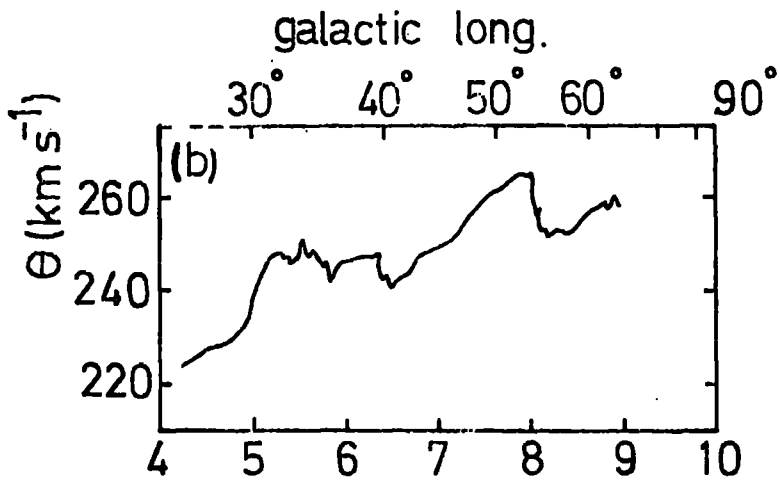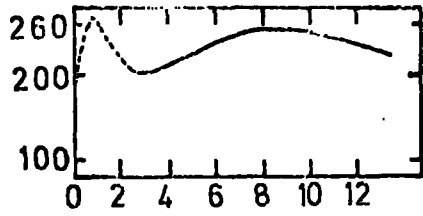
(a)

galactic long.

Figure 3.2:   (a) General rotation curve for the galaxy by Contopolus
and Stromgren (1965).

          (b) Detailed rotation curve for northern hemisphere.

          (c) Detailed rotation curve for southern hemisphere.

If the rotation curve is measured in more detail it is seen to differ
from that given in figure 3.2a as shown in figures 3.2b and 3.2c (Lin 1968).
The deviation from circular rotation is due in part, in the central regions
of the galaxy, to the expanding 3kpc. arm, and to streaming motions within
spiral arms. The difference in the rotation curves for the northern and
southern hemispheres reflect the fact that the streaming motions within the
spiral arms are not circularly symmetric with respect to the galactic centre
but rather that they follow an overall spiral pattern.

Schmidt (1965) developed a mass model for the galaxy which reproduces
the observed values for Oort's constants and $\theta(\lambda)$ for r = 3.5, 6, 8 and 10 kpc.
The model consists of a central mass point of 0.07×10^{11} $M_\odot$, a spheroid of
mass 0.82×10^{11} $M_\odot$, eccentricity e = 0.812 with semimajor axis R_0 and a
nonhomogeneous spheroidal shell exterior to the sun given by

$$\rho(\lambda > R_0) = 1.5 \times 10^3 / \lambda^4 \, M_\odot \, pc^{-3}$$

Figure 3.3 shows the rotation curve of the galaxy as derived from the Schmidt
mass model. Also shown is the corresponding variation of the epicyclic
frequency $\times$ where

$$x^2 = (2\theta)^2 \left\{ 1 + 2\lambda/\theta \, \frac{d\theta}{d\lambda} \right\}$$

which will be of interest when discussing spiral structure in the next chapter.
The Schmidt model of the galaxy is normally considered as the starting point
for a theory of the spiral structure (chapter 4) but a complete theory should
be able to explain the structure seen in the observed rotation curves figures
3.2b and c.

Once a form for $\theta(\lambda)$ has been decided upon it is possible by using
equation 3.2 to infer the distance d from which the hydrogen radio radiation
is received. For r $>$ R_0 this procedure is unambiguous but for $\lambda < R_0$
there are two values of d along any line of sight with the same $\theta(\lambda)$.
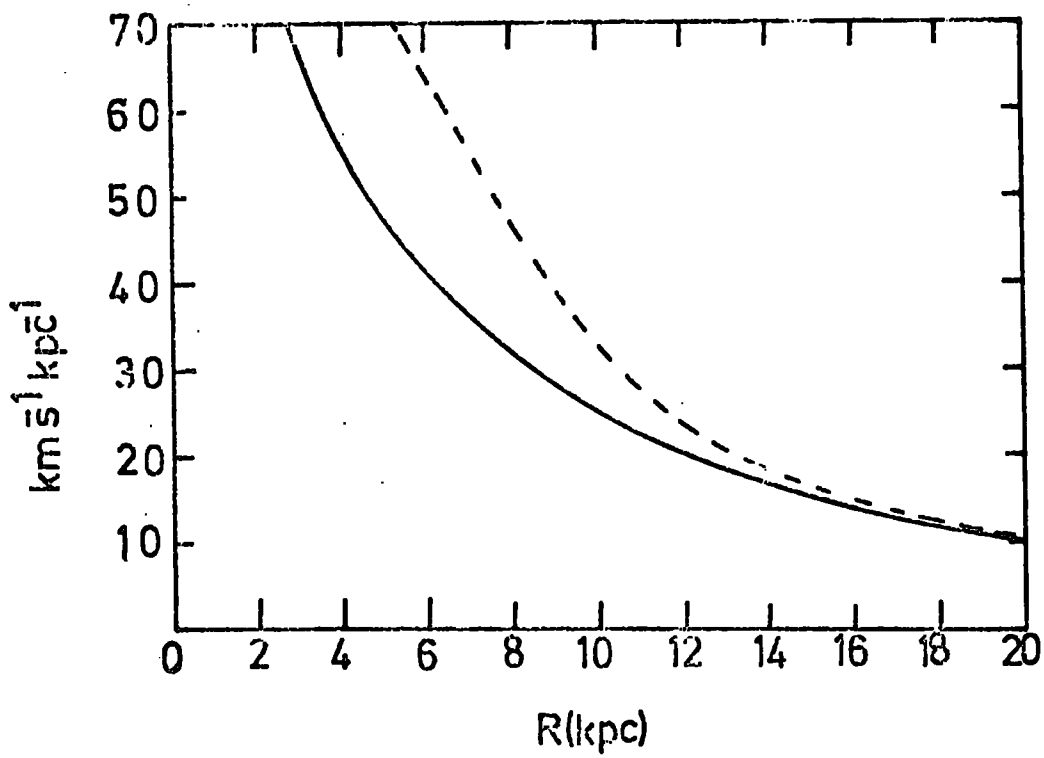The results from this technique for mapping HI will be discussed in the
next chapter.

Figure 3.3: ———— Schmidt rotation curve.

  — — — Epicyclic frequency, χ.

3.3 Properties of the Interstellar Medium

3.3.1 Constituents of the Interstellar Medium

The interstellar medium consists of gas, dust and cosmic rays, the latter being considered, as far as the dynamics are concerned, as a hot tenuous gas. The chemical composition, by weight, of the gas is hydrogen 70%, helium 28% and heavier elements 2%. The commonly quoted figure for the gas density in the plane is 1atom cm^{-3}. The gas is either neutral-atomic, ionised or molecular. These various states of the gas together with their distribution in the galaxy will be discussed below. The 'neutral gas' has a low level of ionisation ($\sim$0.03) which is due to cosmic rays and photo-ionisation of Ca and Na atoms. This level of ionisation is sufficient to 'freeze' the magnetic field. This is important in the effect the density waves have on the magnetic fields. The dust grains will also be charged and tied to the field. The galactic magnetic field is discussed in the next section of this chapter.

3.3.2 Neutral Gas (HI)

The neutral gas is thought to be present in two forms (Clark 1965):- relatively dense clouds (20-20Ck) immersed in a hotter and more tenuous inter-cloud medium ($\sim 10^4$K). Falgarone and Lequeux (1973) give the following values for the gas in the region of the sun. Density in the plane (a) for the intercloud medium 0.16 atoms cm^{-3} (b) for a smoothed average of the cloud material 0.29 atoms cm^{-3}; Thickness (2Z$\frac{1}{2}$) of the disc. (a) cloud and intercloud 360 pc (b) cloud 310 pc (c) intercloud 550 pc. For 4.5$<\lambda<$10 kpc the thickness of neutral gas is approximately constant at 250 pc reducing to 100pc closer to the galactic centre. The thickness at R$>$10kpc increases rapidly as shown in figure 3.4 (Jackson and Kellman 1973). This increase is not seen in the $\ell = 110^\circ - 160^\circ$ direction. In future chapters the variation of the gas density with height above the plane, for $\lambda < 10$ kpc, will be taken as that observed by Schmidt (1956) presented in figure 3.5.
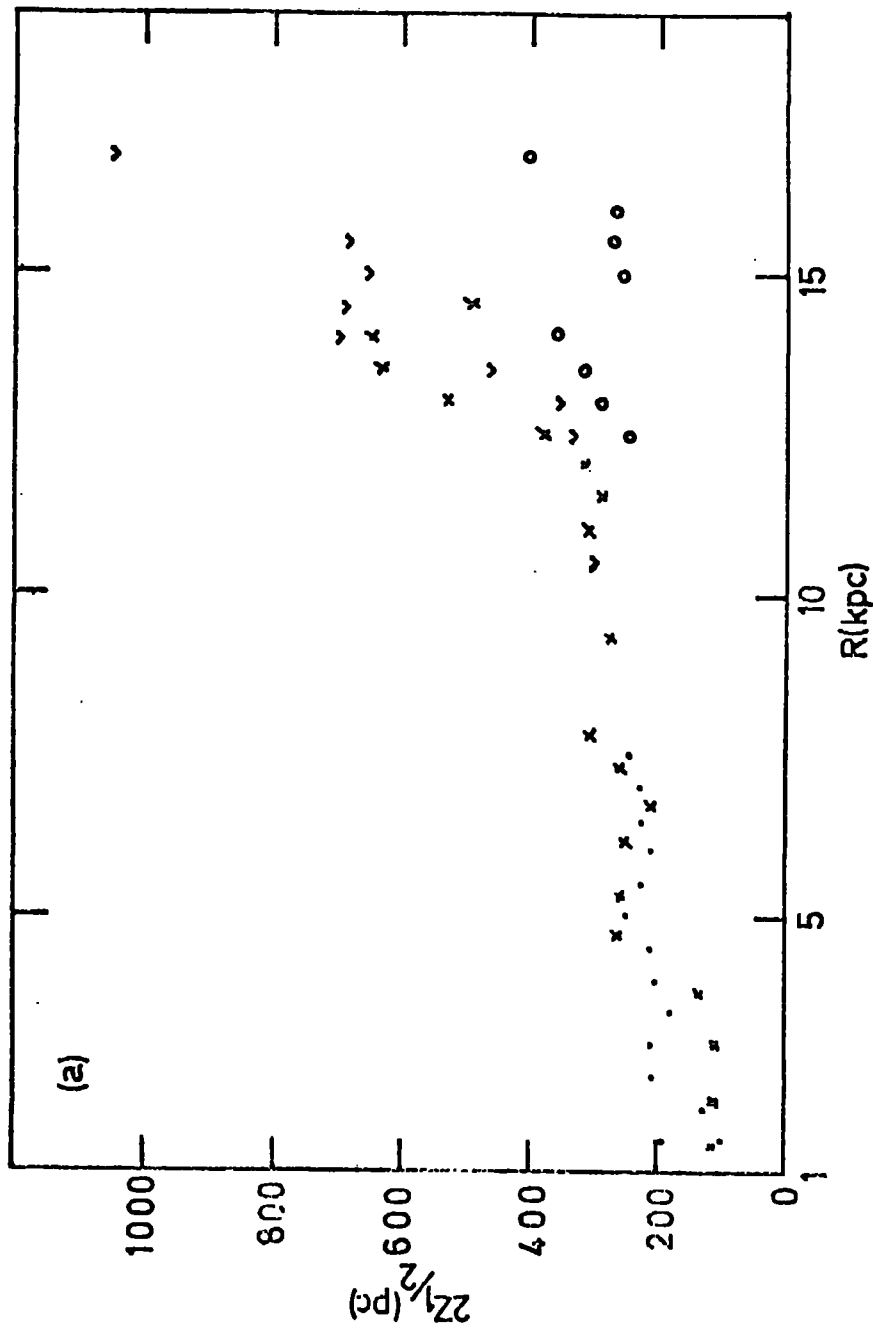
Figure 3.4: Variation of the full width at half maximum of the neutral gas with distance from the galactic centre. 1^{II} ∨ 200° – 330°, x 0° – 105°, • 270° – 360°, ⊘ 110° – 160°. (Jackson and Kellman 1973)
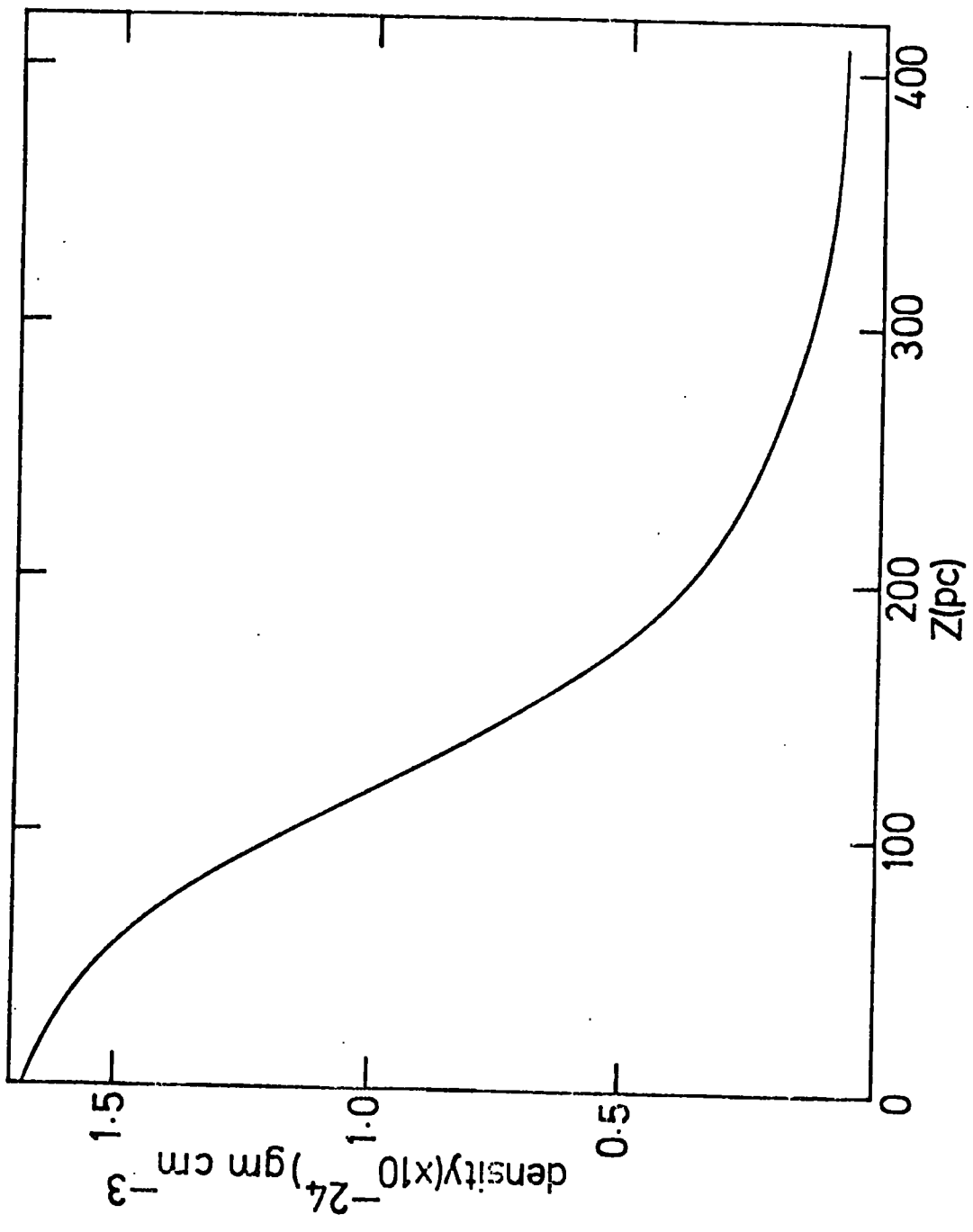
Figure 3.5: Variation of gas density with height above the plane according to Schmidt (1956)

3.3.3 Ionised Gas

Spheres of ionised hydrogen, HII regions, surround young, hot O and B type stars. The gas is ionised completely out to a sharply defined boundary, the Stromgren sphere. The radius of the sphere varies as $n_H^{-2/3}$. For n_H= latom cm^{-3} the radius varies from 100 pc for an O5 star to 1pc for an A0 star. The HII regions are seen optically or as thermal radio sources, the temperature of the gas being 10^4k. Giant HII regions (defined as those having a luminosity greater than four times that of the Orion nebula) indicate sites of star formation and are useful as spiral tracers (Chapter 4). Figure 3.6 shows the radial distribution of giant HII regions in the galaxy compared with the radial surface density distribution of HI. It is interesting to note that the separation between the abundance distribution of HII (centred at 4-8 kpc) and that of HI (peaking at 13 kpc) suggests that there exists a factor other than the average neutral hydrogen gas density which controls the present formation of stars in the galaxy. This will be discussed in the next chapter in terms of density wave theory. The mean density of thermal electrons within a few kiloparsecs of the sun can be obtained from dispersion measures of pulsars whose distances are known. (Lyne 1974). Estimates in the region of $n_e \approx 0.03 cm^{-3}$ have been obtained. The recombination rate of electrons and ions is roughly proportional to the square of the density thus at equilibrium $n_e^2 \propto n_{HI}$. The thickness of the thermal electron disc should therefore be greater than that of the neutral gas by a factor of 2 or $\sqrt{2}$ for an exponential or gaussian distribution of the gas respectively. This is consistent with $2z_{\frac{1}{2}} > 600pc$ (Lyne 1974) and estimated values of 800 to 1000 pc derived from the rotation measures of extragalactic radio sources (Falgarone and Lequeux 1973).

3.3.4 Molecular Hydrogen

In the interstellar medium hydrogen molecules are rapidly dissociated by UV photons in starlight. However, in dust clouds molecular hydrogen is shielded from UV photons and hydrogen atoms rapidly combine to form molecules.
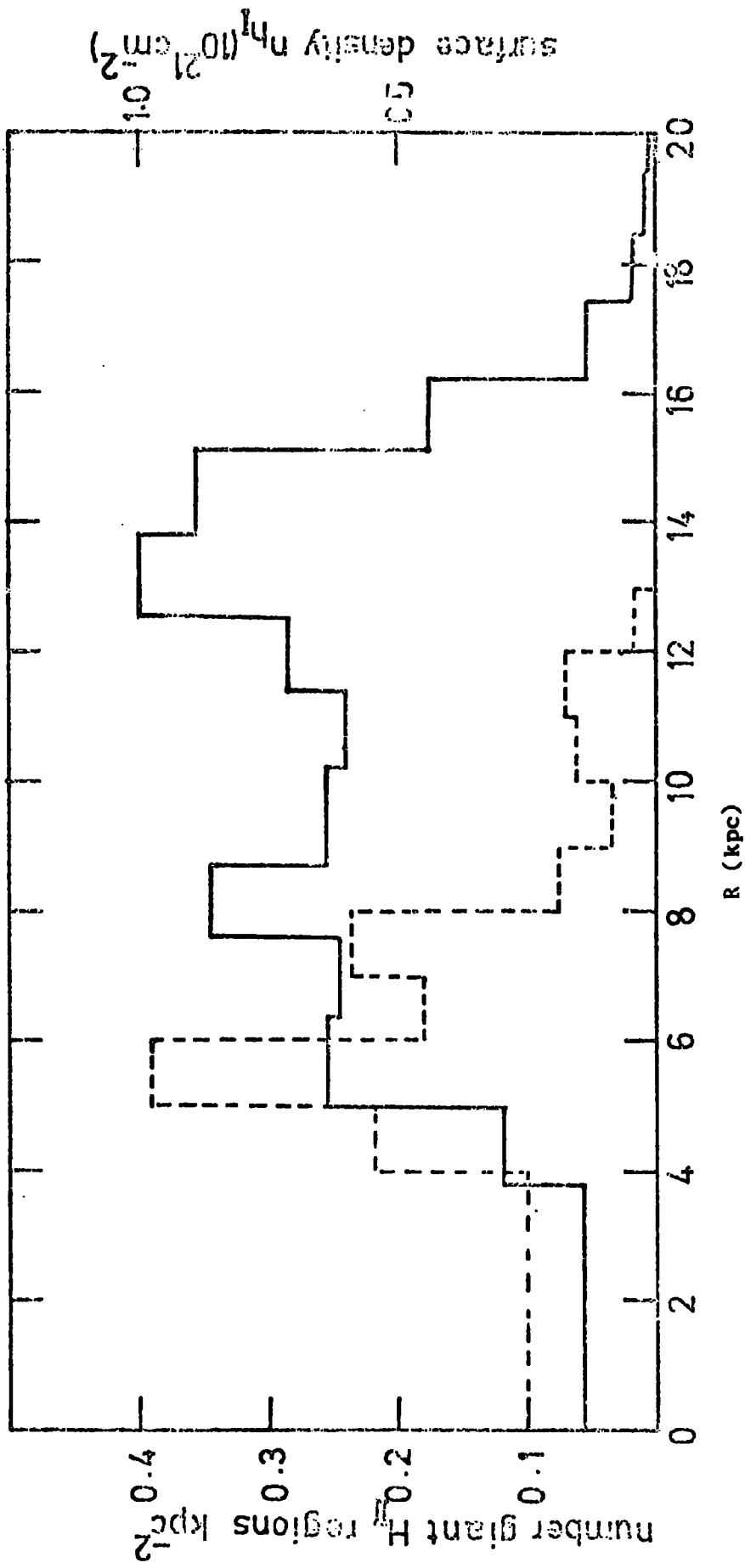
Figure 3.6: Radial distribution of the surface density of neutral gas ———— and giant H_{II} regions ———— (Mezger 1970).

As molecular hydrogen has no observable transition in the optical or radio wavebands its distribution in the galaxy has to be inferred from other measurements. It is detectable via the absorption lines in the far ultraviolet but this only permits observations from rockets and satellites. Satellite data imply (Spitzer et al. 1973) that some 50% of the local interstellar hydrogen is in the molecular form. Jenkins (1976) obtains an average molecular hydrogen density in the region of the sun of 0.2 atoms cm^{-3}. Indirect methods are used to plot the distribution of H_2 throughout the galaxy. Carbon monoxide due to the relative high abundance of its constituents and large dissociation energy (greater than $11eV$) is expected to be the most abundant molecule in the interstellar medium. Jenkins et al. (1973) have measured its abundance in the spectra of reddened stars which also show H_2 lines. They find the abundance ratio to be $N(CO)/N(H_2) \sim 10^{-8}$. Using such techniques for measuring CO throughout the galaxy it is possible to estimate the molecular hydrogen distribution (Gordon and Burton 1976). Figure 3.7 presents the inferred radial distribution of molecular hydrogen surface density. It shows a similar distribution to that of the giant $H II$ regions as would be expected.

3.4 The Galactic Magnetic Field

The existence of a large-scale galactic magnetic field was suggested following the detection of polarisation in starlight (Hall 1949, Hiltner 1949). The presence of this field is of vital importance to the dynamics of the interstellar medium (ISM) and in turn the ISM has an effect on the form of the magnetic field. In the following sections the various methods of observing the field are discussed together with the results obtained.

3.4.1 Interstellar Polarisation of Starlight

Chandrasekhar (1946) predicted that, if Thomson scattering by free electrons plays an important role in the transfer of radiation in the atmospheres of early type stars, then the continuous radiation emerging from these stars should be plane polarised. Hiltner 1949, while attempting to verify
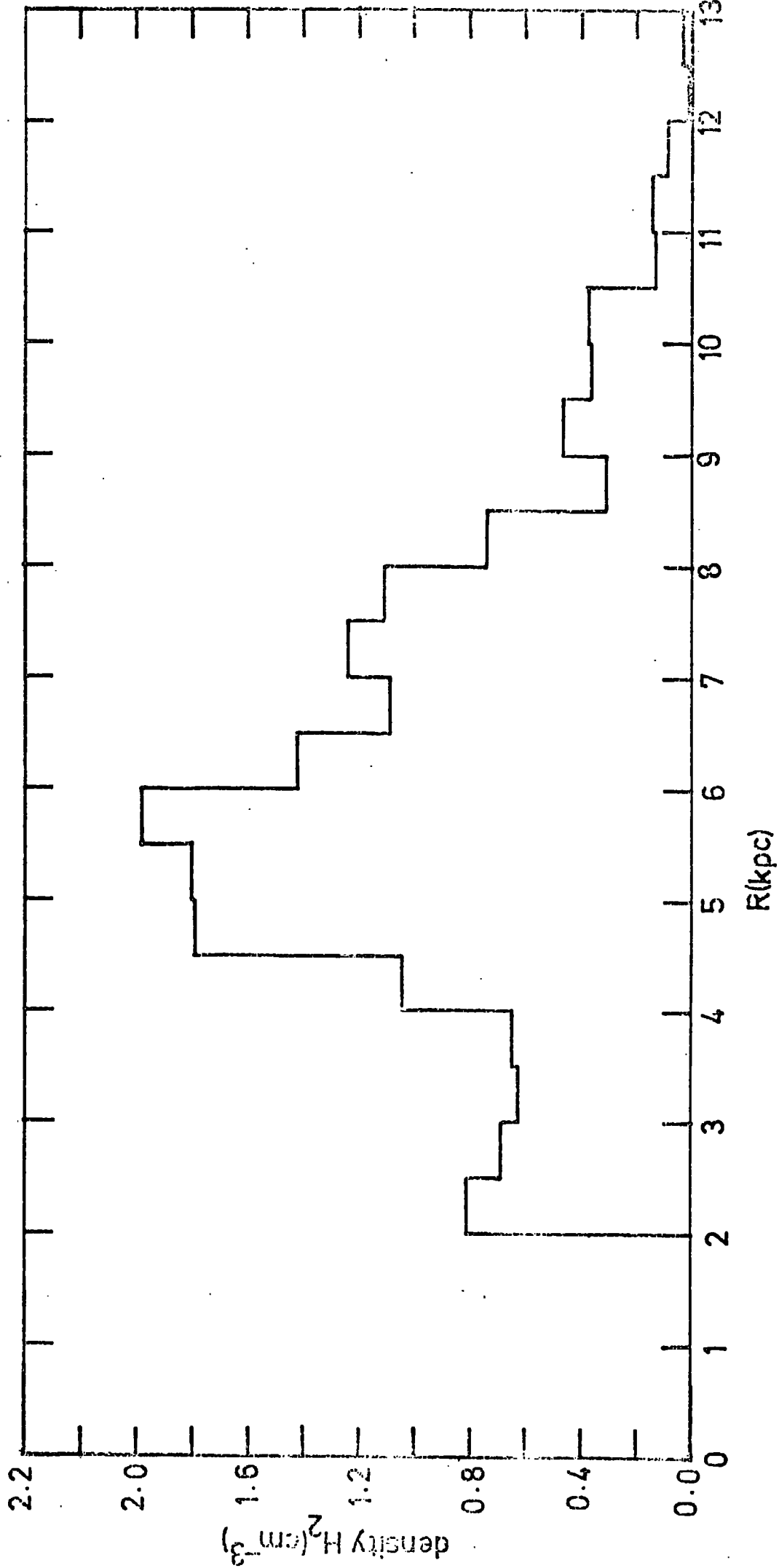
Figure 3.7: Radial distribution of molecular hydrogen volume density. (Gordon and Burton 1976).

Chandrasekhar's prediction, found that radiation from other types of stars is also polarised and concluded that the polarisation was not associated with each individual star but was an effect of the radiation passing through interstellar space. This polarisation is now regarded as being caused by the interstellar dust grains becoming aligned in the magnetic field and scattering the stellar radiation. The dust grains align themselves in the magnetic field by virtue of the fact that they are expected to possess some net electric charge (Davis and Greenstein 1951).

Unfortunately a study of the galactic field using optical polarisation is hampered for two reasons; it gives only a two-dimensional representation of the field - the E-vector of the light is parallel to the projection of the field vector in the plane perpendicular to the line of sight and the magnitude of the field cannot be directly calculated from the observations without making many assumptions about the nature of the grains. Axon and Ellis (1976) have presented a catalogue of the polarisations of over 5000 stars whose distances have been reliably measured. They conclude that the data cannot be totally explained with a simple longitudinal model, i.e. a regular field running in a direction ℓ_o^{II}, b_o^{II} superimposed on an irregular component, but the best direction for the regular field if such a model is considered is $\ell^{II} = 45 \pm 15^\circ$, $b^{II} \approx 0^\circ$. Previously Matthewson 1968 had suggested that the polarisation pattern was consistent with a helical local field. The electric vector plotted at a particular latitude and longitude represents the projection of the magnetic field in that direction on the plane perpendicular to the line of sight. By trying different field configurations Mathewson found that the best fit to his data would be given by a local magnetic field of helical form. However, Gardner et al (1969) interpreted Matthewson's data as being consistent with a longitudinal field directed towards longitude 50° i.e. consistent with Axon and Ellis (1976). In this case for longitudes $\ell^{II} = 140^\circ$ and $\ell^{II} = 320^\circ$ the E-vectors would be parallel to the galactic plane at all latitudes, whereas for $\ell^{II} = 50^\circ$ and $\ell^{II} = 230^\circ$ the polarisation would be randomly orientated. This can be seen in figure 3.8, which is from Axon and Ellis (1976), but many of the vectors seem to form
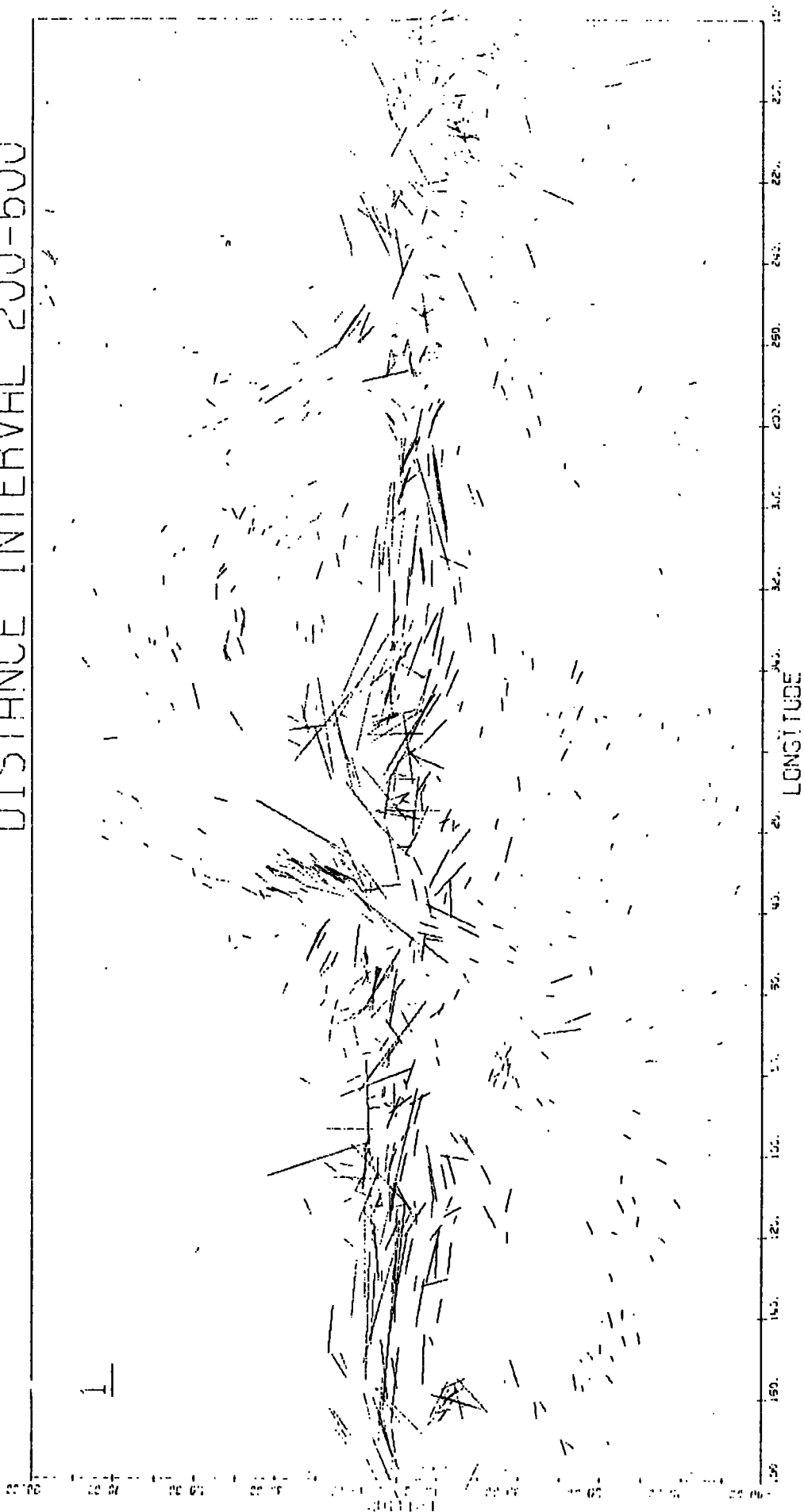
Figure 3.8: Stellarpolarisations for stars in the distance interval 200-600pc. (Axon and Ellis 1976).

curves which might indicate a better fit from a helical model. According
to Jones and Spitzer (1967) a field of only $3\mu G$ is needed to explain the
observed polarisation but, although this is consistent with values obtained
by other methods, this value is highly dependent on the model assumed for
the grains.

3.4.2 Faraday Rotation of Extragalactic Sources

When a plane polarised radio wave of wavelength $\lambda\,(cm)$ traverses an ionised
medium, in which there is a magnetic field, the plane of polarisation under-
goes a rotation through an angle Θ given by $\Theta = 8.1\times10^{\prime\prime}\lambda^{2}\int H_{\ell}\,n_{e}\,d\ell$
radians where H_{ℓ} is the longitudinal component of the magnetic field in gauss,
n_{e} is the thermal electron density of the medium in cm^{-3} and dl is the
element of length along the line of sight in pc. in which the rotation occurs.
The magnetic field is determined by measuring the observed position angle
of the plane of polarisation of the radiation from a given radio source for
several wavelengths λ. From a plot of Θ against λ^{2} one obtains the
rotation measure, $R.M = 8.1\times10^{\prime\prime}\int H_{\ell}\,n_{e}\,d\ell$, which enables the integrated
longitudinal field along the line of sight to be determined if n_{e} is known.
Unfortunately the observed rotation measure is a sum of the rotation measures
due to the galactic field, due to any intergalactic field and due to the
source. Recently Ruzmaikin and Sokuloff (1977) have carried out a regression
analysis using a particular model for the various components of the rotation
measure and obtain the values $H_{galactic} = 4.5\pm1.6\times10^{-6}$ Gauss and $H_{intergalactic}$
$\leq -4.8\pm9.2\times10^{-10}\Omega$ Gauss where Ω is equal to ρ/ρ critical with ρ
the density of the universe equal to ρ critical for the universe to be
just closed. Ω is thought to be ≤ 1 Zeldovich and Novikov (1975).
Figure 3.9 shows a summary of the R.M of 252 extragalactic sources made
by Vallee and Kronberg (1973). This data provides a more uniform coverage
of the sky than any other analysis. The area of the circle is proportional
to the magnitude of the RM. Open circles indicate a negative R.M. equivalent
to a field away from the observer. Interpretation of the Faraday rotation
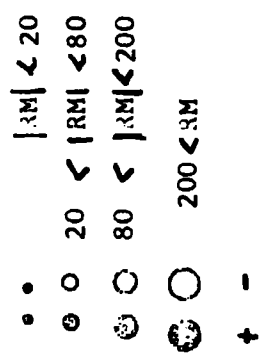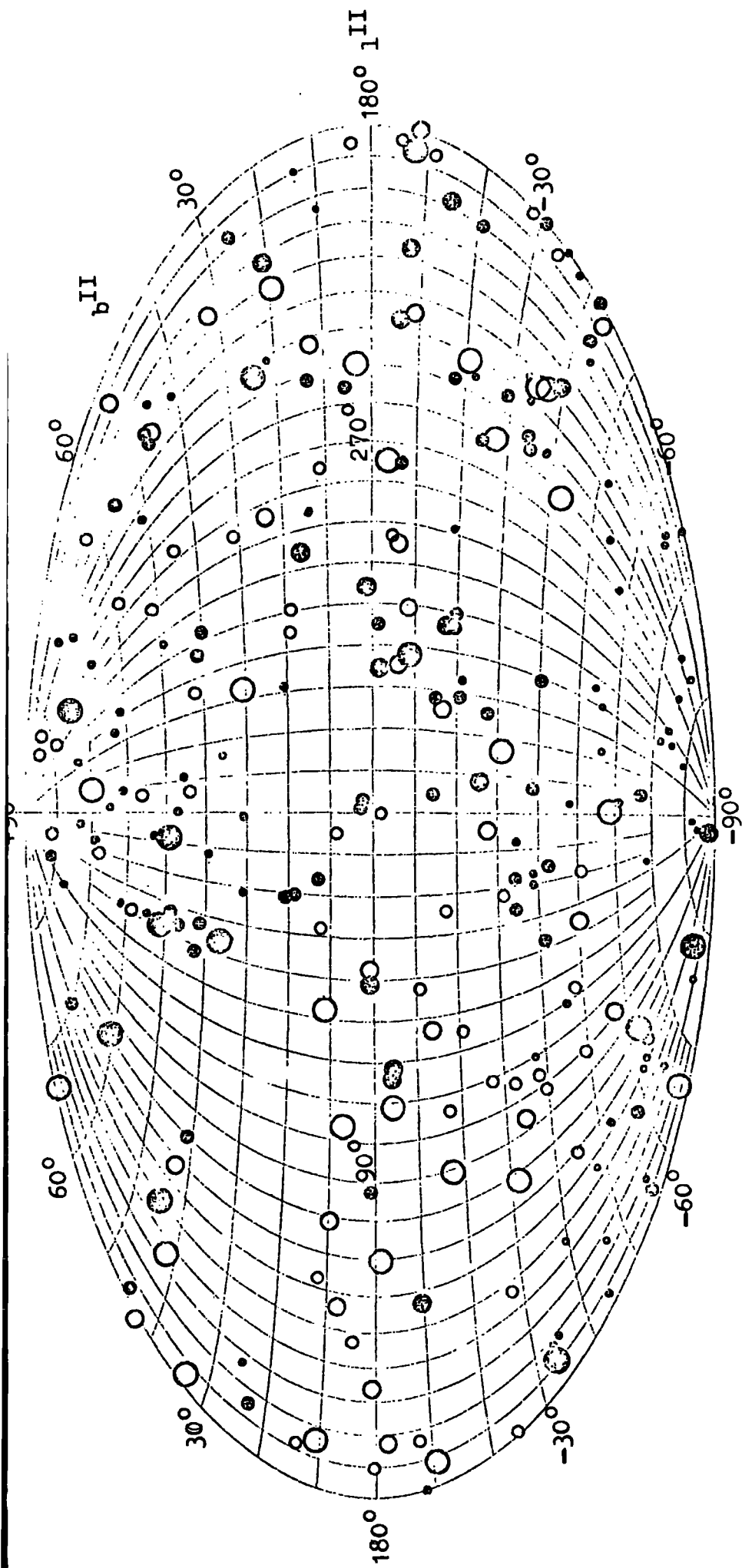in extragalactic objects in terms of magnitude and direction of the galactic

Figure 3.9:

The distribution of the rotation measures
for 252 discrete radio sources as compiled
by Vallee and Kronberg (1973).

magnetic field is difficult, though the measurements seem to be consistent with a longitudinal field directed towards $\ell^{II} \sim 90^{\circ}$ (Gardner et al. 1969, Wright 1973, Verschuur 1974, Vallee and Kronberg 1975) with a magnitude of a 'few microgauss.

3.4.3 Faraday Rotation of Pulsars.

The problem of estimating the magnetic field strength from R.M. of extragalactic objects due to a lack of knowledge of the electron density is removed when pulsars are used as the source of polarised radio emission. Davies et al. (1968) showed that the arrival time, t, of a radio pulse from a pulsar is a function of frequency due to the passage of the pulse through an ionised medium. For a uniform plasma

$$\frac{dt}{d\nu} = -\frac{8100}{\nu^3} \int n_e \, d\ell \quad \text{sec. Hz}^{-1}$$

where $D = \int n_e \, d\ell$ is called the dispersion measure $\left(pc \, cm^{-3} \right)$ and is equal to the line integral of the electron density to the source. For a pulsar it is therefore possible to measure both R.M. and D. to obtain the line of sight component of the magnetic field (weighted by the electron density)

$$H_e = \int n_e \, H_e \, d\ell \, / \int n_e \, d\ell.$$

Figure 3.10 shows the line of sight magnetic field components in the direction of 38 pulsars as compiled by Manchester (1974). It is clear from this figure that the field is pointing away from the sun for longitudes centred on 90° and towards the sun for longitudes centred on about 240°. Figure 3.11 shows those pulsars from figure 3.10 lying close to the galactic plane projected onto a plan view of the galaxy showing the location of the Perseus and Sagittarius arms. None of the observed line of sight magnetic fields appear to include fields from either of these two nearest major arms. For the region centred on $\ell = 60^{\circ}$ the large fluctuating fields are probably due to the presence of the North Polar Spur. Manchester interprets these observations as being consistent with a simple longitudinal magnetic field with strength $2.2 \pm 0.4 \mu G$ directed towards $\ell^{II} = 94 \pm 11^{\circ}$
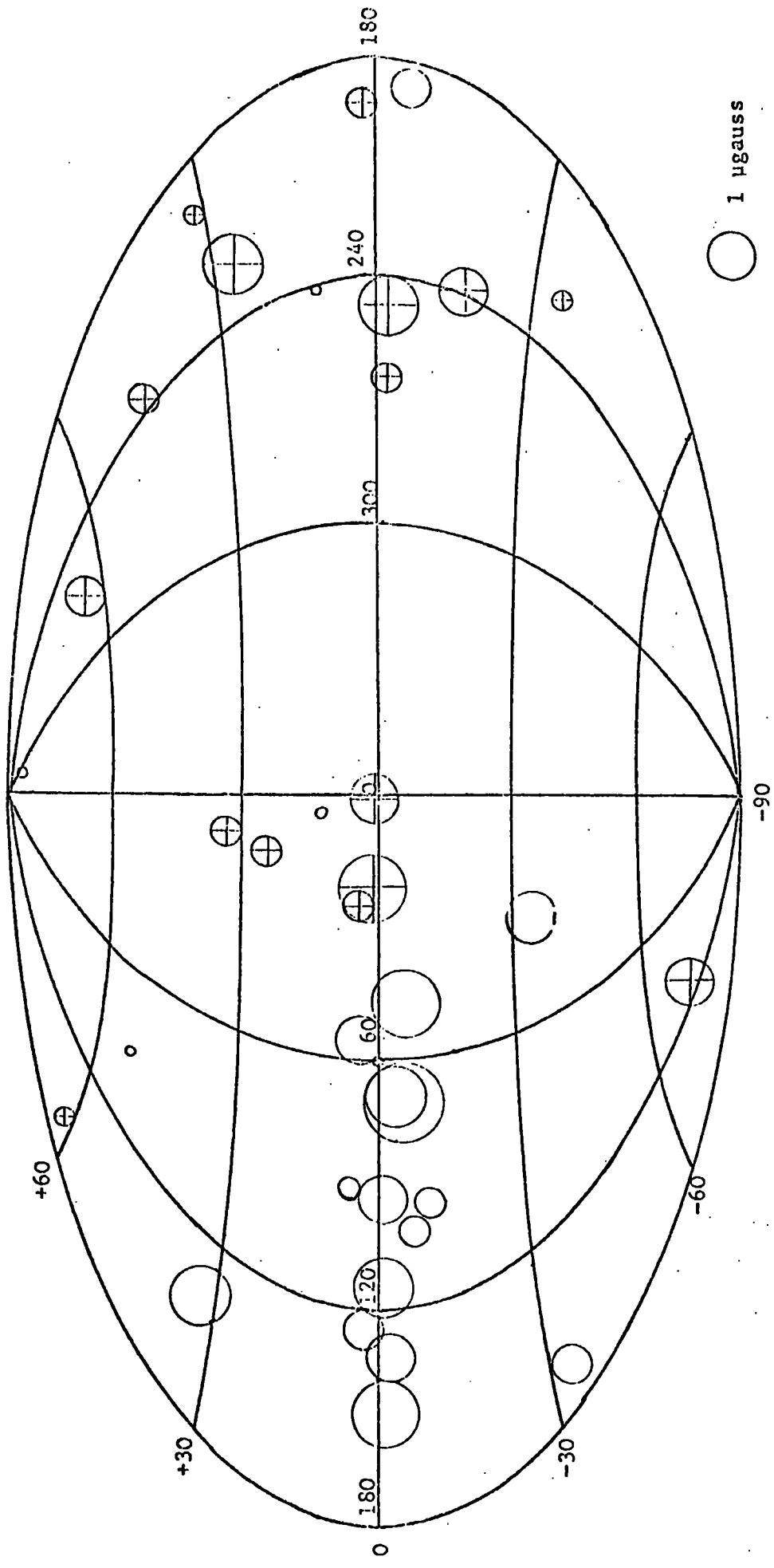
Figure 3./O Line of sight magnetic field components in the directions of 38 pulsars.

For fields of >0.1 ʋgauss the area of the circle is proportional to the magnetic field

strength. For fields directed towards the observer a plus sign is enclosed.

(Manchester, 1974).
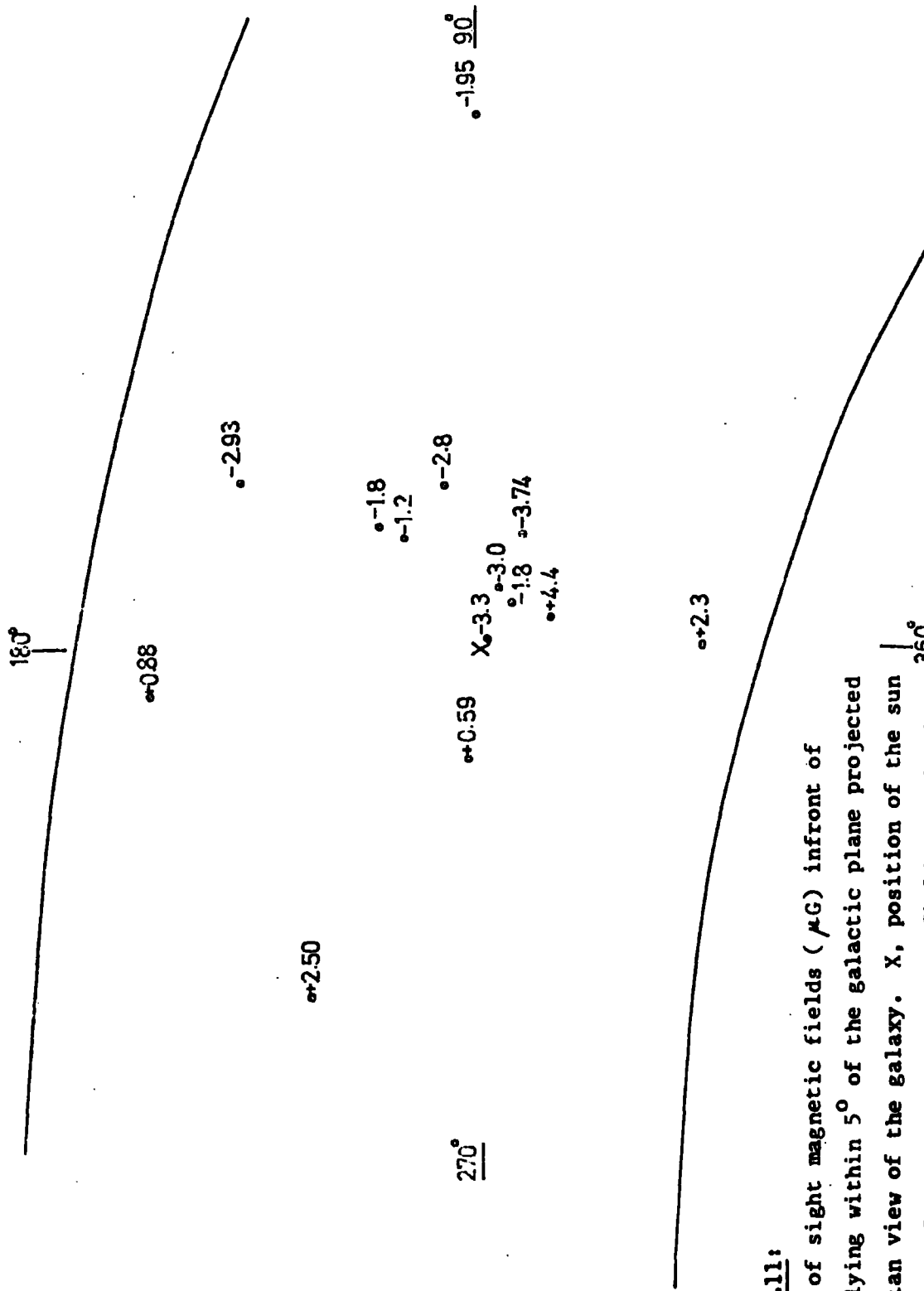
Figure 3.11:

The line of sight magnetic fields (μG) infront of pulsars lying within 5° of the galactic plane projected onto a plan view of the galaxy. X, position of the sun - field away from the observer, + field towards the observer.

and an irregular component of approximately equal magnitude.

There is no doubt that the measurement of the galactic field by using pulsars is the most reliable method known at present. Unfortunately, as seen from figures 3.10 and 3.11 very few pulsars in the southern hemisphere have had their dispersion and rotation measures measured rather limiting the usefulness of the results.

3.4.4. The Zeeman Effect

Bolton and Wild (1954) suggested that the magnetic fields inside clouds of neutral hydrogen are strong enough to cause Zeeman splitting of the 21 cm. line seen in absorption against strong radio sources. Verschuur (1969) postulated that neutral hydrogen clouds contained 'frozen in' magnetic fields and suggested that the magnetic field may be stronger in the clouds as a result of amplification by cloud contraction, proposing that the greater the density of the cloud the stronger the field within it. If a spherical cloud contracts isotropically its density varies in proportion to its radius^{-3} and the field strength in proportion to the radius^{-2}, as required by conservation of magnetic flux. Therefore, the field will be proportional to $n_\mu^{2/3}$. Verschuur 1970 showed that in fact the observed fields and densities within clouds are consistent with such a law. If the density of the uncompressed ISM is considered to be of the order of 1 atom cm^{-3} then a field of a few μG is obtained by extrapolating the line $H \alpha \, n_\mu^{2/3}$. Figure 3.12 presents the observed data with the line $H \alpha \, n_\mu^{2/3}$ superimposed. The reason why points fall beneath the straight line $H_0 = 1.27 \times 10^{-6} \, n_\mu^{2/3}$, where H_0 is in gauss and n_μ in hydrogen atoms cm^{-3} is because only one component of the field in the Zeeman data is observed and therefore the upper envelope of the points should describe the history of the field strength in a contracting cloud.

3.4.5 Galactic Synchrotron Emission.

As shown in appendix I equation I.9 the intensity of synchrotron radiation observed in a particular direction is given by:
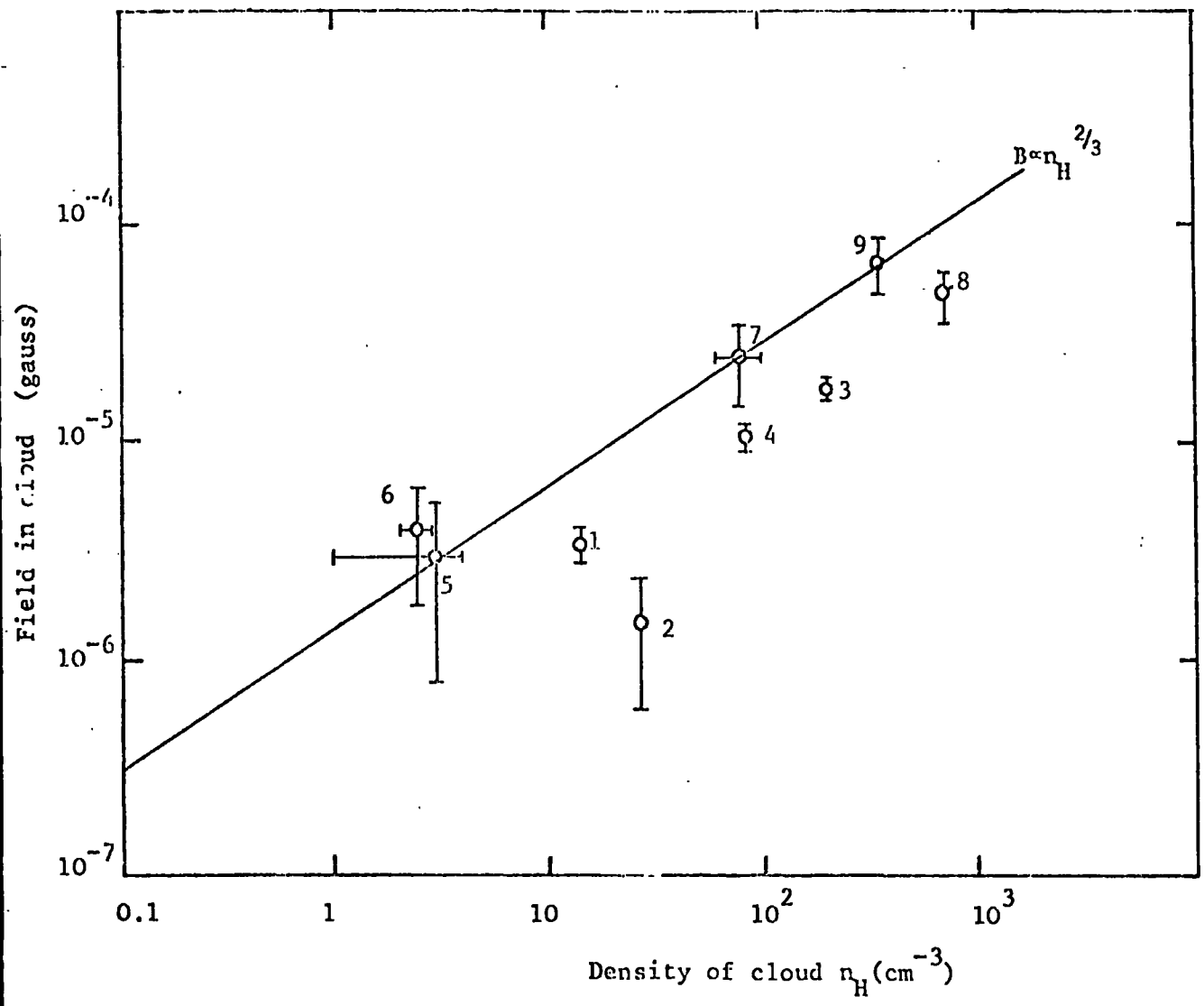
Figure 3.12: Magnetic Fields in neutral hydrogen clouds as a
function of their density. (Verschuur 1970).

	Direction	ℓ	b
1.	Tau A	$185°$	$-6°$
2.	Tau A		
3.	Cas A	$112°$	$-2°$
4.	Cas A		
5.	Cyg A	$76°$	$-16°$
6.	Cyg A		
7.	M17	$15°$	$-1°$
8.	Orion A	$209°$	$-19°$
9.	Orion A		

$$I(\nu) \propto \ell I_o \, H_\perp^{\frac{\gamma+1}{2}} \, \nu^{-\left(\frac{\gamma-1}{2}\right)} .$$

where l is the distance through the emitting region in kpc. I_o is the intensity of electrons at 1GeV measured in $\left(m^2 . s . sA . GeV\right)^{-1}$ and $H_\perp$ is the perpendicular component of the magnetic field to the line of sight in μG. It is therefore clear that if the electron spectrum is known and a value of 1 can be estimated for a particular direction in the galaxy a value can be obtained for the root mean square value of $H_\perp$. (as γ approximately equals 3). Recently Freier et al. (1977), having measured the electron spectrum for energies greater than 8GeV have inferred from measurements of Hirabayashi (1974) of the continuum radiation at 15.5 GHz that $H_{\perp \, r.m.s} \sim 10 \mu G$ looking towards the galactic centre with a line of sight of 25 kpc. Previous estimates of $H_{\perp \, r.m.s}$ by Daniel and Stephens (1967) and by Webber (1968) are in agreement with $10 \mu G$. Badhwar et al. (1977) have looked in the anticentre assuming a line of sight of 4 kpc and from many observations of the electron spectrum they infer an r.m.s field of between 4 and 11.5 μ G depending on which electron spectrum is assumed. It is clear that a value of the magnetic field somewhere in the region of $10 \mu G$ is inconsistent with values obtained from Faraday rotation of pulsars, $2.2 \mu G$, and that implied by the Zeeman splitting of the 21 cm. line ($\geq 3 \mu G$). It should be born in mind, however, that the value obtained for the field from rotation measures is essentially local whereas the values from synchrotron emission are averaged over large regions of the galaxy. Several explanations for this discrepancy have been advanced. Setti and Woltjer (1971) have suggested that as the local radio emissivity as estimated from the emission in front of optically thick HII regions is considerably higher than that obtained when the observed electron spectrum and a magnetic field of $3 \mu G$ are used that the electron density in the galaxy is an order of magnitude greater than the value observed at the earth. This implies that the sun is located in a hole as regards cosmic ray density. As cosmic ray protons are expected to be distributed in the galaxy in a similar manner to cosmic ray electrons such a model might imply a large anisotropy in the

cosmic ray protons and a much increased γ ray flux from Π_0 production. To avoid such a drastic proposal as this two further explanations appear in the literature.

Cowsik and Mittledorf (1974) have advanced the idea of turbulence-enhanced synchrotron emission. This mechanism requires that fluctuations in the magnetic field are correlated with variations in the density and energy of relativistic electrons. In their analysis the following assumptions are made: (a) the plasma is assumed to be a perfect conductor (b) leakage of the relativistic electrons from the region of interest is neglected over time scales characteristic of the compression caused by the turbulent motions of the interstellar gas and (C) the magnetic field is taken as perpendicular to the direction of the compression. If the ratio (original volume)/ (compressed volume) is x, the magnetic field increases from H_0, the initial value to $H = x \, H_0$. In the compressed region the density increases by a factor x and the energy of the particles is also increased by betatron acceleration such that an electron spectrum of the form $N(E)dE = N_0 E^{-\gamma} dE$

becomes $N(E)dE = N_0 \left(\dfrac{x}{x - (x-1)\sin^2\theta} \right)^{\frac{\gamma+2}{2}} E^{-\gamma} dE$

where θ is the pitch angle of the electron in the field H. i.e. the betatron mechanism enhances the spectrum but maintains the slope γ. For $\sin\theta = 0, N = N_0$ i.e. there is no enhancement in the spectrum. Cowsik and Mittledorf chose an exponential functional form for the probability distribution of x. $P(x)dx = \exp(-x)dx$ This distribution has a mean $\langle x \rangle = 1$ and a standard deviation of 1 in agreement with the observation that the fluctuations in H are of about the same magnitude as H. For $\sin\theta = 1$ the enhancement factor for synchrotron emission,

$$EF = \frac{\langle N H^{\frac{\gamma+1}{2}} \rangle}{\langle N \rangle \langle H \rangle^{\frac{\gamma+1}{2}}} = \int_0^\infty x^{\frac{\gamma+2}{2}} x^{\frac{\gamma+1}{2}} \exp(-x)dx = \Gamma\left(\gamma + \frac{5}{2}\right) = 28 \text{ for } \gamma = 2.6$$

For $\sin\theta = 0$ $\quad EF = 1.7$ for $\gamma = 2.6$.

If the distribution of $\sin\theta$ is taken into account the calculated enhancement

is $$\frac{\int_0^\infty \int_0^\pi \left(\dfrac{x}{x-(x-1)\sin^2\theta} \right)^{\frac{\gamma+2}{2}} x^{\frac{\gamma+1}{2}} \exp(-x) \sin\theta^{\frac{\gamma+1}{2}} \sin\theta \, d\theta \, dx}{\int_0^\pi \sin\theta^{\frac{\gamma+1}{2}} \sin\theta \, d\theta}$$

which equals approximately

$$\int_0^\infty x^{\frac{3}{4}(\gamma+1)} \, x^{-\frac{\gamma+1}{2}} \exp(-x) \, dx \approx 12 \text{ for } \gamma = 2.6$$

It therefore seems that such a mechanism is capable of increasing the synchrotron emission up to the observed level with the presently observed values of the field, $3\mu G$ and the electron intensity measured at the earth. If the relativistic electrons are compressed by x with a distribution $P(x)dx = \exp(-x)dx$ it is also to be expected that the thermal electrons are compressed in a similar manner. This means that the rotation measure data on the field needs to be reinterpreted: $\langle H \rangle = \int n_e \, H \, d\ell \big/ \int n_e \, d\ell$ with n_e increased in proportion to x.

$$\langle H \rangle = \frac{\int_0^\infty n_{oe} x \, H_o x \, \exp(-x) dx}{\int_0^\infty n_{oe} x \, \exp(-x) dx} = \frac{\Gamma(3)}{\Gamma(2)} H_o = 2 H_o$$

Therefore $\langle H \rangle$ will be $2H_o$ and as $\langle H \rangle$ is observed to be approximately $3\mu G$ from the Faraday rotation of pulsars the true unperturbed field implied from these measurements, assuming the enhancement mechanism, is $1.5\mu G$. Using this value for H_o will reduce the predicted synchrotron emission by $2^{1.8}$ for $\gamma = 2.6$ which equals 3.5. This means that for a consistent picture of the turbulence-enhanced emission the enhancement factor is in fact only 3 or 4 at the very most. Another difficulty with the above mechanism is that it is not at all clear why the relativistic electrons should remain in a particular region over time scales characteristic of the compression (Assumption 2).

Freier et al 1977 explained the high value of $H_\perp$ r.m.s. by postulating very large fields ($\sim 70\mu G$) in dense clouds occupying $\sim 2\%$ of the line of sight whereas the remaining 98% of the line of sight would have fields of $2\mu G$. This would imply that the linear average was $3.4\mu G$ consistent with Faraday rotation measurements, whereas the r.m.s. field would be $10\mu G$ consistent with

synchrotron observations. Such an explanation when viewed together with the observed local emissivity out to $600pc$ from the sun (Caswell 1976) would require an average of 6 1pc clouds with fields of $\lesssim 70\mu G$. Heiles (1977) however states that the lack of Zeeman splitting in many HI clouds suggests that the fields are usually small with some selected HI regions having fields up to $\gtrsim 20\mu G$.

Further consideration of this discrepancy in the values inferred for the magnetic field will be made in connection with the models of the galactic radiation discussed in chapters six and seven.

As seen from appendix I section I.4 synchrotron radiation is partially plane polarised. Thus the polarisation of the radio continuum can give information on the orientation of the magnetic field in the local region. Wilkinson and Smith (1974) using radio surveys at 240, 408, 610, 820 and 1415 MHz for the region $100^{o} \leq \ell^{II} \leq 180^{o}$, $-40^{o} \leq b^{II} \leq +40^{o}$ studied the radio polarisation and concluded that the field is predominantly longitudinal in the galactic plane directed along the local arm branch superimposed on a substantial random field of magnitude 0.5 to 1.0 times that of the uniform field.

3.4.6 Conclusions Regarding the Galactic Magnetic Field

The most reliable observational evidence seems to be consistent with a local magnetic field of a few μG running in approximately the direction of $\ell^{II} = 90^{o}$ with an irregular component of about the same magnitude superimposed (Osborne et al. 1973). The field is essentially longitudinal in structure. There is some evidence to suggest that the local field may possess some helical structure but this may well be due to the galactic spurs (see Chapter 5). In the following chapters the galaxy is assumed to possess a longitudinal magnetic field running along spiral arms of magnitude $3\mu G$ at the earth with a random component superimposed.

3.5 The Hydrostatic Equilibrium of the Galactic Disk

As the galactic magnetic field is frozen into the gas of the disk of the

galaxy it tends to be prevented from expanding by the gravitational interaction of the stars on the gas. Cosmic rays may be considered, on the galactic scale, as a tenuous hot gas. The equilibrium state for the galactic field can be discussed in conjunction with gas and cosmic ray pressures resulting in the hydrostatic equilibrium of the galactic disk in the Z-direction (height above the plane). For equilibrium

$$\frac{d}{dz}\left(\frac{H^2(z)}{8\pi} + P(z) + p(z)\right) = -\rho(z)g(z) \qquad \text{where} \quad \frac{H^2(z)}{8\pi} \quad \text{is the} \quad 3.4.1$$

magnetic pressure, P is the cosmic ray pressure equal to $\mathcal{U}/3$ where $\mathcal{U}$ is the cosmic ray energy density, p is the pressure of the gas given by $p = \rho u^2$ where u^2 is the mean square gas velocity in the vertical direction and $g(z)$ is the gravitational acceleration perpendicular to the galactic plane.

If the total pressure in intergalactic space is small compared to the total pressure within the disk $H^2(z)/_{8\pi}$ and $P(z)$ must fall-off with Z at least as rapidly as the density ρ otherwise above some height there is not sufficient weight, $\int \rho g \, dz$ to counterbalance the pressure $P(z) + H^2(z)/8\pi$ at that height (Parker 1970).

To obtain some consequences of hydrostatic equilibrium it is instructive to make several approximations. If $H^2/_{8\pi} = \alpha \rho u^2$ and $P = \beta \rho u^2$ $\quad$ 3.4.2 $\quad$ 3.4.3 α and β being constants, i.e. if it is assumed that the pressures are proportional to one another, then $1/\rho u^2 \; d/_{dz}(\rho u^2) = -g \; u^2(1+\alpha+\beta)$ 3.4.4 implying a scale height $h = u^2(1+\alpha+\beta)/\langle g \rangle_h$ $\qquad$ 3.4.5 where $\langle g \rangle_h$ is the mean value of g(Z) over the scale height h. From Badhwar and Stephens (1977) if $h \approx 150$ pc then $\langle g \rangle_h \approx 2 \times 10^{-9} \text{cm s}^{-2}$. Observations suggest that $u \approx 7 \text{ kms}^{-1}$. Substituting these values in equation 3.4.5 results in $\alpha + \beta \approx 1$. Equations 3.4.2 and 3.4.3 can now be combined to give $H^2/8\pi + P \approx \rho u^2(\alpha+\beta)$. P equals approximately $0.5 \times 10^{-12} \text{dyne cm}^{-2}$ from observations of the cosmic ray energy density and therefore a field of 3.5 μG exerts the same pressure as the cosmic rays. If u is taken to be 7 kms^{-1} and the magnetic and cosmic ray pressures are assumed equal then the weight of one or two hydrogen atoms cm^{-3} is sufficient

to confine the field.   As this value for the gas density is approximately
the same as that observed it would suggest that the galactic disk cannot
hold a field of greater than say $5\mu G$ in equilibrium i.e. $\angle H^2 \rangle^{\frac{1}{2}} \lesssim 5\mu G$.
It must be noted in the above that the results are fairly sensitive to
the value taken for $\mathcal{U}$ as it appears as the square in the equations.   A
value of $\mathcal{U}$ as large as $10 \mathrm{kms}^{-1}$ would not be inconsistent with observations.
Bearing this in mind the results obtained above are consistent with the
previously discussed values for the observed galactic magnetic field.
In spiral arms at the peak of the shock, see next chapter, where the fields
are thought to be considerably higher than $5\mu G$ hydrostatic equilibrium is not
applicable as the situation is inherently non-static.   Consideration of
hydrostatic equilibrium and the extent above the plane to which they apply
are of importance when considering the galactic distribution of radio
emission at $b^{\mathrm{I\!I}} > 0^o$.

References

Allen, C.W., 1963 Astrophysical Quantities London Athlone Press, p.251

Arp, H.C.,1965, Ch. 19 Galactic Structure, Stars and Stellar systems
volume $\mathbb{Y}$ ed. A. Blaauw and M. Schmidt

Axon, D.J. and Ellis, R.S., 1976, M.N.R.A.S., 177 499-511

Badhwar, G.D., Daniel, R.R., and Stephens, S.A., 1977 Nature

Badhwar, G.D., and Stephens, S.A., 1977 Ap. J. 212 494-506

Bolton, J.G., and Wild, J.P., 1957 Ap. J. 125 296

Caswell, J.L., 1976, M.N.R.A.S. 177 601-616

Chandrasekhar S. 1946, Ap. J.103 351

Clark, B.G., 1965 Ap. J. 142 1398

Contopolous, G. and Stromgren, B. Tables of Plane Galactic Orbits New York,
N.A.S.A. Institute of Space Studies 1965

Cowsik, R., and Mitteldorf,J ., 1974 Ap. J 189 51-53

Daniel, R.R., and Stephens, S.A., 1967 Proc. Indian Acad. Sci. 65 319

Davies, J.G. et al. 1968 Nature 217 910

Davis, L., and Greenstein, J.L. 1951 Ap.J. 114 206

Elvius, T., 1965, Ch.3 Galactic Structure, Stars and Stellar systems volume
$\mathbb{Y}$ ed. A. Blaauw and M. Schmidt

Falgarone E., and Lequeux J. 1973 Astron and Astrophys.

Freier, P., Gilman, C. and Waddington, C.J., 1977 Ap. J. 213 588-598

Gardner, F.F., Morris D. and Whiteoak J.B. 1969 Aust. J. Phys 22 873

Gordon M.A. and Burton, W.B. 1976 Ap. J. 208 346-353

Hall, J.S., 1949 Science 109 166

Heiles C. 1977 Annual Rev. Astronomy & Astrophys Ch. I 1-22

Hiltner W.A., 1949 Ap.J . 109 471

Hirabayashi, H., 1974 Publ. Astr. Soc. Japan 26 263

Jackson, P.D., and Kellman, S.A., 1974 Ap.J. 190 53-58

Jenkins, E.B., et al., 1973 Ap. J. Lett. 181 122

Jenkins, E.B., 1976 in The Structure and Content of the Galaxy and Galactic
Gamma Rays ed. Stecker, F.W. (N.A.S.A. Goddard Space Flight Centre, preprint)

Jones and Spitzer, L., 1967 Ap. J. 147, 943

Kraft, R.P., and Schmidt, M. 1963, Ap. J. 137, 249

Kwee, K.K., Muller, C.A., and Westerhout G., Bull. Astron. Inst. Neth. 12 211

Lin, C.C., 1968, Ch.1, 43 Galactic Astronomy, Vol. 2 ed. Hong-Yee Chiu and
A. Muriel publ. Gordon and Breach

Lyne, A.G., 1974 I.A.U. 60

Manchester R.N. 1974 Ap. J. 188 637

Mathewson, D.S., 1968, Ap. J. 153 L47

Mezger P.G., 1970, I.A.U. Symp. 38, 107

Oort J. 1927 Bull. Astron. Inst. Neth. 3 275

Oort J.H. 1965 Ch. 21 Galactic Structure, Stars and Stellar Systems, Volume Ⅴ
ed. A. Blaauw and M. Schmidt

Oort, J.H., and Plaut, L., 1975, Astron. and Astrophys. 41 71-86

Osborne, J.L., Roberts, E., Wolfendale, A.W., 1973, J. Phys. A 6 421-58

Parker, E.N., 1970 I.A.U., 39 Interstellar Gas Dynamics 168

Ruzmaikin A.A., and Sckuloff, D.D., 1977 Astron. Astrophys. 58, 247-253

Schmidt, M., 1956, Bull. Astron. Inst. Neth . 13 247

Schmidt, M., 1965 Ch.22 Galactic Structure, Stars and Stellar Systems volume Ⅴ
ed. A. Blaauw and M. Schmidt.

Setti, G. and Woltjer L. 1971 Astrophys. Letts 8 125-128

Spitzer, L., Drake, J.F., Jenkins, E.B., Morton, D.C., Rogerson, J.B., and
York, D.G., 1973 Ap. J. 181 L116

Vallée J.P., and Kronberg, P.P., 1973 Nature 246 49-51

Vallée, J.P., and Kronberg, P.P., 1975, Astron. Astrophys. 43 233

Verschuur, G.L., 1969 Ap. J. 155 L155
Verschuur, G.L., 1970 I.A.U. 39 Interstellar Gas Dynamics p.150
Verschuur, G.L., 1974 Planets, Stars and Nebulae University of Arizona
Press, Tucson Arizona, p.960

Webber, W.R., 1968, Aust. J. Phys. 21, 845

Wilkinson, A., and Smith, F.G., 1974, M.N.R.A.S., 167 593-611

Wright, W.E., 1973 Thesis Cal. Inst. of Tech. U.S.A.

Zeldovich, Ya. B., Novikov, I.D. 1975, The Structure and evolution of the
Universe, Moscow

CHAPTER 4

GALACTIC SPIRAL STRUCTURE

4.1 Introduction

Ever since the observation of spiral structure in external galaxies evidence has been sought to support the thesis that our own galaxy is also of spiral form. It is now well established that our galaxy is a spiral of type intermediate between Sb and Sc in the Hubble classification. From a study of the statistics of spiral galaxies it is easily shown that spiral structure persists for periods of time considerably longer than the time for a spiral consisting always of the same material to become completely wound up by differential rotation. This has led to the density wave theory for the maintenance of spiral structure. The origin of spiral structure is at present still very uncertain.

This chapter describes the methods used and results obtained when mapping the spiral structure of the galaxy together with a summary of density wave theory concentrating on the factors from this theory that are used as a basis for the models developed in chapters six and seven.

4.2 Observations of Galactic Spiral Structure.

The task of mapping spiral structure in the galaxy was initiated soon after Baade and Mayall (1951) reported results of their studies relating to M 31. They found that the spiral arms of M31 were best traced by emission nebulae and by the young O and B stars. In 1953 Morgan et al. presented the first picture of spiral structure in the galaxy. Since 1952 many methods have been used to try and map the spiral structure of our galaxy. Spiral arms in our galaxy appear to be defined primarily by a density of the interstellar medium higher than that in the interarm regions and by the existence of hot, massive early-type stars which have formed out of the gas and which, in turn, have ionised it (HII regions). According to the density wave theory, the spiral

pattern is maintained by a density wave which as it passes through the interstellar medium compresses it and causes stars to form. Ideal spiral tracers are therefore young objects that have not moved far from their sites of creation, the spiral arms. Unfortunately the observation of optical objects is limited to a few kiloparsecs from the sun by interstellar absorption and therefore radio methods have to be used for mapping the large scale spiral structure. Table 4-1 lists many of the objects at present used for mapping spiral structure.

4.2.1 O and B. stars-clusters-associations

O to B2 stars, singly, in clusters or in associations are the ideal optical tracers of spiral structure as they form first out of the compressed gas of the spiral arms. Photometric distances to O to B2 clusters and associations can easily be determined and corrected for interstellar absorption from reddening data for each cluster or association. In regions of low absorption young open clusters have been observed up to distances of approximately 8 kpc from the sun (Moffat and FitzGerald (1974), NGC 3105 8.0 kpc). Figure 4.1 presents a recent compilation by Moffat and Vogt (1973) of approximately 100 young open clusters. In what follows the local arm passing through or near the location of the earth is referred to as the Orion arm whereas the next inner and next outer arms are referred to as the Sagittarius-Carina and the Perseus arms respectively. Figure 4.1 suggests a clear separation between the Orion and Sagittarius arms with a possible joining of them as one moves towards $\ell^{II} = 270^{o}$. The Perseus arm is also fairly well separated from the Orion arm and the sun seems to lie on the inner edge of the Orion arm. Becker and Fenkart (1970) showed, with slightly fewer observed clusters, that when they are superimposed on the galaxy NGC 1232, whose total diameter is practically the same as that for the galaxy, they are found to coincide with the observed spiral arms, at the requisite distance from the centre, as regards width, separation and pitch angle. Such a comparison is of interest but sheds no further light on the spiral structure of our own galaxy.

Table 4.1

Spiral Tracers

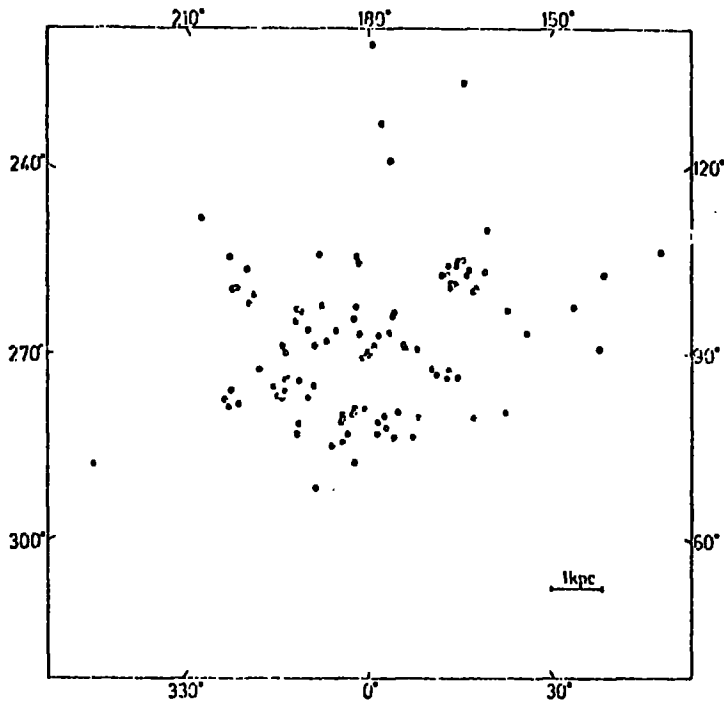| Optical	Radio
1. O and B stars-clusters-associations	1. 21 cm. line observations
2. H II regions	2. H II regions
3. M supergiants	
4. Wolf-Rayet stars	
5. Dust clouds and R-Associations	
6. Cepheids	

Figure 4.1: The distribution of young open clusters (spectral type $\leq$ B2) according to Moffat and Vogt (1973).

4.2.2 H II regions

As already mentioned hot young stars ionise the interstellar
medium producing H II regions which in their turn may be used as spiral tracers.
The most recent work on the mapping of the galaxy using H II regions has been
presented by Georgelin (1975).   Optical observations of H II regions extend up
to about 8 kpc from the sun but beyond this radio techniques are required.
The optical observations (Crampton and Georgelin 1975) rely on spectro-
photometric and kinematic methods for the determination of the distances.
The absolute magnitudes of the exciting stars were determined from MK
spectral types based on calibrations given by Walborn (1972), Balona and
Crampton (1974), Conti and Alsohuler (1971) and Fitzgerald (1969).   The
absolute magnitudes, where possible, were also determined independently from
H_α equivalent width measurements using the Balona Crampton calibration (1974).
An average of these two methods was taken as the absolute magnitude.   In
the absence of spectrophotometric distances, i.e. for distances greater than
a few kpc. kinematic distances were determined.   Figure 4.2 presents the
results obtained by Crampton (1975).   The overall distribution in this
figure is very similar to that shown in figure 4.1.· Georgelin and
Georgelin (1976) have extended the study of H II regions to the whole galaxy
by making use of the radio measurements of the $H109\alpha$ radial velocities (e.g.
Reifenstein et al. 1970).   Before presenting their results they have
weighted each of the H II regions considered by an excitation parameter given
by $\mathcal{U} \propto (S D^2)^{1/3}$ where S is the radioflux emitted by the H II region and D is its
distance.   This removes the difficulty of nearby H II regions seeming to be
of more significant than distant regions just by virtue of their distance
and not by virtue of their true size.   In external galaxies the H II regions
used for mapping the spiral structure are usually referred to as being
'brilliant and extended'.   Georgelin and Georgelin (1976) therefore only
use H II regions with excitation parameters greater than 70 pc cm^{-2} to map
the spiral structure.   Figure 4.3. presents the distribution of H II regions
with a possible spiral structure superimposed.   Georgelin's spiral structure
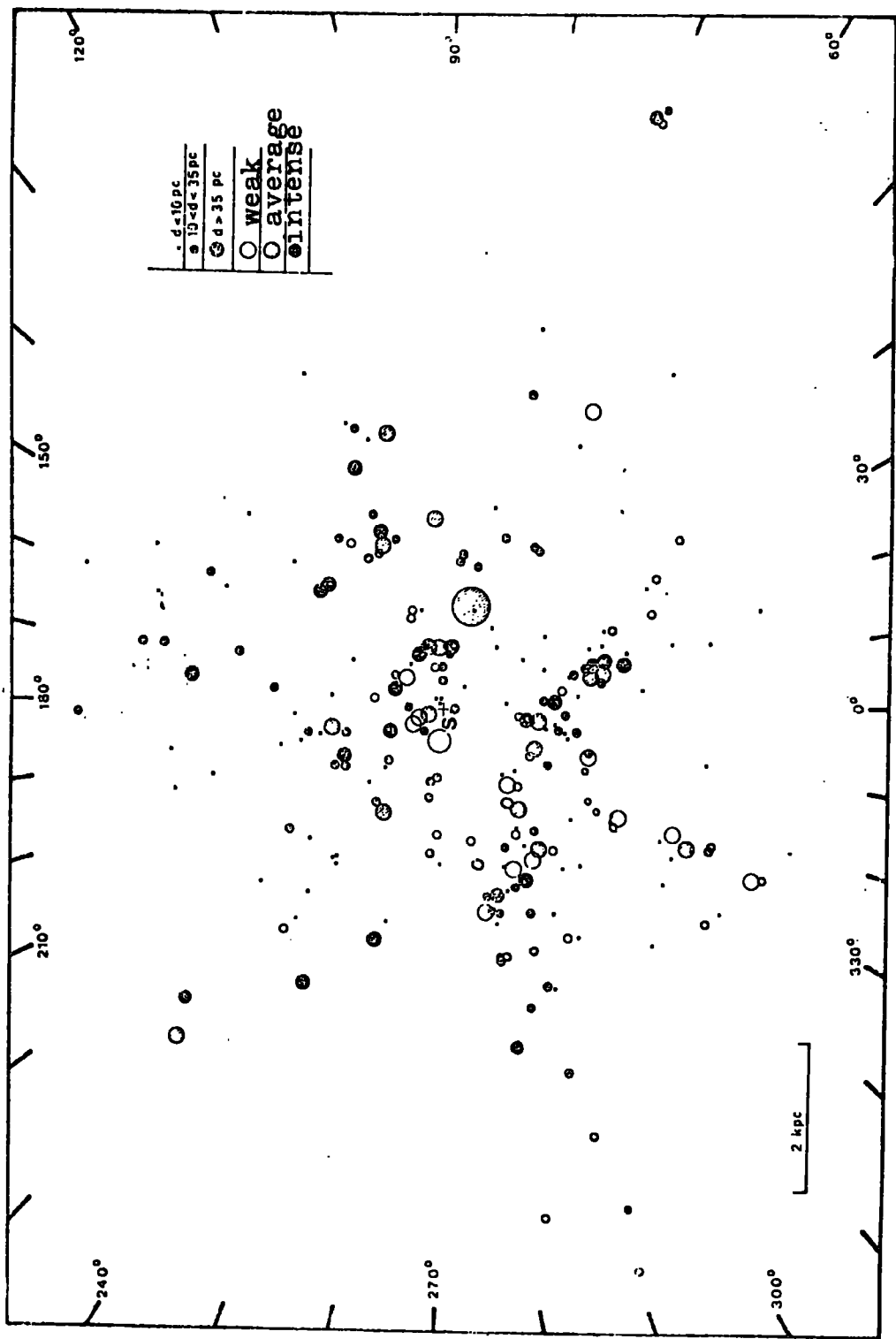will be discussed further in section 4.3.of this chapter.

Figure 4.2: Distribution of H_{II} regions in the solar neighbourhood according to Crampton and Georgelin (1975).
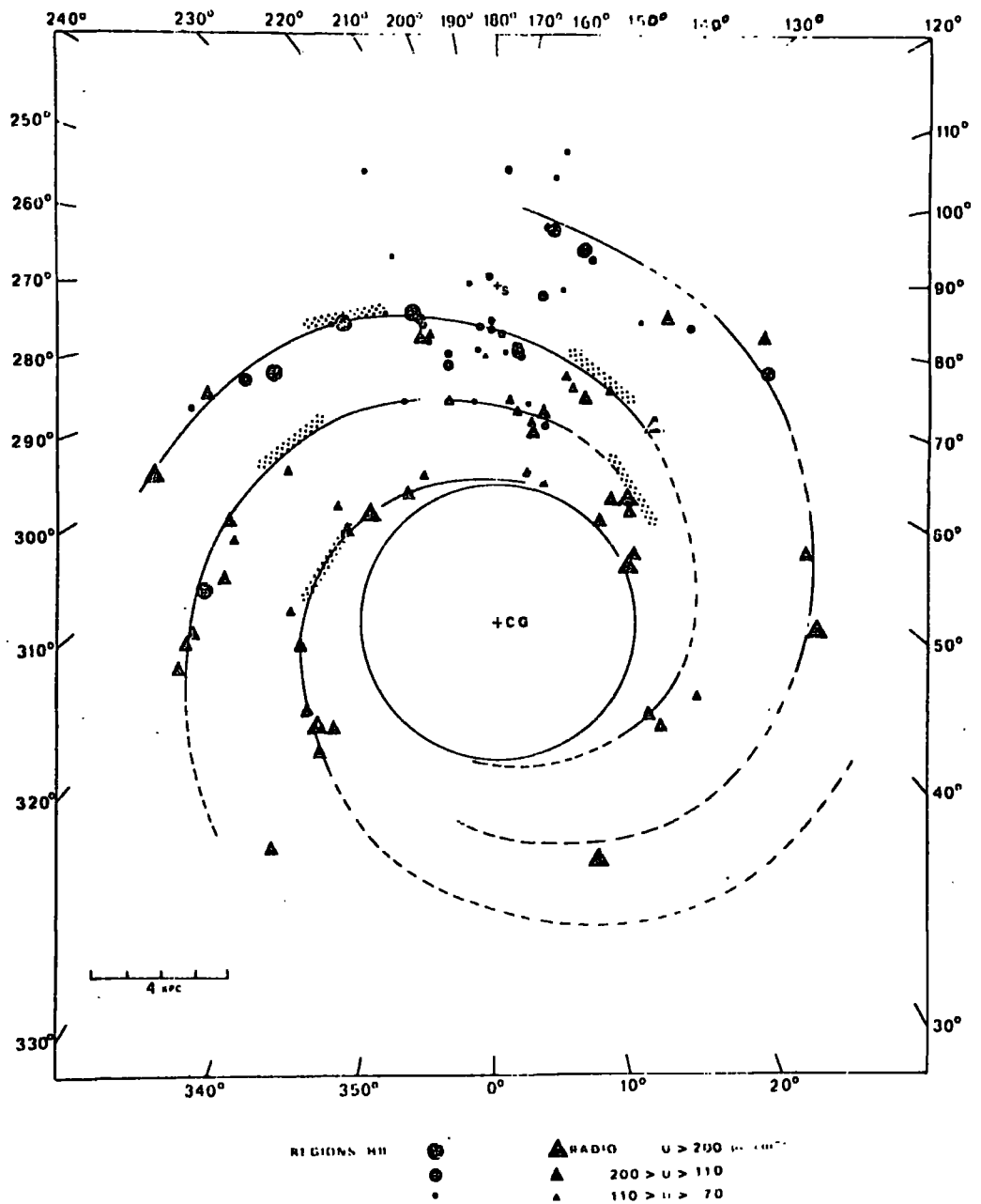
Figure 4.3: The galactic distribution of H_{II} regions with excitation parameter $> 70pc. \, cm^{-2}$. Superimposed is a four armed spiral structure suggested by Georgelin and Georgelin (1976). The dotted portions of the arms are those sections where no observations are available and symmetry has been used to complete the pattern.

4.2.3 M.Supergiants

Intermediate and late-type supergiants up to distances of 5 to
7 kpc from the sun have been studied by Humphreys (1970). Figure 4.4
shows the distribution of stellar associations, O, and galactic clusters, ●,
with supergiant members. Possible spiral features have been outlined.
Humphreys (1970) suggests a possible bifurcation of the Orion arm but
apart from this the distribution shows very similar features to those
seen in figures 4.1 and 4.2.

4.2.4 Wolf-Rayet Stars

Wolf-Rayet Stars are known to be extremely luminous population I
stars and are thus expected to be powerful spiral tracers. Figure 4.5b
shows the distribution of W-R stars in the galaxy as obtained from the
measurements of Smith 1968, 1970 and the revised calibrations to their
luminosity by Crampton (1971). As seen in the figure W-R stars are
observed up to distances of greater than 10 kpc from the sun. This
is partially due to their very high luminosity but is also a reflection
of the fact that they have a very broad distribution in Z, height above the
plane, indicating that most of the more distant ones are well out of the
galactic plane thus avoiding excessive interstellar absorption. As
will be discussed later, spiral structure is thought to be limited to only
a few hundred parsecs from the plane and therefore it is somewhat surprising
that W-R stars seem to show large scale spiral structure. Also shown in
figure 4.5 is the distribution of the rather contraversial stellar rings
identified by Isserstedt (1970) from the Palomar Atlas. The stellar rings
are ellipsoidal shells of stars often still connected with dark material
with minor diameters of about 7 pc. Isserstedt (1977) claims that this
diameter is the same for all stellar rings and therefore their distances
can be determined by measuring their angular diameters. As seen in
figure 4.5 the distribution of stellar rings does indeed seem to show
spiral structure in agreement with the W-R star observations. At present
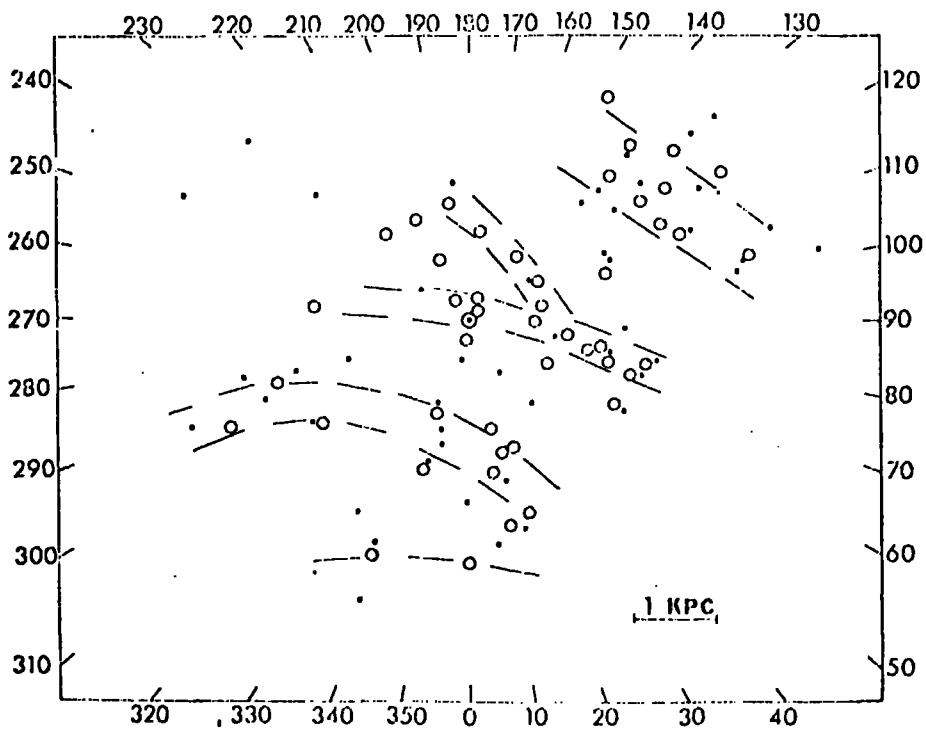there are innumerable criticisms of using stellar rings, if they are indeed

Figure 4.4: The distribution of stellar associations, o, and galactic clusters, ●, with supergiant members (Humphreys 1970). A possible spiral structure is indicated.
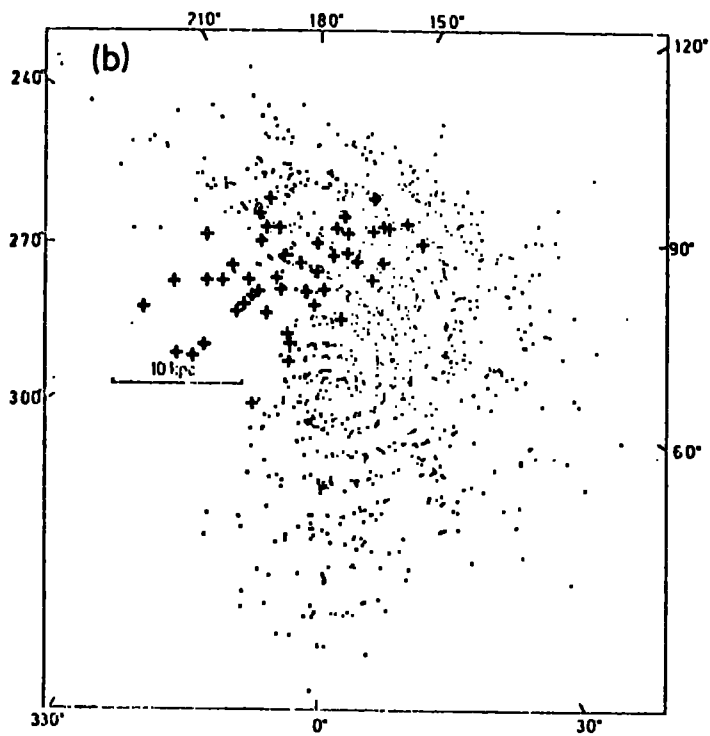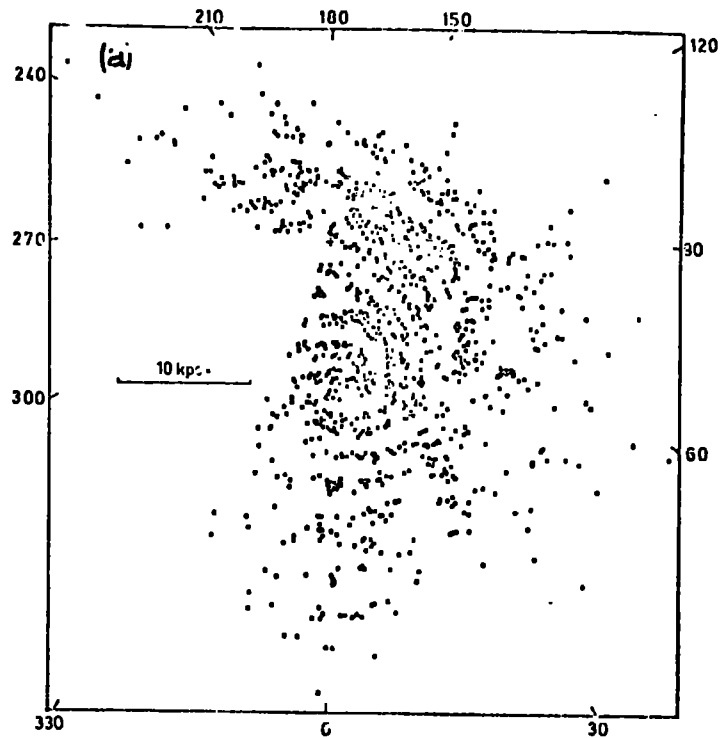
Figure 4.5:

    (a)   Distribution of stellar rings (Isserstedt 1970).

    (b)   The distribution of Wolf-Rayet stars (+)   superimposed on that
           of stellar rings (Schmidt-Kaler 1977).

physically connected systems, to map spiral structure and they will not

be considered further in this thesis.

4.2.5 Dust Clouds and R-Associations

Uranova (1970) has investigated the distribution of dust clouds in the

neighbourhood of the sun and has concluded that the inner edges of the

immediate Perseus and Sagittarius arms are delineated by dust but that

the majority of dust clouds are in fact associated with the local spiral

arm. Racine and van den Bergh (1970) from the distribution of

R-associations, associations of reflection nebulae, suggest that the Orion

arm is inclined to the galactic plane. In Cygnus and Cepheus the Orion

arm is located approximately 50 pc above the plane; crosses the galactic

plane in Cassiopeia and remains below the plane from Perseus to Canis Major.

4.2.6 Cepheids

Classical cepheids with a period of 13 days have probable ages of

$2-3 \times 10^7$ years. Such objects will probably have been formed mainly in

spiral features and most of them should not have moved from their place of

origin by much more than 200 pc; most of this displacement is likely to be

along spiral features. Cepheids with shorter periods with ages of 5×10^7

years or greater, may be at 500 pc or more from their places of origin and

their usefulness as spiral tracers becomes somewhat dubious. Long period

Cepheids can be observed to great distances from the sun, far beyond the

distances to which 0 to B 2 stars can be detected. Figure 4.6 shows the

distribution of Cepheids derived by Tammann (1970) superimposed on the

distribution of early clusters and H II regions from Becker and Fenkart (1970).

The distributions show considerable agreement and the cepheid distribution seems

to delineate a spiral arm closer to the galactic centre than the Sagittarius

arm and indicates a further arm in the anticentre beyond the Perseus arm.

4.2.7 21 cm Observations

As discussed in chapter 3 section 3.2.4, once a form has been found
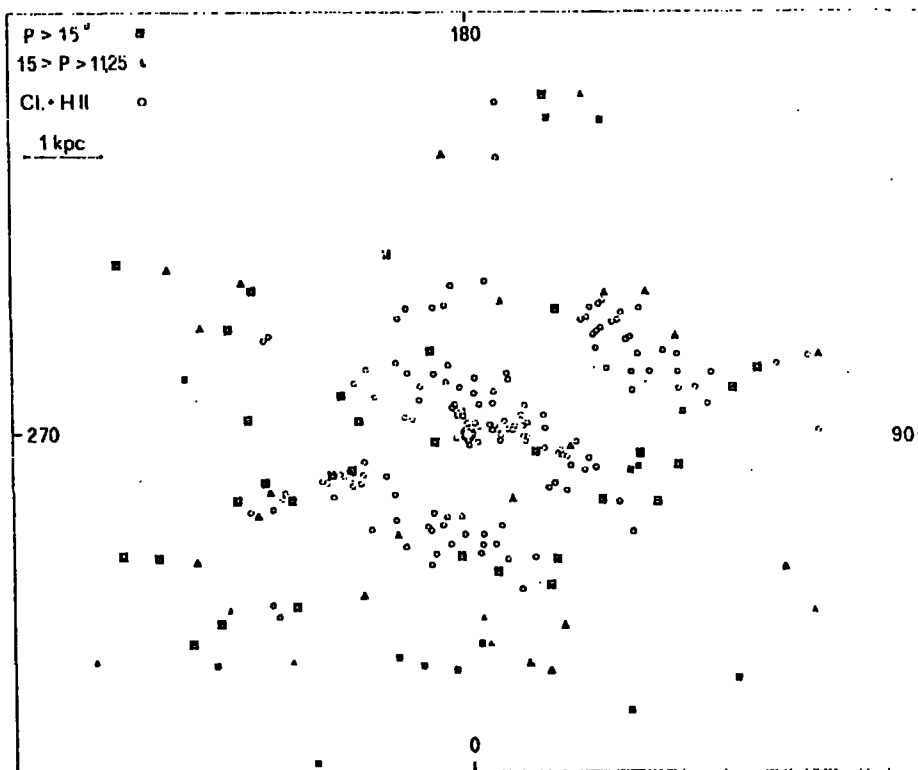
Figure 4.6: The galactic distribution of young objects projected onto the galactic plane. Big squares; cepheids with P > 15 days, big triangles; cepheids with 15 < P > 11.25 days. Small squares and small triangles; cepheids with uncertain distances in the corresponding distance intervals. The open circles are young clusters as compiled by Becker and Fenkart (1970).
Diagram from Tammann (1970).

for $\Theta(\lambda)$ the distribution of neutral hydrogen throughout the galaxy may be determined. The interpretation of the HI profiles is very complex and several interpretations have been made. Within the solar circle there is the distance ambiguity that has to be resolved by considering other observations. (see chapter 3 section 3.2.4). Kerr (1969) and Weaver (1970) have independently analysed the HI data and have obtained differing models for the galactical spiral structure. Figure 4.7 shows their two spiral structures superimposed (taken from Bok 1971). The differences in the spiral structures are caused mainly by different forms taken for the velocity longitude relation. Verschuur (1973) has presented a map for the spiral structure of the galaxy external to the solar circle thus avoiding the distance ambiguity problem. Figure 4.8 presents his inferred spiral structure. It should be noted that the radio data does not show long continuous arms but rather short sections of arms.

4.3 Conclusions regarding the observed Galactic Spiral Structure.

In the previous sections the main methods for delineating spiral structure have been discussed. It is clear that only the observations of HII regions and HI can be used to obtain a reliable picture of the large scale spiral structure. On a local scale all one can conclude is that the sun lies on the inner edge of the Orion arm which might connect onto the Perseus arm in the direction of $\ell^{II} \approx 270^{o}$. The location of the sun in relation to the Orion arm is discussed in more detail in the following two chapters.

In the development of the models presented in the next chapters the observations of Georgelin (1976) of HII regions and Verschuur (1973) of HI have been combined to produce the best observational picture for the spiral structure presently available. For the inner parts of the Galaxy, within the solar circle, the Georgelin map has been taken (Figure 4.3). The spiral structure is seen to be best fitted with a four armed spiral rather than the more commonly accepted two armed spiral. Georgelin's spiral pattern is consistent with the HI measurements in the directions for the tangential
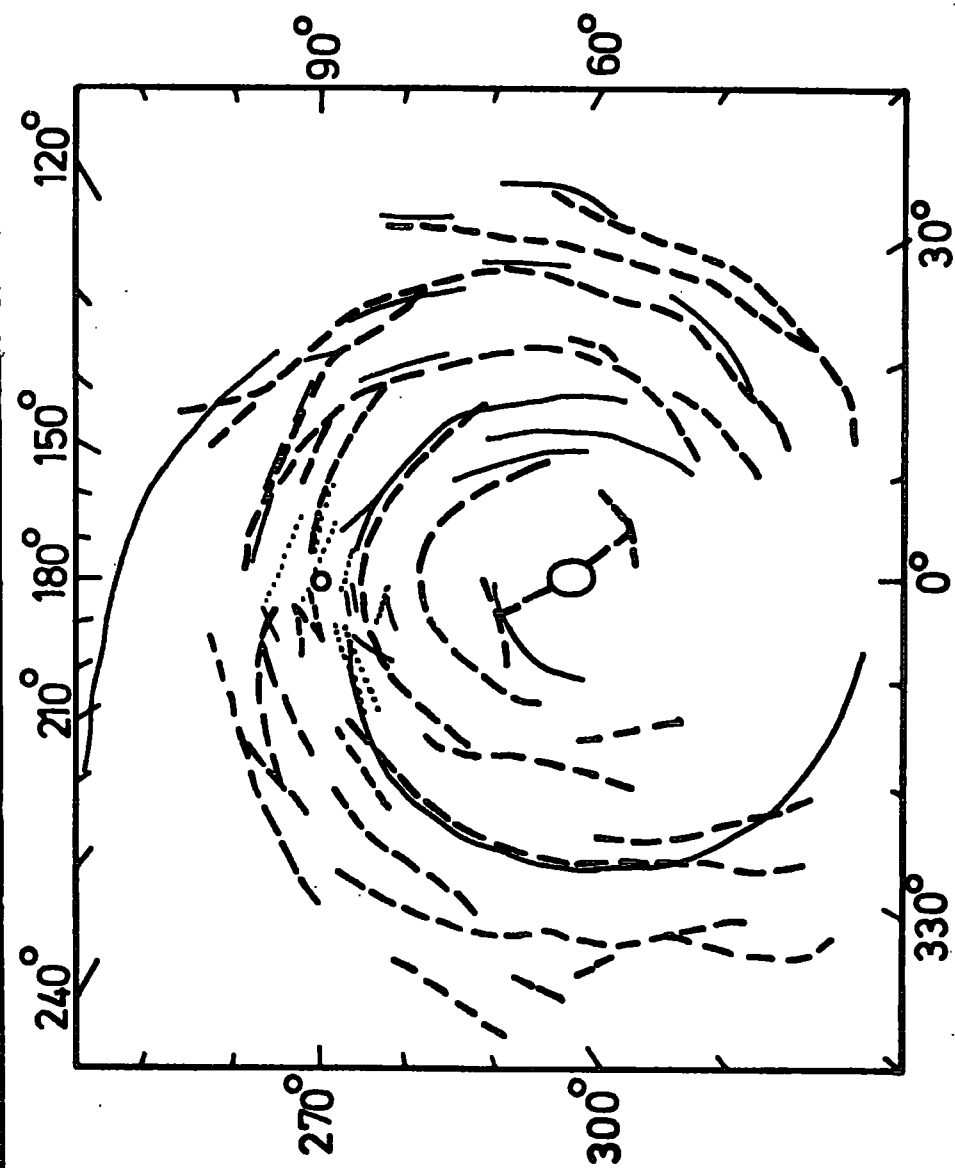
Figure 4.7: Spiral structure as obtained from 21 cm measurements. Kerr's interpretation is given by the thick dashed line and Weaver's interpretation is given by the thin continuous line. The dotted lines are the observed optical features. 0 marks the position of the sun at 10 kpc. from the galactic centre. (Bok 1971).
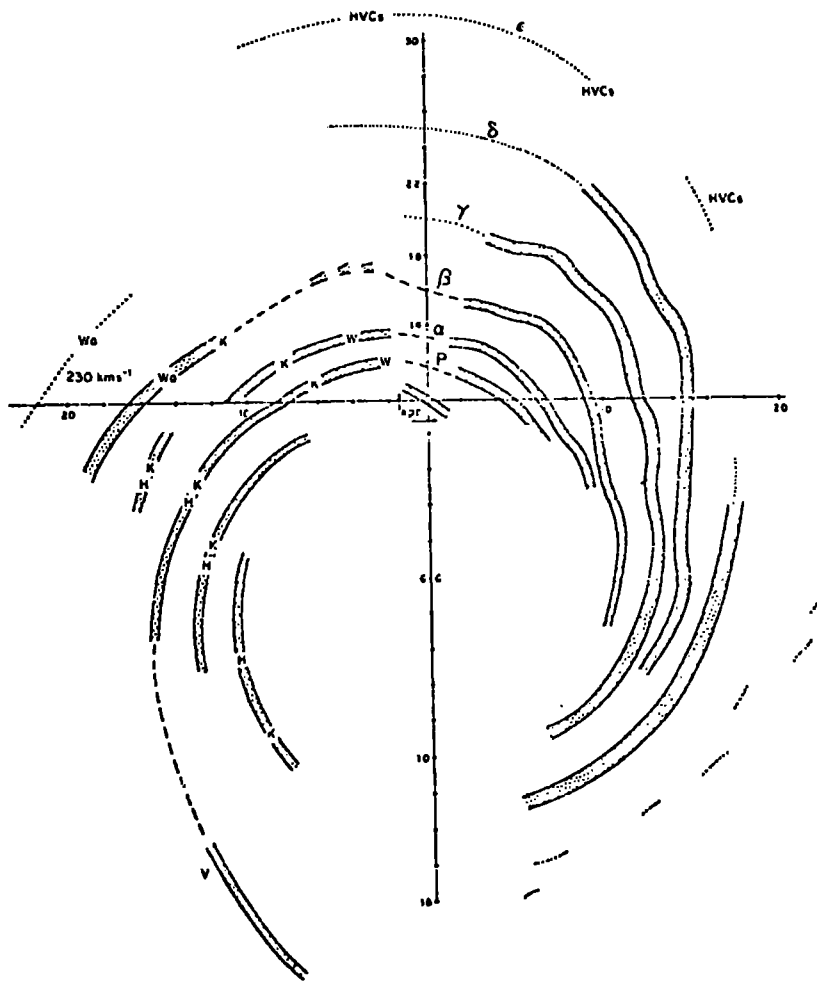
Figure 4.8:   A composite map of the outer spiral structure of the
Galaxy from 21 cm data by Verschuur (1973). K = Kerr
(1970), H = Henderson (1967), Wa = Wannier et al (1972),
W = Weaver (1970), V = Verschuur. HVC's = high velocity
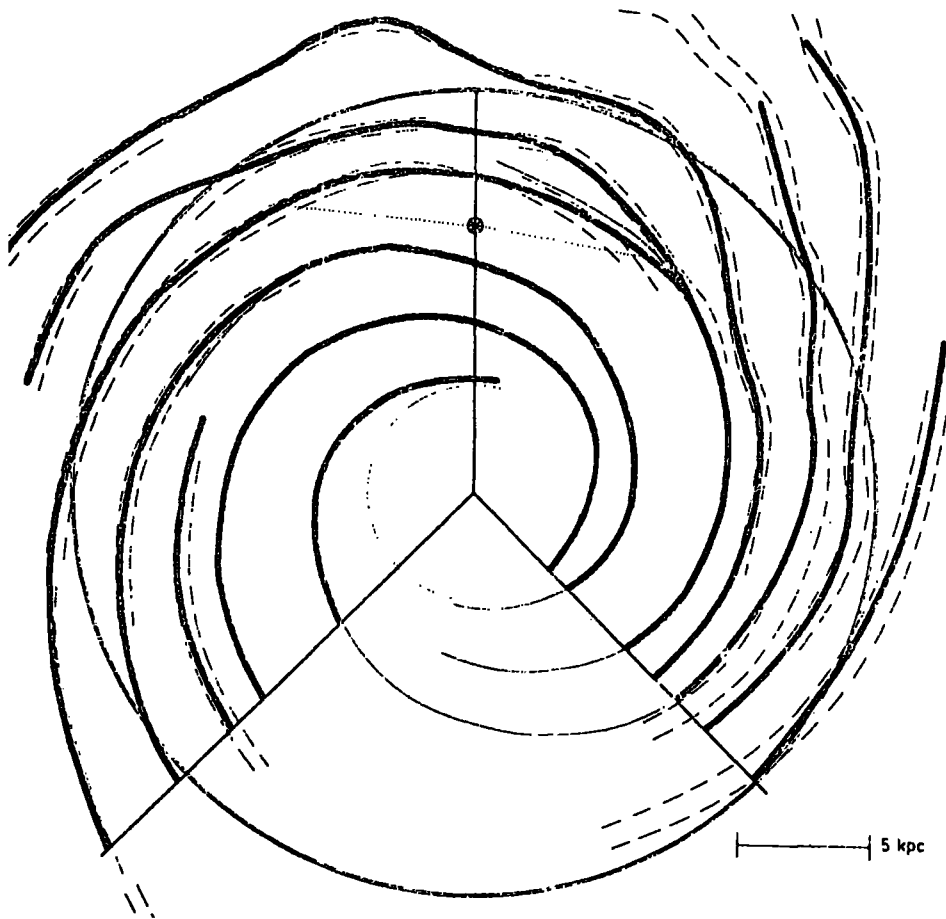clouds.

Figure 4.9: The composite galactic spiral structure used for the remainder
of this thesis. Within 10 kpc. of the galactic centre the H_{II}
map of Georgelin (1976) has been used whereas for distances
greater than this from the galactic centre the H_I map of
Verschuur (1973) has been used. The Georgelin data is shown
by the thin lines and the Verschuur data is shown by the
dashed lines. The thick continuous line represents the assumed
spiral structure. $⊕$ is the position of the earth at 10 kpc. from
the galactic centre and the dotted line passing through the sun
is a representation of the local arm that will be discussed in
detail in the next chapter.

points of the spiral arms. Georgelin finds that the spiral has a pitch angle of approximately 12° inclination. Recently Henderson (1977) has fitted a four armed spiral of inclination 13° to six regions of spiral arms, two observed optically and four observed in the radio. Both the above authors identify the Orion arm as some interarm feature rather than part of the 'grand design' of the galaxy. For regions outside the solar circle the spiral structure presented by Verschuur 1973, figure 4.8 has been assumed. Figure 4.9 presents the composite map of spiral structure used in the remainder of this thesis. It is comforting to note that where the Verschuur and Georgelin patterns overlap there is considerable agreement. The thick dark lines of figure 4.9 represent the ridge lines of the assumed spiral structure. Within 3 kpc of the galactic centre there is not expected to be any regular spiral structure as will be discussed in connection with the inner Lindblad resonance discussed in the next section.

4.4 Density Wave Theory of Spiral Structure

4.4.1 Introduction

Two theories for the maintenance of the spiral structure were introduced in the early sixties. The first associated a given body of matter with each spiral arm i.e. such an arm might essentially be a tube of gas primarily constrained by the interstellar magnetic field. The difficulty with the disrupting influence of differential rotation has already been mentioned. Toomre (1964) suggested that the material clumping is indeed periodically destroyed by differential rotation but is regenerated by gravitational instability. It seems difficult to envisage how such a mechanism alone can account for the relatively regular spiral pattern over the whole of a galactic disk. The second theory advanced (Lin and Shu 1964) suggested that the spiral structure should be regarded as a wave pattern that is rotating about the galactic centre.

At the present time the second of the above two theories is considered to be the more likely although there is still some interest in the first.

(Piddington 1973). The following sections describe the basic ideas of density wave theory concentrating on those areas of relevance to the setting up of the galaxy model in chapter 6.

4.4.2 Linear Theory

Density wave theory limits itself to explaining the maintenance of spiral structure and does not attempt to explain the origin of this structure. The last section of this chapter will briefly mention possible mechanisms whereby the structure might have been created.

The general gravitational field of the galactic disk, produced by the stars, is regarded as having superimposed on it a gravitational field of spiral form rotating at constant angular velocity, Ω_p about the galactic centre whose magnitude is a few percent of the main field. This spiral potential interacts with the galactic gas which tends to concentrate itself in the potential minima producing the spiral arms. The basic linear theory has been developed by Lin and Shu 1964, 1966.

The central relationship for any type of wave motion is that between wavelength and frequency. In the theory of self-generating density waves one must equate the density, given by Poisson's equation, required to sustain the spiral potential with the sum of the responses in density variation in the stellar and gaseus disks to obtain a dispersion relation. Using the WKBJ approximation introduced by Lin and Shu (1964) for tightly wrapped spiral arms they derived a dispersion relation for a stellar disk of infinitesimal thickness with relatively small velocity dispersion (Lin & Shu 1966). The relation gives the local radial wavenumber k once the wave frequency $\omega = m\Omega_p$ and angular symmetry m, the number of arms, are specified.

$$D(\omega, k, m, \Lambda) = \frac{|k| \; \mathcal{J}_\nu(x)}{k_T \; (1 - \nu^2)} = 1 \qquad \qquad 4.1$$

where $\nu = (\omega - m\Omega)/\chi$ is the intrinsic wave frequency measuring the ratio

of the freq. $(\mathcal{R}-\mathcal{R}_p)$ at which a particle passes through the wave pattern,

to the epicyclic frequency, X, i.e. frequency at which the spiral potential

is seen. Figure 3.3 shows the way $\mathcal{R}$ and X vary with galactocentric

distance in the Schmidt model. $k_T = X^2/2\pi G \sigma_{*0}$ is the characteristic

wave number Toomre (1964) of a rotating disk of basic surface density

$\sigma_{*0}(\Lambda)$. $x = k^2 \langle c_\Lambda^2 \rangle / x^2$ is the dimensionless measure of

the mean-square dispersive speed of the stars in the radial direction.

$$4.2. \quad \mathcal{F}_\nu(x) = \frac{1-\nu^2}{x}\left[1 - \frac{\nu\pi}{\sin(\nu\pi)} \frac{1}{2\pi}\int_{-\pi}^{+\pi} \exp\left(-x(1+\cos(s))\right)\cos(\nu s)\,ds\right]$$

is the 'reduction factor' which measures the proportion of low dispersion

stars participating in the wave pattern . Once an equilibrium model for

the stellar disk, e.g. the Schmidt model, has been decided upon and an

estimate of $\mathcal{R}_p$ made together with a value for m the density wave pattern

can be constructed from the dispersion relation. The above dispersion

relation makes no mention of the interaction of the gas with the spiral

potential. Originally Lin 1970 also considered the effect of the gas on

the linear dispersion relation. Now it is realised that the gas behaves

in a highly non-linear fashion and this will be discussed in the next

section. Equation 4.1 is clearly only valid for $1-\nu^2 > 0$ i.e. $\mathcal{R} - \frac{X}{m} < \mathcal{R}_p < \mathcal{R} + \frac{X}{m}$.

Figure 4.10 shows $\mathcal{R} - \frac{X}{2}$ and $\mathcal{R} + \frac{X}{2}$ on the basis of the Schmidt model. This is

for a two-armed spiral. It is seen that if the pattern speed was $11\,kms^{-1}kpc^{-1}$

the pattern would extend from 4kpc outwards without limit. For other values

of m, whatever the value of $\mathcal{R}_p$, the extent of the pattern is very

limited. It should be noted that this does not necessarily exclude the

possibility of spirals with more than two arms as at present there appears

to be no theoretical reason why several modes should not be present at once

or even for there to be a continuum of values of $\mathcal{R}_p$! Roberts (1972) has

found, for example, that in the non-linear situation, basic two-armed

spirals may become multiple armed in their outer regions. Simonson (1976) has

matched a model of two-armed spirals with differing phases to the H$\mathcal{I}$

observations. The model requires several spirals with differing phases to

enable the observed pitch angle of greater than 12° in the outer parts of
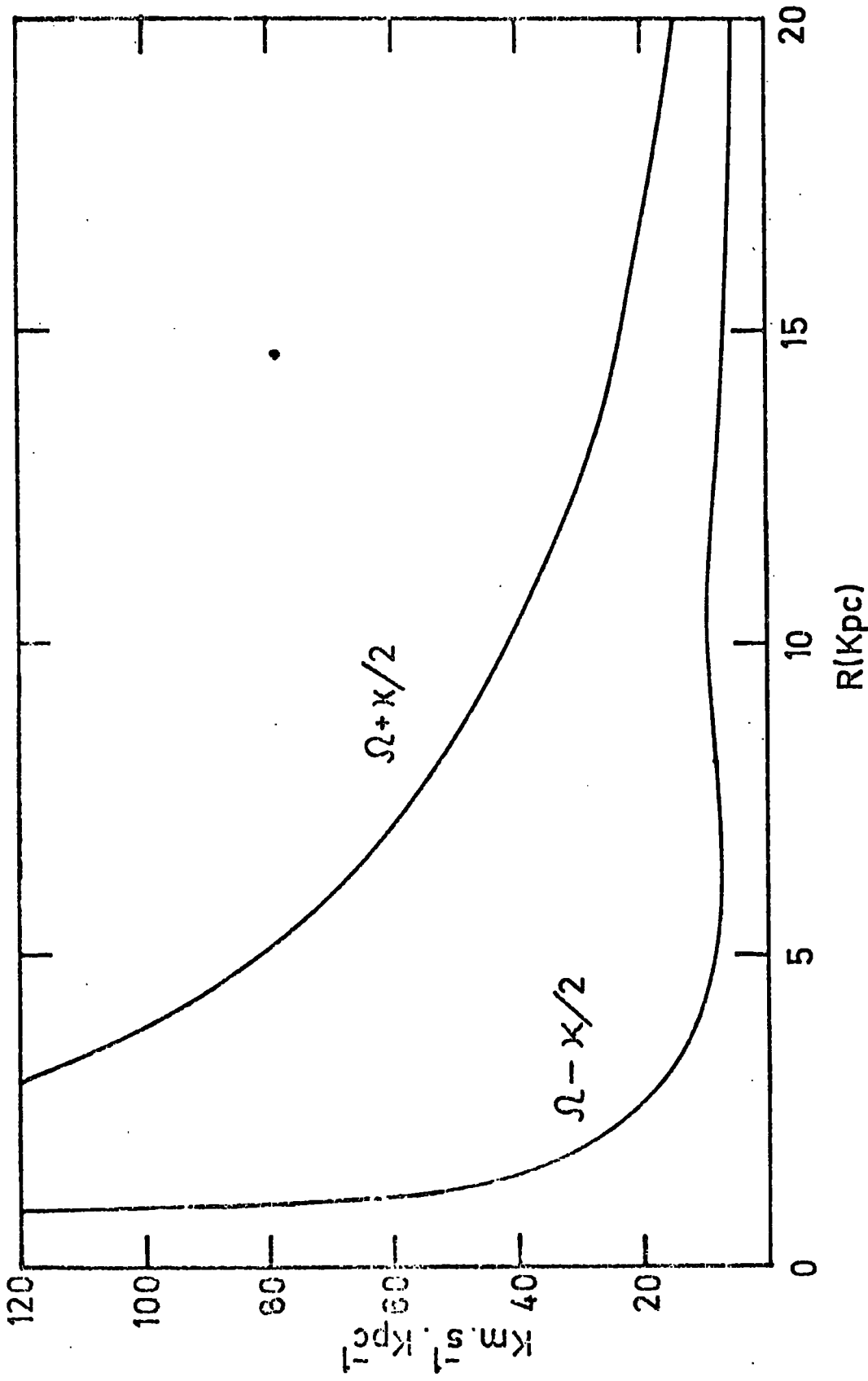
Figure 4.10 The variation of ($\Omega - \kappa/2$) and ($\Omega + \kappa/2$) with galactocentric distance on the basis of the Schmidt model. Spiral structure is expected to be limited to between these two resonances and therefore for a pattern speed of 12.5Km s^{-1} kpc^{-1} the spiral structure would be expected to extend from about 3.5kpc. outwards without limit.

the galaxy to be mirrored in the HI velocity profiles using spirals which have basic pitch angles of 6°-8°. The separation between spiral arms, in the linear theory, is related to the pitch angle by $Sep = 2\pi_A \tan(i)/m$. Therefore for the solar neighbourhood, where the separation is observed to be approximately 3 kpc, a pitch angle of about 8° is required for a two armed spiral. To obtain agreement with the observed pitch angle of 12° and separation the value of m needs to be increased to 4. As already mentioned, however, the m=4 mode has a very narrow extent for any pattern speed. For $\mathcal{R}_p = 20\,kms^{-1}kpc^{-1}$ the pattern would extend from about 8 to 14.5 kpc from the galactic centre. A pattern speed as high as this has been suggested by Nelson (1976) to obtain agreement between the theoretically predicted and observed HI profiles in the anticentre direction. It therefore seems clear that neither a single m=2 or m=4 mode is capable of explaining the observed spiral structure but that a combination of modes is required. It should be mentioned however that Miller (1976), through numerical experiments, has shown that the m=2 mode is the preferred mode to be generated in the galaxy and then maintained.

The limiting cases for the values $\nu = \pm 1$ in equation 4.1 correspond to the Lindblad resonances, $\mathcal{R}_p = \mathcal{R} \pm \varkappa/m$. The inner Lindblad resonance $\mathcal{R}_p = \mathcal{R} - \varkappa/2$, inside which no spiral pattern is expected, in our galaxy is tentatively associated with the expanding 3 kpc arm within which no spiral structure has been observed.

On the basis of a two-armed linear model Lin and Shu 1967 produced a possible spiral pattern for the galaxy. The pattern speed was assumed to be between 11-13 km s^{-1}kpc^{-1} to arrive at the correct spacing between the Perseus and Sagittarius spiral arms. Figure 4.11 presents the spiral pattern derived by Lin and Shu (1967) using the linear theory with $\mathcal{R}_p = 11\,kms^{-1}kpc^{-1}$. It should be noted that the Orion arm is not considered to be part of the spiral pattern but rather a spur or an interarm branch. The best value for the spiral potential is found to be about 5% of the disk potential. Lin et al. (1969) were able to show that
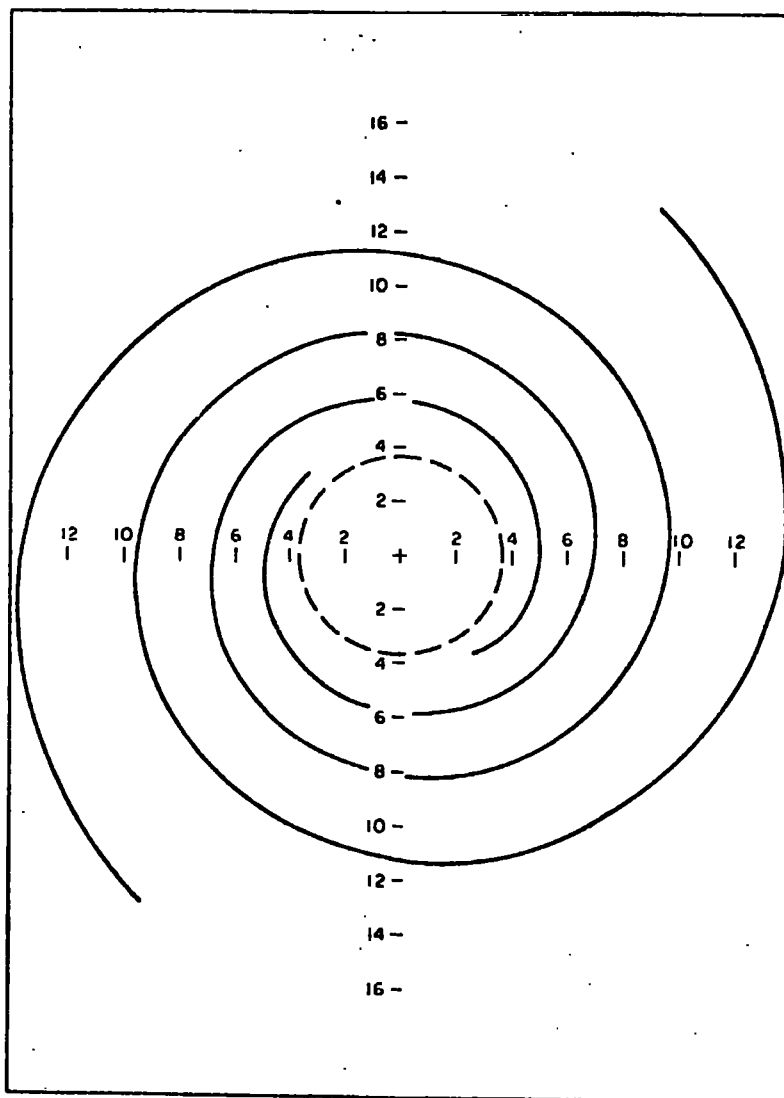
Figure 4.11: The spiral pattern as derived by Lin and Shu (1967) on the basis of linear theory. The pattern speed is taken to be 11 km.s^{-1}. kpc^{-1}. The dotted line indicates the position of the inner Linblad resonance.

such a theoretical model was able to reproduce many of the observed features of the galaxy. They were able to predict the systematic motion of gas in the spiral arms and reproduce the observed rotation curves as shown in figures 3.2b and c.

It is now generally accepted that such a linear theory is capable of explaining the overall structure of our galaxy and also that of many external galaxies, Roberts et al. (1975), but that a more detailed non-linear analysis is required when considering the behaviour of the gas in the spiral potential minima.

4.4.3 Non-Linear Theory.

Figure 2.12a gives the (A, Θ) coordinate system for the galactic disk. For the basic potential field of the disk, the Schmidt model, the velocity of the gas in this coordinate system is U_Θ with $U_A = 0$ i.e. the motion is purely circular. If a spiral potential is superimposed then additional velocities U_{Θ_1} and U_{A_1} are imparted to the gas due to this potential. When considering a spiral potential it is convenient to use the coordinate system shown in figure 2.12b. ξ is a line of equispiral potential inclined at a pitch angle i to the circumferential direction and η is the coordinate perpendicular to ξ. As the spiral pattern is assumed to be rotating at a speed of Ω_p these coordinates for convenience are assumed fixed in the Ω_p rotating system. The gas velocities may now be written as

$$\omega_{\xi_0} = (\Omega - \Omega_p) A \sin i \qquad 4.3$$

and $\omega_{\eta_0} = (\Omega - \Omega_p) A \cos i$ $\quad 4.4$ for the Schmidt field and $\omega_{\xi_1} = U_{A_1} \cos i + U_{\Theta_1} \sin i$

and $\omega_{\eta_1} = U_{A_1} \sin i + U_{\Theta_1} \cos i$ for the spiral field velocities.

$W_\xi = \omega_{\xi_0} + \omega_{\xi_1}$ and $W_\eta = \omega_{\eta_0} + \omega_{\eta_1}$ are the resultant velocities in the (ξ, η, Ω_p) coordinate system. A streamtube is defined to be a line with varying Θ_{Ω_p} roughly concentric with the galactic centre. The streaming motions will not be exactly concentric due to the perturbing field.

The density response of the interstellar gas to a small background

spiral gravitational field is found to be rather large (Roberts 1969,

Fujimoto 1966) resulting in the development of galactic shocks. Figure

4.13 shows the density variation along a streamtube in the non-linear

theory. A shock is seen to form within the potential minimum. Undergoing

the basic rapid rotation about the galactic centre, the gas flows through the

slower rotating wave pattern and shock in a continuing process from left to

right in figure 4.13. The passage of the gas through the shock is

envisaged as the mechanism by which star formation is started. Also

shown in figure 4.13 is the way in which $W_{\perp}$ and $W_{\parallel}$ vary along a stream-

tube about their unperturbed values of $\omega_{\perp_0}$ and $\omega_{\parallel_0}$ defined in equations

4.3 and 4.4. Shocks form if the spiral potential of fractional amplitude F

compared with the Schmidt field is sufficiently large to cause $W_{\perp}$ to become

supersonic. In fact two situations are possible within a galaxy. If

$\omega_{\perp_0} > C_S$, the acoustic speed of the gas, most of the gas on the streamtube

is moving at supersonic speeds while only a small portion is moving subsonically.

Shocks forming in this situation tend to be strong and give rise to narrow

regions of high gas compression. Figure 4.14 is a plot of the variation of $\omega_{\perp_0}$

against r for our galaxy assuming $\mathcal{R}_p = 12.5\,km\,s^{-1}\,kpc^{-1}$ with $\tan(i) = 1/7$.

In our galaxy C_S is thought to have a value somewhere in the range $7-12\,km\,s^{-1}$

suggesting that the shocks in our galaxy are strong, giving rise to narrow

regions of high gas compression. If on the other hand $\omega_{\perp_0} < C_S$ most

of the gas on a streamtube is moving subsonically while only a small portion

is moving supersonically. In this situation the shocks tend to be weak and

yield rather broad regions of relatively low compression (Shu 1973). Figure

4.15 gives the TASS (Two Armed Spiral Shock) pattern for the galaxy as

derived by Roberts (1969). The darkly shaded areas of this diagram show

the location of young stars and the lightly shaded areas show the regions of

concentration of neutral hydrogen gas.

In the above the galactic magnetic field has been assumed to have a

negligible effect on spiral structure. Roberts and Yuan (1970) introduced

the galactic magnetic field into the formulation of the TASS pattern.

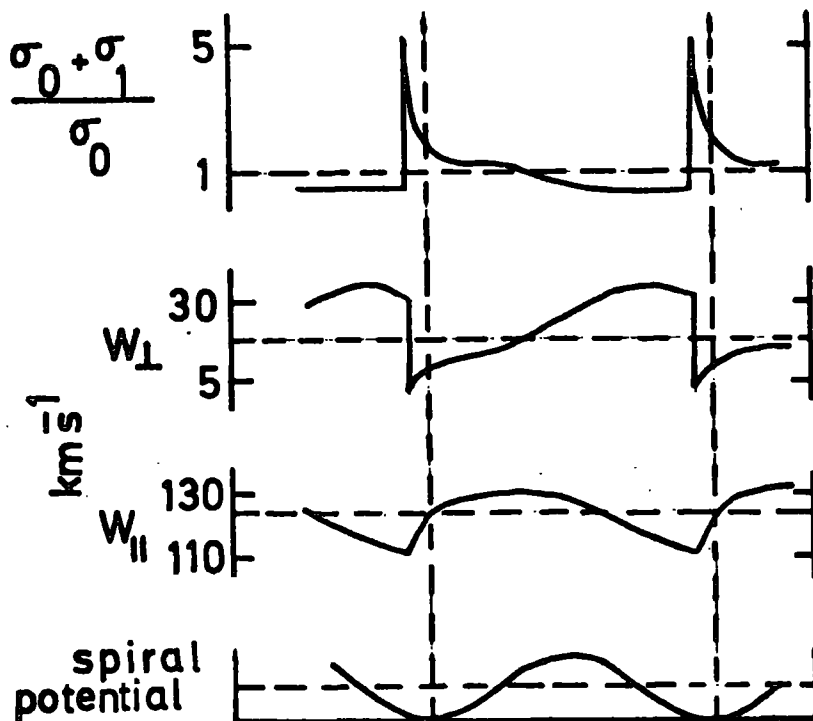The magnetic field is found to have the effect of increasing the effective

Figure 4.13: A typical solution in the TASS picture for $\Omega_p = 12.5 \text{km.s}^{-1}$ kpc.$^{-1}$ with tan (i) = 1/7. The variation of density contrast, $W_\perp$ and $W_{/\!/}$ along a streamtube at r=10 kpc. with a spiral field 5% of the Schmidt field is shown. A mean dispersion speed of 10 km.s^{-1}. has been assumed.
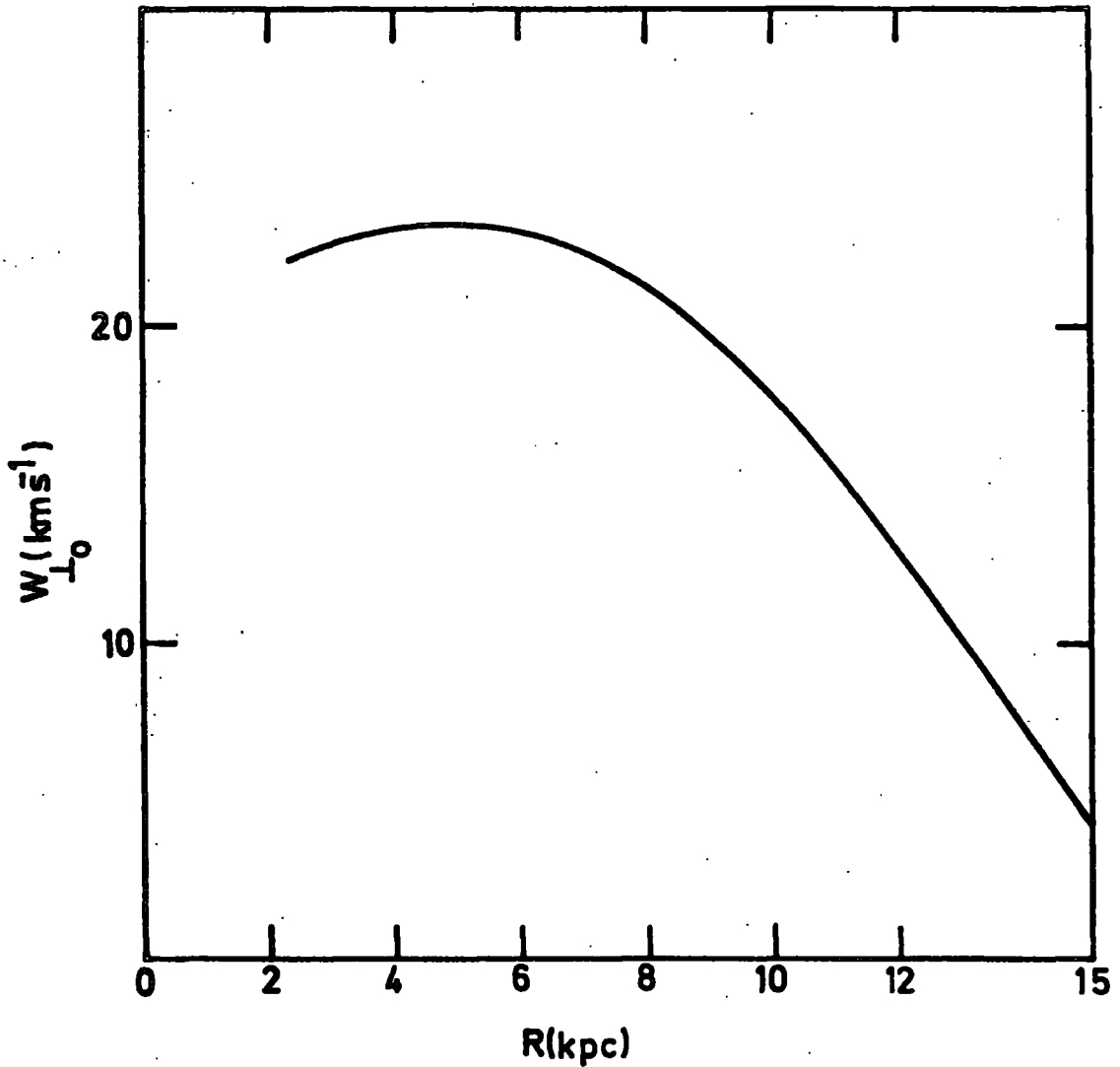
Figure 4.14: Variation of $W_{\perp_o}$ with radius for the galaxy. As the effective acoustic speed of the galaxy is thought to be in the range 7-12 $km.s^{-1}$ it is clear that for most of the galaxy we would expect strong shocks giving rise to narrow regions of high gas compression.
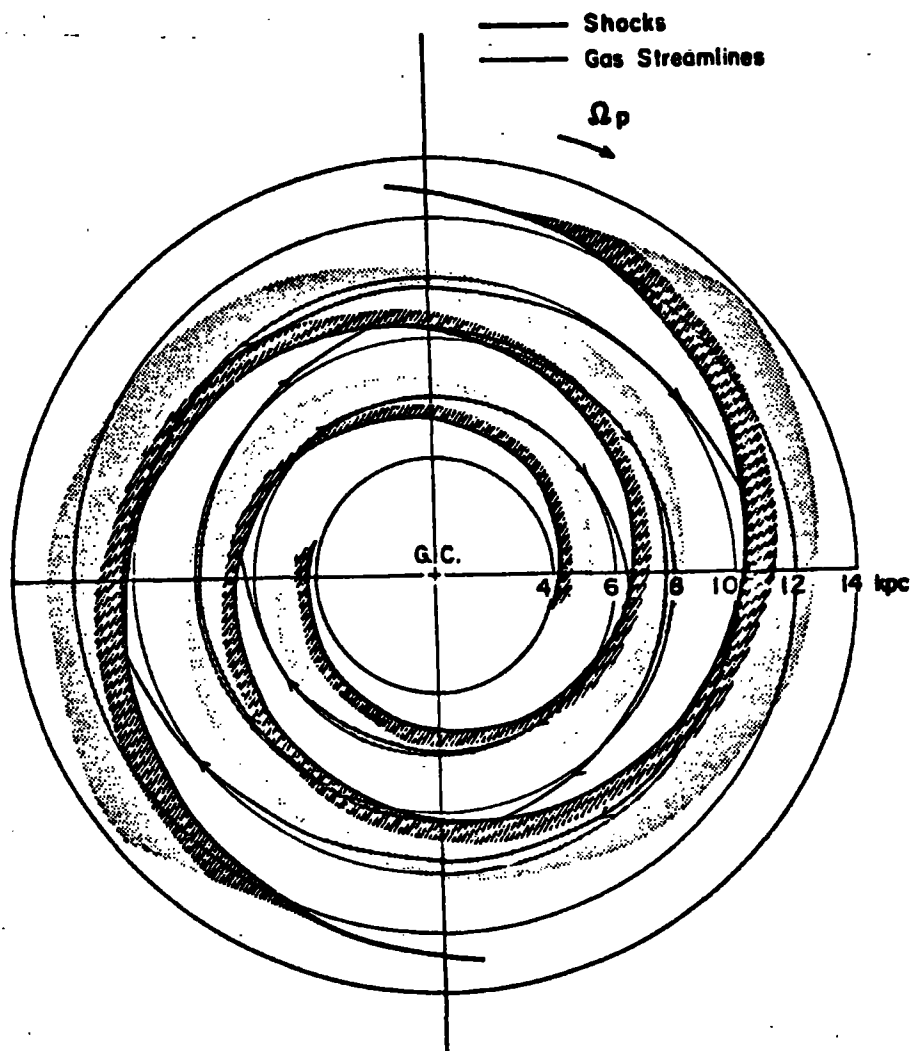
Figure 4.15: TASS pattern for the galaxy (Roberts 1969). Each streamtube appears as a sharp-pointed oval with a sharp turning point at each shock. The parameters are the same as those listed for figure 4.13.

square dispersion speed of the gas. Rather than this just being equal to the sum of the squares of c_t , the effective turbulent dispersion speed of the gas, partly kinetic and partly due to turbulence and c_λ , the effective speed of the gas due to the pressure of cosmic-ray particles, the effective square dispersion speed a_s^2 equals $c_t^2 + c_\lambda^2 + a_m^2$ where $a_m = \langle H_0^2 \rangle / 4\pi \langle \rho_0 \rangle^{1/2}$ is the Alfvèn speed. c_t has a value in the region of $7 kms^{-1}$ and a_m has a value of also about $7 kms^{-1}$ for a field of $3\mu G$. This suggests that the contribution of the galactic magnetic field to the dynamics of the gas is about as important as the turbulence of the gas. Increasing a_s^2 by introducing a_m^2 has the effect of damping down the compression in the density waves, i.e. there is essentially an extra pressure that the forcing mechanism for the density wave has to overcome. Roberts and Yuan (1970) present profiles along streamtubes for the variation of gas compression when the magnetic field is included. The amplitude of the shocks is fairly constant out to about 11 kpc after which point the amplitude begins to fall fairly rapidly. Figure 4.16 shows this variation representative of the regions of the galaxy within 10 kpc.

4.4.4 Spiral Structure above the plane

So far the theoretical ideas on density wave theory have been limited to an infinitesimally thin galactic disk. In equation 4.1 a further reduction factor T can be introduced equal to $\left(1 + |k| z_0\right)^{-1}$ Vandervoort (1970) to account for the finite thickness , z_0 , of the stellar disk. Recently Saha 1974 has considered the case of the density wave in a full three-dimensional hydromagnetic theory. His analysis is linear in nature and therefore does not give any insight as to how the peak compression in a shock decreases as one moves out from the galactic plane. Here this 'demodulation' will be considered in terms of magnetohydrodynamic shock theory. The subscript 1 will refer to that parameter before the shock and the subscript 2 will refer to that same parameter after the shock. It should be pointed out that the following ideas only lead to an understanding of the way in which the modulation is thought to decrease with z and not to an accurate quantitative description.
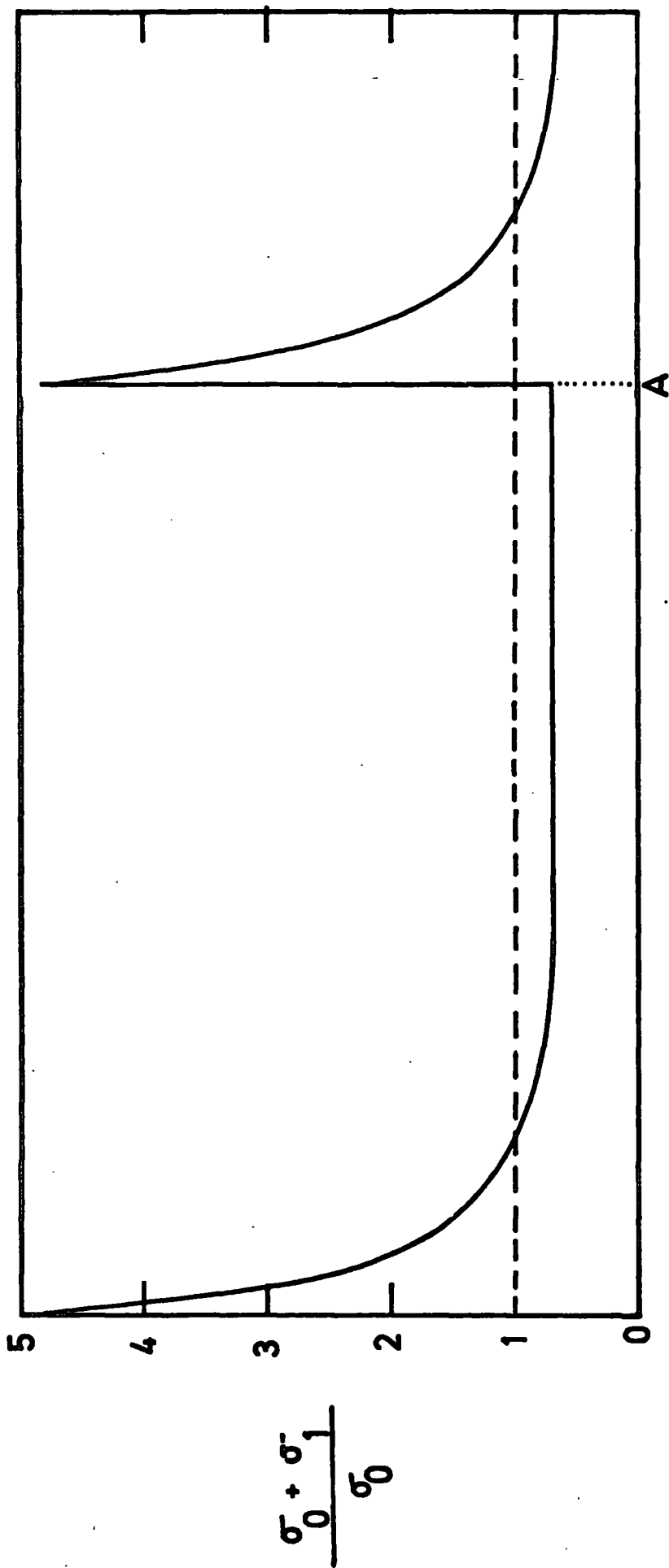
Figure 4.16: Variation of the gas density along a steamtube in the TASS picture with a magnetic field of 2-3 μG. a_s=8km.s^{-1}, F=5%, tan(i) = 1/7, $\mathcal{R}_p$ =12.5km.s^{-1}, and r= 10kpc.

In the case of a shock wave without magnetic fields the Rankine-Hugoniot jump condition equations (Kaplan 1958) lead to the following relation between the velocities and densities on either side of the shock $u_1/u_2 = \rho_2/\rho_1$. If a magnetic field is introduced the shock strength ρ_2/ρ_1 is in general decreased. For a shock propagating in the direction of the magnetic field, the magnetic field does not effect the shock in any way. On the other hand a shock propagating perpendicular to the magnetic field is considerably affected by this field. This is the situation that arises in the galaxy; the field is essentially longitudinal in nature with the shock propagating in a radial direction. For a magnetic field inclined to the shock only the perpendicular component of that field is affected by the shock. The hydromagnetic Hugoniot equations for the case of the magnetic field perpendicular to the shock can be written as:

$$\rho_1 u_1^2 + P_1 + H_1^2/8\pi = \rho_2 u_2^2 + P_2 + H_2^2/8\pi \qquad 4.5$$

for the conservation of momentum.

$$\frac{\gamma P_1}{(\gamma-1)\rho_1} + \frac{u_1^2}{2} + \frac{H_1^2}{4\pi\rho_1} = \frac{\gamma P_2}{(\gamma-1)\rho_2} + \frac{u_2^2}{2} + \frac{H_2^2}{4\pi\rho_2} \qquad 4.6$$

for the conservation of energy

4.7 $\rho_1 u_1 = \rho_2 u_2$ for the conservation of mass, and

4.8 $H_1 u_1 = H_2 u_2$ for the conservation of flux.

From 4.7 and 4.8 $H_1/H_2 = \rho_1/\rho_2$ 4.9 which expresses the fact that the magnetic field is frozen into the gas. In the above equations P is the gas pressure and γ is the ratio of the specific heats equal to 5/3 for a monatomic gas. $C_s(1) = (\gamma P_1/\rho_1)^{1/2}$ isthe accoustic speed of the gas before the shock. Making the following substitutions; $M = u_1/C_s(1)$, the Mach number, $Q = H_1^2/8\pi P_1$, $A = \rho_2/\rho_1$ and $R = P_2/P_1$ one obtains from equation 4.5.

$$\gamma M^2 (1 - 1/A) = (R-1) + Q(A^2 - 1) \qquad 4.10$$

and equation 4.6 becomes

$$\gamma M^2 \left(1 - \frac{1}{\lambda^2}\right) = \frac{2\gamma}{\gamma-1} \left(\frac{R}{\lambda} - 1\right) + 4Q(\lambda - 1) \qquad 4.11$$

Eliminating R from equations 4.10 and 4.11 and excluding the solution r=1=R

corresponding to no shock one obtains

$$Q(2-\gamma)\lambda^2 + \left[\gamma(Q+1) + \frac{1}{2}\gamma(\gamma-1)M^2\right]\lambda \qquad 4.12$$
$$- \frac{1}{2}\gamma(\gamma+1)M^2 = 0$$

which reduces to

$$\frac{5}{18} V_A^2 \lambda^2 + \left[\frac{25}{8} V_A^2 + \frac{5}{3} c_s^2(1) + \frac{10}{18} u_1^2\right]\lambda - \frac{20}{9} u_1^2 = 0 \qquad 4.13$$

when $\gamma = 5/3$ and V_A^2 is the square of the Alfven velocity equal to

$H_1^2/4\pi\rho_1$. Solving equation 4.13 for r, the strength of the shock, gives

$$\lambda = \frac{-(5V_A^2 + 6c_s^2 + 2u_1^2) + \left((5V_A^2 + 6c_s^2 + 2u_1^2)^2 + 32 u_1^2 V_A^2\right)^{1/2}}{2V_A^2} \qquad 4.14$$

Equation 4.14 enables the variation in shock strength with height above the

plane to be determined once the variation in the magnetic field, gas density,

c_s^2 and u_1^2 are known. Here it is assumed that the magnetic field,

the sound speed and the velocity of entry into the shock, u_p are all

constant for heights above the plane up to several hundred parsecs. They

are assumed to have the values observed in the plane namely $H = 3\mu G$, $c_s^2 = 49 \, (kms^{-1})^2$

and u_1 is set equal to 35 kms^{-1}. The gas density is assumed to vary in the

manner shown in figure 3.5.

Figure 4.12 shows that for a galactocentric distance of 8 kpc ω_{λ_0}

is of the order of 18kms^{-1} and figure 4.12 shows that W_λ is approximately

twice ω_{λ_0} just before the shock. For this reason u_1 equal to 35 kms^{-1} is

taken as a realistic representative value. Using equation 4.14 the way

in which the compression falls with height above the plane has been

determined. Figure 4.17 shows this. The compression has disappeared

by 500 pc above the plane and the compression demodulation curve has

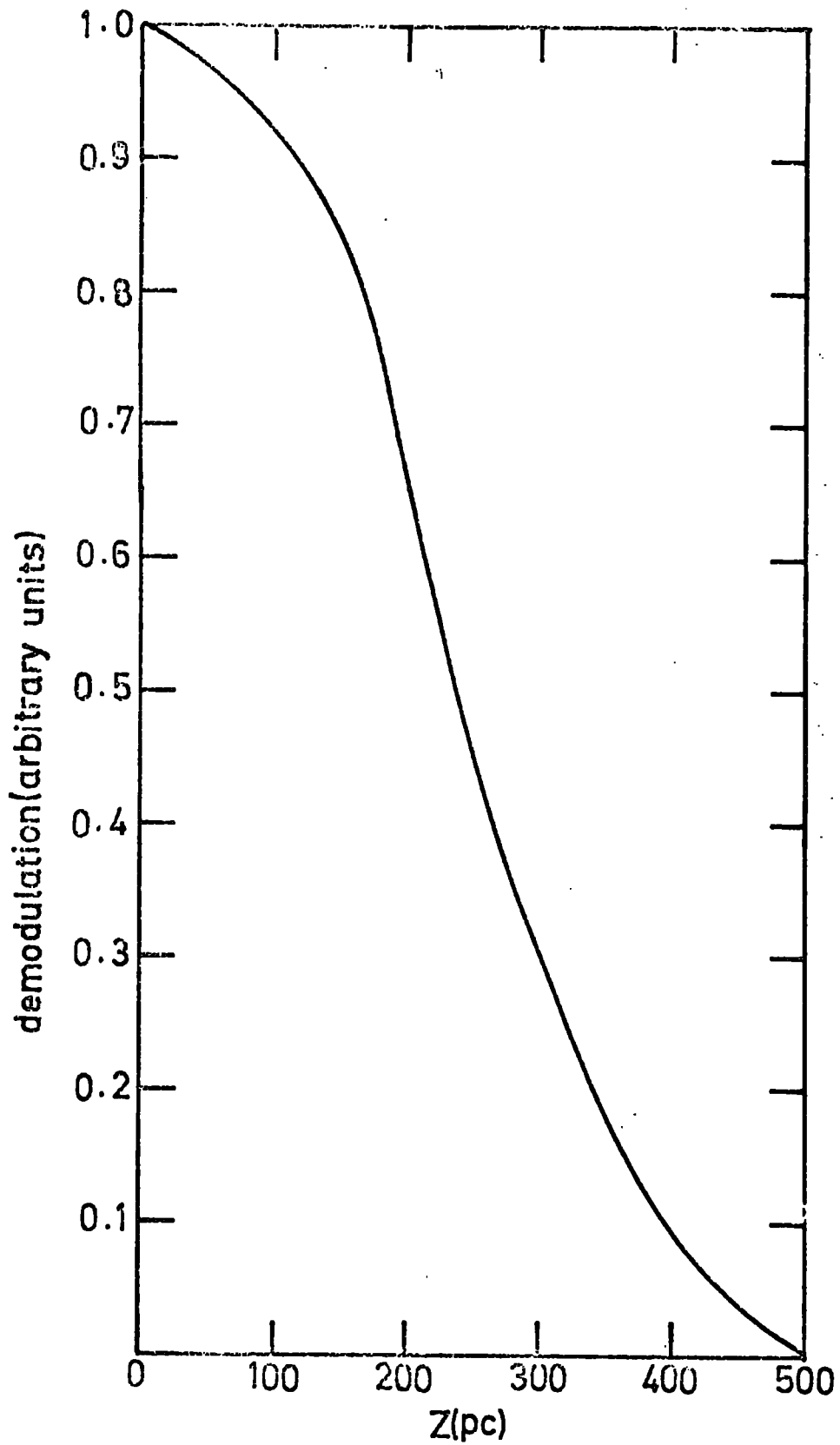a width, $2l_{\frac{1}{2}}$, of 480pc.

Figure 4.17: The way in which the compression falls-off with height above the plane as given by equation 4.14.

Figure 4.18 shows the way in which the magnetic and gas pressures vary with height above the plane in such a model. As density is falling the gas pressure drops much more quickly than the magnetic pressure. The two pressures become equal at about 200 parsecs from the plane. This may be interpreted as the magnetic pressure gradually damping the density contrast as it increases as compared to gas pressure.

If figure 4.17 is assumed to be the way in which the demodulation occurs how thick would one expect the observed spiral arms to be? Obviously the observed spiral arms must be somewhat thinner than this as the formation of O and B stars requires gas as well as the presence of the shock. As the gas density falls with height above the plane as well as the shock strength the half width of the observed spiral arms will be less than 240 pc, the demodulation halfwidth. The halfwidth of the gas is approximately 135 persecs, figure 3.5. If, naively, the way in which the density of spiral tracers fall off above the plane is taken to be just proportional to $l_{gas_{\frac{1}{2}}}^{2}$ and $l_{demodulation_{\frac{1}{2}}}^{2}$ then the halfwidth of spiral arms would be somewhere in the region of 85 persecs. Table 3.1 shows that spiral tracers in general seem to have halfwidths somewhat smaller than this but the agreement, such as it is, is reasuring that the halfwidth for demodulation obtained above is approximately correct. It should be emphasised, however, that the spiral arm halfwidth is not very sensitive to the demodulation halfwidth as the density halfwidth is considerably less than the demodulation halfwidth.

In chapter 3 section 3.3.3 mention was made of the fact that the radial distributions of giant HII regions and the surface density of neutral hydrogen do not agree indicating that there is some other factor than the density of HI that effects the rate of star formation. Having in the previous sections of this chapter inferred that star formation is triggered by the passage of interstellar gas through the spiral shocks it is not unreasonable to assume that the other factor effecting star formation is the frequency at which the interstellar material encounters shocks. Shu (1973) explains the increase in
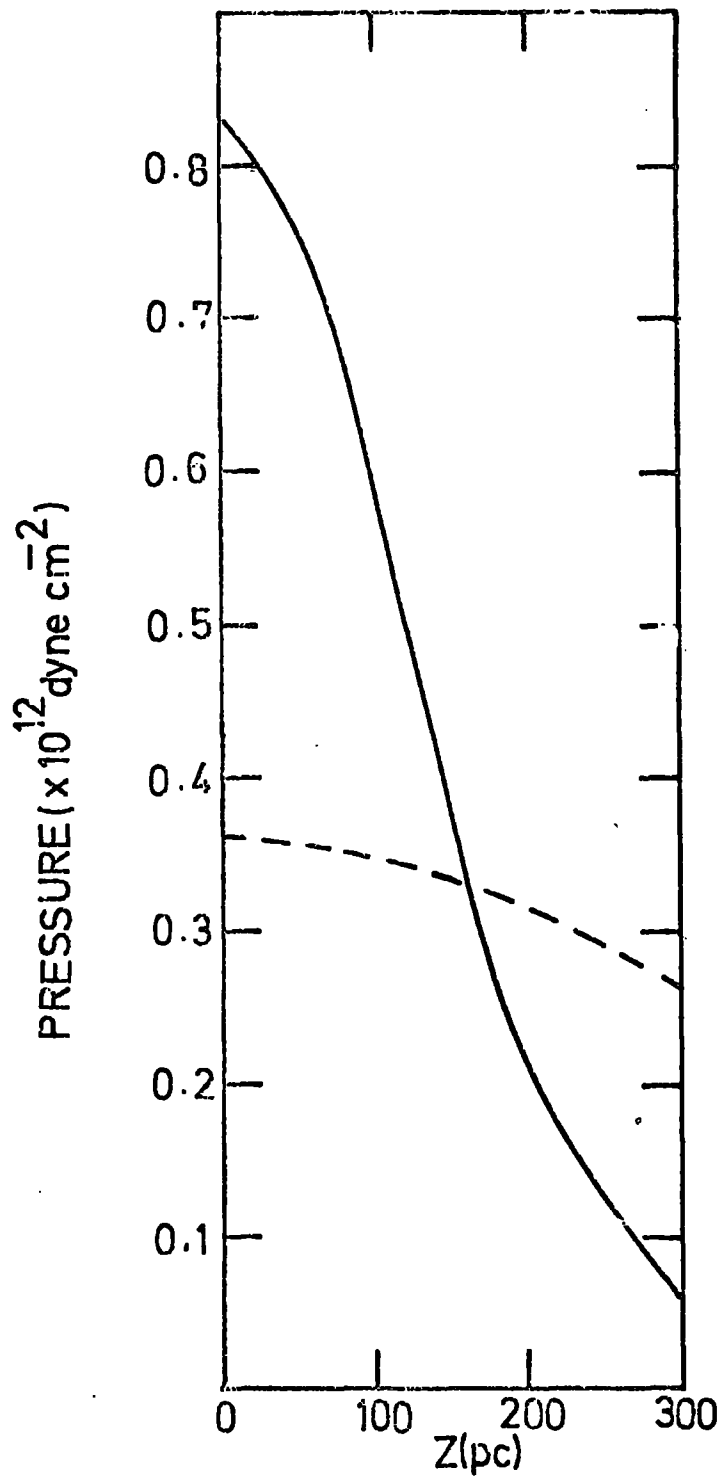
Figure 4.18: The variation of gas (_____) and magnetic (-----)
pressure with height above the plane assuming the
magnetic field and sound speed to be constant with
the gas density falling as given by Schmidt.

the ratio of HII/HI with decreasing radius as being due to (a) the kinematical increase inward of the frequency $(\Omega - \Omega_p)$ at which the interstellar gas is periodically compressed and (b) the dynamical increase inward of the effective peak compression $(\mathcal{P}_{peak}/\mathcal{P}_0)$ of the interstellar gas. Figure 4.19 shows a plot of $(\Omega - \Omega_p)(\mathcal{P}_{peak}/\mathcal{P}_0)^2$ for the spiral model of Roberts 1969, indicating that such a variation is capable of explaining the H_{II}/H_I ratio.

4.5 Origin of Galactic Spiral Structure (Roberts 1977)

Toomre (1969) has shown that a group of spiral waves such as described above would tend to propagate in the radial direction and eventually disappear in several rotations of the galaxy. Thus apart from the problem of the generation of the spiral waves initially there is also the problem of their regeneration. Several possible mechanisms have been put forward: local instability mechanisms for the generation of spiral modes; the feedback mechanism of Lin 1970, Felman and Lin 1973 which involves a wavelike oval distortion of the central regions; interactions with external companions (Toomre 1970, Toomre and Toomre 1972) e.g. the Magellanic clouds; the role of resonant interactions (Lynden-Bell and Kalnays 1972) and the ejection of massive gas clouds from the nucleus of the galaxy (van der Kruit et al. 1972). At present there is still no detailed theory to explain the presence of density waves in galaxies although they have in fact been observed directly in external galaxies (Strom et al. 1976).
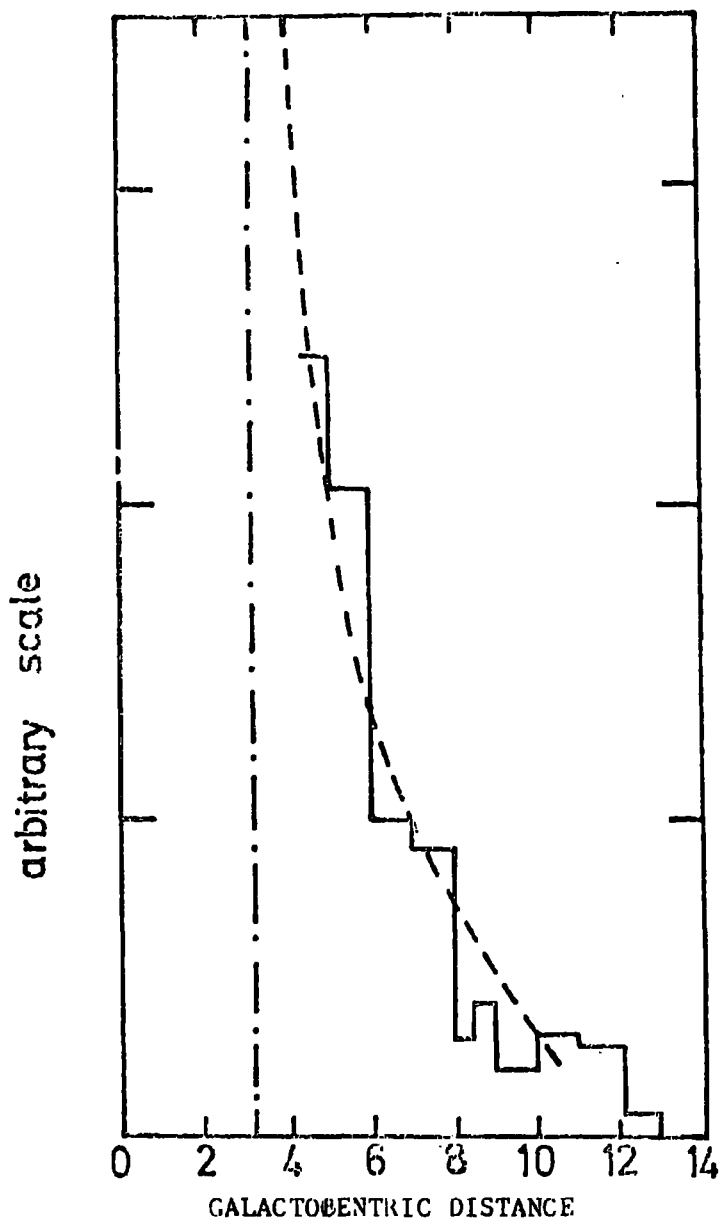
Figure 4.19: Solid lined histogram; variation of the ratio of H_{II}/H_{I} with galactic radius. Dashed line; $(\mathcal{R} - \mathcal{R}_p)$ $(\rho_{peak}/\rho_0)^2$. Dotted-dashed line; position of the inner Lindblad resonance.

References

Baade, W. and Mayall, N.U. 1951 in Problems of Cosmical Aerodynamics (Drayton, Ohio: Control Air Documents Office), p.165

Balona, L., Crampton, D., 1974, M.N.R.A.S. 166 203

Becker, W., Fenkart, R., 1970, I.A.U. Symp. 38 205

Bok B.J. 1971 Highlights of Astronomy volume 2, 63-87

Conti, P.S., Alschuler W.R. 1971 Ap. J. 170 325

Crampton, D., 1951 M.N.R.A.S. 153 303

Crampton, D., Georgelin, Y.M., 1975, Astron. Astrophys. 40 317

Felman, S.I., Lin, C.C. 1973 Stud. App. Math. Vol II.1

Fitzgerald, M.P., 1969 Publ. Astron. Soc. Pacific 81 71

Fujimoto M. 1966 I.A.U. Symp. 29 453

Georgelin, Y.M. 1975 Thesis Univ. of Provence

Georgelin, Y.M. and Georgelin, Y.P., 1976 Astron. Astrophys. 49 57-79

Henderson A.P., 1977 Astron. and Astrophys. 58 189-196

Humphreys R.M. 1970 Astron. J. 75 602-623

Isserstedt J. 1970 Astron. Astrophys. 9 70

Isserstedt J. 1977 Vistas in Astronomy Vol. 19 123-132

Kaplan S.A. 1958 Interstellar Gas Dynamics Ch.III

Kerr F.S. 1969 Am. Rev. Astron. Astrophys 7 39

Lin C.C. and Shu F.H. 1964 Ap. J. 140 646

Lin C.C. and Shu F.H. 1966 Proc. Nat. Acad. Sci. 55 229

Lin C.C. and Shu F.H. 1967 I.A.U. Symp 31

Lin C.C. Yuan C., and Shu, F.H. 1969 Ap. J. 155 721-746

Lin C.C. 1970 in Galactic Astronomy Volume 2, Ch.1 , eds Hong-Yee Chiu and A.Muriel

Lin C.C. 1970 I.A.U. Symp.38, 377   Publ. Gordon and Breach

Lynden-Bell D. Kalnajs A.J. 1972 M.N.R.A.S. 157 1

Miller, R.H. 1976, Ap. J. 207 408-413.

Moffat A.F.S. and Vogt N. 1973 Astron. Astrophys. 23 317

Moffat A.F.J. and Fitzgerald M.P. 1974 Astron. Astrophys. Suppl. Ser. <u>16</u> 25-32

Morgan W.W., Whitford A.E., and Code A.D. 1953 Ap. J. <u>118</u> 318

Piddington J.H. 1973 M.N.R.A.S. <u>162</u> 73

Raane R. and van den Bergh S. 1970 I.A.U. Symp 38, 219-221

Reifenstein E.C., Wilson, T.L., Burke, B.F., Mezger P.G. and Altenhoff W.F. 1970 Astron. Astrophys. <u>4</u> 357

Roberts W.W. 1969 Ap. J. <u>158</u> 123

Roberts W.W. Yuan C. 1970 Ap. J. <u>161</u> 877-902

Roberts W.W. 1972 Ap. J. <u>173</u> 259-283

Roberts W.W., Roberts M.S., Shu F.A., 1975 Ap. J.<u>196</u> 381-405

Roberts W.W. 1977 Vistas in Astronomy Volume 19 91

Saha G. 1974 Indian J. Phys. <u>48</u> 203-214

Schmidt-Kaler Th. 1977 Vistas in Astronomy Vol.19 69-89

Shu F.H. 1973 N.A.T.O. Advanced Study Inst. Interstellar Medium

Simonson III S.C. 1976 Astron. Astrophys. <u>46</u> 261-268

Smith L.F. 1968 M.N.R.A.S. <u>140</u> 409

Smith L.F. 1970 M.N.R.A.S. <u>141</u> 317

Strom S.E., Jensen E.B., and Strom, K.M., 1976 Ap.J. <u>206</u> 211-214

Tammamn G.A. 1970 I.A.U. Symp 38 236

Toomre A. 1964 Ap.J. <u>139</u> 1217

Toomre A. 1969 Ap.J. <u>158</u> 899

Toomre A.1970 I.A.U. Symp. 38 334

Toomre A. and Toomre J. 1972 Ap.J. <u>178</u> 623

Uranova T.A. 1970 I.A.U. Symp. 38, 228-231

van der Kruit P.C. Oort S.H. Matthewson D.S. 1972 Astron. Astrophys. <u>21</u> 169

Vandervoort P.O. 1970 Ap.J. <u>161</u> 87

Verschuur G.L. 1973 Astron. Astrophys. <u>27</u> 73-76

Walborn W.R. 1972 Astron. J. <u>77</u> 312

Weaver H.F. 1970 I.A.U. Symp.38, 126

CHAPTER 5

OBSERVATIONS OF THE CONTINUUM RADIATION

5.1 Introduction

The frequency range over which the observed galactic radiation is
mainly synchrotron in nature is confined at the high frequency end by the
increasing proportion of thermal emission (as this has a flatter spectrum
than the synchrotron radiation). At low frequencies the absorption of
the synchrotron radiation by thermal electrons limits its observation.
For these reasons the best frequency range to observe the synchrotron
radiation is in the region of hundred to a few hundred megahertz.

The profiles of the radiation along the galactic plane derived in this chapter
are at 150 and 408 MHz but information is also used from surveys at 85 MHz.
The most recent presentation of a whole sky map is that of Landecker and
Wielebinski (1970). This is a combination of several surveys at 85 and 150
MHz and is used as a basis for the 150 MHz profile. The profile at 408 MHz
is derived mainly from the Surveys of Green (1974) and Seeger et al (1965).
The profiles are restricted to the longitude range $30^{\circ} < \ell^{II} < 330^{\circ}$. For
directions passing closer than this to the galactic centre the corresponding
closest approach line of sight to the galactic centre lies within the inner
Lindblad resonance where no regular spiral structure is expected. Rather
than finding arbitrary distributions of electron density and magnetic field
which will account for the longitude profile in the region $30^{\circ} > \ell^{II} > 330^{\circ}$ this
section is not considered.

Both derived profiles are corrected for thermal radiation, spur emissions,
sources and the extragalactic radiation. In the final section of this
chapter the derived profiles are compared with those presented by previous
authors, in particular that used by Paul et al. (1976).

5.2 150 MHz Profile

Figure 5.1 shows the complete sky map as presented by Landecker and Wielebinski

<u>Figure 5.1.:</u>

The complete sky map at 150 MHz. as compiled by Landecker and Wielebinski (1970)

The contours are in units of ^{o}K brightness temperature, as defined in appendix I. This has been used as the basis for the derived profile but the original surveys have been consulted directly. Table 5.1 lists the surveys consulted in the preparation of the profile. The survey of Turtle and Baldwin at 178 MHz has been normalised to the Landecker and Wielebinski survey by comparing the two over their whole region of overlap. Details of the galactic plane have been obtained from survey 3 for the regions around $\ell^{\text{I}} \ni 310^{o}$ and from survey 4 for regions around $\ell^{\text{I}} \in 290^{o}$ Survey 5 has been used to obtain additional information of the shape but not the absolute magnitude of the profile. The derived profile is presented in figure 5.2. The resolution along this profile varies according to which survey has been used. This resolution is indicated in figure 5.3. It should be noted that when surveys at different frequencies using different instruments are combined great care is required as the spectral index, which relates the brightness temperatures at different frequencies may vary with galactic longitude and the base levels and scales of the various surveys may be different. For this reason more weight is placed on surveys 1, 3, 4 at 150 MHz than on the other surveys.

5.3   408 MHz Profile

Table $\underline{\text{Y}}$-2 lists the surveys from which the 408 MHz profile is derived. The profile is derived almost entirely from surveys 1 and 2 combining them by comparing the brightness temperatures in their overlap region. The higher resolution surveys 3 and 4 are used to confirm the fine structure of the profile. Survey 1 was in fact made at a resolution of $2'.86 \times 2'.86$ but the published data has been integrated by the author over $/\delta^{\text{I}}/\leq 3^{o}$ $\delta\ell^{\text{I}} = 0^{o}.5$ The profile at 408 MHz is presented in figure 5.4.

5.4. Corrections to the observed profiles

It is necessary to correct the profiles presented in figures 5.2 and 5.4 for emission occuring from other mechanisms and sources not related to the overall structure of the galaxy.

T A B L E V.1.

Survey	Frequency	Range of ℓ^{II} along the galactic plane	Resolution ΔRA x ΔDec.	Instrument
1. Landecker and Wielebinski (1970)	150 MHz 80 MHz	5° - 65° 5° - 65°	$2^o.2$ x $2^o.2$ $3^o.8$ x $3^o.5$	Parkes 210^{ft} "
2. Turtle and Baldwin (1962)	178 MHz	220° - 0° - 27°	$1^o.25$ x 5°	Cambridge
3. Wielebinski et al (1968)	150 MHz 85 MHz	290° - 0° - 60° 290° - 0° - 60°	$2^o.2$ x $2^o.2$ $3^o.7$ x $3^o.7$	Parkes 210^{ft} "
4. Hamilton and Haynes (1969)	153 MHz	200° - 0° - 45°	$2^o.2$ x $2^o.2$	Parkes 210^{ft}
5. Hill et al (1959)	85 MHz	256° - 0° - 45°	50' x 50'	Cross-type Fleurs Sydney
6. Yates et al (1967)	85 MHz	240° - 0° - 10°	$3^o.8$ x $3^o.5$	Parkes 210^{ft}
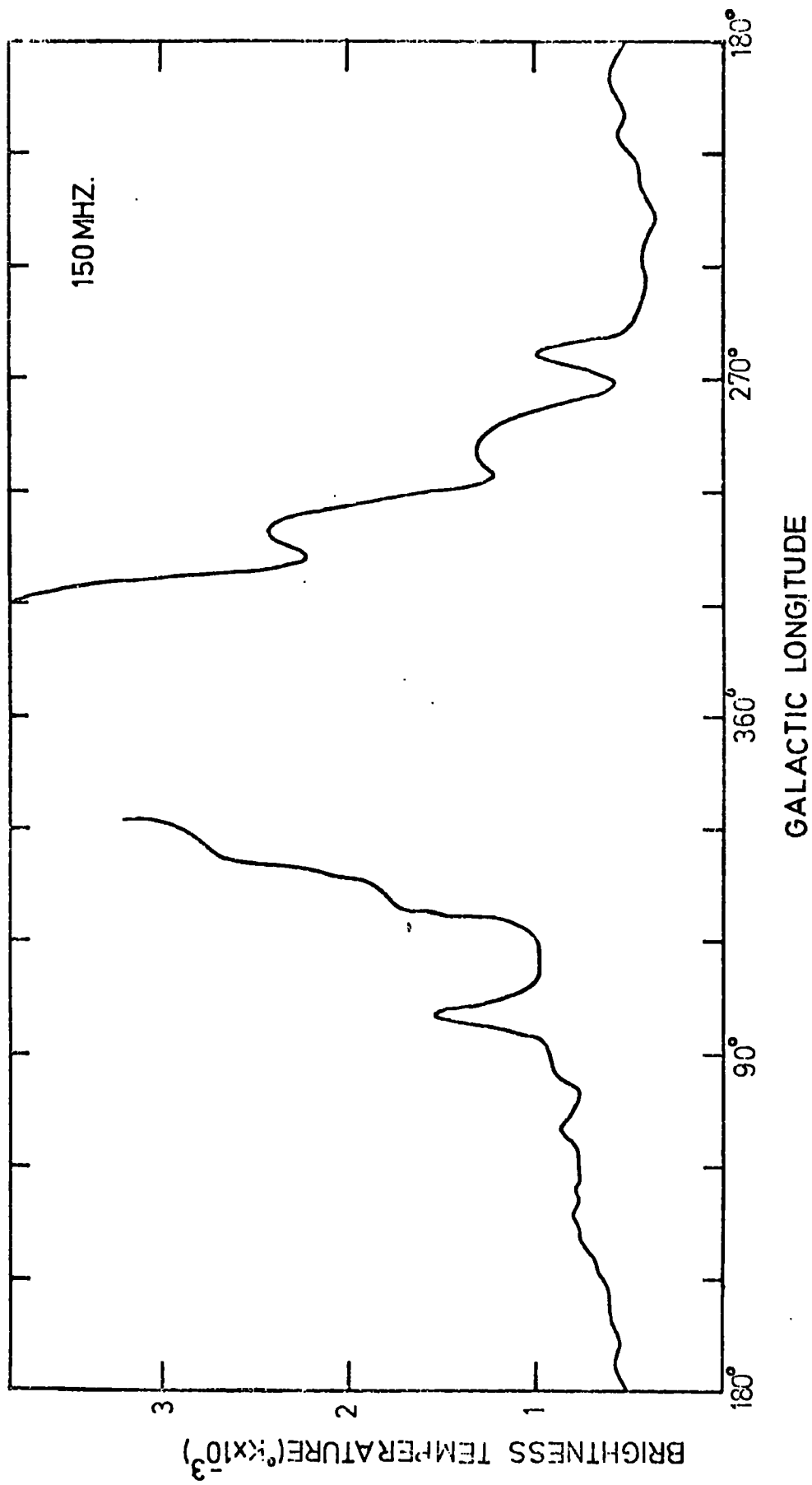
Figure 5.2: Galactic plane profile at 150 MHz as obtained from the raw data.
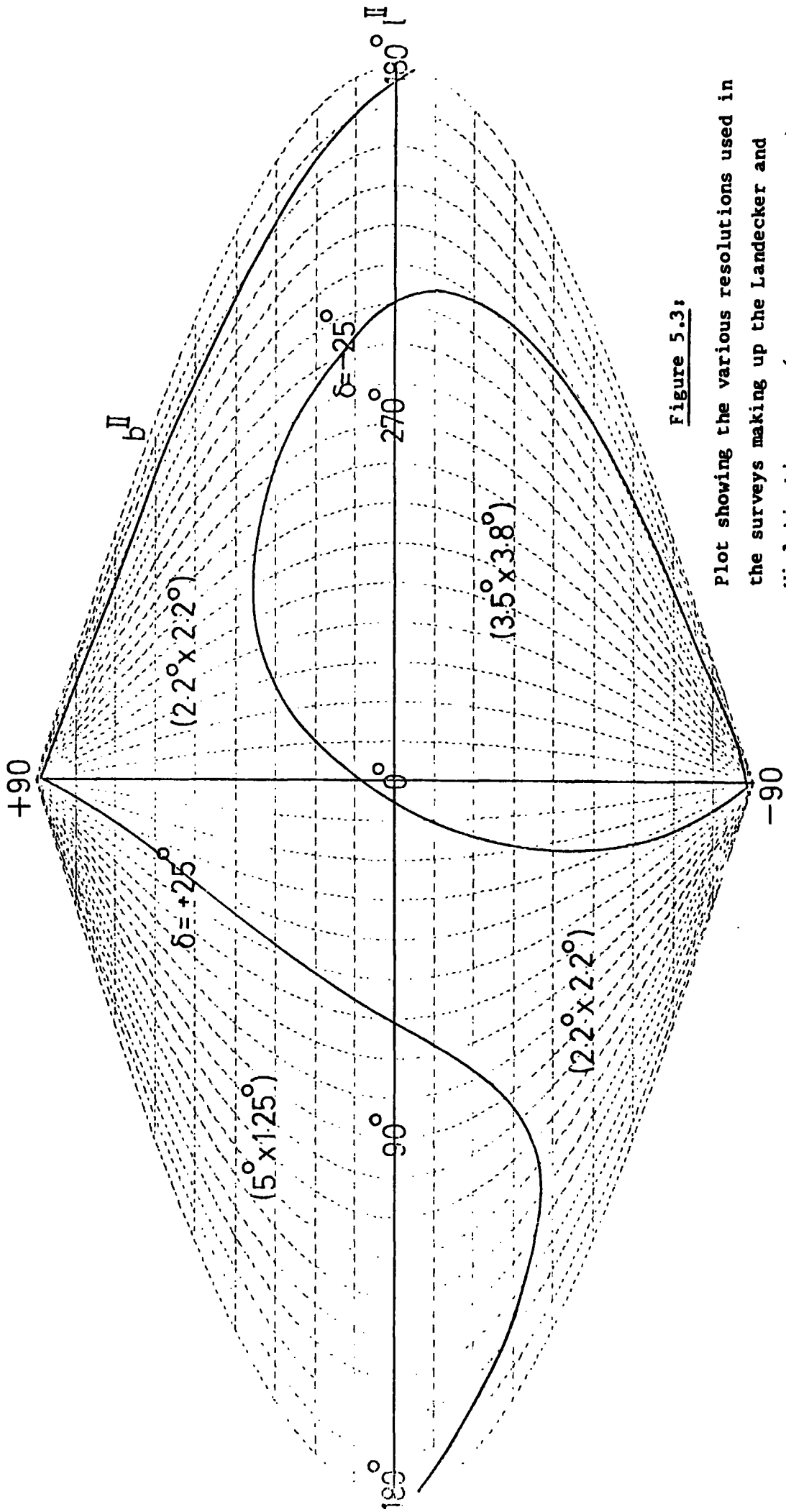
Figure 5.3:

Plot showing the various resolutions used in the surveys making up the Landecker and Wielebinski map. (Δ DEC $\times$ Δ RA)

T A B L E V.2.

Survey	Frequency	Range of ℓ^{II} along the galactic plane	Resolution $\Delta RA \times \Delta Dec.$	Instrument.
1. Green(1974)	408 MHz	$195° - 0° - 55°$	$0°.5(\ell^{II}) \times 6°(b^{II})$	Molonglo
2. Seeger et al (1965)	400 MHz	$0° - 240°$	$1°.7 \times 2°.2$	Dwingeloo
3. Komesaroff(1966)	408 MHz	$280° - 355°$	$47'.5 \times 47'.5$	Parkes 210ft
4. Haslam et al (1974)	408 MHz	$25° - 90°$	$37' \times 37'$	Bonn 100^m
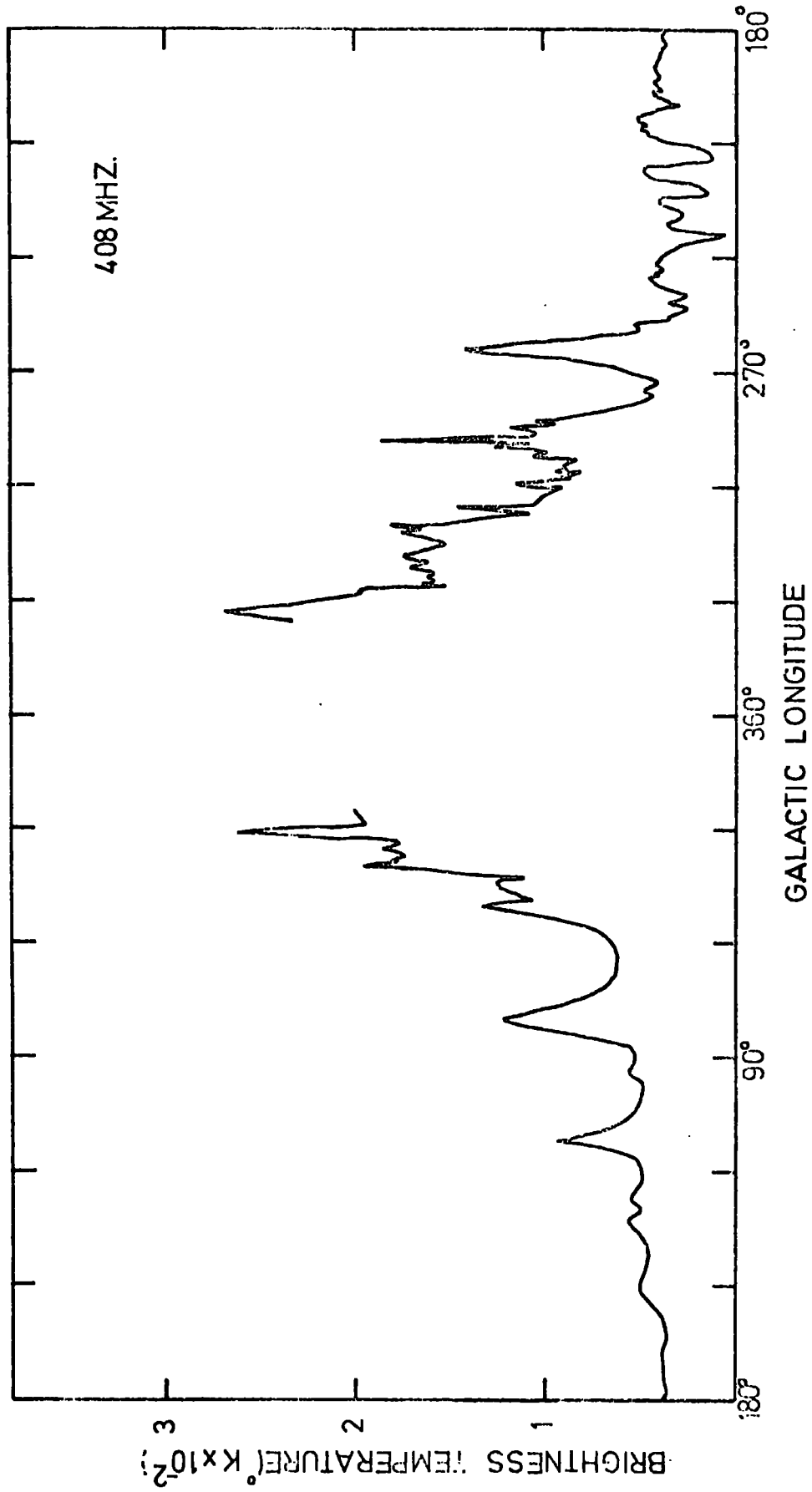
Figure 5.4: Galactic plane profile at 408 MHz as obtained from the raw data.

5.4.1 Extragalactic Contribution

The extragalactic contribution at a few hundred megahertz is due to the integrated emission from all external galaxies and radio sources. In theory it is possible by assuming that the spectral index for the galactic radiation is constant and by fixing a value for the extragalactic spectral index to obtain the absolute intensity of the two components. Such an analysis as this has been carried out by Bridle (1967) using scaled antennae at various frequencies and an assumed extragalactic temperature index of $\beta = 2.75$ (this is the mean spectral index observed for extragalactic radio sources). Bridle obtains the value $48^{\pm} 9$ k at 150 MHz for the extragalactic background.

Further indications of the extragalactic background might be obtained from the minimum observed sky brightness at 150 MHz. As seen from figure $\underline{\text{V}}$-1 this is approximately $150°K$ occurring in the region $\ell^{II} \approx 180°$ $b^{II} \approx 50°$. Unfortunately, this observed temperature is the sum of the extragalactic contribution, any halo contribution and some local emission so that any conclusion drawn from this value is not very helpful as regards obtaining a value for the extragalactic contribution (see comments on other derived longitude profiles at the end of this chapter).

Another approach to obtaining the value for the background is through the study of number counts of radio galaxies with powers above some threshold. Unfortunately cosmological evolution of the radio galaxies is of great importance introducing large uncertainties. Using the model of Doroshkevich et al. (1970) for the cosmological evolution of radio sources a value of 32-37 K at 150 MHz is quoted by Longair (1971).

In this analysis an extragalactic component of 50 K at 150 MHz is assumed.

5.4.2 Thermal Radiation

This is the free-free radiation produced by the more distant encounters between unbound charged particles where Coulomb forces are small and the particles can be considered to continue travelling in straight lines. The

emission coefficient may be determined by integrating the emission produced during each encounter over the velocity distribution of the particles. (The Maxwellian distribution relevant to the particular thermal electron temperature, T_e) . As the thermal emission spectrum is considerably flatter ($\beta = 2.1$) than the synchrotron emission spectrum ($\beta = 2.8$), thermal emission tends to dominate at high frequencies. Hirabayashi (1974) has carried out surveys of the galactic plane at 4.2 GHz and 15.5 GHz and has made an estimate of the various components contributing to the observed emssion at particular longitudes. By comparing the spectra of his high frequency surveys with those obtained using lower frequencies (1.4 and 2.7 GHz) an estimate of the thermal and non-thermal radiation for various positions close to the galactic plane have been made. For two regions within the Cygnus X complex a constant spectral index of $\beta = 2.1$ is found to satisfy all the observations considered implying that this region is substantially thermal in nature. For all the other seven locations positive curvature in the spectra is observed. The spectral index is close to $\beta = 3.0$ for the lower frequencies and approaches 2.1 for the higher frequencies, the former value is assumed to be that for the synchrotron index and the latter corresponds to the index of thermal emission. From this curvature Hirabayashi has separated the two components using values for the thermal electron temperature obtained from recombination line studies. The results for one of the locations considered are presented in figure 5.5 with extrapolation to lower frequencies. This graph has been used to estimate the contributions to the observed radiation at the lower frequencies of 150 and 408 MHz. At 150 MHz approximately 7% of the observed emission is thermal whereas at 408 MHz the value is 19%.

To obtain some indication of the way in which the percentage of thermal emission varies with longitude the work of Large et al. (1961) has been referred to. Figure 5.6 shows the contribution of thermal emission to the overall radiation at 150 MHz assumed in this work. Thermal emission peaks at approximately the galactic centre but this is of no interest as the
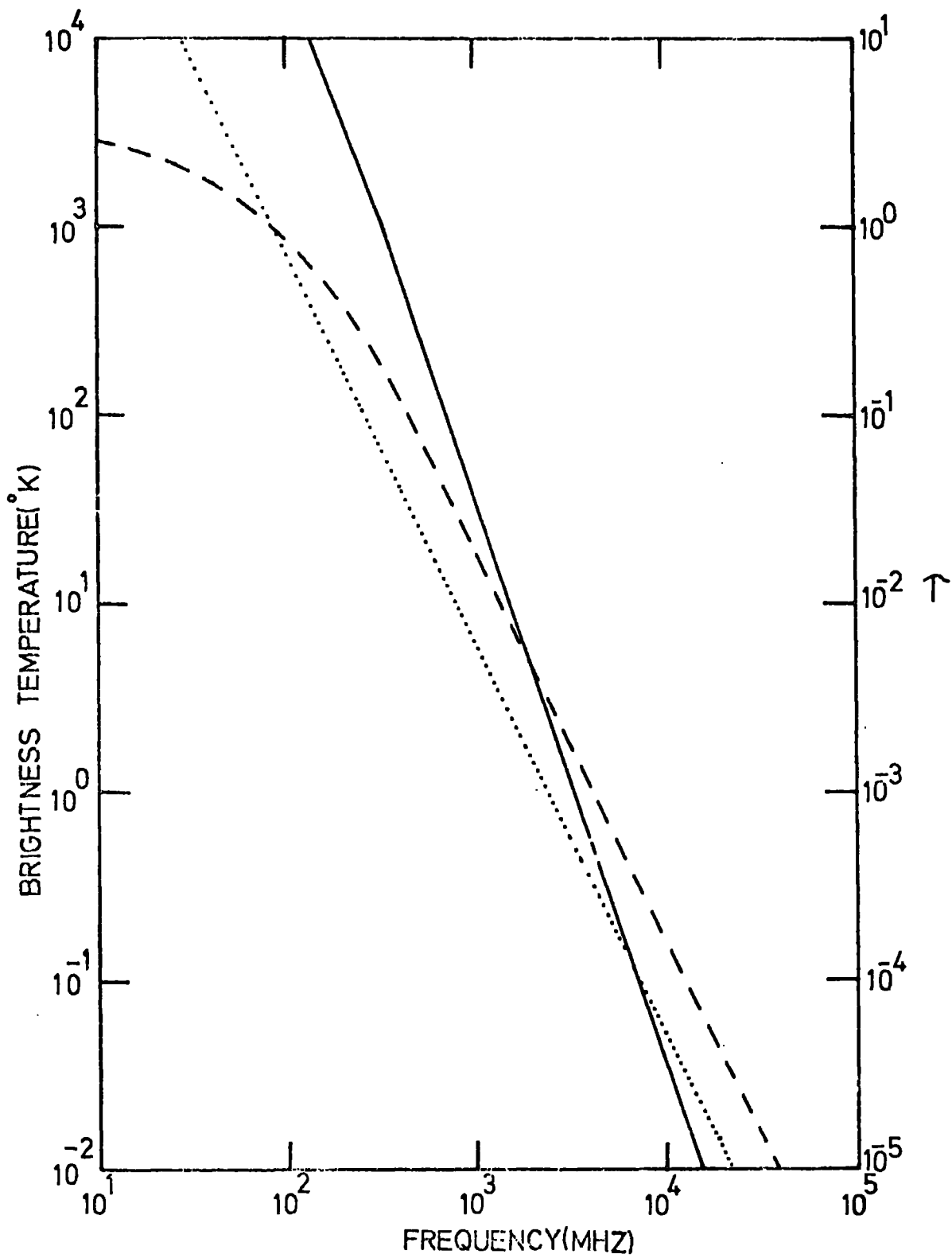
Figure 5.5: Separation of the observed radiation into thermal
(-------) and non-thermal (_____) components for
$1^{II}=23.94^{o}, b^{II}=0.32^{o}$. (Hirabayashi 1974) The optical depth
variation with frequency is also shown (.............).
T_e is taken to be $3430^{o}K$ as inferred from recombination
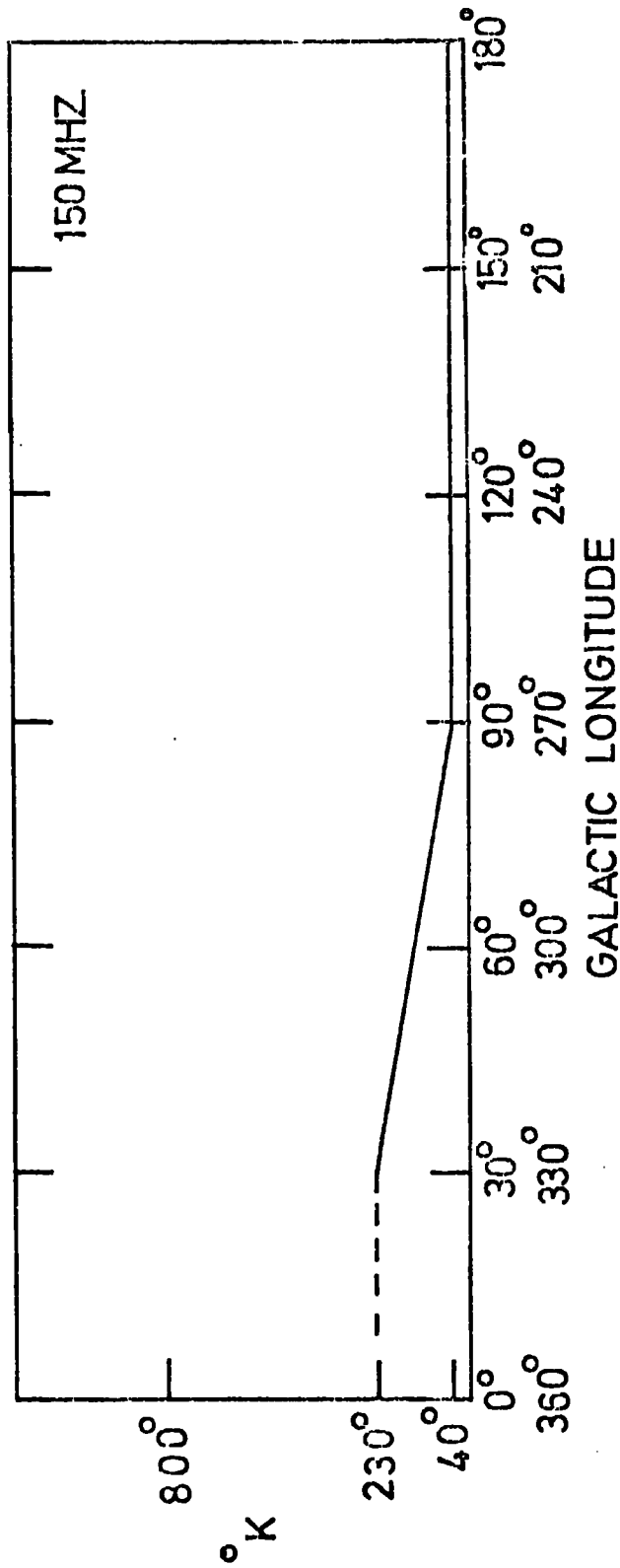line observations.

Figure 5.6:   The assumed variation of thermal emission at 150MHz. with galactic longitude.

present study excludes this region.

5.4.3 Galactic radio Spurs.

The existence of the galactic spurs was established in the early 1960s.
Following their discovery in the continuum radio emission H_α and 21 cm emission
were discovered in positions correlated with the radio spurs (Meaburn
1965, 1967, Lozinskaja 1964, Berkhuijsen et al. 1970). Figure 5.7 shows
the three major spurs designated by the North Polar Spur (Loop I), Cetus Arc
(Loop II) and Loop III plotted on the Landecker and Wielebinski continuum map.
Where the ridge lines of emission become ill-defined they are continued by plotting
the small circles that best fit the observed ridges. Since their discovery
several theories have been suggested to explain the nature of the spurs.
The two main theories explain the spurs in terms of large nearby supernova
remnants (Hambury Brown et al. 1960, Berkhuijsen et al. 1970, Haslam et al.
1971) or in terms of helical structure in the galactic magnetic field
(Matthewson 1968). The geometry of the galactic loops at low galactic
latitudes can be used to distinguish between these theories (Berkhuijsen et
al. 1971). If the spurs are 'radio tracers' of the helical magnetic field
the hypotheses of Rougoor (1966) and Matthewson (1968) predict that the different
spurs should join across the plane to form a helical structure. Alternatively
if the spurs are SNR's they would be expected to appear on opposite sides of
the galactic plane such that they follow the same small circle. Yates (1968)
has claimed to have followed Loop I along its small circle to southern latitudes
whereas the 820 MHz map of Berkhuijsen (1972) shows no connection between the
north polar spur and the $\ell^{II} = 50°$ end of Loop II. Loop III has been shown to
continue on a small circle when crossing the galactic plane when the circle is
superimposed on the 408 MHz survey of Haslam et al. (1970), 820 MHz survey of
Berkhuijsen (1972) and the 13 MHz Survey of Andrew (1969). Assuming the
spurs to be SNR's Van der Laan (1962) has developed models of spheres expanding
in a magnetionic medium to reproduce their observed continuum features and
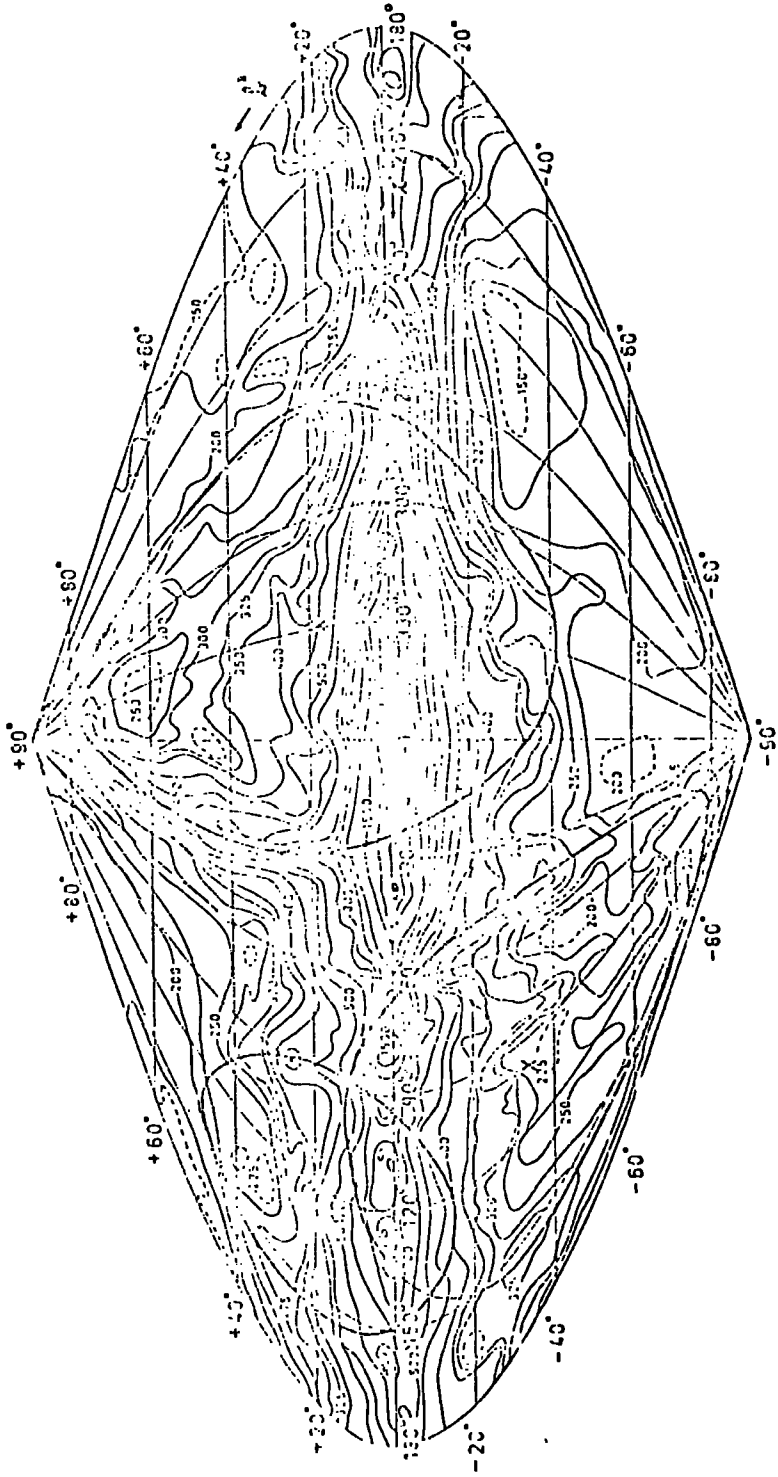polarisation characteristics (Spoelstra 1972).

Figure 5.7:   The ridge lines of the three major spurs superimposed on the Landecker and Wielebinski map.

T A B L E   V.3.

	North Polar Spur	Cetus Arc	Loop III
Angular Radius	67°	50°	45°
Distance to centre	115 pc	110 pc	150 pc
Magnetic Field	$5\,\mu G$	$5\,\mu G$	$5\,\mu G$
Electron Density	$0.03\ cm^{-3}$	$0.05\ cm^{-3}$	$0.08\ cm^{-3}$
Spectral Index	2.75	2.75	2.75
Coordinates of centre	ℓ^{II} 325° b^{II} $+17.5^{\circ}$	110° $-32^{\circ}.5$	125° $+15^{\circ}.5$

Table V-3 gives various parameters for the spurs assuming them to be SNR's and using the Van de Laan model to obtain the parameters regarding their structure. Using the Van de Laan model, with the parameters presented in this table, Spoelstra (1972) has presented intensity plots of the emission expected for the three major spurs. Figure 5-8 shows the $b^{II} = 0$ profiles across these intensity plots. The absolute magnitude of the intensity has been obtained by requiring that (i) any components in the background with symmetry about, or associated with, the small circles are removed, (ii) the temperature of regions enclosed by the small circles is reduced in such a way as to produce symmetry in the background brightness temperature about the galactic plane (Yates 1968). The profiles in figure 5.8 have been subtracted from the observed continuum profile figure 5-2.

5.4.4 Source Contributions

The sources that contribute significantly to the continuum emission as observed in the galactic plane are:-

i) Cas A supernova remnant ($\ell^{II} \simeq 112^{\circ}$, $b^{II} \simeq -2^{\circ}$)

ii) Cygnus X complex ($\ell^{II} \gtrsim 80^{\circ}$, $b^{II} = 0^{\circ}$)

iii) Vela supernova remnant ($\ell^{II} \simeq 264^{\circ}$, $b^{II} \simeq -3^{\circ}$)

i) Cas A supernova remnant (4.0' x 3.8'). It is well established that the peak in the continuum emission in this region is from the remnant of a supernova which exploded in AD 1667$\pm$ 8.

ii) Cygnus X complex. As mentioned in section 4.2, Hirabayashi (1974) finds for the two locations considered within the complex that the spectral index is constant at -2.1 implying that the source is mainly thermal in nature. For this reason the peak in the radio emission at $\ell^{II} \simeq 80^{\circ}$ should not be considered as the manifestation of some feature in the spiral structure but rather as some spatially confined thermal source.

iii) Vela Supernova remnant (220' x 180', approximately 10^4 years old). Using the surveys of this remnant by Milne (1968) at high resolution in the

(a) 1 unit = $90 ^{+}_{-} 25°$K at 150MHz.

(b) 1 unit = $30 ^{+}_{-} 10°$K at 150MHz.
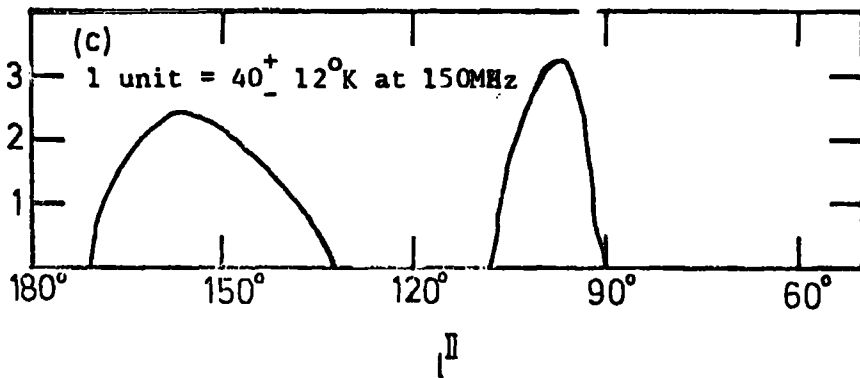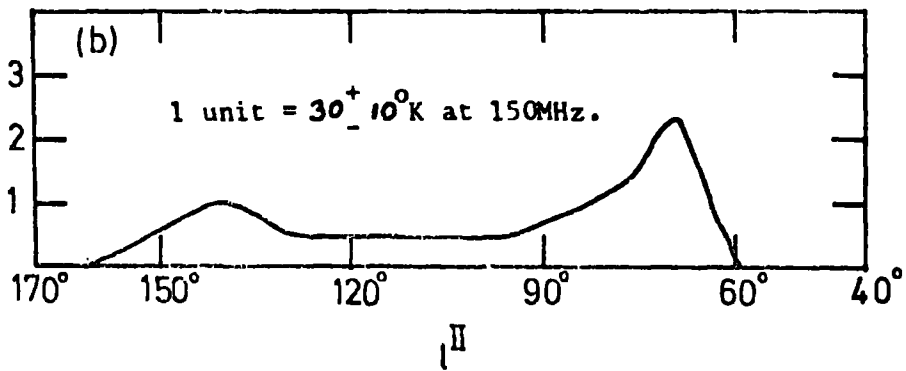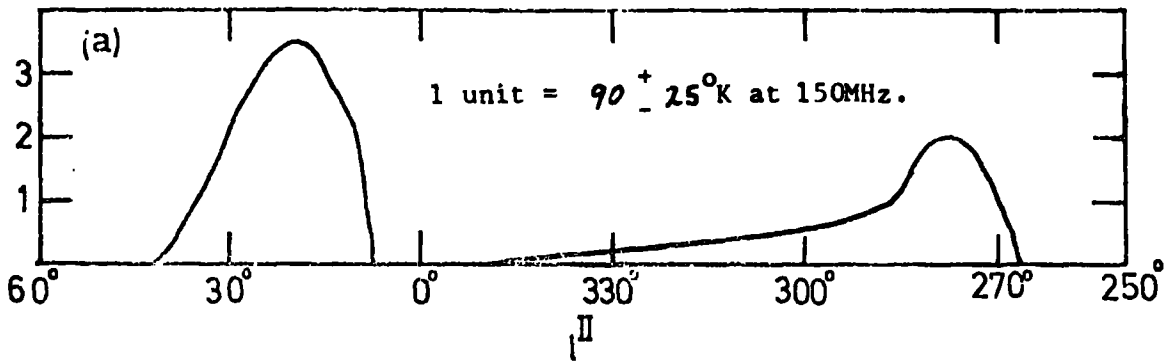
(c) 1 unit = $40 ^{+}_{-} 12°$K at 150MHz

Figure 5.8: Profiles of emission at 150MHz. along the galactic plane
for the galactic spurs as predicted by Spoelstra (1972).
(a), North Polar Spur; (b), Cetus Arc; (c), Loop III.

frequency range 400-2650 MHz an estimate has been made of the remnants contribution to the observed radiation at 150 MHz at the resolution of 3.5^O x 3.8^O appropriate to this region of the Landecker and Wielebinski survey. The 408 MHz Milne survey with a beamwidth of 48 arc minutes has been convolved with the 3.5^O x 3.8^O beam to obtain the contribution from the SNR at $\ell^{II} = 264^O$, $b^{II} = 0$. This is found to be about 580 K at 150 MHz.

The two peaks of emission at $\ell^{II} = 80^O$ and $\ell^{II} = 264^O$ are considered to be sources rather than manifestations of a local spiral arm as assumed by other authors (see Section 6).

5.5 Corrected Profiles

The corrections as discussed in the previous sections have been subtracted from the 150 MHz profile of figure 5.2 to produce the profile of the synchrotron radiation presented in figure 5.9. Table 5.4 presents the corrected 150MHz profile digitised at two degree intervals. The corrections have also been scaled by the appropriate spectral index β (i.e. 2.75 for extragalactic, 2.1 for thermal and 2.75 for spurs) and applied to the 408 MHz profile. The final 408 MHz profile of synchrotron radiation multiplied by $\left(\frac{408}{150}\right)^{2.8}$, corresponding to an electron spectral index of 2.6, is also presented in figure 5.9. It should be noted that the very sharp peak at $\ell^{II} = 288^O$ in the 408 MHz profile is due to the Carina nebula. Observations by Gardner et al. (1970) and by Shaver and Goss (1970) indicate that this source is largely thermal in nature. The close agreement between the corrected profiles at 150 and 408 MHz when scaled as in figure 5-9 indicates that in the relevant energy region the electron spectrum has a similar spectral index throughout the galactic plane. The sources at $\ell^{II} = 80^O$, 112°, 264° and 288° stand out particularly on the 408 MHz scaled profile due to their spectral indices differing from that of the background.

5.6 Comparison with other derived profiles

At this point it is appropriate to compare the above derived profile at
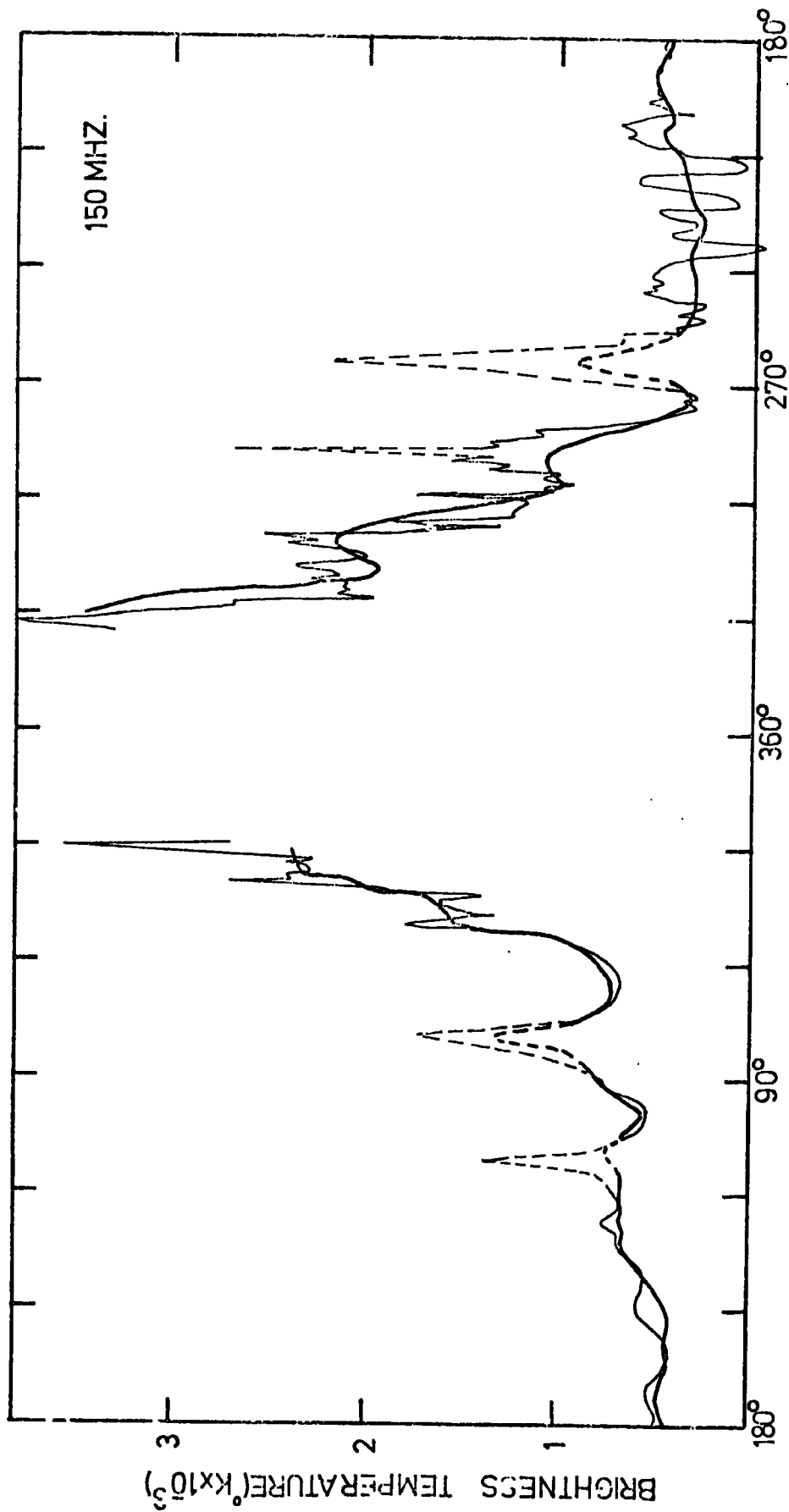
Figure 5.9: The corrected profiles at 150MHz. (——————) and 408MHz. scaled by $(408/150)^{2.8}$, (———————).
Dotted regions indicate emission from the sources discussed in the text.

Table **Ⅴ**.4

${}_1\Pi_0$	0°	2°	4°	6°	8°
30	2500	2500	2480	2460	2420
40	2320	1800	1650	1610	1570
50	1640	1160	950	880	830
60	790	760	760	760	760
70	780	820	870	1020	1220
80	1340	1040	910	860	820
90	775	740	680	640	560
100	540	580	630	680	720
110	740	700	670	660	660
120	660	660	660	660	660
130	650	660	640	620	590
140	560	520	485	460	440
150	420	420	420	420	430
160	430	420	420	420	440
170	460	460	470	470	440
180	420	420	460	490	500
190	510	490	480	460	440
200	420	430	460	450	420
210	380	360	350	340	340
220	330	310	280	260	260
230	260	290	310	320	320
240	320	310	310	300	310
250	320	320	340	380	460
260	600	760	900	680	520
270	420	400	400	460	560
280	700	750	900	1000	1060
290	1070	1040	1000	980	1080
300	1280	1480	1720	1920	2080
310	2160	2150	2040	1980	1920
320	1970	2200	2700	3100	3300
330	3430				

150 MHz with those used by other workers. All are based upon the Landecker and Wielebinski map but the data have been treated in different ways. The profile of Price (1974) is closest to the present one. An important difference is in the treatment of the maxima at 80° and 264°.

As stated above, in this thesis these maxima are regarded as being mainly due to the relatively nearby Cygnus complex and Vela supernova remnant although some small enhancement in the background radiation cannot be ruled out. Price takes them to be manifestations of the large-scale structure of the galaxy. In order to account for maxima in these directions he adjusts the position of the sun relative to the Lin and Shu spiral pattern, upon which he bases his interpretation, so that it lies on the inside edge of the adjacent outer arm. There is an inconsistency in his argument here as, in fixing their pattern, Lin and Shu identified the outer arm with the Perseus arm which lies at a distance of more than 1 kpc from the Sun.

In constructing their profile Paul et al. (1975) and Jakel et al. (1975) include radiation out to 10° in latitude on either side of the galactic plane. The former authors take the average of the brightness temperatures at latitudes of 5° and 10° omitting contributions from $|b^{II}| < 5^o.$ The latter authors integrate the emission from $b^{II} = -10^o$ to $b^{II} = +10^o.$ The present profile, which, because of instrumental resolution is effectively an average of the emission within 1° or 2° of the galactic plane, shows a much sharper peaking within 90° of the galactic centre. It should be noted in passing that the reason for inclusion of radiation out to $|b^{II}| = 10^o$ by these authors was to enable a comparision to be made with the longitude profile of gamma radiation which was available summed over this range of latitudes. If, however, the gamma-rays, are the result of pion production in the interstellar gas most of them will be distributed within 3° of the galactic plane and the breadth of the observed distribution is largely due to the angular resolution of the gamma-ray detectors. The present profile of radio emission is therefore the appropriate one to compare

with the gamma-ray profile.

Few authors have carried out subtractions from the profiles as done above. Paul et al. (1976) subtracted the minimum sky brightness of $150^{\circ}K$ as an assumed extragalactic background which as discussed in section 4.1 must be too large.

Chapter 5. - References

Andrew. B.H. 1969   M.N.R.A.S. <u>143</u> 17

Berkhuijsen, E.M., Haslam, C.G.T., Salter, C.S. 1970, Nature <u>225</u> 364

Berkhuijsen, E.M., Haslam, C.G.T., Salter C.S., 1971. Astron. Astrophys. <u>14</u> 252-262

Berkhuijsen, E.M., 1972 Astron. Astrophys. Suppl. <u>5</u>. 263-312.

Bridle A.H., 1967. M.N.R.A.S. <u>136</u> 219-240

Doroshkevich, A.G., Longain MS, Zeldovich Ya B, 1970, M.N.R.A.S., <u>147</u> 139-48

Gardner, F.F., Milne, D.K., Mezger P.G., Wilson, T.L., 1970 Astron. Astrophys <u>7</u>
                                                                      349-<u>3</u>58

Green, A.J. 1974. Astron. Astrophys. Suppl. <u>18</u> 267-307

Hamilton, P.A., R.F. Haynes 1969 Aust. J. Phys. <u>22</u> 839-41

Hanbury Brown R, Davies R.D., Hazard. C. 1960 Observatory <u>80</u> 191

Haslam, C.G.T., Kahn F.D., Meaburn J. 1971 Astron. Astrophys. <u>12</u> 388-397

Haslam, C.G.T., Quigley, M.S.S., Salter C.S., 1970 M.N.R.A.S., <u>147</u> 405

Haslam, C.G.T., Wilson, W.E., Graham, D.A., Hunt G.C., 1974, Astron. Astrophys Suppl.
                                                                      <u>13</u>   359-394

Hill, E.R., Slee O.B., Mills, B.Y., 1959. Aust. 5. Phys. <u>11</u> 530

Hirabayashi, H. 1974 Publ. Astron. Soc. Japan <u>26</u> 263-287

Komesaroff, M.M. 1968 Aust. J. Phys. <u>19</u> 75-92.

Landecker, T.L., Wielebinski R. 1970. Aust. J. Phys. Astrophys. Suppl. <u>16</u>.

Large M.I., Matthewson, D.S., Haslam, C.G.T., 1961 M.N.R.A.S. <u>123</u>   123-132

Longain, M.S., 1971   Rep. Prog. Phys. <u>34</u> 1125-1248

Losinskaya, T.A.. 1964   Astr. Cink (USSR) No. 299

Matthewson D.S., 1968 Ab. J. <u>153</u> 647.

Meaburn, J. 1965 Nature <u>208</u> 575

Meaburn, J. 1967 Z. Astrophys. <u>65</u> 93

Milne, D.K. 1968 Aust. S. Phys. $\underline{21}$ 201-19

Paul J., Casse' M., Cesarsky, C.J., 1976. Ap. J. $\underline{207}$ 62-77

Price, R.M., 1974 Astron. Astrophys. $\underline{33}$ 33-38

Rougoor, G.W., 1966 Ap. J. $\underline{144}$ 852

Seegen Ch. L., Westerhout Gart, Conway R.G., Hoekenna T. 1965. Bull. Astr. Inst.
                                                    Netherlands $\underline{18}$ 11-41

Shaver, P.A., Goss W.M. 1970 Aust. J. Phys. Astrophys. Suppl. $\underline{14}$ 1-196

Spoelstra T.A.Th. 1972 Astron. Astrophys. $\underline{21}$ 61-84

Turtle A.S. Baldwin J.E. 1962 M.N.R.A.S, $\underline{124}$ 457

Van der Laan H. 1962 M.N.R.A.S. $\underline{124}$ 125

Wielebinski R., Smith D.H., Cardenas Garzon X, Aust. J. Phys. $\underline{21}$ 185-92.

Yates K.W., Wielebinski R., Landecker T.L., 1967 Aust. J. Phys. $\underline{20}$ 595

Yates, K.W., 1968 Aust. J. Phys. $\underline{21}$ 147

CHAPTER 6

Models of the Galactic Continuum Radiation.

6. 1. Introduction.

To model the observations of the galactic continuum radiation one needs to calculate the brightness temperature for all lines of sight from the earth. Using Appendix I equation 10, this brightness temperature is given by

$$T_b(\nu) \propto \int_0^\infty I(s) \, H_\perp(s)^{\frac{\gamma+1}{2}} \, ds \qquad 6.1.$$

As seen from this equation the observed brightness temperature at a frequency, ν, $T_b(\nu)$ depends on the electron intensity I (S), the electron spectral index γ and the perpendicular component of the magnetic field $H_\perp$ (S) for all points, S, along the line of sight. Therefore to model the observed emission models must be constructed for the way in which the magnetic field, electron intensity and spectral index vary throughout the galaxy.

This chapter describes the setting up of such models and the methods used in the calculating of the emission. The results obtained from such models are presented in the next chapter and discussed in conjunction with previous work on the interpretation of the continuum radiation.

6. 2. The structure of the Galactic Magnetic Field.

As discussed in chapter III there is considerable evidence to support the Thesis that the galactic magnetic field is predominantly azimuthal in structure with a superimposed irregular component. In this work the field is considered to have a two component structure: a regular component that runs in the direction of the spiral arms and a superimposed isotropically orientated random component. The magnitude of the regular component is assumed to be a constant factor F times that of the random component throughout the galaxy for interarm regions. The ratio, F, changes for arm regions as discussed at the end of this Section.

As will be seen, the resultant profile of synchrotron emission is very sensitive to the value of F so this is regarded as a free parameter. The magnetic field is taken to have an overall radial dependence given by

$$ H(R) \propto \left[1 - \exp\left(-\frac{R^2}{4}\right) \right]\left[\exp\left(-\frac{R^2}{R_0^2}\right) \right] . \qquad 6.2. $$

R, the distance from the galactic centre is measured in kpc.

The first term in equation 6.2 ensures that the field falls to zero at the galactic centre as would be expected from the dynamo theory of field generation (White 1977). The precise form of this term is not important as the emission only to within 30° of the galactic centre, corresponding to approximately 4 kpc, is going to be modelled as discussed in Chapter 5.

The second term determines the rate of radial fall-off in the field strength beyond R $\gtrsim 4$ kpc where the dynamo generated field is thought to be at a maximum (White 1977). Since there is no information on this, apart from the synchrotron radiation itself, R_0 is treated as a free parameter.

As the magnetic field is tied to the gas it is expected that the magnetic field should be compressed in a similar manner to the gas by the density wave. Figure 6.1 a(4.16) shows the way in which the gas density varies along a stream tube in the TASS picture. This profile was con- structed for an average distance of 10 kpc from the galactic centre. As shown by Roberts + Yuan (1970) this profile varies only by a small amount as one moves towards the galactic centre but beyond 11-12 kpc the peak compressions reduce and the width of the maxima increase. Towards the anticentre the amount of synchrotron emission expected from various modulations of the magnetic field is insensitive to the precise form of this modulation so long as the total emission is constant.
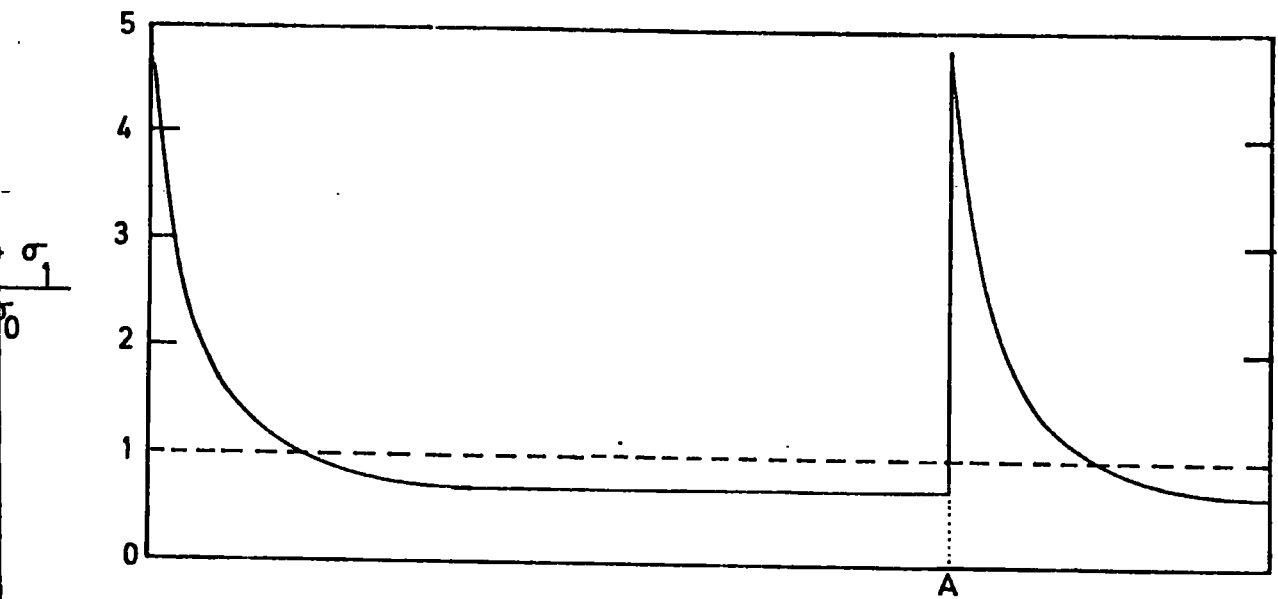
(a) Variation of density contrast along a steamtube equivalent to the
     radial variation of magnetic field strength between arms of
     separation A.
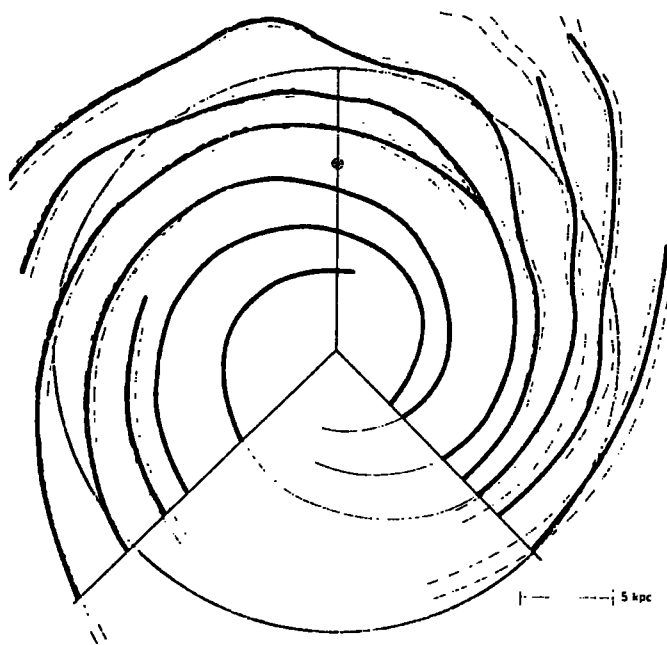
(b) Assumed spiral structure.   ⊕ location of the Sun.

     ● .... representation of the local arm.

Figure 6.1:

Figure 6.1a (4.16) shows the density variation along a stream tube but this variation also approximates the density variation between spiral arms of radial separation A kpc. The two variations would be identical if streamtubes always crossed the galactic shocks at the same inclination. In fact there is a discontinuous change in their direction at the shocks of a few degrees.

This magnetic field strength variation is taken to be the same as the density variation and may be represented by

$$\left[4.1 \; exp \left(-13.7 \, a/A \right) + 0.7 \right] \qquad 6.3$$

where A is the radial separation of the two arms adjacent to the point being considered and a is the distance to the inner of these arms.

The magnetic field geometry in the galactic plane for the regular component is assumed to follow the shape of the observed spiral structure. The spiral structure presented in figure 6.1b (4.9) as derived from HI and HII measurements is assumed. It should be noted here that the form assumed for the field modulation is based on the TASS pattern as presented by Roberts (1969), figure 4.15, whereas the spiral pattern assumed in this work is more irregular and in fact basically four armed. The TASS pattern has been used to indicate the way in which the modulation in the plane is thought to behave but is not considered to be completely theoretically consistent with the spiral pattern used here which as discussed in chapter 4, probably requires several spiral modes to be present at the same time.

The location of the sun with respect to the magnetic field geometry is of considerable importance. As discussed in chapter 4 and indicated in figure 4.9 the sun is not thought to lie on a major spiral arm, part of the large scale spiral structure, but rather to be associated with some interarm branch. Whether the sun is actually in the peak of an interarm branch or not has dramatic consequences on the amount of emission

expected from the galaxy as the regular magnetic field at the sun is observed to be $3\mu G$ and this determines in turn the overall strength of the field in the galaxy. If the sun were located in an arm position then the interarm regular field would be considerably less than $3\mu G$ resulting in lower emission from the galaxy as a whole than if the sun were in an interarm position with regular field of $3\mu G$. The position of the sun with respect to an arm: interarm position is in fact found to be fairly well defined by the fitting of the models to the data as discussed in the next chapter. As the geometry of the local feature is not well known the dotted line in figure 4.9 is taken as a representation of the local arm when the sun is in an arm position.

The calculation of $H_{\perp}^{\frac{Y+1}{2}}$ for the regular field required in the evaluation of equation 6.1 is simple. $H_{Aeg.}$ is obtained using

$$H(R) \propto \left[exp\left(-R^2/R_0^2\right) \right]\left[1 - exp\left(-R^2/4\right) \right]\left[0.7 + 4.1\, exp\left(-\frac{13.7a}{A}\right) \right] \qquad 6.4$$

normalised such that its value is $3\mu G$ at the sun and the perpendicular component of this is given by $H(R)\, sin(\Theta)$, where Θ is the angle between the line of sight and the magnetic field direction determined by the spiral structure of the galaxy. The situation is not as simple when the random component of the field is considered. The random component of the field is modified when arm locations are considered. For field lines orientated perpendicular to the shock, the shock does not affect their orientation but for field lines inclined to the shock their component parallel to the shock is enhanced altering their resultant orientation. If the spiral arm shock front is regarded as being perpendicular to the X-AXIS as shown in figure 6.2 then the magnetic field components in the directions Y and Z will be enhanced by the factor ρ_2/ρ_1 by the presence of the shock, where ρ_2/ρ_1 is the ratio of gas densities behind and in front of the shock. As shown in equation 4.9, $\frac{H_1}{H_2} = \frac{\rho_1}{\rho_2}$ for a magnetic field perpendicular to the shock.

(a)

(b)

$$(H_z^2 + H_y^2)^{1/2} = H\sin(a)$$

(c)
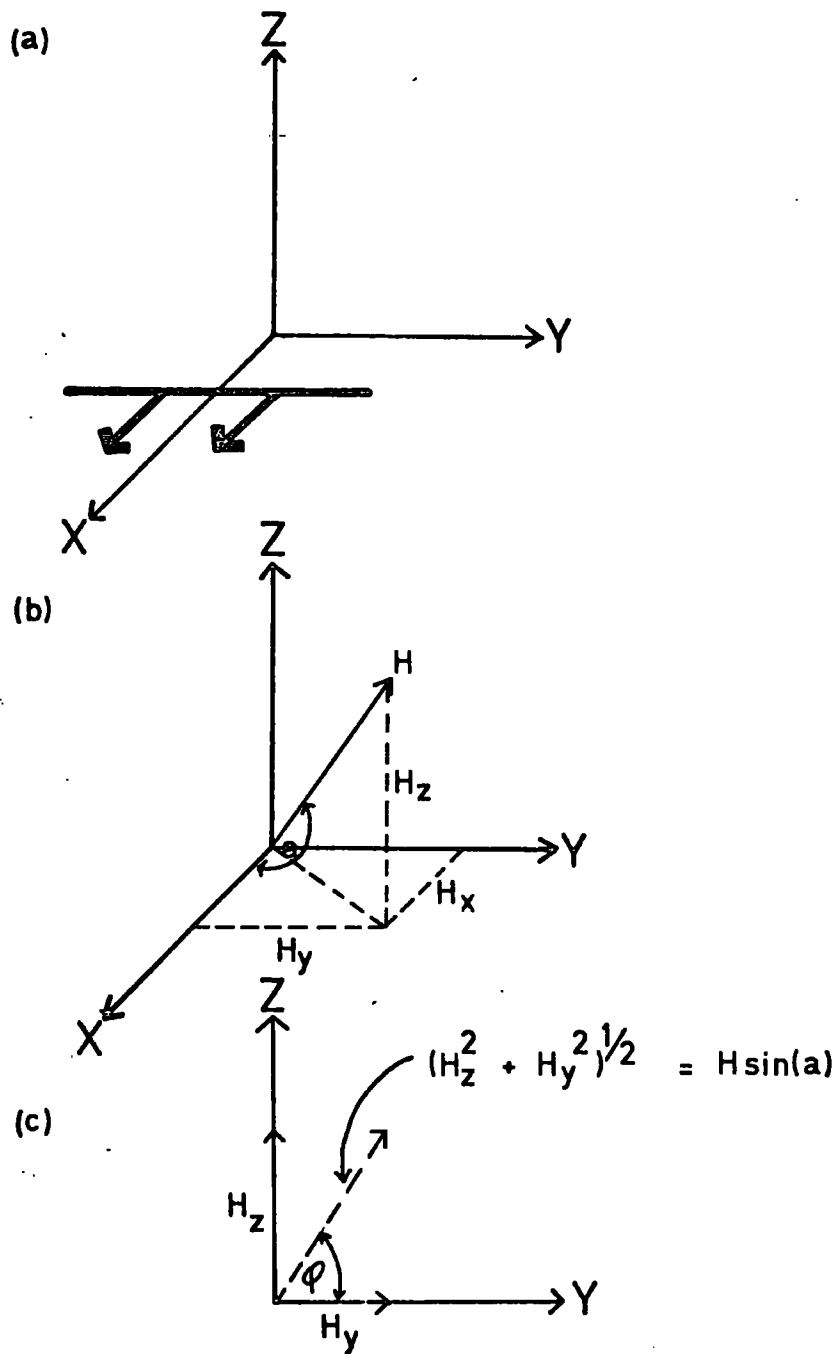
Figure 6.2:

(a) Coordinate system, X and Y in the plane of the Galaxy, showing the location of the shock front associated with the spiral arms.

(b) Decomposition of the randomly orientated magnetic field vector H. a is the angle between H and the X-axis.

(c) Projection of H onto the Y-Z plane making an angle φ with the Y-axis.

The components of a randomly orientated magnetic field $\vec{H}$

for the uncompressed field are given by

$$\vec{H} = \hat{x} H_x + \hat{y} H_y + \hat{z} H_z \qquad 6.5$$

and for the compressed field by

$$\vec{H}' = \hat{x} H_x + \hat{y} \frac{P_2}{P_1} H_y + \hat{z} \frac{P_2}{P_1} H_z \qquad 6.6$$

$$= \hat{x} H_x' + \hat{y} H_y' + \hat{z} H_z'$$

Figure 6.2b shows the orientation of $\vec{H}$ with respect to the co-ordinate

system. The angle, a, is the angle between $\vec{H}$ and the x-axis

$$\cos a = H_x / H \qquad 6.7$$

The angle ϕ is the angle between the y-axis and the projection of H onto

the Y-Z plane as shown in figure 6.1c.

$$\tan \phi = H_z / H_y \qquad 6.8$$

Using equations 6.7 and 6.8 and figure 6.2 an expression can be obtained

for the uncompressed and compressed fields in terms of a and ϕ.

$$\begin{aligned}
H_x &= H \cos a \\
H_y &= H \sin a \cos \phi \\
H_z &= H \sin a \sin \phi
\end{aligned} \qquad 6.9$$

$$\begin{aligned}
H_x' &= H \cos a \\
H_y' &= P_2/P_1 \, H \sin a \cos \phi \\
H_z' &= P_2/P_1 \, H \sin a \sin \phi
\end{aligned} \qquad 6.10$$

When compressed regions, spiral arms, are considered lines of

sight may always be considered to lie in the plane of the galaxy as the

compressed regions are very narrow in Z, height above the plane

(Chapter 4 section 4.4.4) and are always sufficiently far from the Sun

that the angle between the line of sight and the galactic plane, X-Y

plane, is very small.
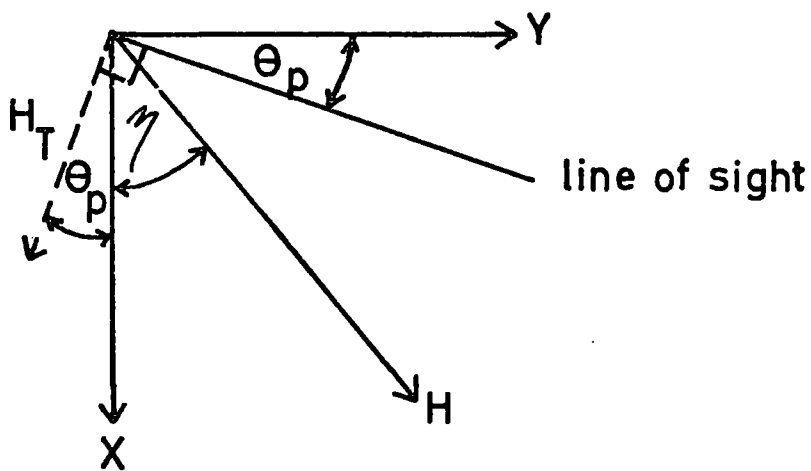
Figure 6.3:

The geometry in the plane of the Galaxy. θ_p is the angle between the line of sight and the Y-axis and η is the angle between H and the X-axis. H_T is the perpendicular component of H to the line of sight in the plane of the Galaxy.

Assuming this to be the situation, if the line of sight is assumed to make an angle Θ_p with the Y-axis then figure 6.3 describes the geometry in the plane of the galaxy. The component of the arbitrarily directed magnetic field perpendicular to the line of sight in the X-Y plane is given by

$$H_T = \left(H_x'^2 + H_y'^2 \right)^{1/2}$$

which as

$$\eta = tan^{-1}\left(H_y'/H_x' \right)$$

$$H_T = \left(H_x'^2 + H_y'^2 \right)^{1/2} \cos\left(\Theta_p + tan^{-1}\left(H_y'/H_x' \right) \right).$$

If the H_z component of H is also considered then

$$H_\perp (irregular) = \left(H_z'^2 + H_T'^2 \right)^{1/2}$$

$$= \left[H_z'^2 + \left(H_x'^2 + H_y'^2 \right) \cos^2\left(\Theta_p + tan^{-1}\left(H_y'/H_x' \right) \right) \right]^{1/2} \qquad 6.11$$

This may be expressed in terms of H, a and ϕ using equation 6.10 to give

$$H_\perp (irregular) = H\left[\left({P_2}/{P_1} \sin a \sin\phi \right)^2 + \left(\cos^2 a + \left({P_3}/{P_1} \sin a \cos\phi \right)^2 \right) \right. $$
$$\left. \cos^2\left(tan^{-1}\left({P_2}/{P_1} \tan a \cos\phi \right) + \Theta_p \right) \right]^{1/2} \qquad 6.12$$

To calculate the synchrotron emission from equation 6.1 for the random component an $H_{eff}^{\frac{\gamma+1}{2}}$ as defined in appendix I section 3 must be calculated. For interarm regions where there is no compression this $H_{eff}^{\frac{\gamma+1}{2}}$ will just equal $\beta(\gamma) H^{\frac{\gamma+1}{2}}$ as derived in the appendix but for compressed regions this will be modified. Proceeding as in appendix I $H_{eff}^{\frac{\gamma+1}{2}}$ may be obtained by integrating equation 6.12 over all possible values of a and ϕ such that

$$H_{eff}^{\frac{\gamma+1}{2}} = H^{\frac{\gamma+1}{2}} \frac{1}{4\pi} \int_{a=0}^{\pi} \int_{\phi=0}^{2\pi} \left[\left({P_2}/{P_1} \sin a \sin\phi \right)^2 + \left(\cos^2 a + \left({P_3}/{P_1} \sin a \cos\phi \right)^2 \right) \right. $$
$$\left. \cos^2\left(tan^{-1}\left({P_2}/{P_1} \tan a \cos\phi \right) + \Theta_p \right) \right]^{\frac{\gamma+1}{4}} \sin a \, da \, d\phi \qquad 6.13$$

In this expression Θ_p may equally well be considered as the angle between the line of sight and the magnetic field direction.

As the expression needs to be known for all locations in the galaxy

an approximate form was looked for that reduced to the expression
given in appendix I for interarm regions.

For $\gamma = 2.6$ 6.14

$$H_{eff}^{\frac{\gamma+1}{2}} = 0.6861 \left(\frac{p_2}{p_1}\right)^{1.8} \left(1 - 0.477\left(1 - \left[\frac{p_2}{p_1}\right]^{-2}\right)\cos^2(\theta_p)\right) H^{\frac{\gamma+1}{2}}.$$

Equation 6.14 is found to agree with numerical solutions to equation
6.13 to within 1.2% for $\theta_p = 45°$ with $\frac{p_2}{p_1} = 4.$ and to within
comparable accuracy for other values of θ_p and $\frac{p_2}{p_1}$.

Therefore for the random field the emission is calculated by
obtaining H using equation 6.4 and multiplying it when raised to the
power $\frac{\gamma+1}{2}$ by the additional factors given in equation 6.14
which depend on $\frac{p_2}{p_1}$, given by $(4.1 \quad \exp. \ (-13.7a/A) \ + \emptyset.7) \ /\emptyset.7$,
and θ_p the angle between the line of sight projected onto the plane
and the regular magnetic field direction.

The random field having been partially regularised by the galactic
shocks might be expected to remain in that configuration after the
density wave has passed. It is more likely however that the field is
fairly rapidly randomised again by turbulence caused by supernovae for
example. The expression given in equation 6.14 is an upper limit to
the regularisation of the field but on the time scales associated with
the passage of the peak of the compression this turbulence would have
a negligible effect on the field.

6.3. Cosmic Ray Electron distribution.

For a magnetic field of $3 \mu G$ synchrotron emission between 150 MHz
and 400 MHz is produced by electrons in the energy range of 1 to 10 GeV as
shown in appendix I. The similarity of the profiles presented in figure
5.9 for brightness temperatures at 150 MHz and 408 MHz scaled by $\left(\frac{408}{150}\right)^{2.8}$

suggests that the spectral index of the electrons in the energy range
1-10 GeV is approximately constant at $\gamma = 2.6$ throughout the galaxy
thus enabling the intensity of electrons of energy E throughout the galaxy
to be separated into spatial and energy dependent parts.

$$I(E,R)\,dE = I_0(R)\,E^{-\gamma}\,dE .$$

From the summary spectrum of the electron density measured at the earth
presented in fugure 2.1, Io (R = 10 kpc) = $80 \begin{smallmatrix}+70\\-30\end{smallmatrix}$ $(M^2 . \text{s. sA. GeV})^{-1}$.
All the models considered are consistent with this value for Io. For
the spatial dependence of the electron intensity two extreme cases are
considered. For Model A the electron intensity is assumed constant for
$4 < R < 15$ kpc; for $R > 15$ kpc it is zero. Cosmic ray electrons
probably originate in supernovae or supernova remnants, as discussed
in Chapter 2 section 2.3.2, which are probably concentrated in the
spiral arms of the galaxy. For electrons with a mean free path of about
1 pc corresponding to a diffusion coefficient of 0.1 $kpc^2 My^{-1}$, as
calculated in chapter 2 to be consistent with the L/M ratio, the distance
propagated in a million years from their site of origin is approximately
10 kpc. As the peak of the density wave is thought to remain in the
same region of the galaxy for a few million years this suggests that the
electrons are capable of diffusing away from their sites of origin
sufficiently fast to enable an equilibrium intensity to be established
throughout the galaxy. Wentzel (1968) and Kulsrud and Pearce (1969)
have shown that cosmic rays of GeV energies will be scattered by self-
generated hydromagnetic waves, provided that the interstellar gas density
is not so large that the waves are rapidly damped . Skilling (1971) and
Holmes (1974) predict that close to the galactic plane there exists a
'free zone' of weak scattering bounded by a 'wave zone' of strong
scattering. If such a free zone extends throughout the galaxy the cosmic
rays may propagate sufficiently fast from their sources that any galactic

radial gradient in the source density will be largely smoothed out.
For Model B the cosmic rays are assumed to be strongly scattered
throughout the disc so that they will be tied to the gas resulting in
the field being compressed in a similar manner to the gas by the density
waves i.e. Io (R) $\propto$ H (R). It is also probable that the rate of input
of cosmic rays from discrete sources is correlated with the rise in the
gas density with the result that the electron intensity is proportional to
some higher power of the magnetic field. For Model B Io (R) is taken
proportional to $H^2(R)$ for $4 < R < 15$ kpc and zero for $R > 15$ kpc. This
is the relation that Paul et al (1976) deduce from the similarity that
they claim to find between the profiles of gamma radiation and
synchrotron emission along the galactic plane. As discussed in
section 6 of chapter 5 this similarity is not present when the data is
correctly handled somewhat invalidating their deduction of this relation.

It must be remembered however that as the brightness temperature
depends on the product of $H_{\perp}^{\frac{\gamma+1}{2}}$ and Io (R) models of the
synchrotron emission are unable to distinguish between a radial
dependence of H and/or Io. Therefore a particular value of Ro^2 in
equation 6.2 may imply a magnetic field falling as exp $(-R^2/Ro^2)$
with the electron intensity radially constant but it may equally imply
that both the magnetic field strength and electron intensity are
radially dependent.

6.4. Method of Calculation.

The integration along the line sight requires the regular magnetic
field strength H(S) and Θp(S), the angle between the line of sight and
the regular field direction, to be calculated for all intervals, S, along
the line of sight. As the magnetic field strength varies discontinuously
a small step length along the line of sight is required. A step length
of 0.015 kpc is found to give sufficient accuracy.

6.4.1. Calculation of H(R) for any location in the galaxy.

As the spiral structure used in this analysis has no analytical form the spiral arms were digitised and four point Lagrangian interpolation used. For the longitude range $180° < \ell^{II} < 330°$ the arms were digitised at every $15.0°$ about the galactic centre (X) whereas for $30° < \ell^{II} < 180°$ the arms were digitised at every $7.5°$ as in this region the arms are more irregular. The arms were digitised out to beyond 15 kpc from the galactic centre so that emission right out to the 15 kpc boundary could be accurately determined. Different forms were used for the interpolation depending on whether the point of interest on the arm had two digitised points on either side of it or only one point on one side but three on the other. The three possible situations are given by :

(i)
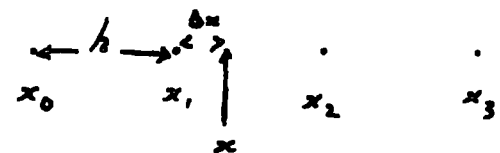
$$x_0 < x_1 < x_2 < x_3$$

$$y = \frac{1}{6h^3}\left[\Delta x^3(-y_0 + 3y_1 - 3y_2 + y_3) + \Delta x^2 h(3y_0 - 6y_1 + 3y_2) + \Delta x h^2(-2y_0 - 3y_1 + 6y_2 - y_3) + h^3 6y_1\right] \qquad 6.15$$

(ii)
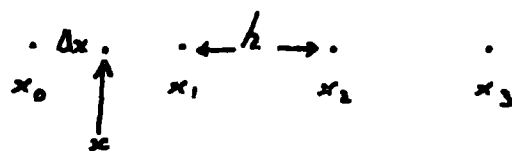
$$y = \frac{1}{6h^3}\left[\Delta x^3(-y_0 + 3y_1 - 3y_2 + y_3) + \Delta x^2 h(6y_0 - 15y_1 + 12y_2 - 3y_3) + \Delta x h^2(-11y_0 + 18y_1 - 9y_2 + 2y_3) + 6h^3 y_0\right] \qquad 6.16$$

(iii)
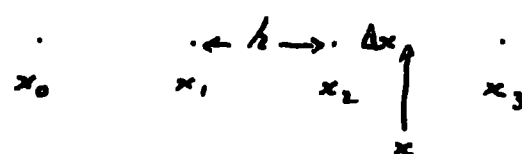
$$y = \frac{1}{6h^3}\left[\Delta x^3(-y_0 + 3y_1 - 3y_2 + y_3) + \Delta x^2 h(3y_1 - 6y_2 + 3y_3) + \Delta x h^2(y_0 - 6y_1 + 3y_2 + 2y_3) + 6h^3 y_2\right] \qquad 6.17$$

where x_i represents the angular location along the arms with respect to the galactic centre and Y_i is the corresponding radial distance at which the digitised point is located. The x_i's are all separated by a constant angular amount h equal to $7^o.5$ or 15° depending on which half of the galaxy is being considered. x is the angular location of the point being considered lying an angular separation Δx from the nearest x_i such that $x_i < x_i + \Delta x$ and y is the resultant interpolated radial distance. Once the radial location of the inner and outer arms with the same value of X as the point on the line of sight being considered have been determined, the form of H(R) can be found by using equation 6.4.

6.4.2. Calculation of the angle Θ between the line of sight and the regular magnetic field direction.

As the pitch angle of the observed spiral structure is not constant it was calculated from the digitised spiral arm grid. For interarm locations the pitch angle was assumed to be the same as that for the closest section of spiral arm. For the three dimensional case,

$$b^{II} > 0^o, \quad \cos \Theta = \cos b^{II} \cos \Theta_P$$

where Θ_P is the angle between the line of sight projected onto the plane and the regular field direction. The perpendicular component of the regular field is therefore given by the expression.

$$H_\perp (regular) = H(R) \sin \left(\arccos \left(\cos b^{II} \cos \Theta_P \right) \right)$$
$$= H(R) \sin \Theta$$

As seen from equation 6.14 the perpendicular component of the irregular field also depends on the angle Θ_P.

6.4.3. Brightness temperature determination.

Once the two magnetic field perpendicular components have been determined for every location along the line of sight the total emission may be calculated using Simpson's integration formula. The total emission is then the sum of the two emissions with the appropriate F factor included. The F factor is determined from the normalisation of the calculations to the observations.

6.4.4. Normalisation Procedure.

For γ = 2.6 and at a frequency of 150 MHz equation I.11 leads to the expression given below for the calculated brightness temperature for Model A for a particular direction in the galaxy

$$T_b = 0.0498 \, I_o \int_{o_s}^{s} \left[H_\perp(\text{reg}) \right]^{1.8} + \left[H_\perp(\text{irreg}) \right]^{1.8} ds \qquad 6.18$$

$$T_b = 0.0498 \, I_o \int_{o}^{s} \left\{ \left[H(R) \sin\theta \right]^{1.8} + 0.686 \left(\frac{H(R)}{F} \right)^{1.8} Y(R) \right\} ds$$

where Io is the cosmic ray electron intensity constant throughout the galaxy for Model A, H(R) is the regular field magnitude normalised such that it is 3 μG at the earth, F is the ratio of the magnitudes of the regular to irregular fields and Y(R) is the factor that takes into account that only parallel components of the irregular field are enhanced by the shocks. Equation 6.18 may be written in the form.

$$T_b = C \; (\text{Regular} + \text{irregular}/\text{RATIO})$$

where Regular and Irregular are the contributions to the total brightness temperature from the two field components and C and RATIO are constants determined from equation 6.18. If two directions in the galaxy are chosen and the calculated brightness temperature required to agree with the observed brightness temperature then a series of values of C and RATIO can be found such that this condition is satisfied for varying values of R_o^2, the radial dependence of the magnitude of the regular magnetic field. C is required to equal 0.0498 Io with Io equal to 80 ($m^2. \, S.\, S\text{A}. \, \text{geV.}$)$^{-1}$ thus selecting a particular value of R_o^2 and RATIO. In all the models considered here the directions in the galaxy have been chosen to be the anticentre $\ell^{\text{I\hspace{-1pt}I}}$ = 180°, $b^{\text{I\hspace{-1pt}I}}$ = 0° and the direction in the plane corresponding to the peak of emission observed at approximately $\ell^{\text{I\hspace{-1pt}I}}$ = 310°, $b^{\text{I\hspace{-1pt}I}}$ = 0°. The location of the sun with respect to the spiral arms can considerably affect the

values of R_o^2 and RATIO. The sun is considered to be either located in an arm of variable compression or at a distance of 0.5 kpc from an arm of full compression in the direction of the anticentre. Fits to the normalisation points are not always possible for all these locations of the sun. The overall shape of the $\cancel{b}^{II} = 0^o$ longitude profile as compared with the observed profile is used to find the best of the locations for the sun. The reasons for selecting the above locations for the sun will be discussed in the next chapter. For Model B the normalisation procedure is similar to that as described above except that equation 6.18 now reads:

$$T_b = 0.0498 \int_o^s I_o \beta H^2(R) \left[(H(R) \sin \theta)^{1.8} + 0.686 \left(\frac{H(R)}{F} \right)^{1.8} Y(R) \right] ds$$

$$6.19$$

where $\quad I_o \beta H^2(R)$

is the intensity of electrons at distance R from the galactic centre normalised by β such that it equals Io at the earth.

$$T_b = C_{II} \quad (Regular + Irregular/RATIO_{II})$$

may now be used with the integrals Regular and Irregular now being proportional to $H(R)^{3.8}$ rather than $H(R)^{1.8}$ to obtain values of CII and RATIO II to agree with the normalisation directions for various Ro ^{2}'s . Model B is found to be more restrictive on the possible locations of the sun as will be seen in chapter seven when the calculations are discussed.

6.4.5. Calculation of the emission away from the plane.

As discussed in chapter 4 section 4.4.4. the spiral arms are thought to have a full width $2Z_{1/2}$ of about 480 pc. Figure 4.17 shows the way in which the compression of the gas falls-off with height above the plane and this is also the way in which the field is thought to fall in the spiral arms with height above the plane. The uncompressed field in this analysis is assumed constant within a few kiloparsecs of the plane.

The curve in figure 4.17 may be approximated by the analytical expression

$$f(z) = 1 + 0.7715z - 17z^2 + 22.914 z^3 \qquad z < 0.5 kpc$$
$$= 0 \qquad z > 0.5 kpc$$

which has the value 1 on the plane and 0 at 0.5 kpc above the plane.
The electron density is expected to fall with height above the plane in
some particular way depending on the diffusion of the electrons from the
source region. Various forms will be taken for this I (z) factor as
discussed in the next chapter. The regular magnetic field at a location
above the plane of the galaxy is therefore given by

$$H(R,z) \propto \left[exp(-R^2/R_0^2) \right]\left[1 - exp(-R^2/4) \right]\left[0.7 + 4.1 f(z) exp(-13.7a/A) \right]$$

and the emissivities for the regular and irregular field components are
given by 0.0498 (H (R,z) Sin θ)$^{1.8}$ I_0 $I(z)$ and

$$0.0498 \times 0.686 \left(\frac{H(R,z)}{F} \right)^{1.8} I_0 I(z) Y(R) \,{}^{o}K kpc^{-1}$$ respectively for

Model A and $\quad 0.0498 \left(H(R,z) sin \theta \right)^{1.8} H^2(R,z) I_0 \beta I(z)$ and

$$0.0498 \times 0.686 \left(\frac{H(R,z)}{F} \right)^{1.8} Y(R) H^2(R,z) I_0 \beta I(z) \,{}^{o}K kpc^{-1}$$

for Model B.

As discussed in section 6.2 the Y (R) factor is assumed to be
independent of z to a first approximation. Therefore once a form of
I (z) has been chosen the synchrotron emission from the galaxy may be
calculated for 30° < ℓ^{II} < 330° $\qquad$ − 90° ≤ b^{II} ≤ + 90°.
I (z) is chosen such that the temperature at the pole is equal to the
observed temperature of approximately 220°K.

6.5. Convolution.

Before the calculated brightness temperature distribution can be
compared with the observed distribution the calculated temperatures need
to be convolved to the beam shapes used in making the observations.

Figure 5.3 shows the various HPBW's used in producing the composite Landecker and Wielebinski map at 150 MHz. The scans were all made at constant declination. The beam shapes are assumed to be gaussian except for the 5° x 1.25^O beam that is gaussian in declination but a straight average in right ascension. The calculated ℓ^{II}, b^{II} grid of brightness temperatures were converted to a grid in R.A. and declination and the standard convolution formula applied to obtain the brightness temperature for direction i, T_{bi} .

$$T_{bi} = \frac{\displaystyle\sum_{j}^{\infty} T_{bj} \; \exp - \left[\frac{RA_{ij}^2 + Dec_{ij}^2}{\sigma_{RA}^2 \cos^2\Theta_{ij} + \sigma_{dec}^2 \sin^2\Theta_{ij}} \right]}{\displaystyle\sum_{j}^{\infty} \exp - \left[\frac{RA_{ij}^2 + Dec_{ij}^2}{\sigma_{RA}^2 \cos^2\Theta_{ij} + \sigma_{dec}^2 \sin^2\Theta_{ij}} \right]}$$

where $\displaystyle\sum_{j}^{\infty}$ is a summation over all grid points T_{bj} lying within about a beam width of the point being considered, T_{bi} . RA_{ij} and Dec_{ij} are the separation in right ascension and declination between the points i and j. σ_{RA} and σ_{dec} are the half widths at half maximum of the aerial beam to which the calculated values are being convolved. Θ_{ij} is the angle the line joining point j to point i makes with the right ascension coordinate axis. Having convolved the calculated brightness temperatures the extragalactic component is added and the emission from the spurs, as expected from

the Van de Laan model as discussed in chapter 5, is also added. The calculated brightness temperature distribution as modified above is now compared directly with the Landecker and Wielebinski map.

6.5. Flow diagram of the Calculation of the Continuum emission.

Figure 6.4. presents the flow diagram for the complete calculation of a computed 150 MHz synchrotron map.

1) A location of the sun is decided upon: it is either assumed that the sun is in an arm of compression $k = (0.7 + q)/0.7$ where $q = 4.1$ for full compression or in an interarm position with an arm of full compression situated at 0.5 kpc towards the anticentre.

2) For the chosen location of the sun the normalisation program finds the values of R_0^2 and F such that agreement is reached with the observed brightness temperatures at $b^{II} = 0^O$ $\ell^{II} = 180^O$ and 310° after convolution and with the value of I_0 at the sun. Physically realistic values of F are not necessarily always found. F may be negative indicating that no fit is possible.

3) The values of R_0^2 and F are used in the main programs to calculate the brightness temperature distribution at intervals of 2^O in galactic latitude and 1^O in galactic longitude.

4) The calculated brightness distribution is convolved to the required beamwidths.

5) The convolved calculated brightness temperature distribution is combined with the emission expected from the galactic spurs, thermal emission and extragalactic emission and contoured onto a sinusoidal projection in ℓ^{II} and b^{II}.

6) Comparison is made with the Landecker and Wielebinski all sky map, the $b^{II} = 0$ longitude profile and with latitude profiles at various values of ℓ^{II}.
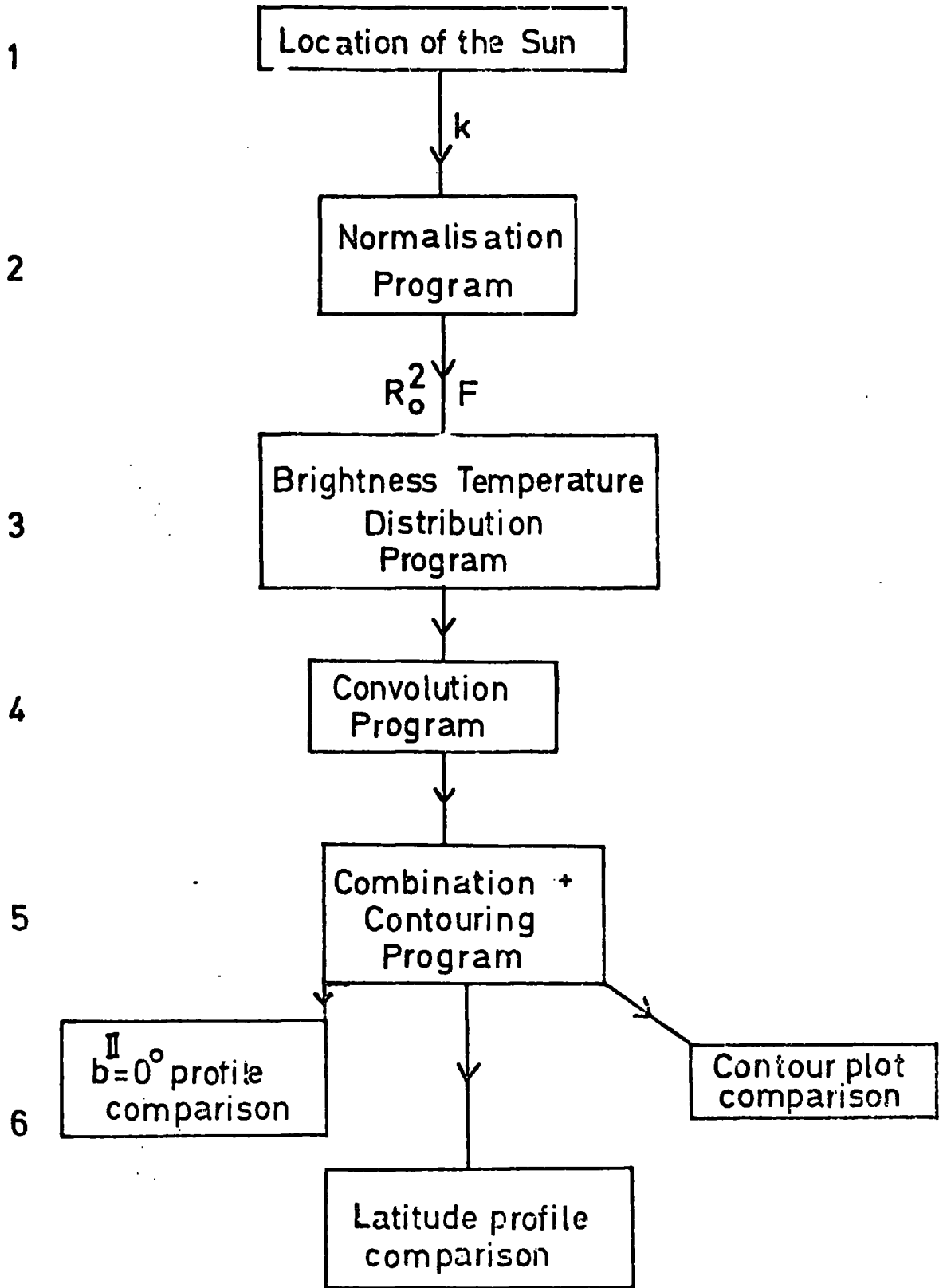
Figure 6.4:

Flow diagram for the complete calculation of a computed 150MHz synchrotron map. A full explanation appears in the text.

References

Holmes J.A. 1974, M.N.R.A.S. <u>166</u>   155

Kulsrud R and Pearce W.P. 1969 Ap. J. <u>156</u>   445

Paul J. Cassé M and Cessarsky C.J. 1976

Roberts, W.W. 1969 Ap. J. <u>158</u>   123

Roberts W.W. & Yuan C. 1970 Ap. J. 161   877-902

Skilling J. 1971 Ap. J. <u>170</u>   265

Wentzel D. 1968 Ap. J. <u>152</u>   987

CHAPTER 7

Results from the Continuum Models

7.1 The Halo Problem

The suggestion that the high latitude distribution of observed continuum emission requires the galaxy to possess a large 'halo' of relatively uniform emissivity was first put forward by Shklovskii in 1952 . Since this date there has been continued discussion as to whether such a halo exists and if it does what form it takes. Several approaches have been taken to investigate the halo:-

i) The disc and halo regions have been modelled and synthetic maps of the sky at a particular frequency produced to compare with the observations.

ii) The spectrum of the radio emission for different directions in the galaxy have been analysed in terms of three components with differing spectral indices corresponding to the disc emission, halo emission and extragalactic emission. Recently this method has been improved by Webster (1975) by the use of T-T plots.

iii) Edge-on external galaxies have been observed to see if radio haloes are present perhaps leading to the conclusion that the galaxy might also possess such a halo if the observations prove positive.

In the following paragraphs these various methods of halo investigation will be discussed and also the present situation as regards the various diffusion models developed to explain the existence of such haloes.

7.1.1. Investigation of the radio halo by modelling.

This is the approach that is used in this thesis. Up to now the modelling of the continuum radiation has always involved a very simple model for the galactic disc. The early analysis carried out by Shklovskii (1952), Baldwin (1955a) and Mills (1959) led to the

conclusion that a strong radio halo exists. This conclusion was later questioned by Baldwin 1967 and Burke 1967 who suggested that the enhanced emission from the local spiral arms and spurs might be capable of explaining the entire observed radiation without the need for a bright radio halo. These early analyses proposed a halo with essentially a constant emissivity. This situation is very difficult to explain in terms of diffusion of electrons from their sources in the galactic plane with free escape at some height above the plane but rather requires a model in which the electrons are confined in the large halo volume by partially reflecting boundaries.

Price (1974) claims to explain the high latitude brightness temperature distribution by placing the earth on the inner edge of a non thermal spiral feature. As discussed in chapter 5 section 6 Price used the Lin and Shu pattern (1967) to represent the spiral structure and moved the sun with respect to this pattern to obtain a fit to the observations. This is inadmisable as Lin and Shu identified the outer arm of their pattern with the Perseus arm which lies at a distance of more than 1 kpc from the sun. Price also requires a purely phenomenological base disc component in addition to a spiral component to explain the disc emission. In the models developed in this thesis such a base disc component is equivalent to the emission produced by the regular field while the spiral component is produced by the irregular field. As shown in chapter 4 section 4.4. spiral arms in fact have a very narrow emissivity width in the Z direction and therefore the placing of the sun in an arm gives a much too low pole temperature rather than a large value as Price assumed and used as evidence against a halo. This point will be discussed again in connection with the results for Model B.

More recently Baldwin (1976) using a simple model of the emmisivity in the disc of the galaxy has derived a Z distribution for the emissivity that agrees with observation at various longitudes for low latitudes, $b^{\pi} \leq 15^{\circ}$. The Z distribution found is a thick disc of half width at half maximum of about 350 pc and an equivalent half thickness of approximately 750 pc.

In this thesis the modelling technique is put on a firmer footing by using a physically realistic model for the galactic disc including spiral structure within the framework of density wave theory. Rather than comparing the predicted emission with the observed emission for a limited number of directions in the galaxy a complete comparison over the whole (ℓ^{π}, b^{π}) space is carried out.

7.1.2. Spectral Investigations of the radio halo

Anand, Daniel and Stephens (1968) have attempted this type of investigation of the halo but many difficulties are encountered. Absolute measurements of the sky brightness over a wide range of frequencies are required to a high degree of accuracy and a fore-knowledge of the spectra of the various components of the radiation. Recently Webster (1975) has modified this technique by introducing the method of T - T plots to halo investigation. Using observations from scaled antennas at different frequencies plots are made of the brightness temperature at one frequency, T_{ν_1}, against that at a second frequency, T_{ν_2} for varying right ascensions. By assuming that the halo spectrum is steeper than that of the disc and that the halo radiation is weaker in the general direction of the anticentre than in any other direction it is possible to show that a radio halo gives rise to a characteristic shape for a T - T plot. In general the T - T plots show a closed loop and the separation of the two branches of the loop is the signature of a radio halo with a steep spectrum. By modelling a

a uniformly emitting spherical halo to fit the T - T plots, produced
from the observations of Bridle (1967), Sironi (1974) and Webster (1974),
Webster concluded that the galaxy possesses a halo of characteristic
parameters; radius Rh = 12.5 kpc and emissivity $\mathcal{E}_h$ (81.5 MHz.   )
= 40K kpc $^{-1}$ i.e. 30 times weaker than the disc emission. This results
in the conclusion that the halo density of cosmic rays and magnetic
field intensity are significantly less than in the disc. Webster's
results contradict the results of Bulanov et al. (1975) and Dogiel et al
(1975) who showed in the framework of diffusion calculations that the
average emissivity of the halo at frequencies $\nu \gtrsim 15$ MHz must be
close to that of the disc. Recently Bulanov et al (1976) have advanced
an explanation for the differing interpretations of essentially the
same data. Webster assumes that both the disc and the halo possess
constant spectral indices whereas if a realistic diffusion model is
assumed the spectral index shows a gradual change from disc to halo.
This results in Webster obtaining a greatly reduced halo luminosity
and an enhanced disc luminosity.

Strong (1977) has carried out a 3-D diffusion calculation fitting
the T - T plots to show that this is indeed the case. He finds that the
average magnetic field in the halo may be in the region of 0.2 of that in
the disc, the diffusion mean free path $\sim$ 1 par sec and the full width
to half - maximum of the emission at 17.5 MHz.   about 6 kpc.

7.1.3. Indications of a radio halo from the observation of external galaxies.

Recently by the use of aperture synthesis telescopes it has become
possible to map edge-on external galaxies in order to search for the
presence of radio haloes. As early as 1955 Baldwin (1955b) was able to
indicate that $M31$ possessed a halo but unfortunately recently
this interpretation has been questioned by Wielebinski (1976) who
suggests that the halo may just be a manifestation of background sources.

Van der Kruit and Allen (1976) having evaluated all of the available results conclude that a faint radio halo probably does exist around M 31, but the question of its brightness it not yet satisfactorily resolved.

Allen et al 1977 have presented high resolution radio maps of NGC 891 at wavelengths of 49.2, 21.2 and 6.0 cm. The observations indicate that the radiation from NGC 891 has one component which shows a very strong concentration to the plane of the galaxy and another more extended component extending to Z distances of 6 kpc above the plane of the galaxy. The narrow component of emission has a thickness of less than 700 pc and NGC 891 as a whole has an equivalent width in Z of 1.8 kpc for the volume emissivity.

Ekers and Sancisi (1977) have presented observations of NGC 4631 at 610 and 1412 MHz. which also indicate that this edge - on galaxy possesses some form of radio halo with an equivalent thickness in Z of approximately 3 kpc.

It is important that these galaxies are compared in their other properties with the Galaxy before any conclusion can be reached as to what the existence of haloes about them indicates for the Galaxy. Table 7.1, taken from Allen et al 1977, summarises the properties of the two galaxies in comparison with our own galaxy. The most important difference is in the total luminosity which is significantly greater for both NGC 891 and 4631. The equivalent thickness of the radio disc for our galaxy as inferred by Baldwin (1976) is consistent with the values found for the two galaxies. Comparison with these two external galaxies indicates that it is possible and perhaps likely that the galaxy possesses a thick disc or halo consistent with the interpretation made by Baldwin (1976) but it does not prove that such a halo exists.

T A B L E   7.1

Parameter	NGC 891	NGC 4631	Galaxy
Assumed distance (Mpc)	14	5.2	-
Total mass (10^{11} $M_\odot$)	3	0.7	1.8
Radio luminosity (10^{21} WHz^{-1}) at 21cm.	18	4.2	1.4
Flux density of disc (Jy) at 21cm	0.74	1.0	0.12
Equivalent thickness of radio disc in Z (kpc) at 21cm	1.8	3	1.5
Exponential scale length λ_0 of radio emissivity in λ at $z = 0$ (kpc) at 21cm.	5	4	6
Face-on surface brightness at $\lambda = \lambda_0$ (K) at 21cm.	5	1.6	0.3

7.1.4. Physical Mechanism for the production of radio haloes.

The radio emission away from the galactic plane is usually understood in terms of the diffusion of electrons from their sources in the disc interacting with magnetic fields at large Z values either produced in a dynamo mechanism or blown upwards from the disc by instabilities produced by the disc cosmic rays. Extensive work on two and three dimensional diffusion of electrons has been carried out by the Russians in particular by Bulanov, Dogiel, Ptuskin and Syrovatskii. Most diffusion calculations lead to the idea that if the halo exists its spectrum will be considerably steeper than that of the disc and that the electron density will fall with distance from the plane and that in all likelyhood to obtain haloes extending out beyond a few kiloparsecs it would be necessary for the particles to be convected outwards driven by a galactic wind as discussed by Ipavich (1975) and by Owens and Jokipii (1977). Diffusion models of particles freely escaping from the plane of the galaxy are incapable of explaining uniformally emissive haloes. Such models require the postulation of some huge confining volume with reflecting or partially reflecting boundaries.

7.2. Previous work.

Before discussing the results of the various models described in chapter six mention must be made of the previous two dimensional model presented by French and Osborne (1976) from which the present work is an extension. In this model it was assumed that irregularities in the spiral arms would have the effect of smoothing out the sharp peaks predicted by density wave theory for the spiral arm enhancement to produce a cosine squared variation of the magnetic field between arm and interarm regions. Later calculations showed that this was not in fact the case and the resultant radio brightness temperature distribution was more likely to show several sharp peaks corresponding to the several possible tangential directions to the fluctuating arms rather than a smooth peak of the cosine squared variation. In the cosine squared

model with the density ratio in the arm to interarm region being 5 : 1

the best fit to the observations was obtained for Model A with $R_o^2 = 125$

and F = 1.1 with the sun in an interarm position. These are not very

different from the results disoussed below.

7.3. Results of the 2-D Model Calculations.

7.3.1. Introduction.

Initially models of the galactic plane will be discussed for both

the Model A and B distributions of electrons and then various 3 -

dimensional models will be considered.

7.3.2. Model A.

For this case of constant electron density throughout the galaxy

initially the sun was assumed to be located in an arm of variable

compression. Figure 4.9 showing the composite spiral structure used in

this analysis also has superimposed on it an arm running through the

location of the sun. This is orientated such that the tangential

directions from the sun approximately correspond to $\ell^{II} \approx 265^o$ and ℓ^{II}

$= 80^o$ the locations of the two maxima in the observed galactic plane

profile that have been identified by some previous authors as mani-

festations of a local arm. As discussed in chapter 5 this is not in

fact thought to be the case. Observational evidence for the Orion arm

is rather meagre but such a location for the arm as given in figure 4.9

is consistent with the observations presented in chapter 4. As the

Orion arm is not thought to be part of the 'grand design' of spiral

structure its compression is unknown. Figure 7.1 presents the galactic

plane profile for a model A1 in which the compression k of the solar arm is

given by (0.7 + 0.5) /0.7 $\approx$ 1.7 rather than the full compression of

6.9 as for the major spiral arms. The emission from the whole galaxy is

increased or decreased depending on whether the sun is respectively in

an interarm or arm region since the absolute value of the regular field

at the sun is fixed. It is reasonable to expect that for the calculated
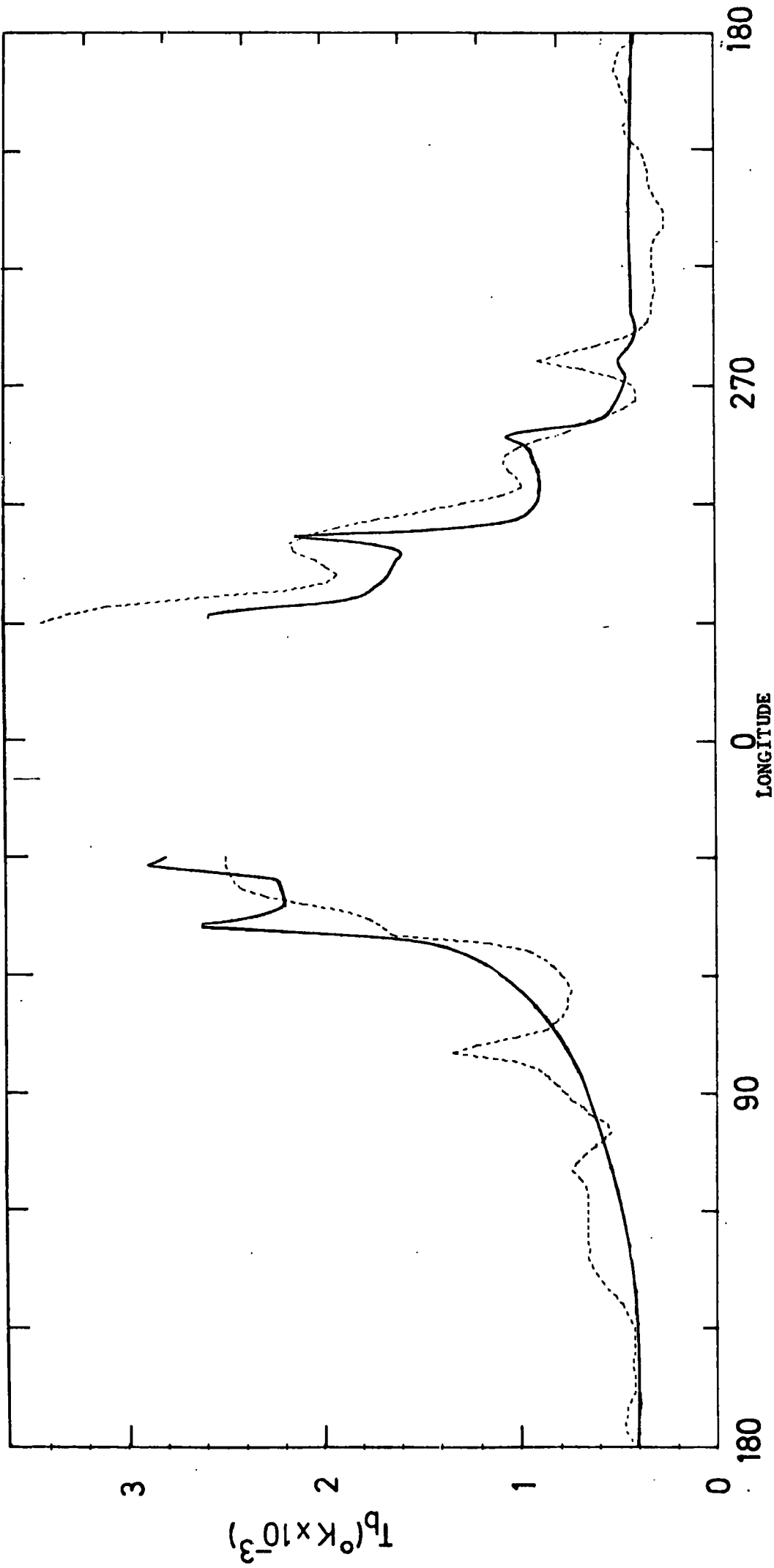
Figure 7.1: Longitude profile for Model A.1. The observed 150 MHz profile is shown for comparison (dashed line).

profile to fit the observed profile a weak compression for the solar

arm is more likely than a strong compression as the emissivity from the

central parts of the galaxy is known to be considerably larger than that

implied from the observed values of the electron density and magnetic

field strength at the earth. The fit in figure 7.1 such that agreement

is forced at ℓ^{II} = 180° and ℓ^{II} = 310° requires a rather small

value of F = 0.375 and a rather large value of Ro^2 = 249 resulting in

the profile being too angular and too low in the central regions of the

galaxy. If the compression of the solar arm is further decreased such

that the sun is in fact in an interarm region, Model A.2, the fit is

improved, as seen in figure 7.2, and the parameters are now Ro^2 = 195

and F = Ø. 7179 resulting in the local emissivity

$$\mathcal{E}_\nu (sun) = 0.0498 \, T_o 3^{1.8} \left[(\sin \theta)^{1.8} + \frac{0.686}{F^{1.8}} \right] = 64°K \, kpc^{-1} \, for \quad \ell^{II} = 180° \atop b^{II} = 0°$$

where θ, the angle between the line of sight and the regular field

direction is approximately constant at 80°. This value of the local

emissivity can be directly compared with measurements made on the

emissivity by observing optically thick H_{II} regions at a few tens of MHz

If an H_{II} region is optically thick and completely fills the telescope

beam then the brightness temperature observed is a sum of the thermal

electron temperature of the H_{II} region and the brightness temperature

between the H_{II} region and the observer. In practice the background

temperature adjacent to the absorption feature and the 'hole' depth

corresponding to the emission from behind the H_{II} region are measured

enabling the foreground emission to be determined from:-

T foreground = (surrounding temperature) - (hole depth) - T_e

where T_e is the thermal electron temperature of the H_{II} region. Recently

Caswell (1976) using a survey at 10 MHz has identified nine optically

thick H_{II} regions that give fairly reliable values for the local

emissivity. At 10 MHz he assumes the thermal electron temperature to
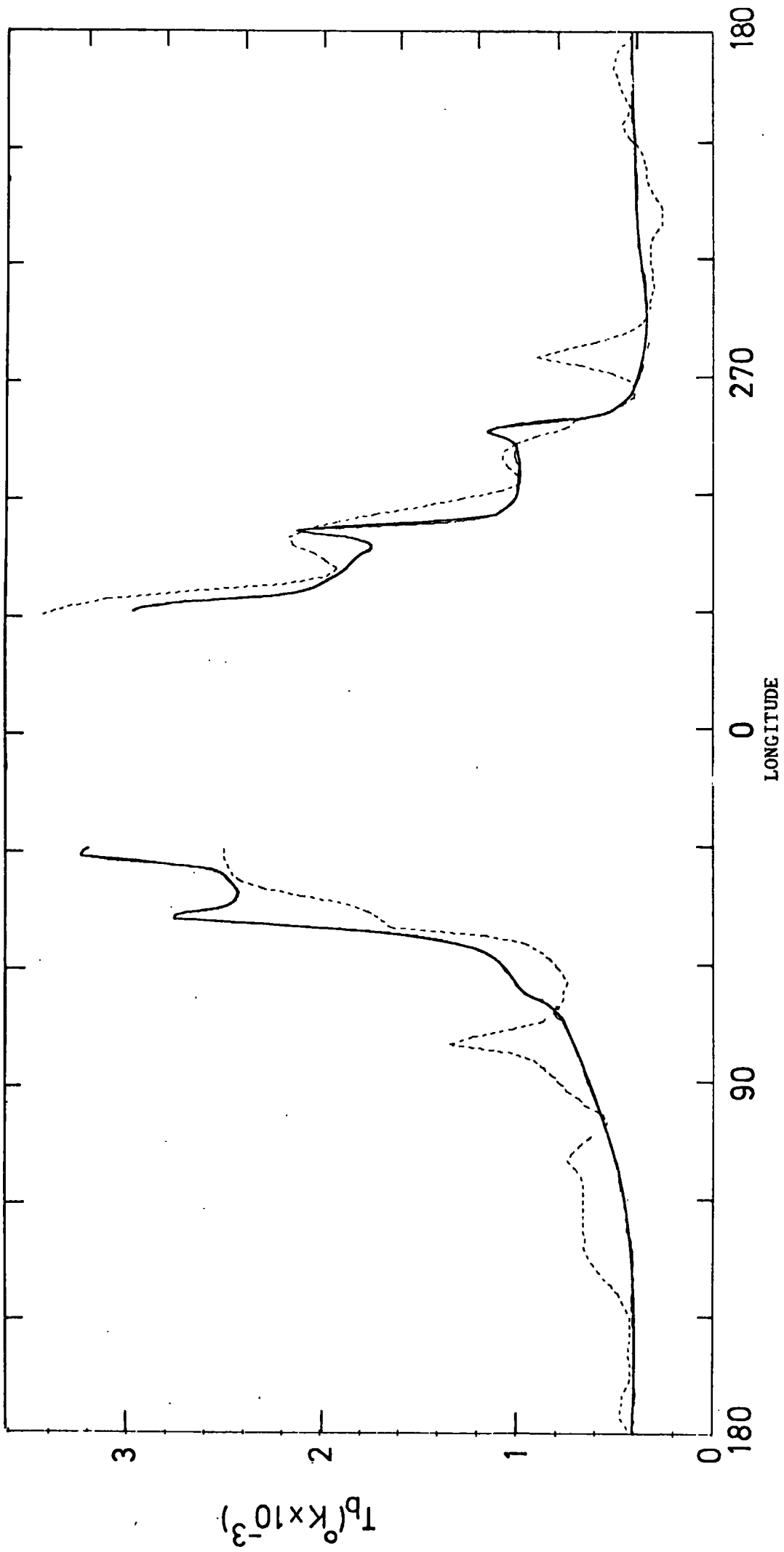
Figure 7.2. Longitude profile for Model A.2.

be 6 x 10³K, consistent with recombination line measurements. Similar analyses of optically thick H_{II} regions have previously been carried out by Bridle (1968), Andrew (1969), Roger (1969), Parish (1972) and Jones and Finlay (1974).

Table 7.2. summarises the results from the various authors converted to the expected local emissivity at 150 MHz   A recent compilation of radio measurements at various frequencies by Webster (1977) indicates that the galactic radio spectrum shows a break at about 100 MHz   such that at low frequencies the spectrum flattens to β = 2.4. If the electron spectrum is assumed to have a break at 3 Ge V from 2.6 to 1.8 then the radio spectrum calculated for an $H_\perp$ of $3.6 \mu G$ has a break at 85 MHz   The values in Table 7.2 have been calculated assuming that β changes from 2.8 to 2.4 at 85 MHz.

There seem to be many discrepancies between the various sets of observations. In the case of the earlier surveys this may be due either to the telescope beams not being completely filled by the source or the source not being sufficiently optically thick. Both these situations lead to an over estimate of the local emissivity. The measurements of Parrish in particular show that the emissivity distribution is perhaps rather anisotropic. This is clearly seen in the values of $\mathcal{E}_\nu$ (local) obtained using IC 410 and NGC 2175. For the purposes of comparison with the various models the recent data by Caswell will be used. Caswell's results indicate a local emissivity of approximately 288°K kpc^{-1} for distances of less than 1 kpc from the sun, which is considerably higher than the value implied by Model A.2. Most of the Caswell measurements are made within the ℓ^{II} = 90° to 270° directions, i.e. looking away from the galactic centre. Improved agreement with the Caswell measurements can be obtained if a local arm is introduced between the sun and the perseus arm. For model A.3 an arm parallel to the dotted arm in figure 4.9 located 0.5 kpc towards the anticentre is introduced. This arm is assumed to have the same compression as the major arms. The resultant profiles are presented in figure 7.3.

Author	Frequency of Observation (MHz)	Name of Source	Coordinates		Distance (kpc)	Emissivity at 150MHz ($^\circ$K kpc^{-1})
Andrew	13	–	161.5	-13.0	0.4± 0.15	< 260
"	13	–	174.3	- 0.5	1.6± 0.6	203 ± 80
Bridle	10	IC 1805	134.0	1.0	2.0± 0.2	51 - 84
Roger	22.25	IC 1805	134.0	1.0	2.0± 0.2	150.4
"	22.25	IC 1848	137.0	1.0	"	± 33
Parrish	50	W51	48.0	0.35	6.0	330
"	50	NGC 6820	59.0	0.1	2.0	< 229
"	50	NGC 1499	157.	-12.3	0.3	< 114
"	50	IC 410	175	- 1.7	2.0	0
"	50	NGC 2175	189	0.5	2.0	> 152
"	50	NGC 2244	200	2.2	1.5	252
Jones and Finlay	29.9	Carina Nebula	287	- 0.5	2.5	154
	29.9	RCW 108	336.7	- 1.3	1.3	634
Caswell	10	NGC 7822	118	+ 5.0	0.65	224
"	10	NGC 1805	134.5	+ 1.0	2.2	88
"	10	NGC 1848	137.0	+ 1.0	2.1	
"	10	NGC 1499	160.5	-12.5	0.44	319
"	10	IC 405	172.5	- 1.5	0.65	354
"	10	S 249	189.0	+ 4.0	1.9	138
"	10	λ Ori.neb.	196	-12.0	0.5	289
"	10	NGC 2264	203	+ 2.5	0.71	265
"	10	Barnard Loop	208	-20.0	0.5	253
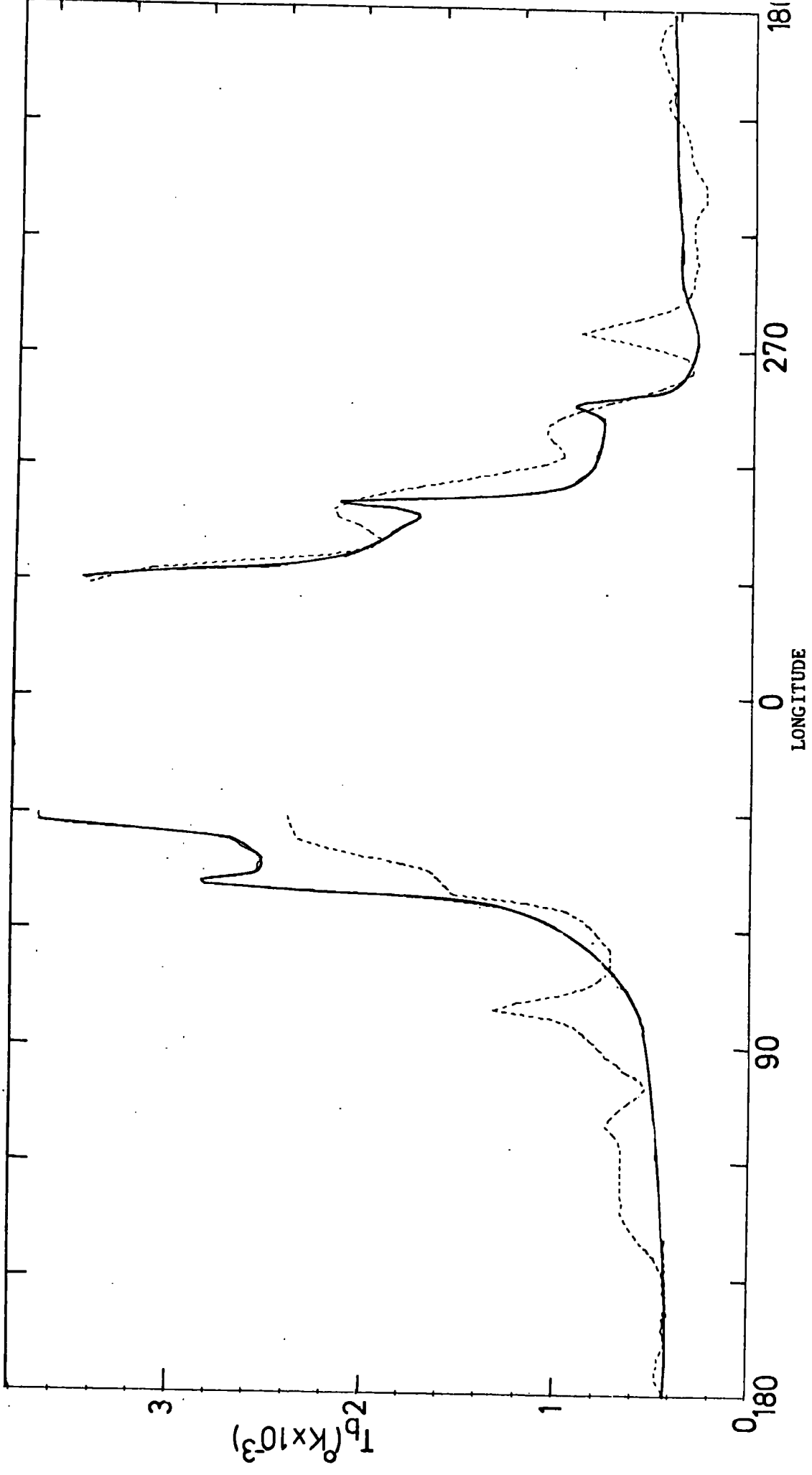
Figure 7.3: Longitude profile for Model A.3.
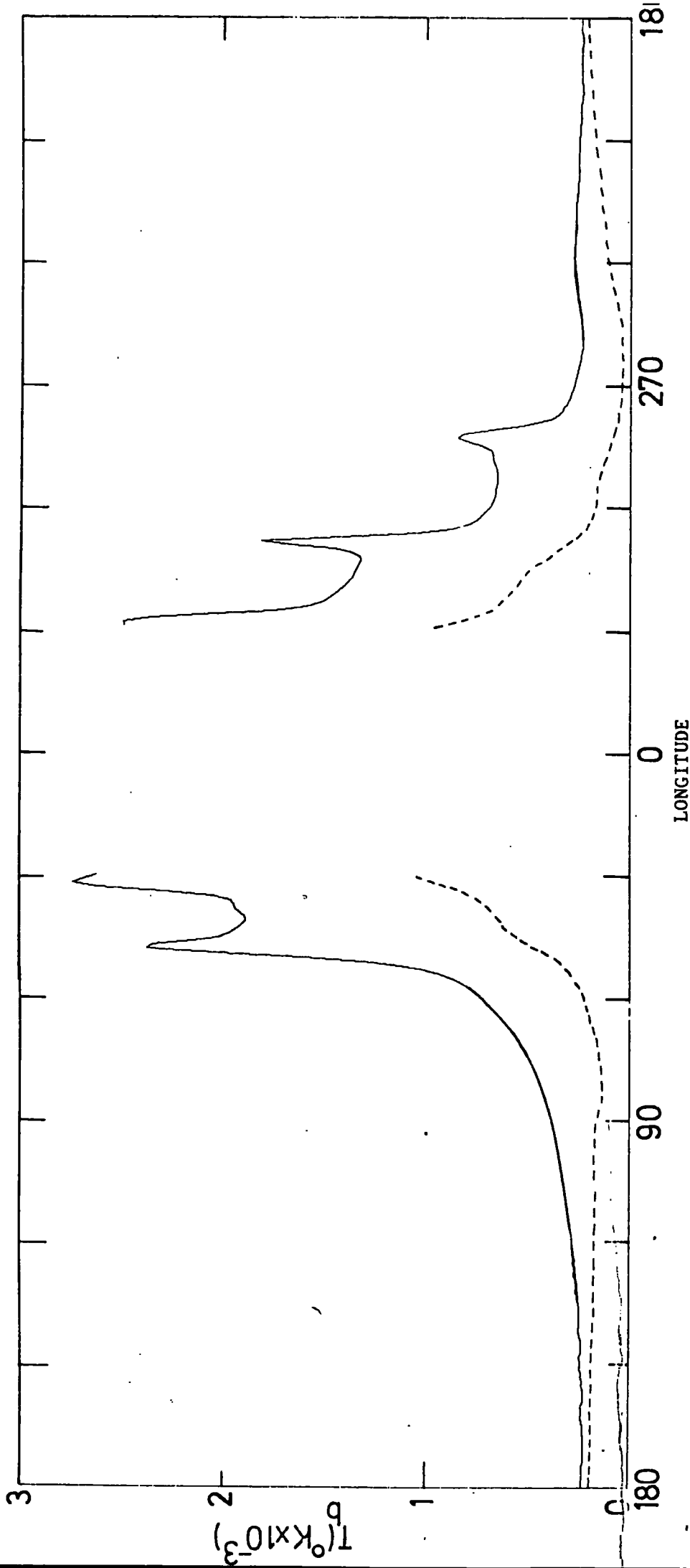
Figure 7.5: Decomposition of the profile for Model A.3. into Regular (dashed line) and Irregular (solid line) components.

It is clear that as most of the H_{II} regions investigated by Caswell lie at distances equal or greater than 0.5 kpc from the sun the introduction of suoh an arm in this region will greatly inorease the foreground temperature and therefore the implied local emissivity. The value of R_O^2 for this model as oompared with model A.2 is reduced as the extra arm significantly increases the emission in the anticentre direotion. The parameters required for a fit of Model A.3 are $R_O^2 = 131$ and $F = \emptyset.75$. The introduction of such a looal spiral arm is still oonsistent with the observations of the Orion arm presented in ohapter 4. Direot comparison between the calculated and observed temperature in front of the H_{II} regions will be made when the results for the final three dimensional models have been presented.

Figure 7.4 presents for Model A.3 the way in which F and R_O^2 vary with I_O such that the calculated longitude profile agrees with observation at the two normalisation longitudes. If a smaller value of I_O, less than 80 $(m^2. s. sa. GeV.)^{-1}$ is accepted as being oonsistent with observation then a smaller value of F is required to oompensate, i.e. more irregular field is required. The resulting value of the looal emissivity differs only marginally from the value obtained for $I_O = 80$ $(m^2. s. sa. GeV.)^{-1}$. For a larger I_O a larger value of F is required, i.e. more regular field. Figure 7.5 shows the oontribution to the resultant longitude profile for model A.3. from the regular and irregular oomponents of the magnetio field. The irregular component is the component that shows the tangential directions to spiral arms whereas the regular oomponent only shows a fairly smooth inorease towards the galactic centre as long lines of sight passing through spiral arms are compensated by Θ being near zero. This regular component is equivalent to Price's (1974) base disc oomponent. (seotion 7.1.1.).

7.3.3. Model B.

For the situation where the eleotron density is assumed to be modulated in proportion to the magnetic field squared many looations of the sun are
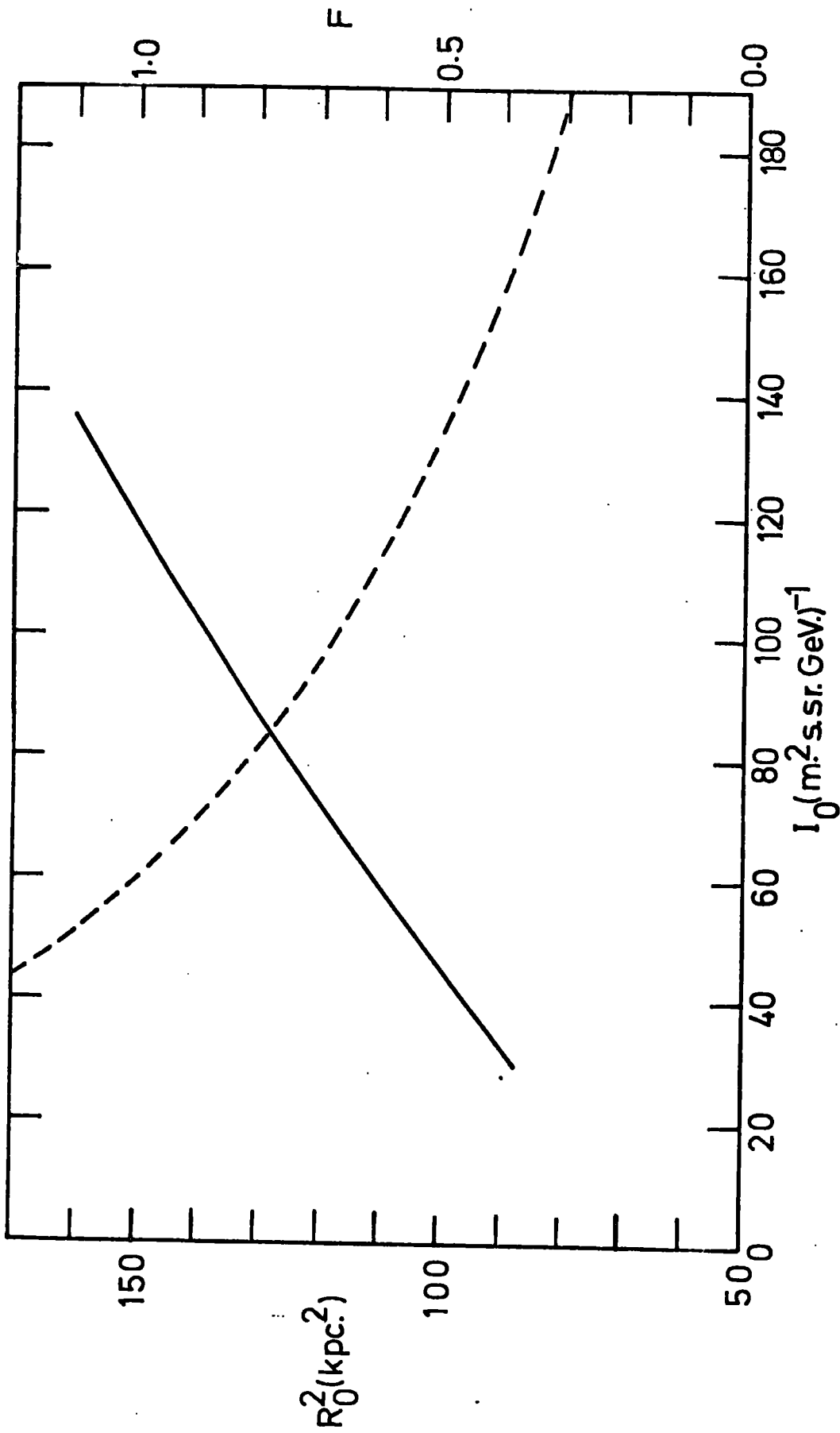
Figure 7.4: Variation of R_o^2 (dashed line) and F (solid line) with I_o for Model A.3.
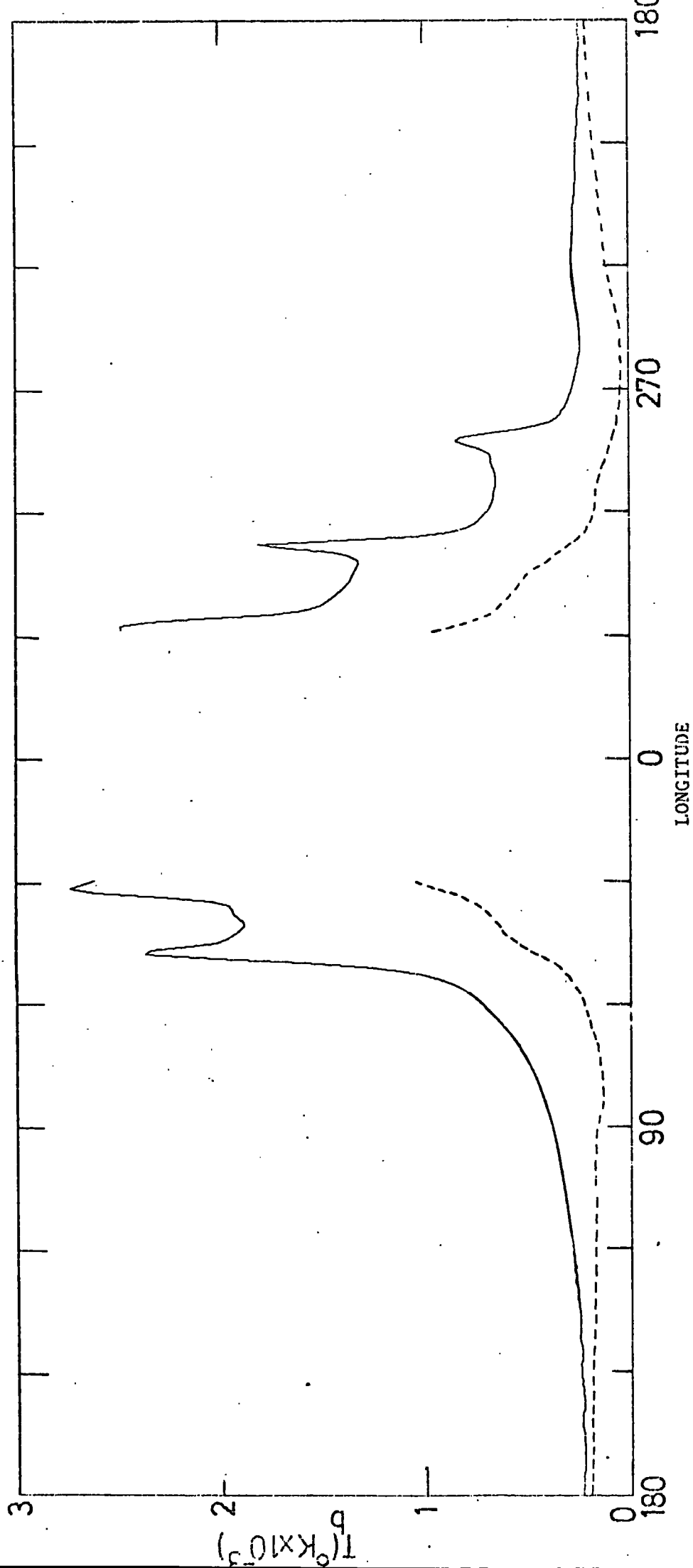
Figure 7.5: Decomposition of the profile for Model A.3. into Regular (dashed line) and Irregular (solid line) components.

eliminated as no physical fit to the normalisation longitudes exists. If the sun is in an arm of full compression a fit is only possible for an irregular field component approximately 100 times greater than the regular component producing, as to be expected, a longitude profile that is dramatically more angular than the observed profile. For the sun in an interarm region no physical fit is possible, i.e. for a fit F is negative. The only possible fits are for the sun in an arm of small compression. Figure 7.6. presents the best fitting profile which has the sun in an arm of compression k = 1.7 with R_o^2 = 327 and F = 1.1. This fit is seen still to be rather too angular. This is of course due to the fact that the emissivity is now varying as $H^{3.8}$ causing the arm emission to be considerably greater than that from Model A. The peaks at $\ell^{II} \approx 80_o$ and $\ell^{II} \approx 260^o$ are due to the tangential directions to the local arm that was introduced such that peaks were produced at these longitudes. In the following sections it will be shown that Model B is inconsistent with the high latitude observations thereby rejecting the hypothesis that I_o is proportional to H^2.

Before continuing to the 3 - dimensional models it should be noted that the profiles so far presented have been arrived at by an .iterative procedure. They have all been convolved in ℓ^{II} and b^{II} in agreement with the observational beams assuming the final Z dependance as derived in later sections. Model A.3 is used as the basis for all the 3 - dimensional models that are now going to be discussed. The parameters characterising the various 2 - dimensional models are summarised in Table 7.3.

7.4. Results of the 3 - D Model Calculations.

7.4.1. Model B.

A model in which the sun has to be located in a spiral arm, such as Model B, runs into severe difficulties when the emission at high latitude is considered. If the demodulation of the spiral arms with height above
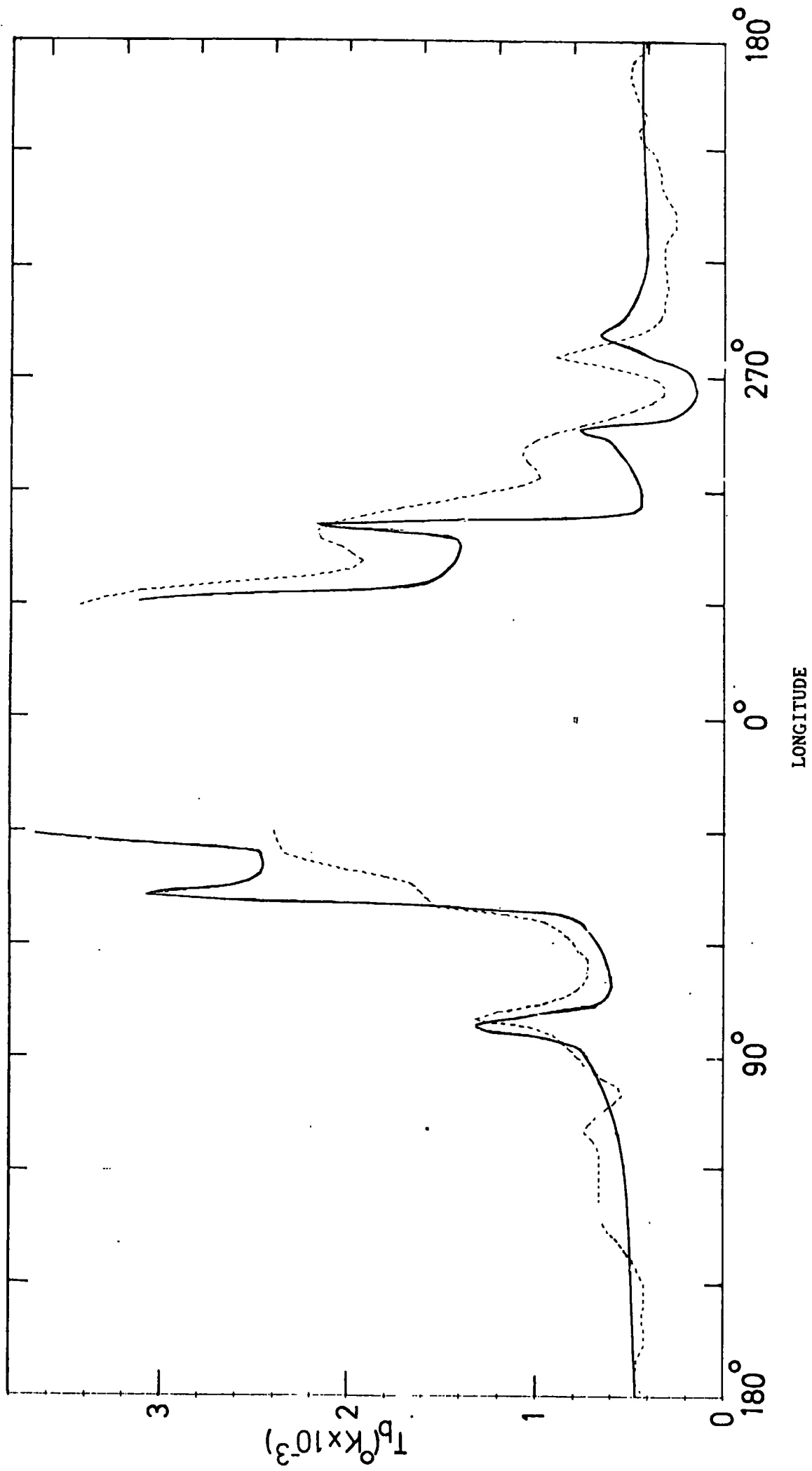
Figure 7.6: Longitude profile for Model B.

T A B L E 7.3

Model	Location of the Sun	R_o^2	F	$\mathcal{E}_\nu$ (local)
A.1	In an arm of compression k = 1.7	249	0.375	144K kpc^{-1}
A.2	In an interarm region	195	0.7179	64K kpc^{-1}
A.3	In an interarm region with a local arm at 0.5kpc towards the anti-centre.	131	0.75	62.5K kpc^{-1}
B	In an arm of compression k = 1.7	327	1.1	45.7K kpc^{-1}

the plane is given by figure 4.17. the emissivity at 0.5 kpc above the
plane, even if the electron density is kept constant, is only 6 K kpc^{-1}.
Since the emission within 0.5 kpc of the plane is only 11.5K this leaves
a further 158.5K to be obtained from high$^{\pi}$emission such that the
calculated pole temperature agrees with the observed value of 170K.
(after 50K extragalactic has been taken into account). Therefore for
Model B a uniformally emitting halo with a line of sight of 26.4 kpc in
the direction b^{π} = 90° is required to obtain agreement with observation.
Such a vast halo seems highly improbable. Model B is therefore rejected
as a viable model for the distribution of electrons in the galaxy.

7.4.2. Model A.

In all the following the demodulation of the spiral arms with height
above the plane is assumed to be that given in figure 4.17.

7.4.2.1. Model 3D 1

This model assumes that the electron density falls linearly with
height above the plane as suggested in chapter 2 from a simple one
dimensional diffusion approximation. The magnetic field is assumed
constant at the value in the plane for interarm regions. An equivalent
half width of 2.75 kpc is required to obtain agreement with the
observed pole temperature. For a linear fall-off this requires the
electron density to fall to zero at a height of 5.5 kpc above the plane.
Figure 7.7 shows the predicted contour plot of the distribution of
brightness temperature for this model after the addition of spur
emissions, according to Van de Laan, and an extragalactic background of
50°K. To facilitate comparison with the Landecker and Wielebinski all
sky map figure 7.8 a -f shows latitude cuts for various longitudes
across figure 7.7 in comparison with the Landecker and Wielebinski data.
These cuts have been excluded from the region 60° - 150° as this region
is known to be confused by source complexes. It is clear from these
profiles that for longitudes ℓ^{π}> 270° and ℓ^{π}< 90° the predicted
profiles are too broad for $/b^{\pi}/ > 5^o$.   For the remaining longitude
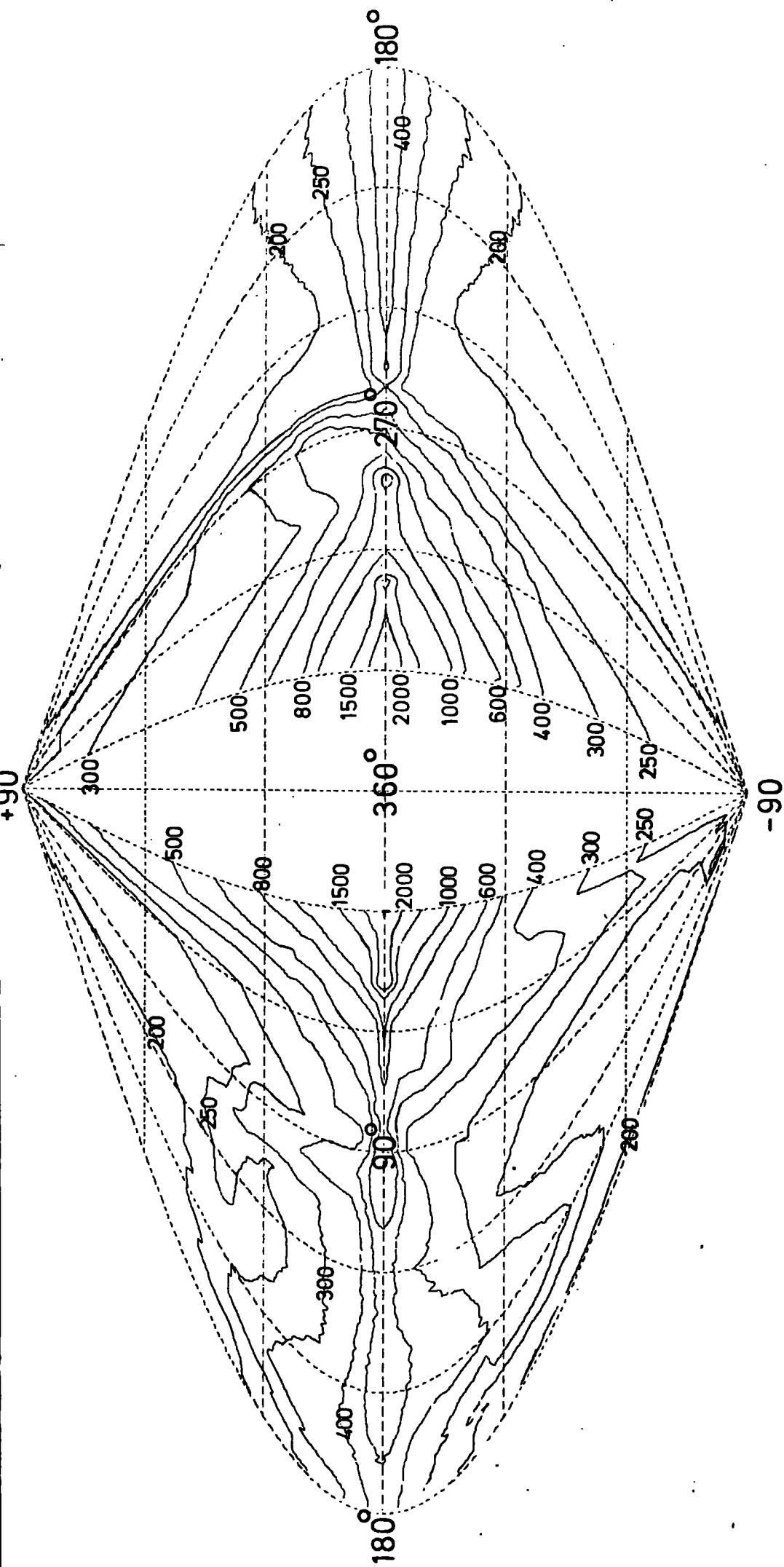
Figure 7.7: Distribution of brightness temperatures (°K) for Model 3D 1 presented on a sinusoidal projection similar to that used by Landecker and Wielebinski in the presentation of their observational data.
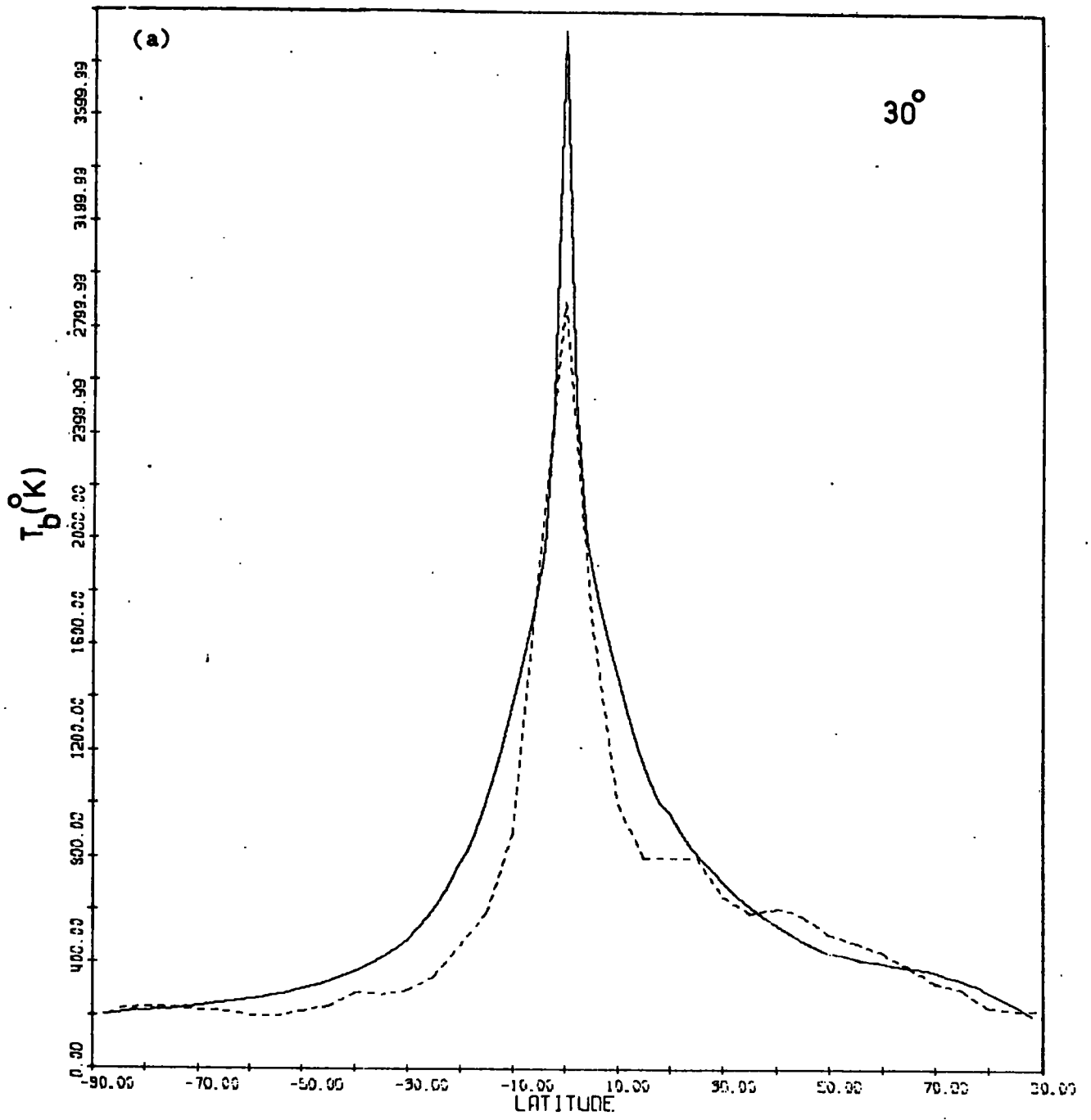
Figure 7.8: Latitude cuts across figure 7.7 for various longitudes.
The dashed lines represent the observations.
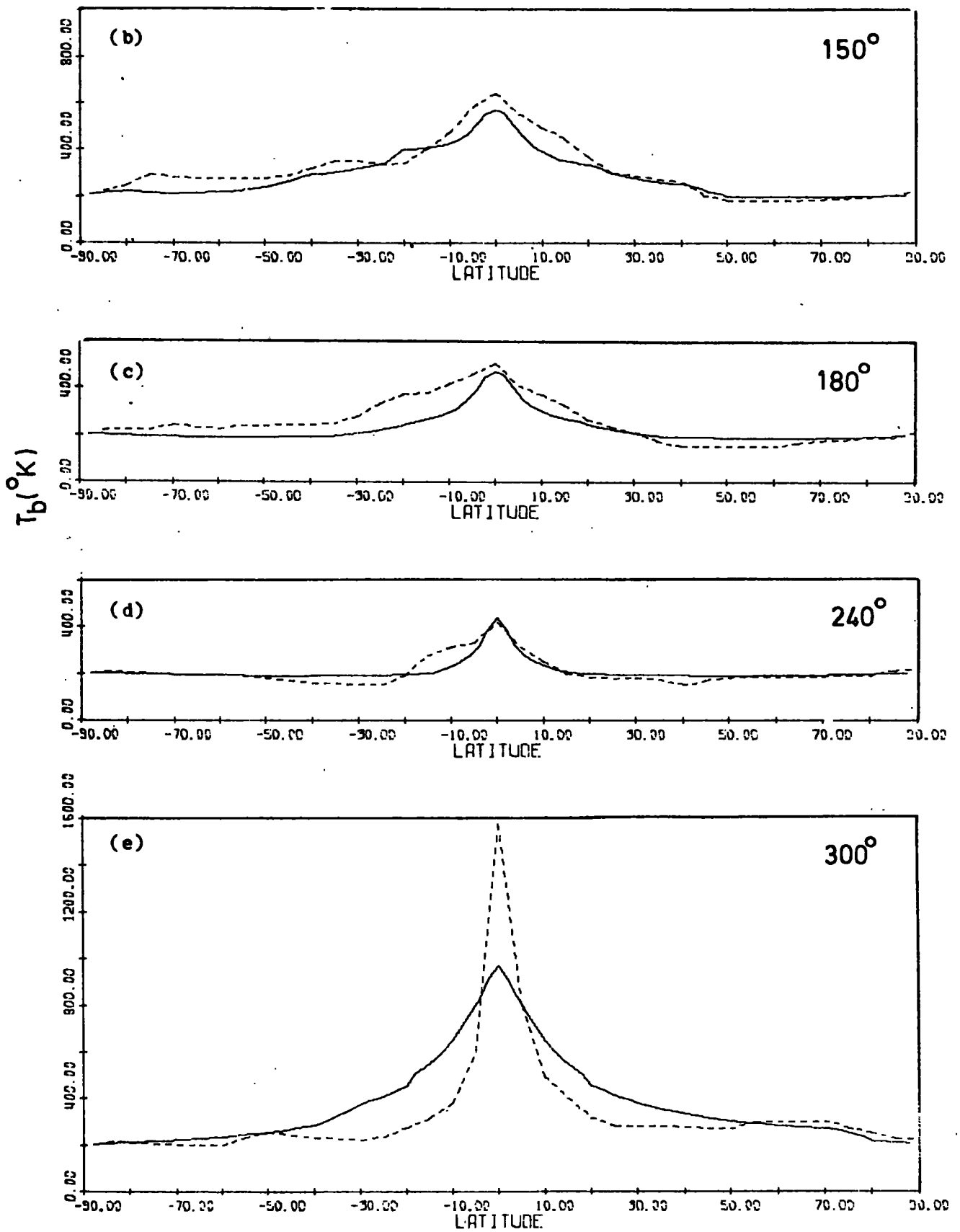
Figure 7.8 cont.
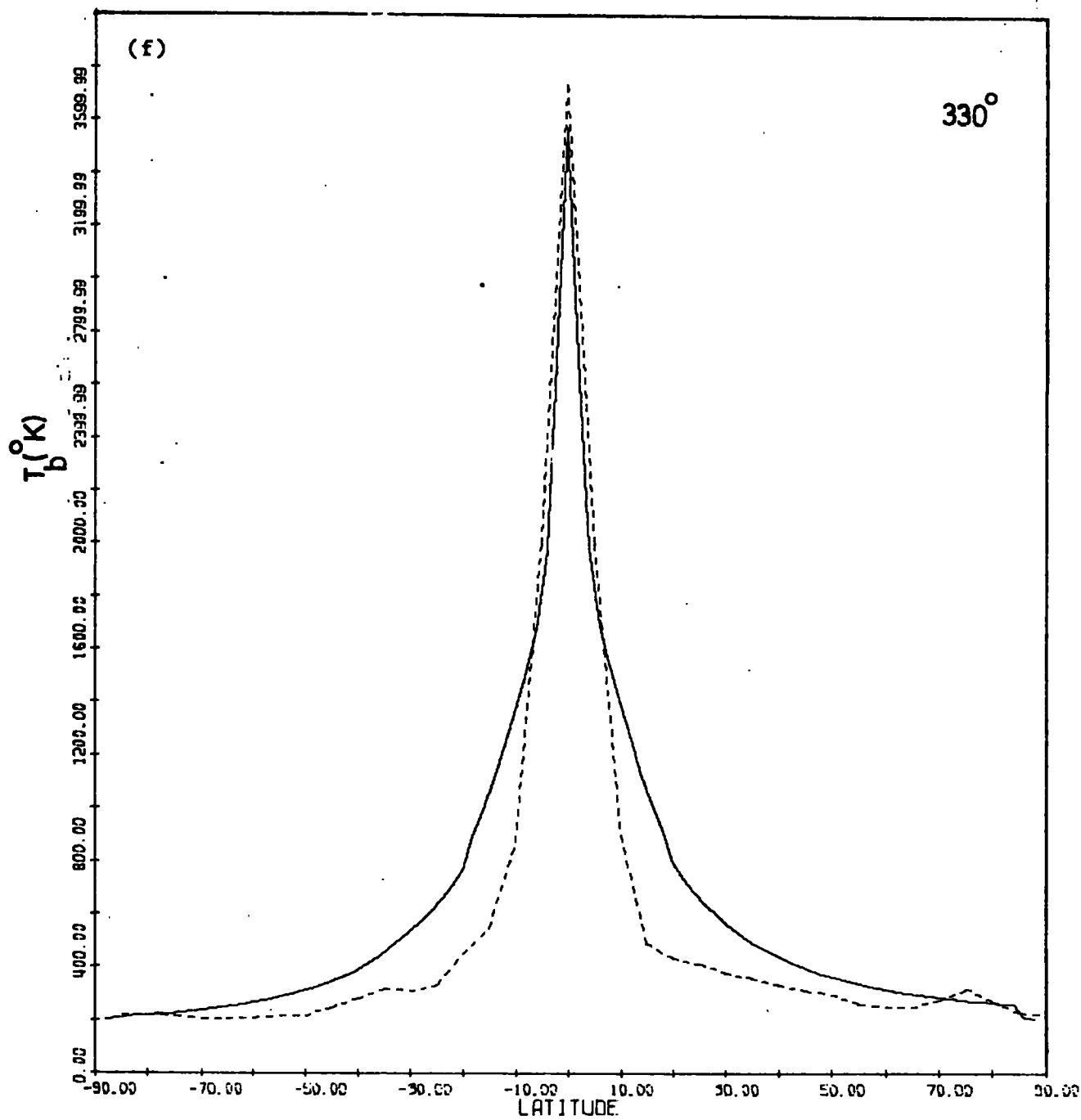
Figure 7.8 cont.

range the fit is reasonable. To decrease the emission occurring at intermediate latitudes the width of the emissivity disc needs to be decreased. The thickness of the spiral arms in Z only affects the profiles for $|\ b^{II}\ | < 5^o$.

7.4.2.2. Model 3D 2.

The width of the emissivity disc at the earth cannot be decreased as the pole temperature and local emissivity are fixed. One therefore needs to postulate that the width of the emissivity disc decreases as one approaches the galactic centre in order to narrow the latitude profiles for directions. towards the galactic centre. As discussed in chapter 3 section 3.3.2 the scale height of the neutral gas is observed to decrease for R < 10 kpc and increase for R > 10 kpc (Jackson and Kellman 1974). Figure 3.4 shows that in the limit $2\overline{z_{\frac{1}{2}}}$ decreases to half its value at the sun at 4 kpc from the galactic centre and increases to twice its value at the sun at 15 kpc. Such a variation may be represented by the polynominal.

$W (R) = W_{sun} (0.591 - 0.0652R + 0.0106R^2)$ 7.1.   where R is the galactocentric distance and Wsun is the width, scale height, of the distribution at the sun, R = 10 kpc and W(R) is the width corresponding to a radial distance R. It is possible to argue that if the magnetic field is tied to the gas and in their turn the electrons are tied to the field then it might be expected that the width of the electron distribution would decrease with decreasing R in a similar manner to the way in which $2\overline{z_{\frac{1}{2}}}$ for the gas decreases. Here one is extrapolating rather as the width of the gas is only a few hundred parsecs whereas the electrons have a width of several kiloparsecs. If equation 7.1 is applied to Model 3D 1 then the results presented in fugures 7.9 a - f are obtained for Model 3D 2. As can be seen from figure 7.9 the introduction of such a fluting of the emissivity disc has indeed narrowed the profiles for $\ell^{II} = 30^o$ and 330° when they are compared with figures 7.8a and 7.8f respectively.
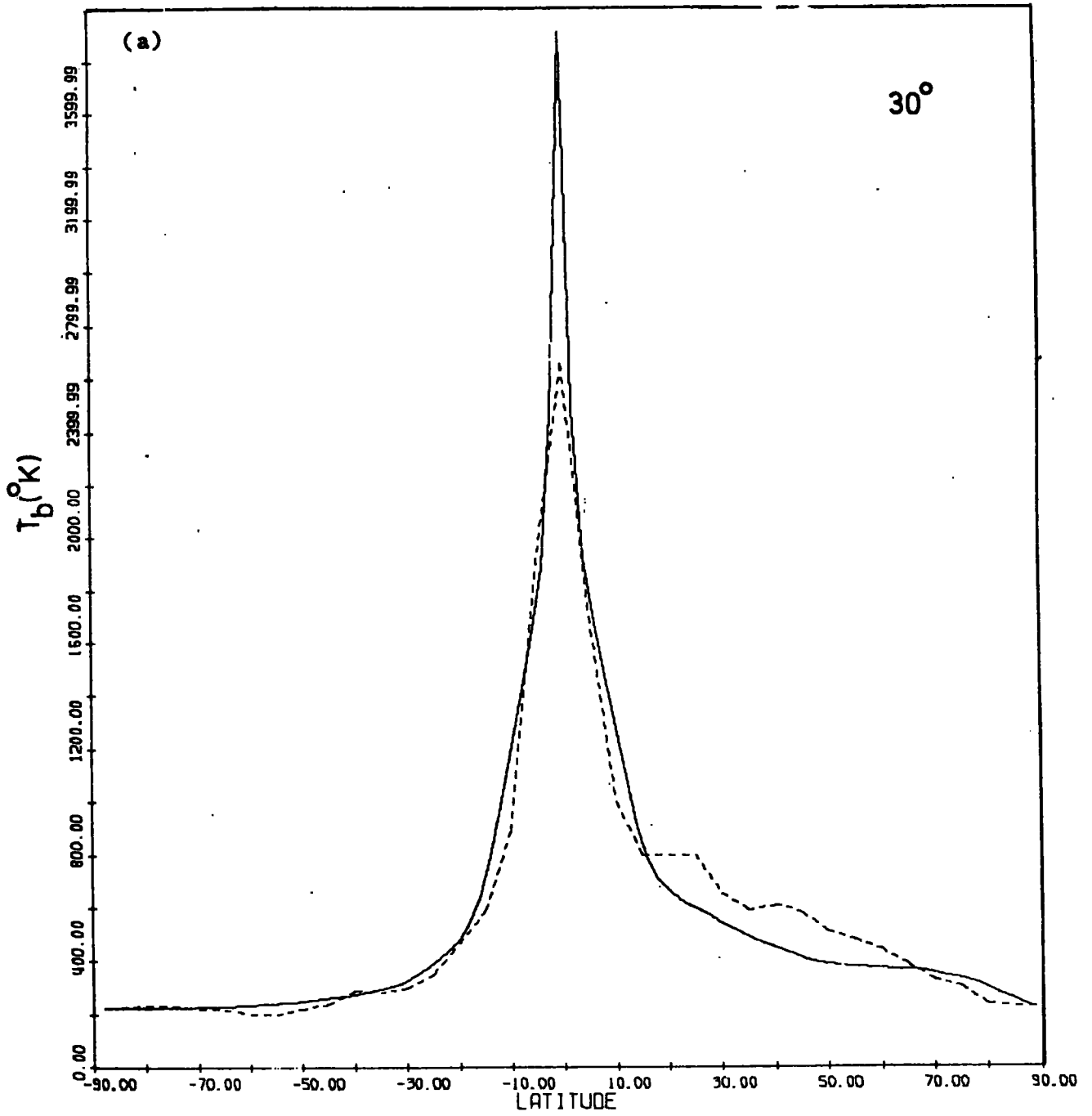
Figure 7.9: Latitude cuts for Model 3D 2.
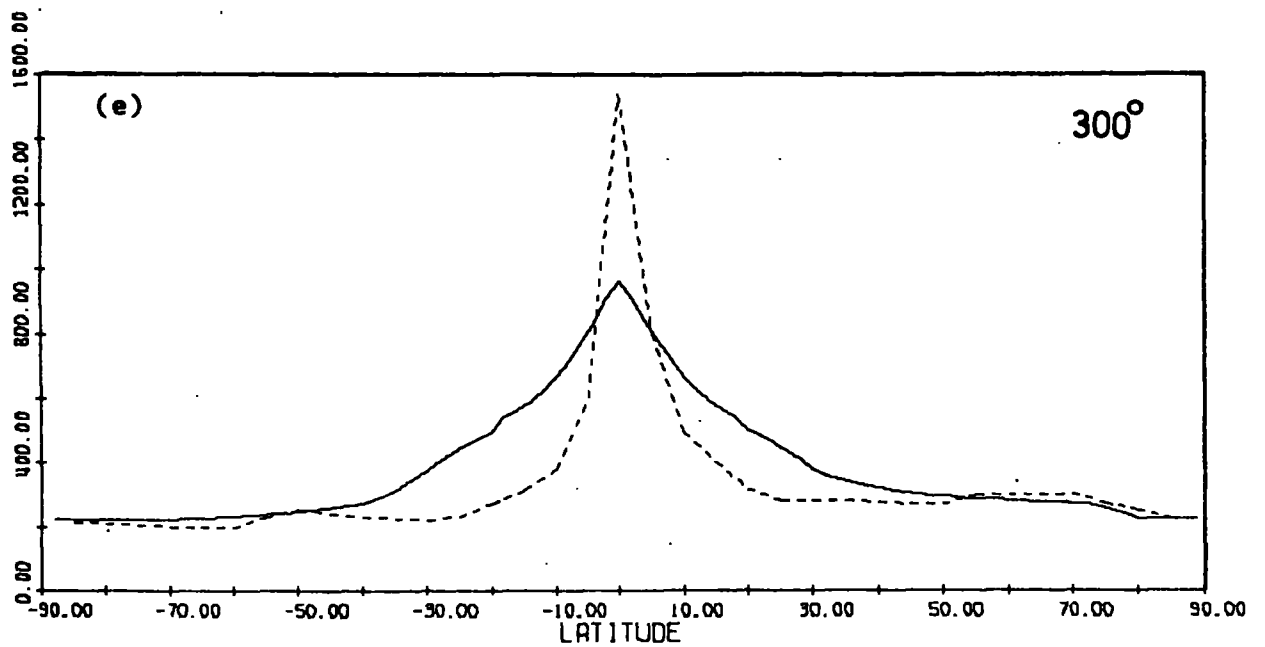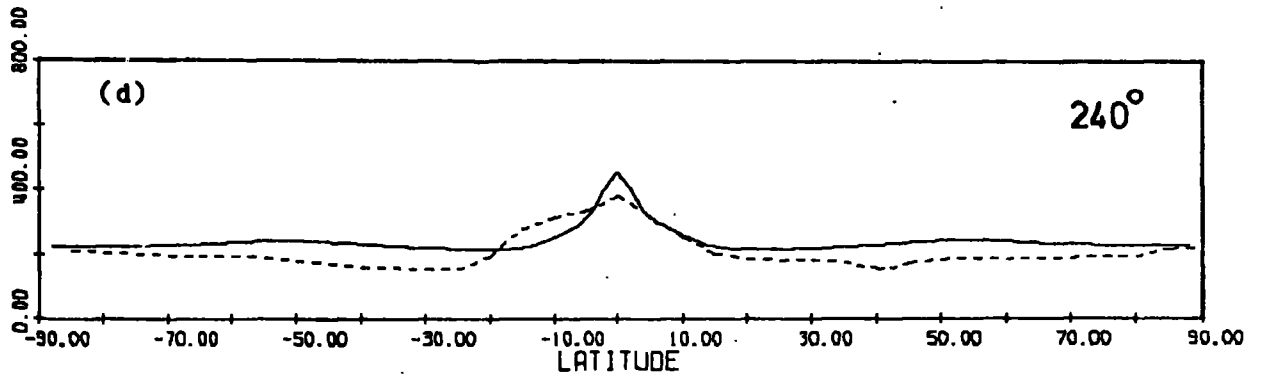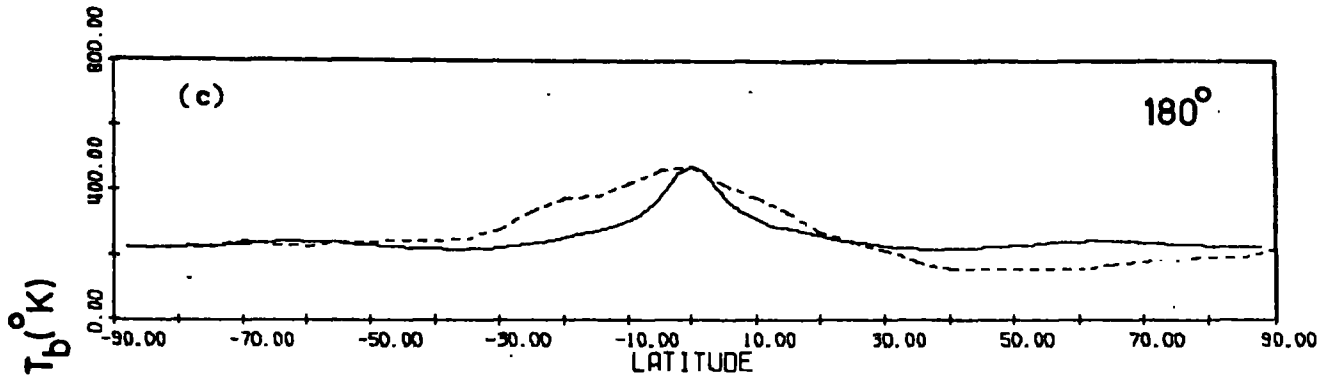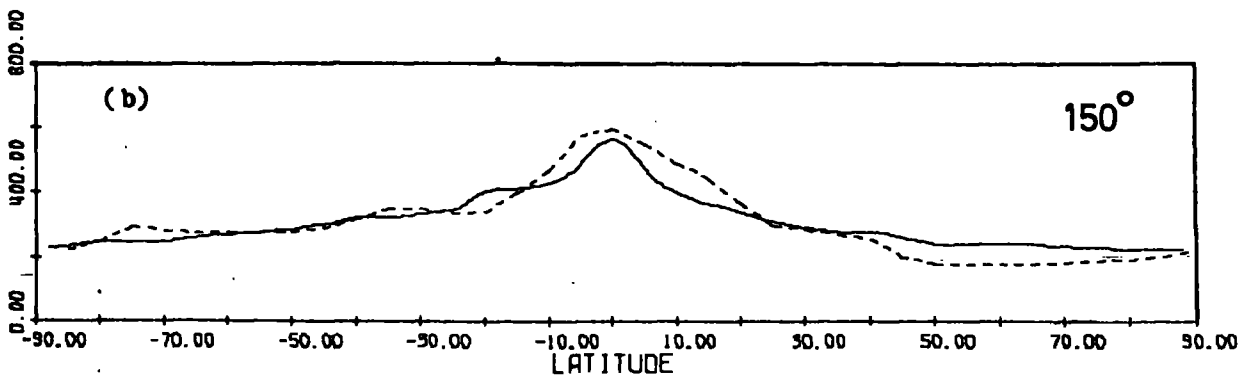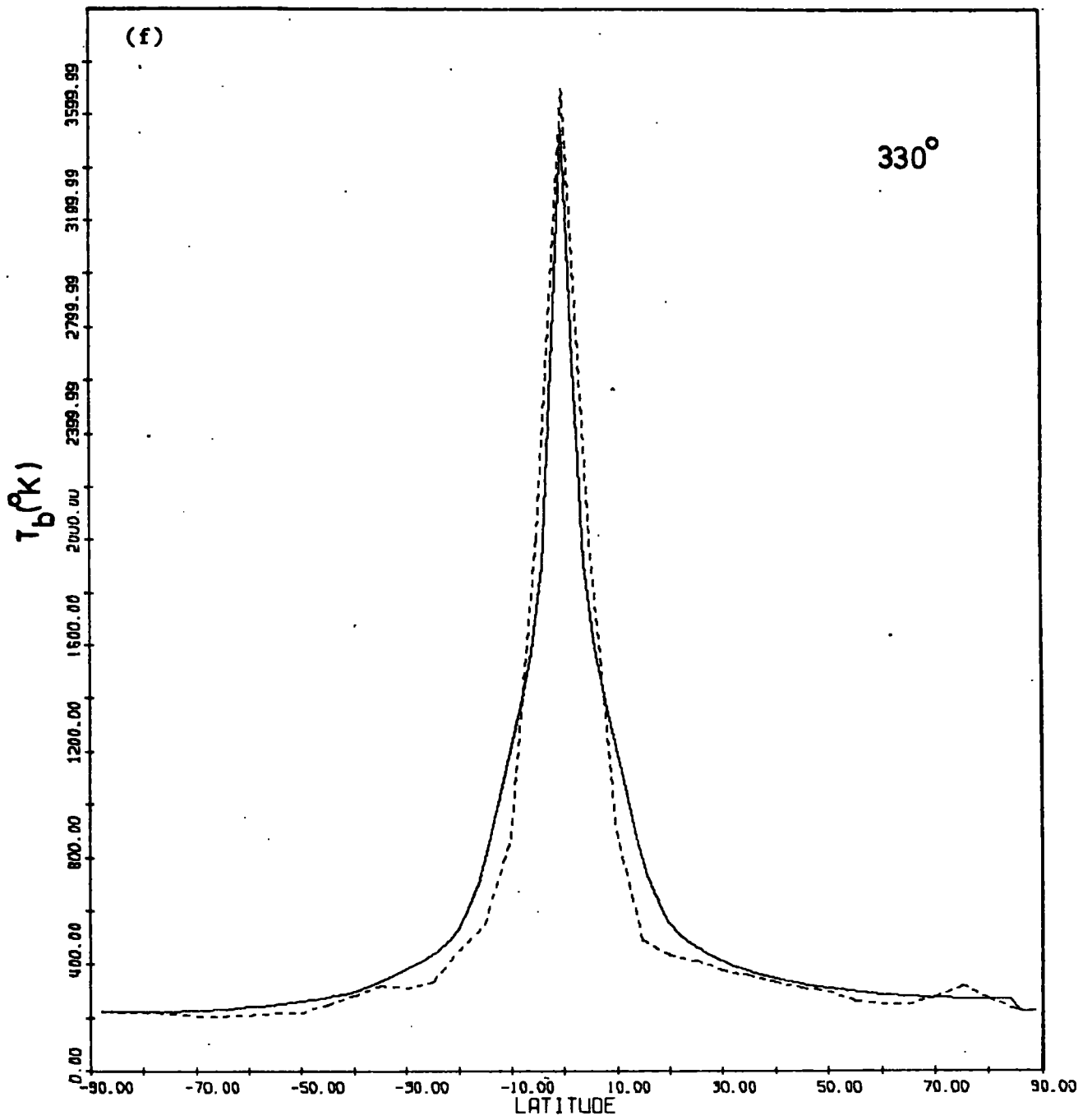
Figure 7.9 cont.

For the profiles $\ell^{II} = 150°$, $180°$ and $240°$ the agreement is still fair but the emission from latitudes between $|30°|$ and $|80°|$ now seems to be above rather than below the observations. This is due to the emissivity disc increasing in thickness for R $>$ 10 kpc. The $\ell^{II} = 300°$ profile is still much broader than the observations. This is due to the fact that for this longitude the closest distance of approach to the galactic centre is only 8.6 kpc and therefore the width of the Z distribution of electrons has not changed significantly from 5.5 kpc. (W(8.6 kpc) = 4.5 kpc).

Before considering further variations of the electrons distribution it is worthwhile investigating the effect of a greatly increased extra-galactic contribution.

7.4.2.3. Model 3D 3. This model has the same electron distribution as the previous model but with an extragalactic contribution of 100K instead of 50K. Although this is at variance with observation it is instructive to consider this situation as the possibility exists that the sun has some emission region close by it which gives the effect of a further isotropic component. This will also give some indication of the effect of a very large diffuse halo on the latitude profiles. As the extragalactic contribution has been increased it is necessary to renormalise the 2-dimensional disc model. The new parameters are found to be $R_o^2 = 114$ and $F = \emptyset.77$ resulting in a local emissivity of $60°K$ kpc^{-1}. The profile is not significantly different from the profile presented for Model A.3 and will not therefore be presented here. The temperature required at the pole resulting from galactic emission is now reduced to 120K and therefore an equivalent thickness of 2 kpc is required for consistancy with observation. The half width of the emissivity distribution at the sun is therefore decreased to 4 kpc. Figure 7.10 presents the results for model 3D 3. The profiles appear flatter for
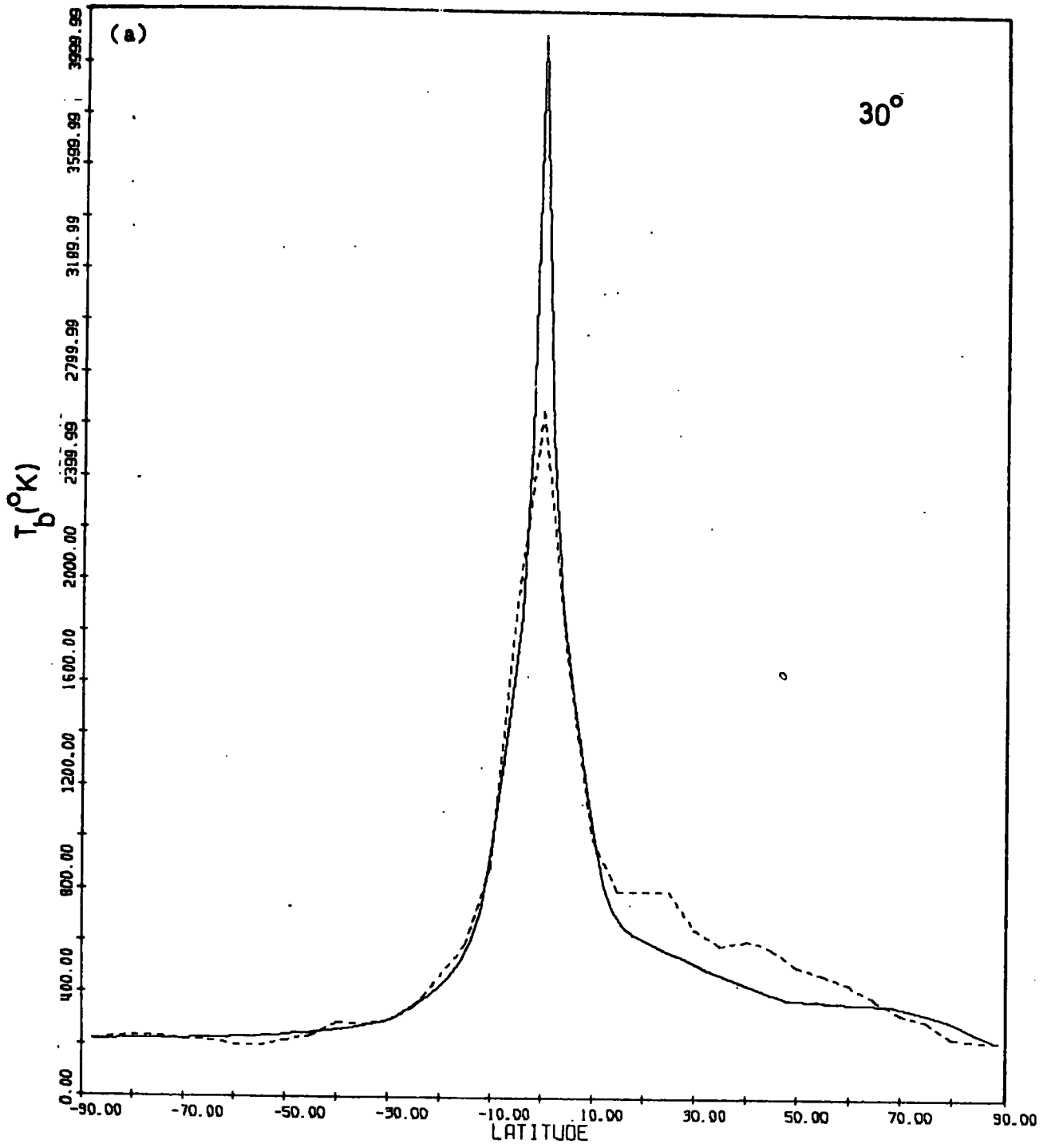
Figure 7.10: Latitude cuts for Model 3D 3.
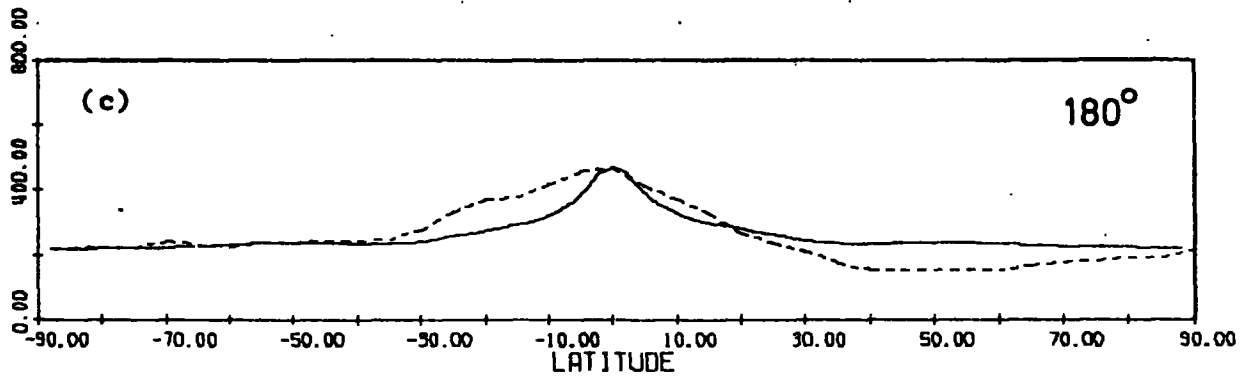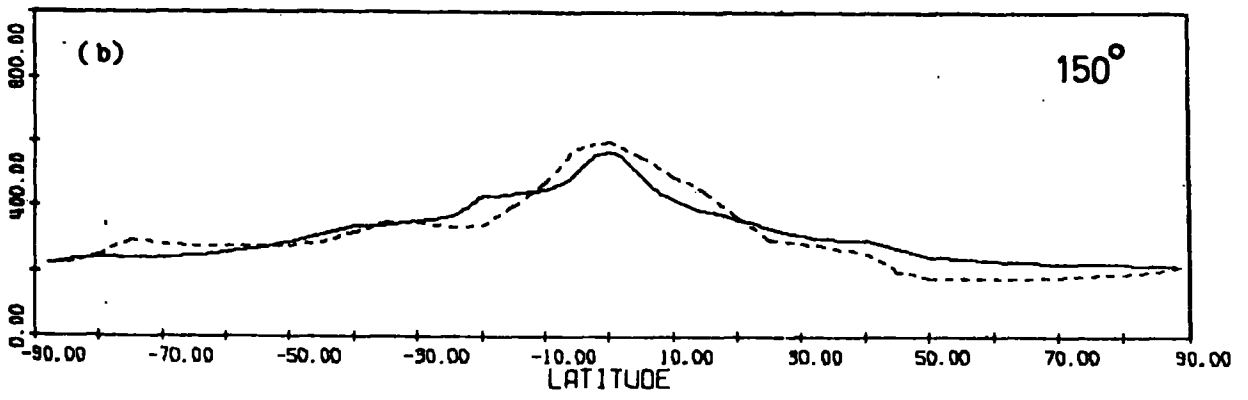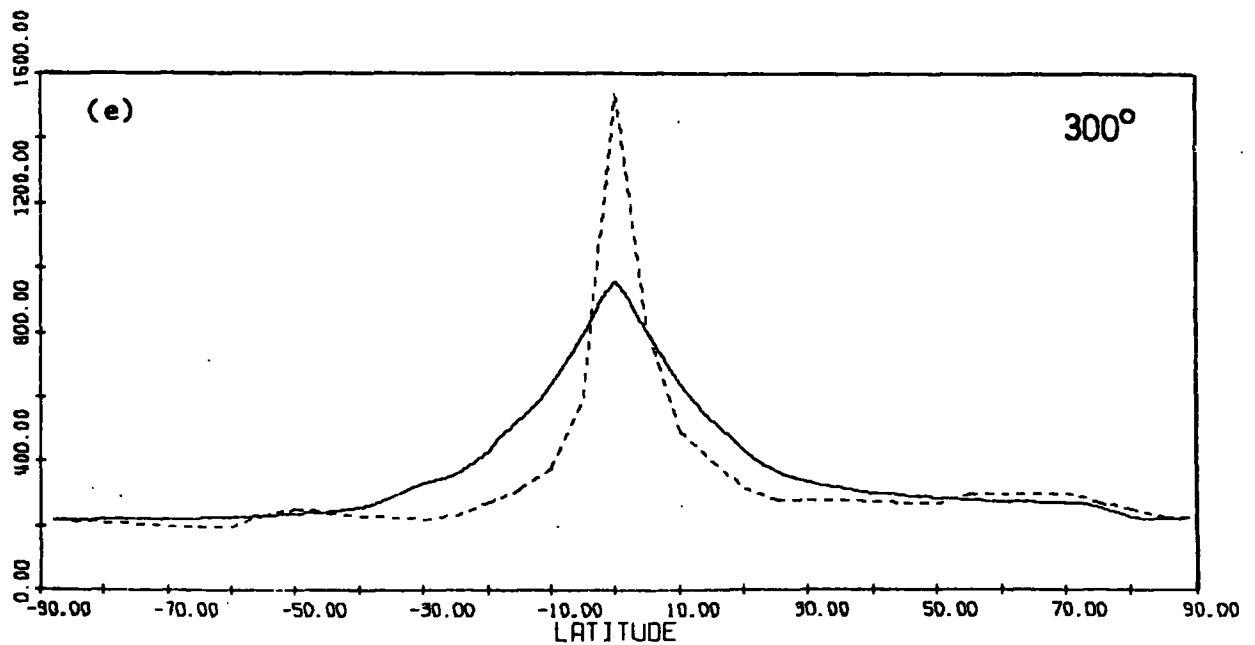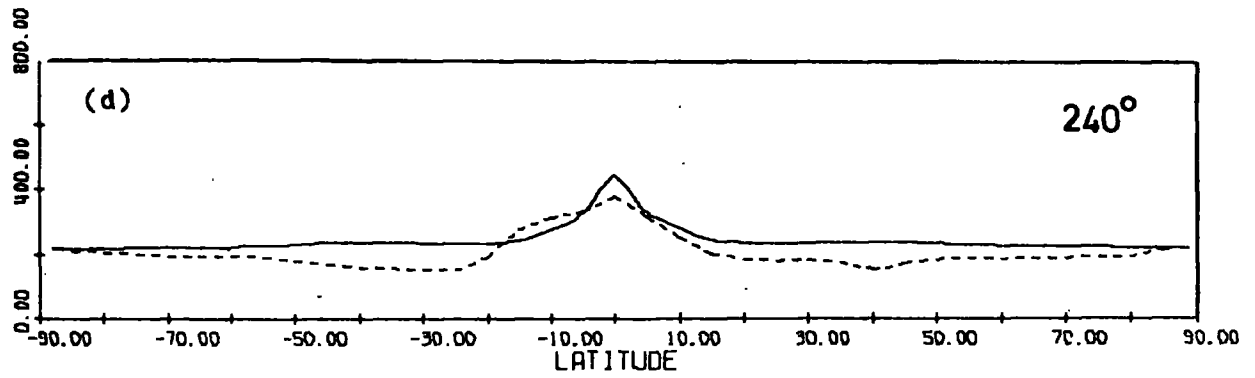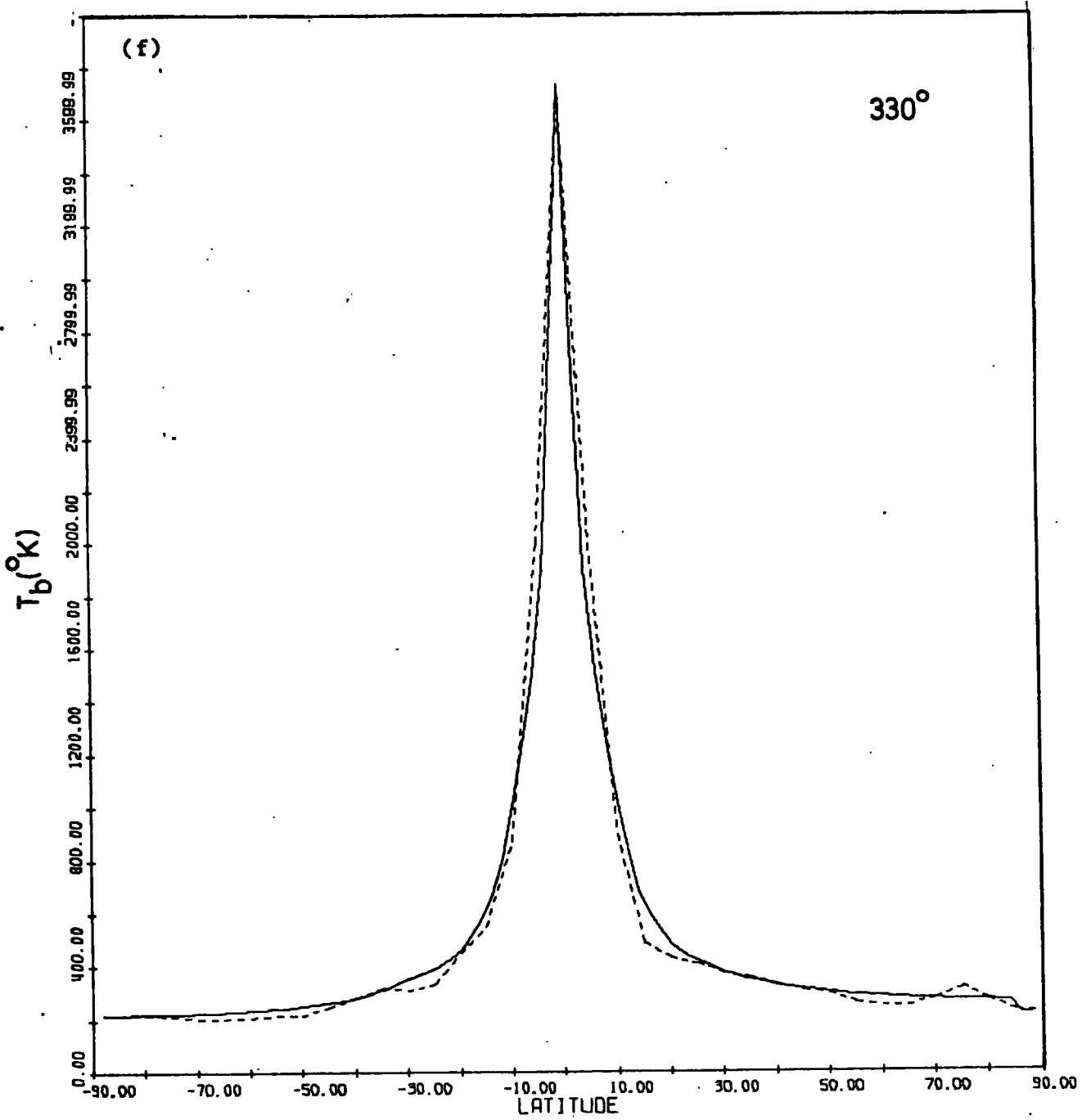
Figure 7.10 cont.

intermediate and high latitudes as would be expected. The fits at ℓ^{II} = 330° and 30° are slightly improved, the fits for ℓ^{II} = 150°, 180° and 240° are about as good as for Model 3D 2 and the fit at ℓ^{II} = 300° is marginally improved. This fit will be compared with the final fit and discussed in the next chapter. To avoid such an introduction of an extra ad hoc isotropic component further models will now be considered.

7.4.2.4. Model 3D 4

To try and further reduce the emission predicted for intermediate latitudes an exponential decrease of electron density with height above the plane will be considered rather than the presently assumed linear variation. Such an exponential variation might be expected if the mean free path for electron propagation increases with height above the plane. This is in fact probably the situation as the field probably becomes more regular as one moves to larger values of Z due to the supernovae, that produce the large scale randomising of the field, being restricted to the plane of the galaxy and therefore there are fewer irregularities to scatter the electrons thus causing their mean free path to increase with increasing Z . In Model 3D 4 the electron density is assumed to vary according to exp $(-Z/2.86kpc)$ and is truncated at Z = 8.58 kpc. This electron density variation is assumed for all values of R. Figures 7.11 presents the results for Model 3D 4. The fit for directions towards the galactic centre is marginally better than that for a linear fall-off, Model 3D 1, figure 7.7 and 7.8. For directions away from the galactic centre the fit is essentially unaltered. If a varying width to the electron distribution is now introduced a considerable effect on the width of the profiles is to be expected. Before considering such a model a phenomenological halo model will be considered.

7.4.2.5. Model 3D 5. As many previous authors have postulated large uniformally emitting haloes it was thought instructive to consider such a model in the framework of the derived 2-dimensional model, Model A.3.
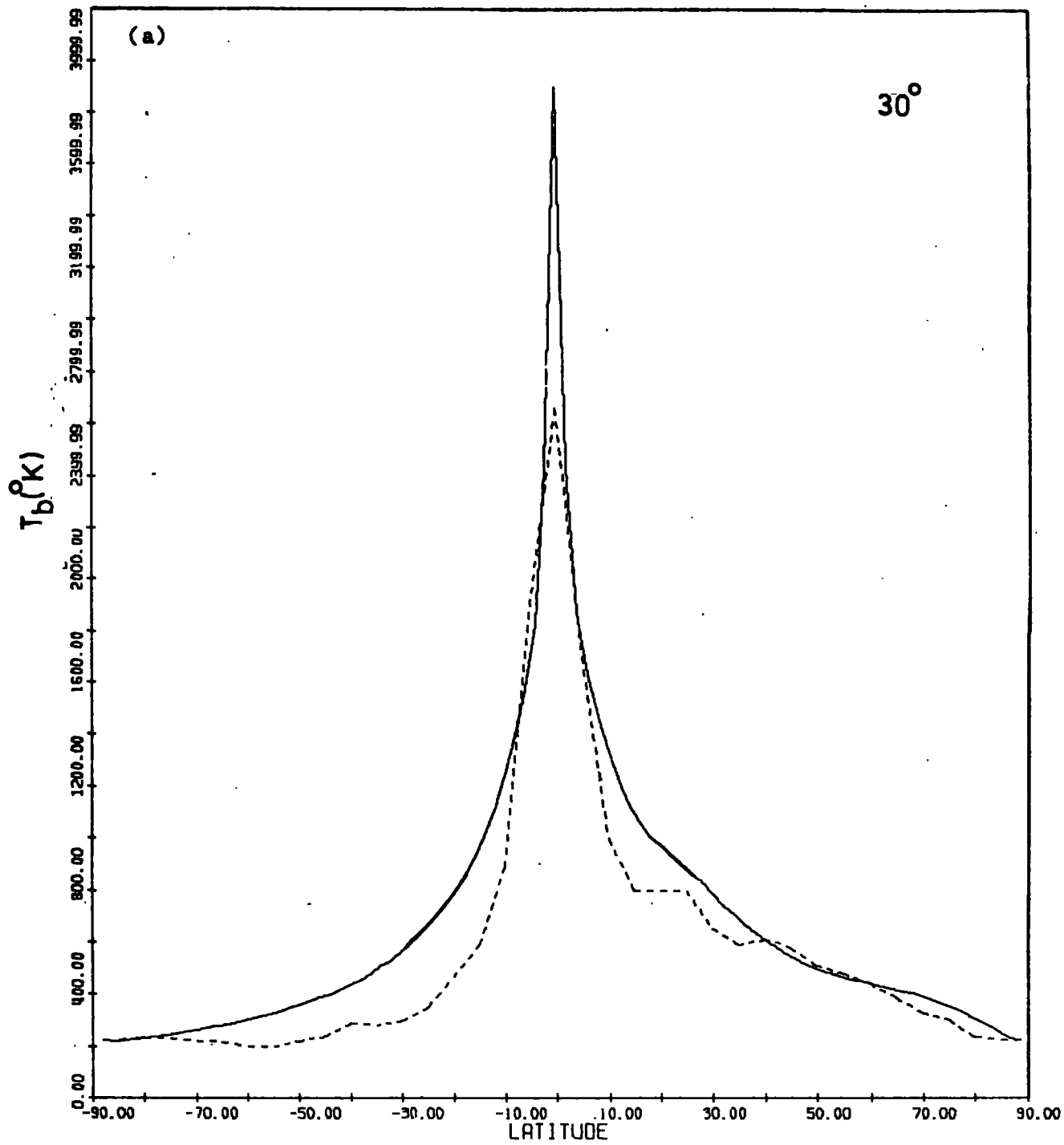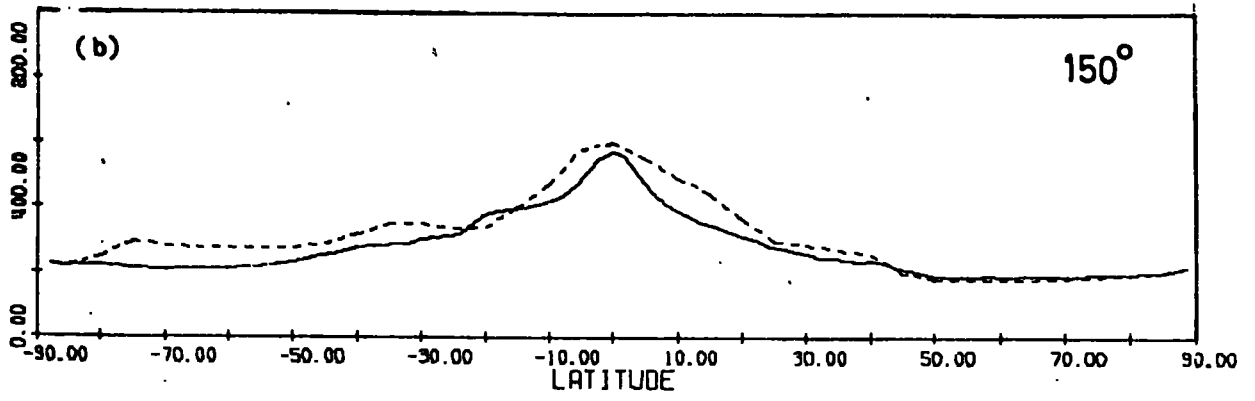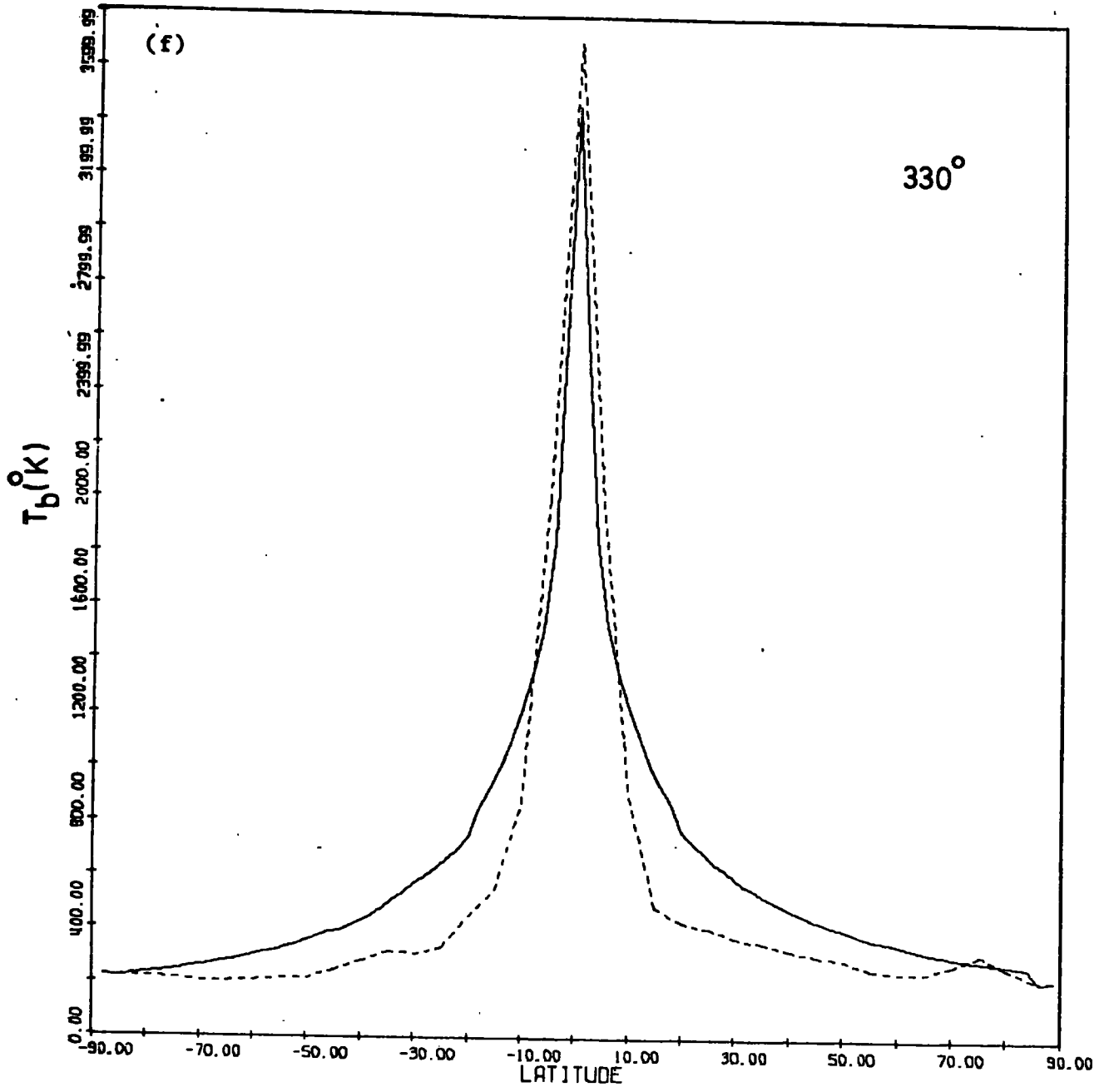
Figure 7.11: Latitude cuts for Model 3D 4.
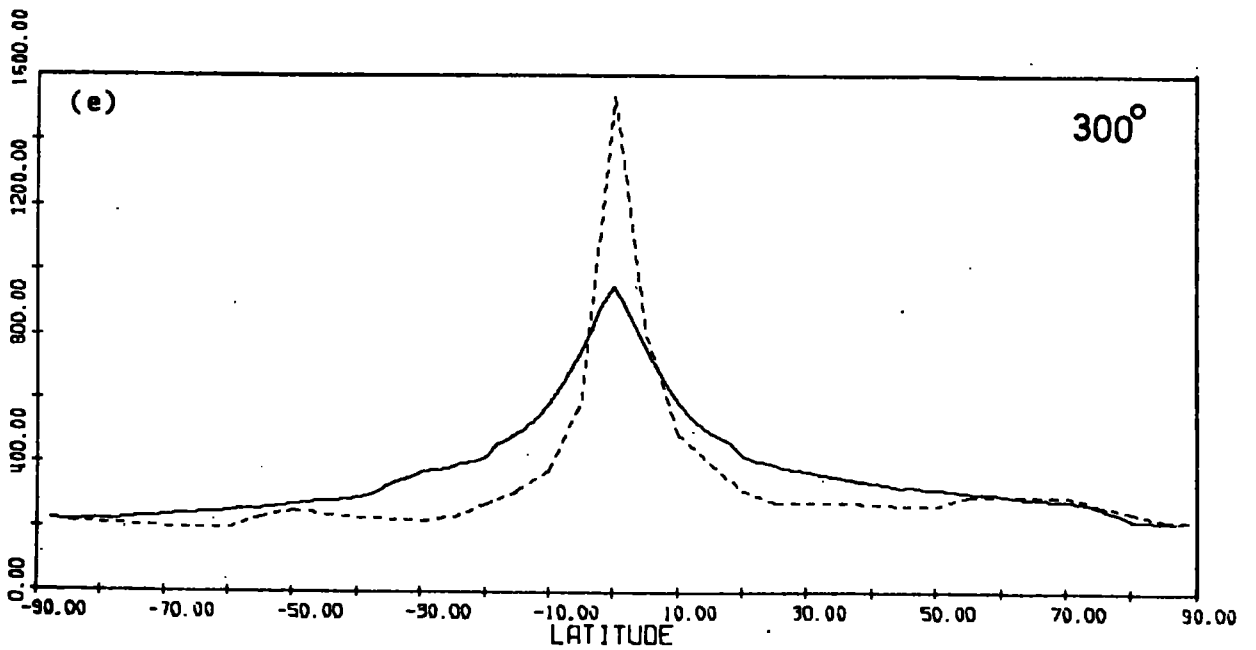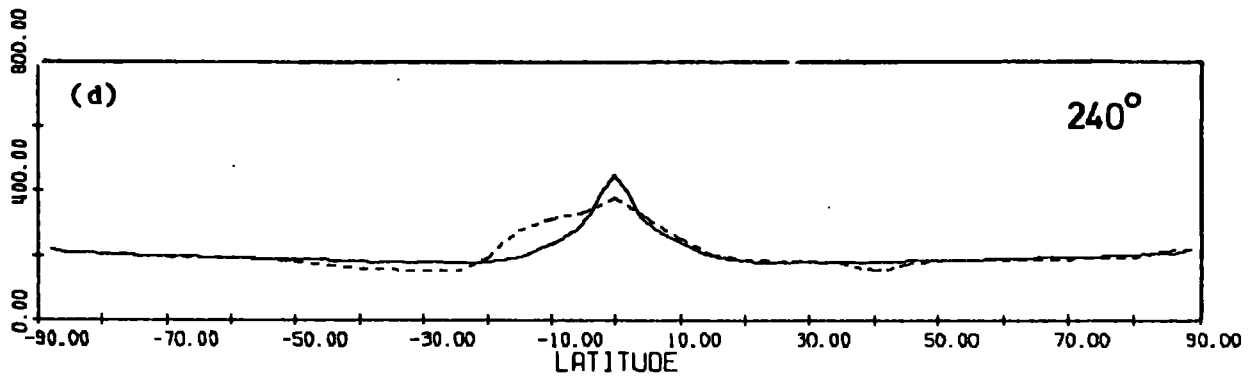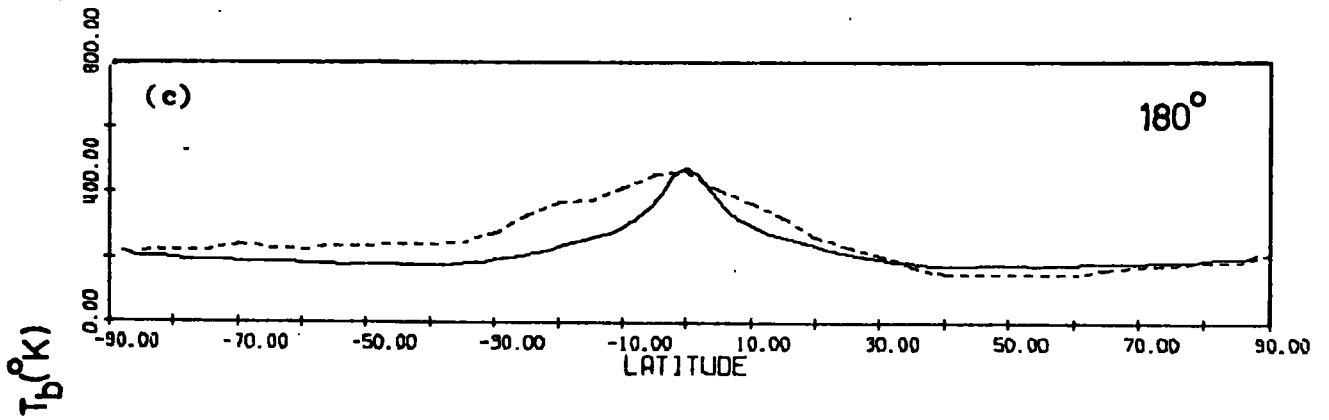
Figure 7.11 cont.

The halo is taken as being spherical centred on the galactic centre with a radius of 15 kpc. The galaxy is assumed to have a disc of half width 1 kpc in which the electron density is constant. For agreement with the pole temperature it is required that the electron density in the halo is 0.169 times that in the disc. Figure 7.12 presents the results from such a model. A uniformally emitting halo is seen to produce several characteristic tracers in the latitude plots. For the directions $\ell^{\pi} = 30°, 330°$ and to some extent $300°$; large quantities of emission are produced for intermediate latitudes causing a large discrepancy between the observed and predicted profiles. This could be reduced but only by the introduction of a much larger, much weaker halo. As discussed for Model B such a large halo is considered unphysical. For the directions $\ell^{\pi} = 150°$, $180°$ and $240°$ a minimum is observed at latitudes of approximately $\pm 45°$. This is characteristic of any large low emission halo. Such a minimum is in fact clearly seen in the observations. The calculated profile at $\ell^{\pi} = 300°$ is in fair agreement with the observations for such a model. A possible way of reducing the intermediate latitude emission for directions towards the galactic centre is by making the halo oblate. The pole temperature must still agree with the observed temperature and this immediately puts a limit on how oblate the halo can be made. In fact making the halo oblate reverts to having a thick disc.

Table 7.4 summarises the various 3-D models discussed in the previous sections.

7.4.2.6. Model 3D 6.

In this, the final Model, the best features of the previous models are combined to obtain a fit to the observational data. The electron density is assumed to fall approximately exponentially with height above the plane with the width of the distribution varying with galactic radius.
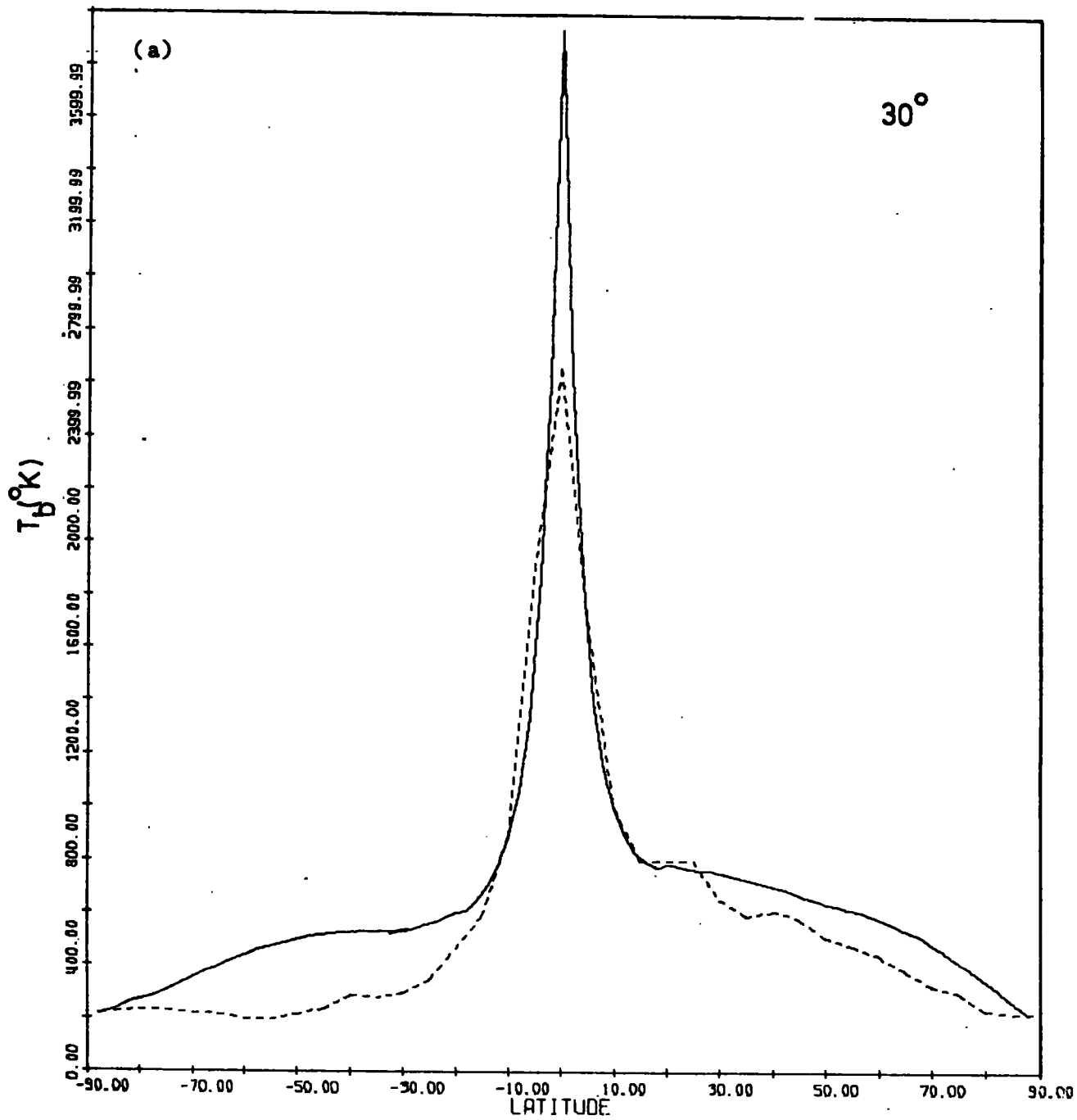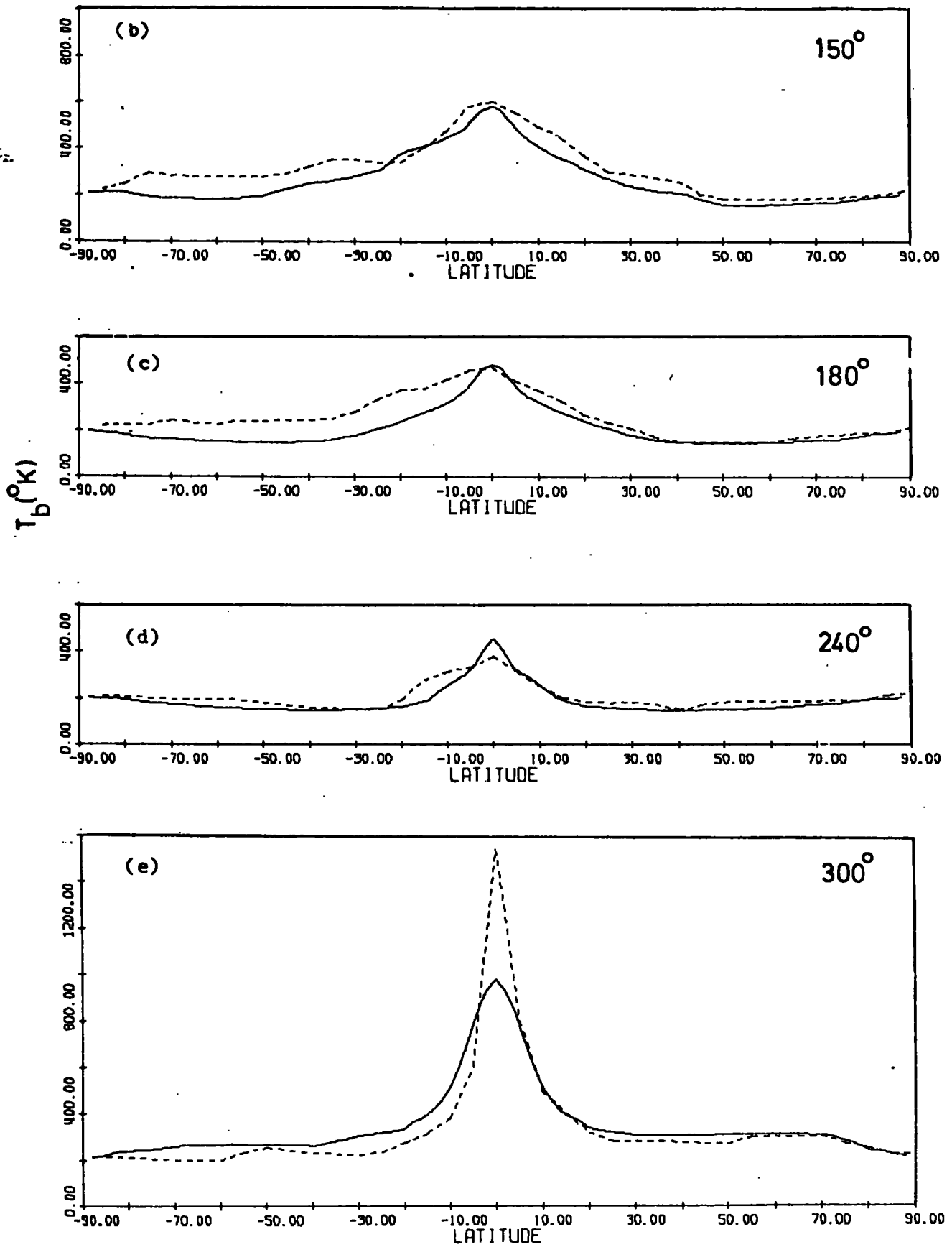
Figure 7.12: Latitude cuts for Model 3D 5.
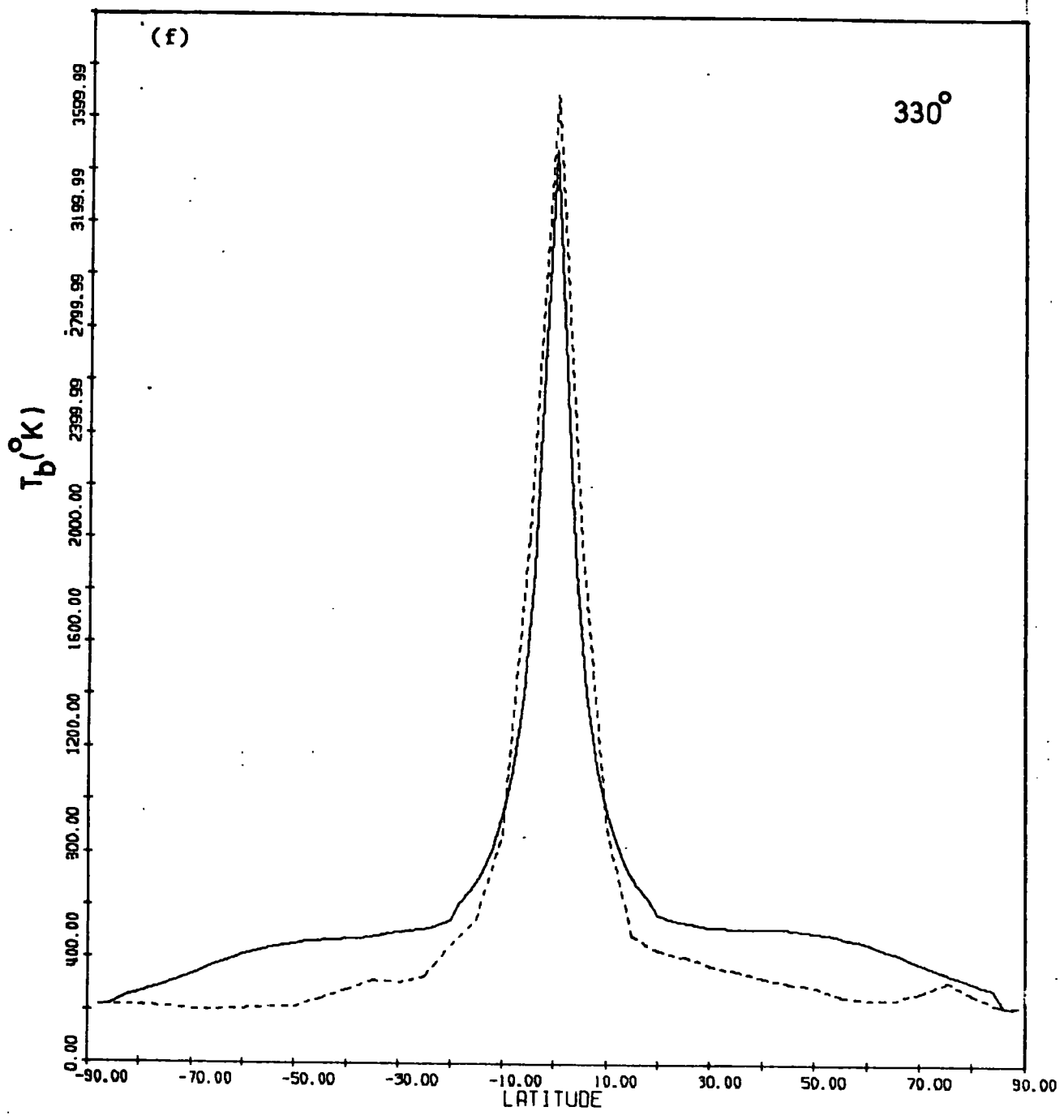
Figure 7.12 cont.

Figure 7.12 cont.

T A B L E   7.4.

Model	Characteristics	Comparison with observations
Model B	Very large low emissivity halo required due to the sun being in an arm.	Such a model is rejected as a spherical halo with a radius of at least 36 kpc is required.
3D1	Linear fall off of electron density constant for all R	Profiles for $\ell^{\mathit{II}} = 30,330^{\circ}$ and 300° too broad, agreement for anticentre directions.
3D2	Linear fall off of electron density varying with R in accordance with equation 7.1.	Improved fit for $\ell^{\mathit{II}} = 30,330^{\circ}$ but $\ell^{\mathit{II}} = 300^{\circ}$ profile still too broad. Anticentre profiles essentially unchanged.
3D3	As for model 3D2 but with the extragalactic contribution increased to 100°K $R_o^2 = 114$, $F = 0.77$, $\mathcal{E}_{\nu} = 60^{\circ}$K kpc^{-1}	Improved fit as compared with that for Model 3D2.
3D4	Exponential variation in electron density, exp $(-\mathbf{Z}/2.86)$ for $\mathbf{Z} < 8.58$ kpc and zero for $\mathbf{Z} > 8.58$ kpc, constant for all R.	Slight improvement of the fit obtained for Model 3D1
3D5	Halo model. Constant electron density out to 1 kpc and then 0.169 of plane value for a spherical halo of radius 15 kpc.	Fit fair except for intermediate - high latitudes for directions towards the galactic centre where the predicted emission is too high.

Figure 7.13 shows the way in whioh the eleotron density falls with increasing Z. Rather than a true exponential, the distribution is forced to zero at Z = 10.85 kpo, the value required to obtain the correct pole temperature. For ease of oaloulation the variation of the electron density at the sun is represented by the polynomial.

$$N_e(z) = N_e(0) \left(1 - 0.35528\, z + 0.04733\, z^2 - 0.002127\, z^3\right) \qquad 7.2$$

where N_e (0) is the electron density at the plane. This is rescaled for other galaotocentric distances such that its width deoreases for R $<$ 10 kpc and increases for R $>$ 10 kpo according to

$$w(R) = 0.591 - 0.0652\, R + 0.0106\, R^2 \qquad 7.3$$

The resultant variation of the electron density is given by:-

$$N_e(R,z) = N_e(0) \left(1 - 0.35528\, \frac{z}{w(R)} + 0.04733 \left(\frac{z}{w(R)}\right)^2 - 0.002127 \left(\frac{z}{w(R)}\right)^3\right) \qquad 7.4$$

In this model as in the previous models the magnetic field is assumed constant at the Z = 0 value. It should be remembered, however, that the variation given by equation 7.4 for the electron density in fact gives the required fall of emissivity i.e. the resultant fall associated with both the eleotron density and magnetic field deoreasing with height above the plane. As seen in figure 7.13 the Z - variation, particularly for R $>$ 10 kpo, parallels a halo distribution and therefore should produce minima in the latitude profiles at approximately b^{II} = + 45° for antioentre directions. The problem of the emission being too large for intermediate latitudes at $270° < \ell^{II} < 90°$ should be avoided as this pseudo-halo decreases in size as one approaohes the galactic oentre. Figures 7.14 and 7.15 present the results for Model 3D 6. As seen from figure 7.15 the distribution of eleotrons used here does produoe minima in tho profilos at b^{II} = ± 45° for antioentre directions without produoing too muoh emission at intermediate latitudes for galaotio centre directions. The profiles presented in fugure 7.15
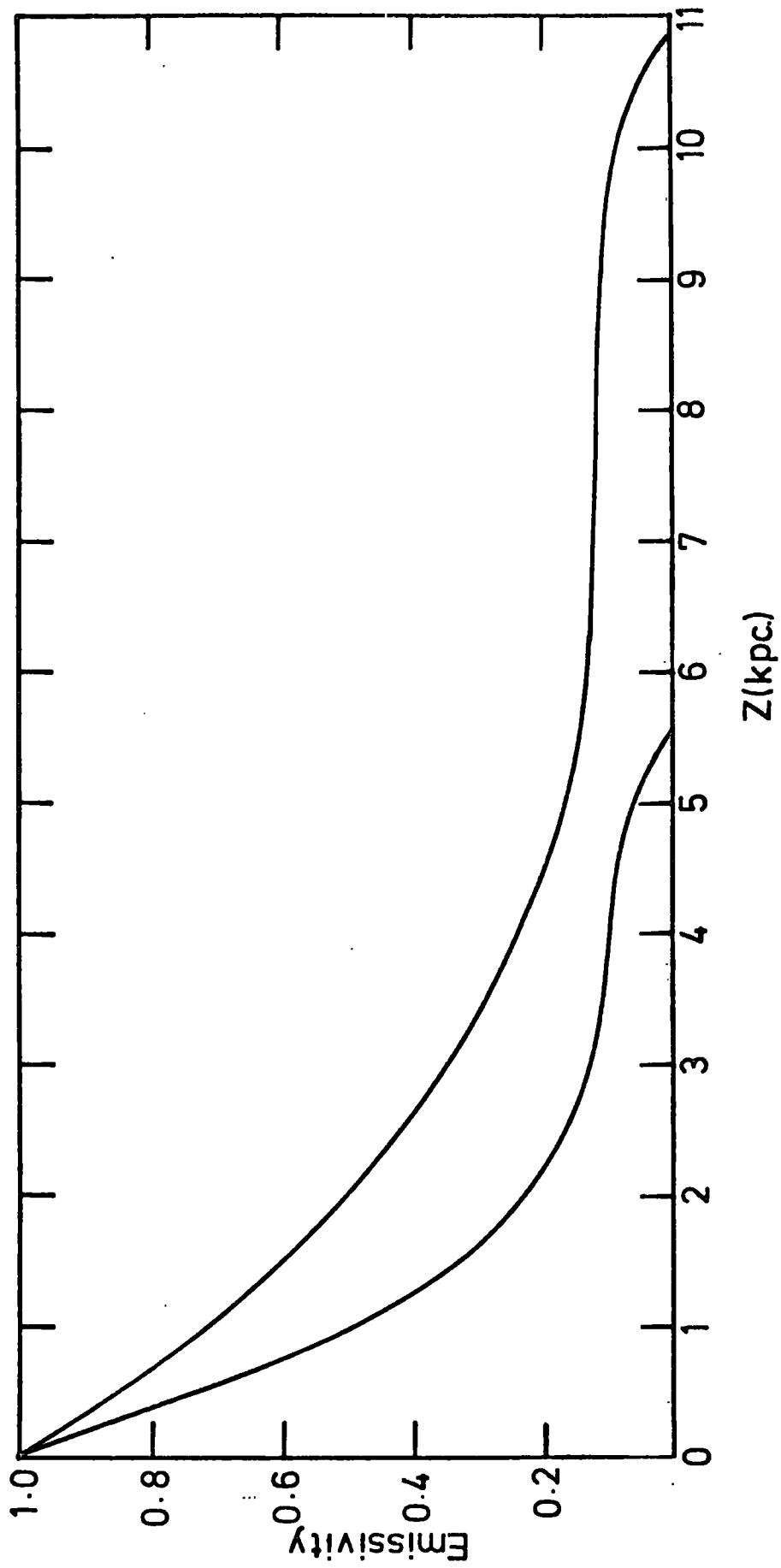
Figure 7.13: Fall-off of emissivity with height above the plane. The upper line represents the fall-off for R = 10 kpc and the lower line represents the fall-off for R = 4 kpc.
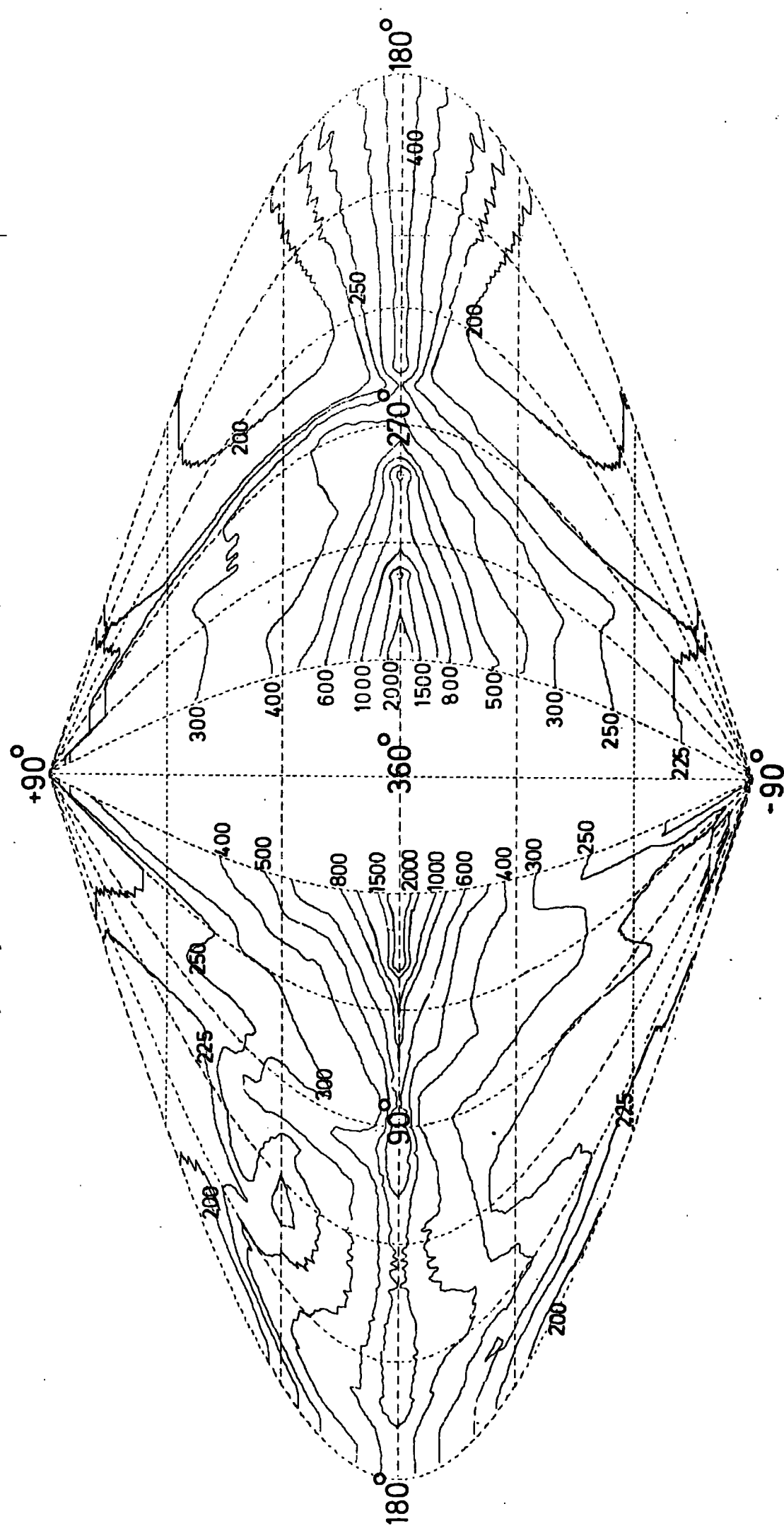
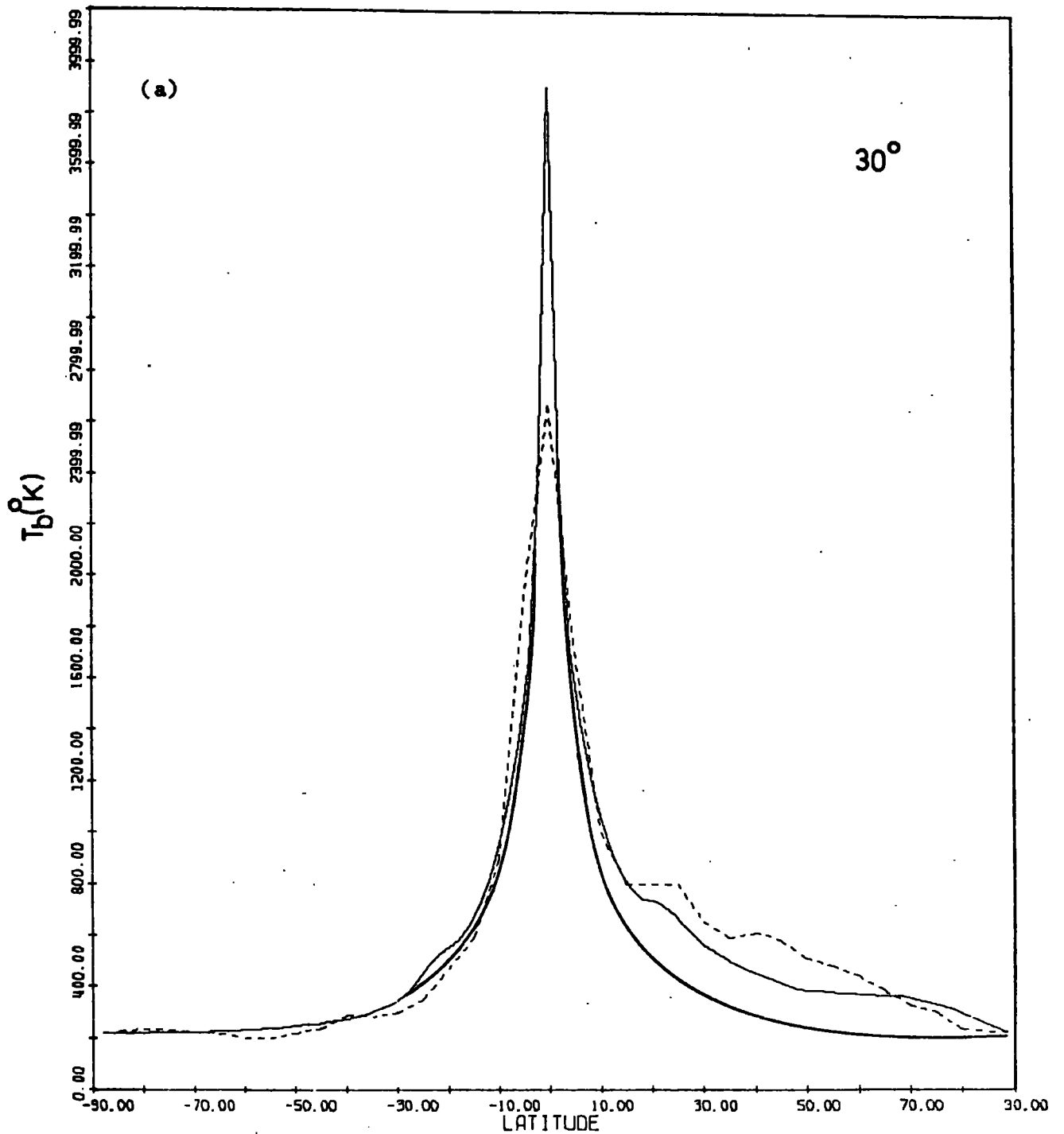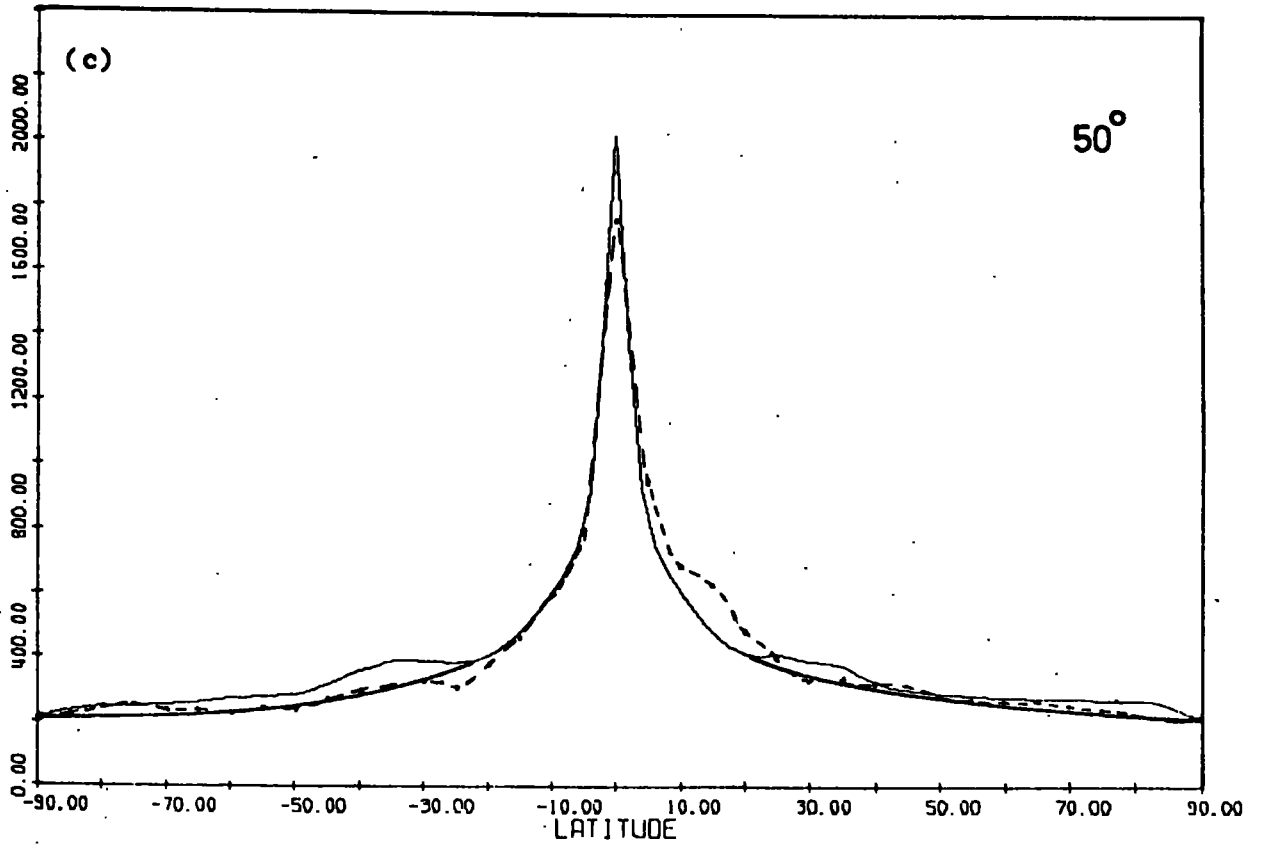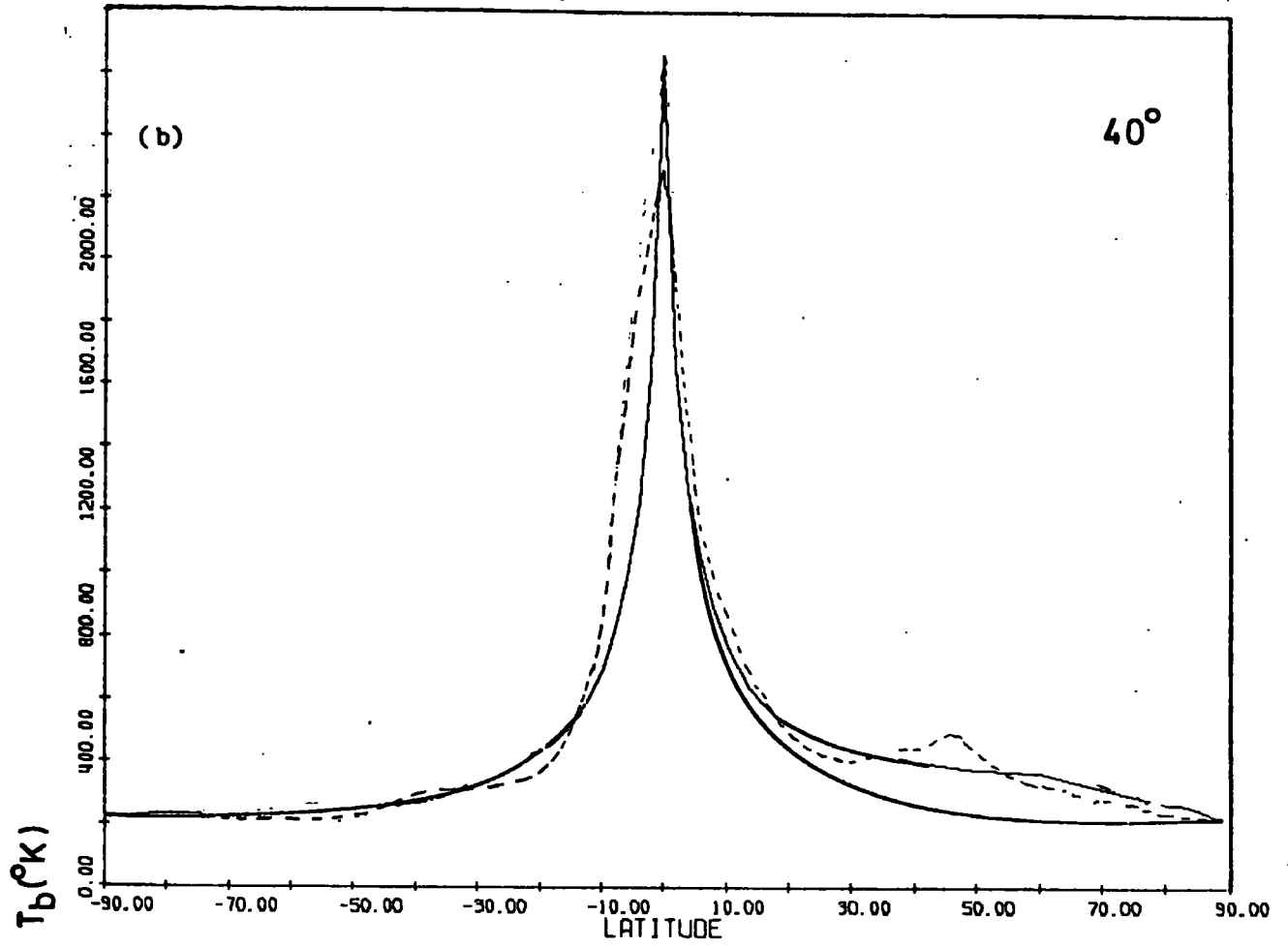Figure 7.14: Contour plot of brightness temperatures for Model 3D 6.

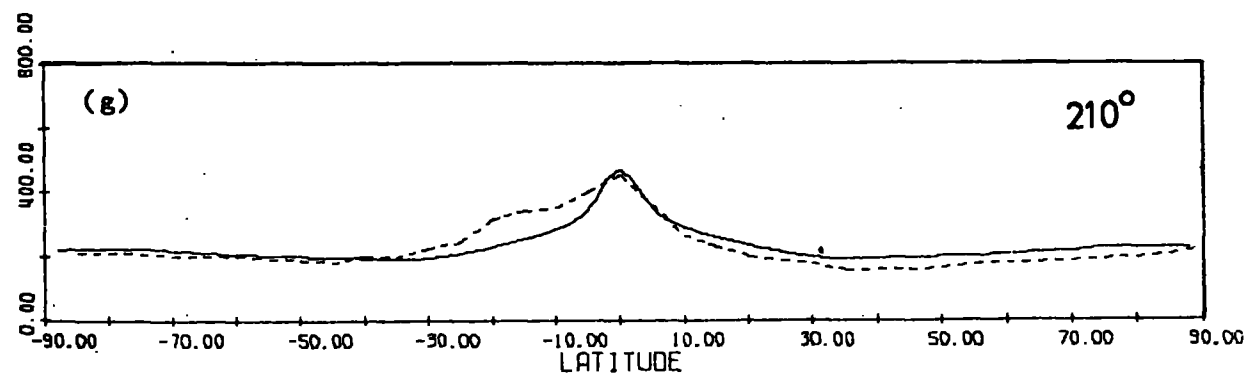Figure 7.15: Latitude cuts across figure 7.14 for various longitudes. The lower solid line represents the predicted emission before the addition of the spur emissions.

(b)   40°

(c)   50°

(L) 300°
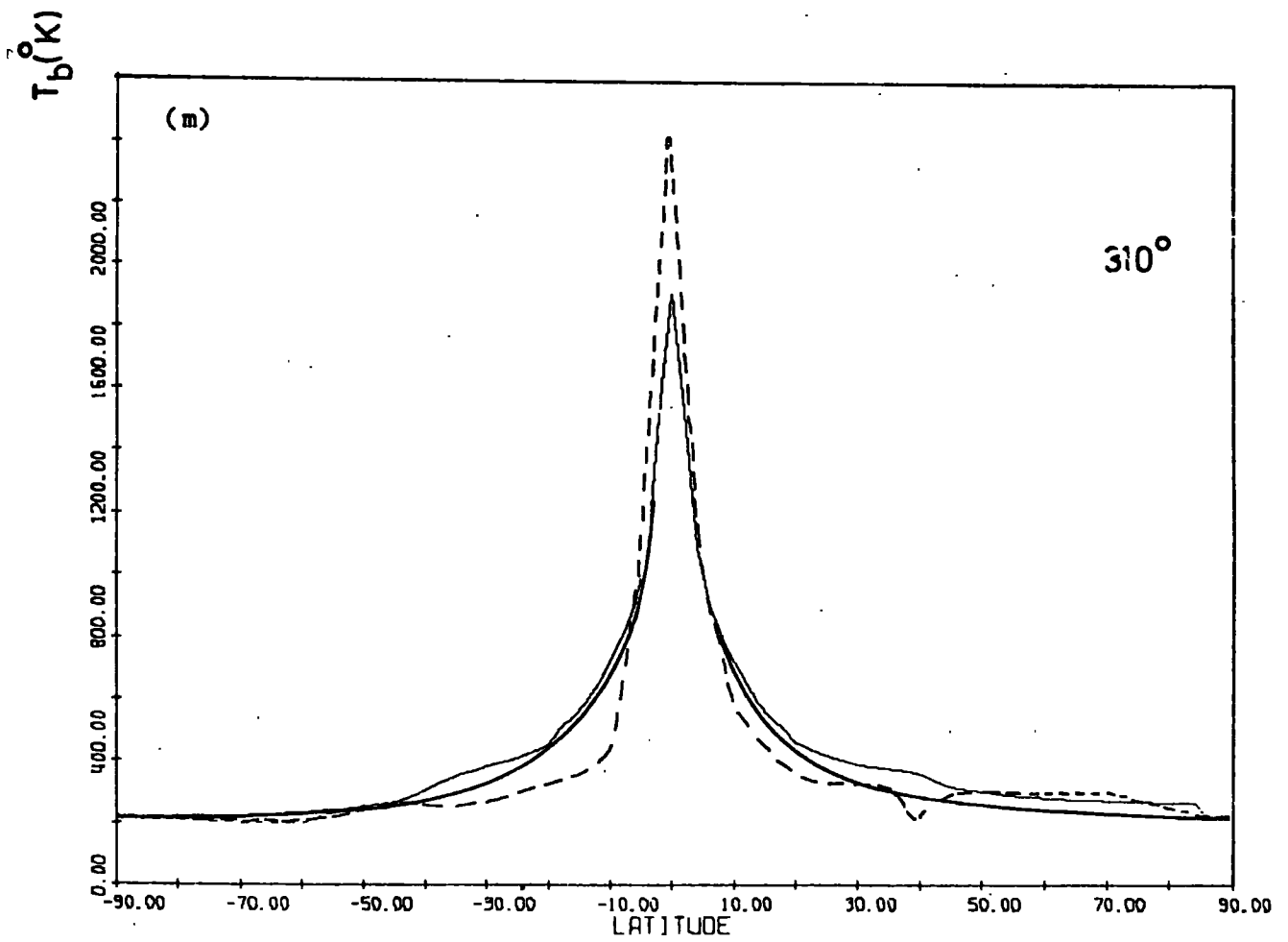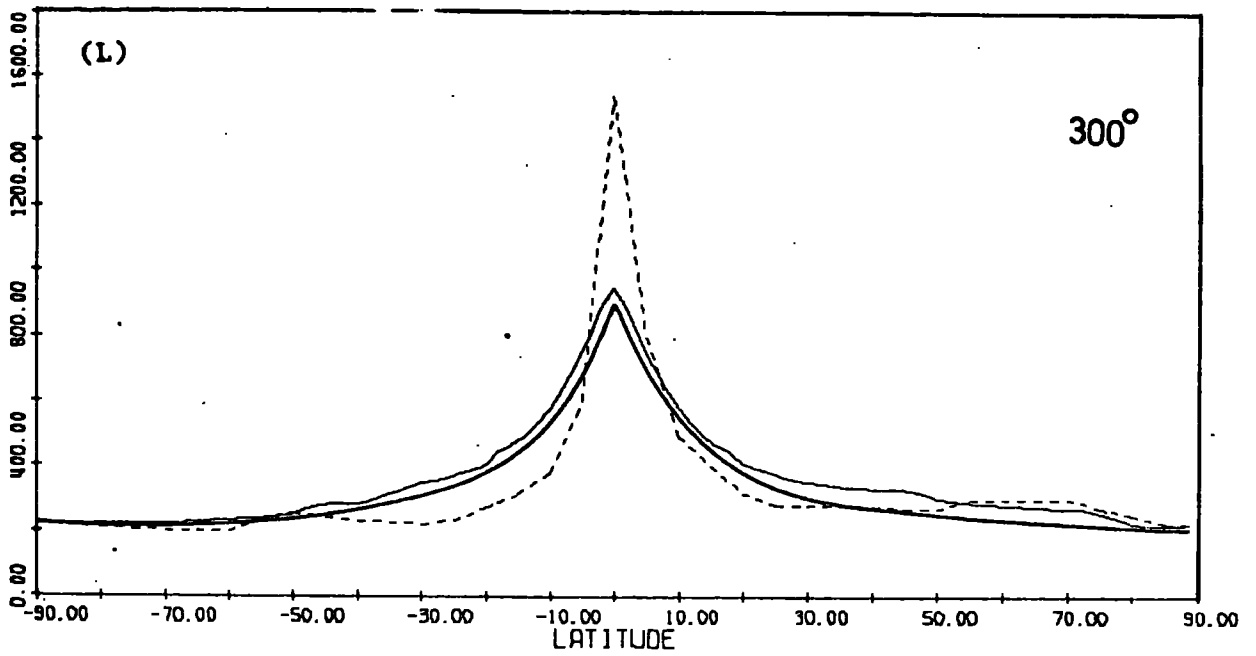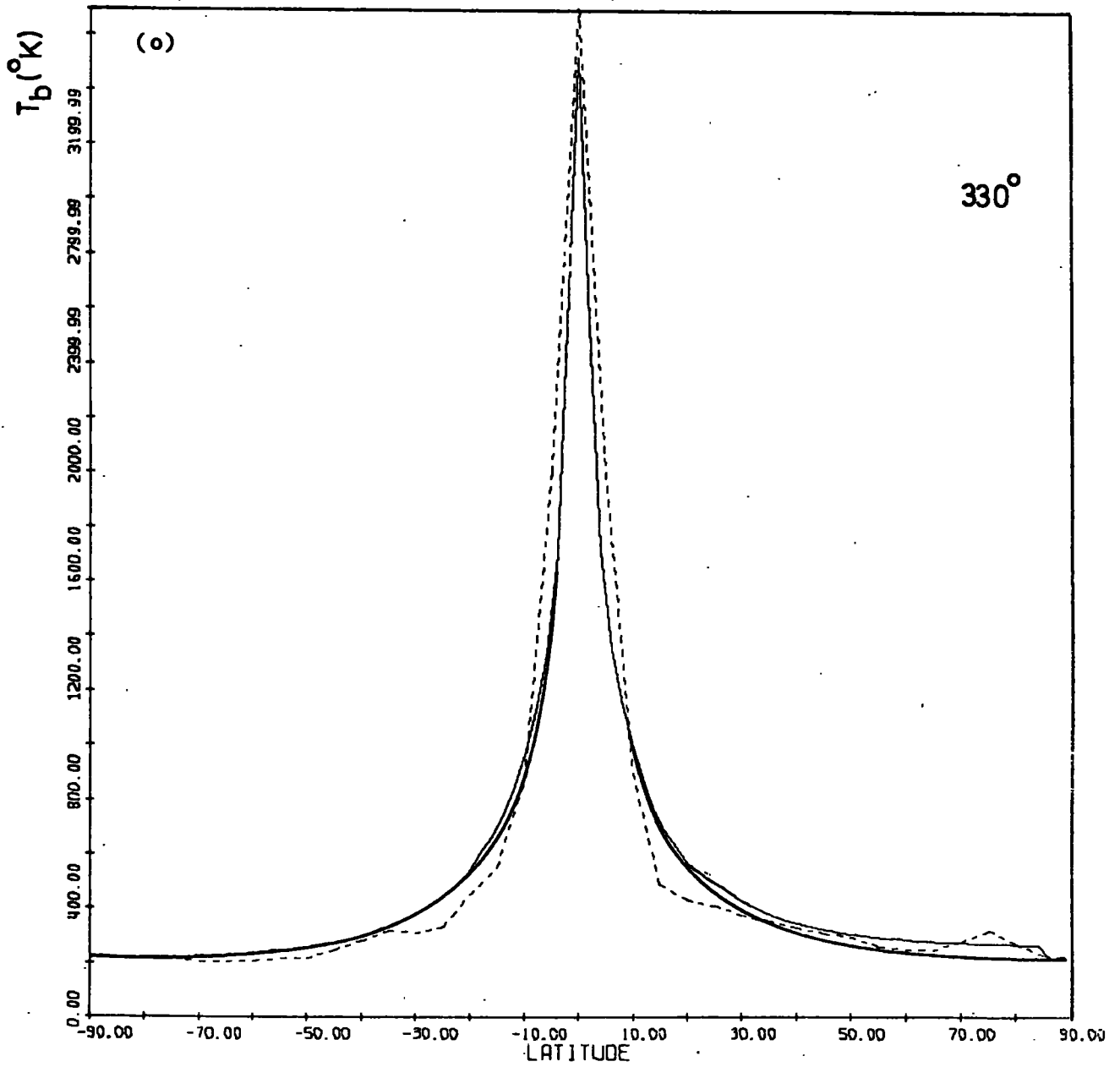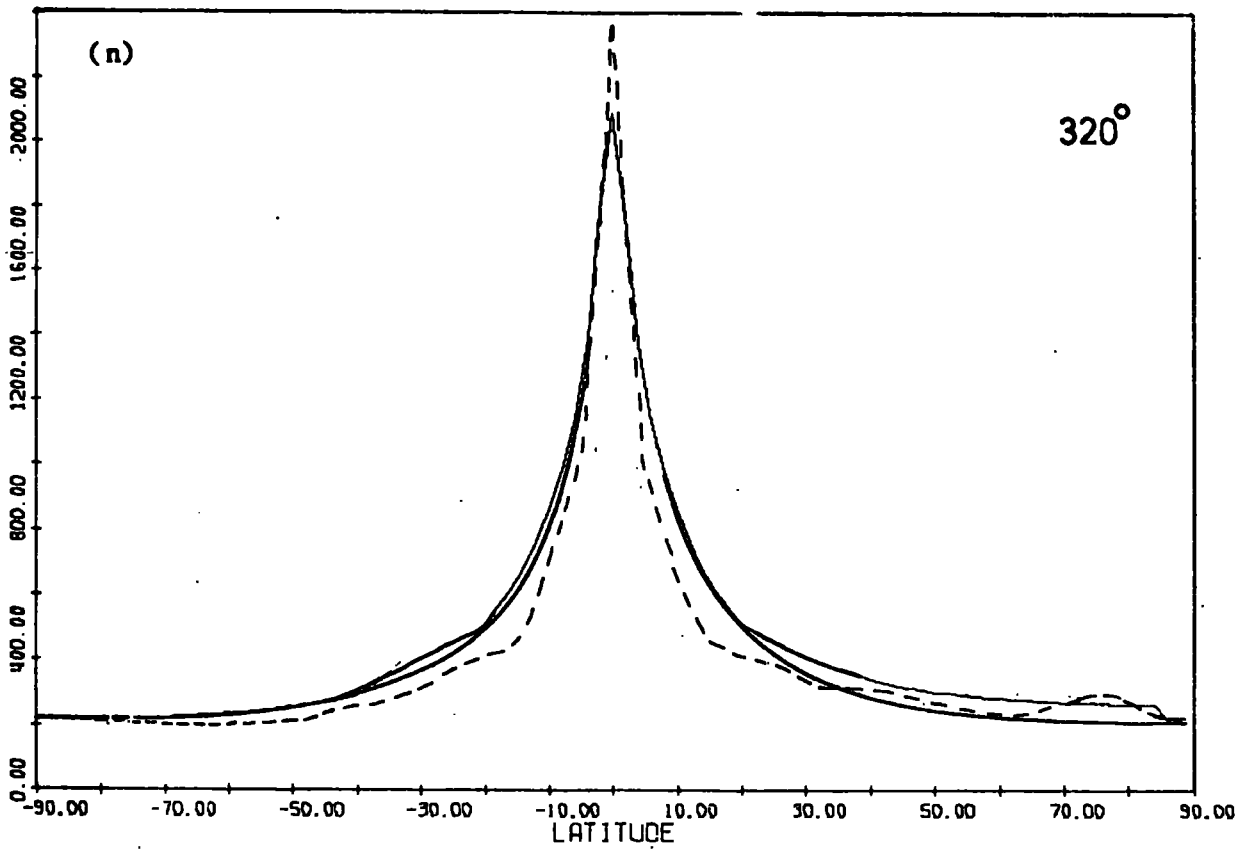
(m) 310°

$T_b^\circ (K)$

LATITUDE

(n)   320°

(o)   330°

$T_b(^oK)$

LATITUDE
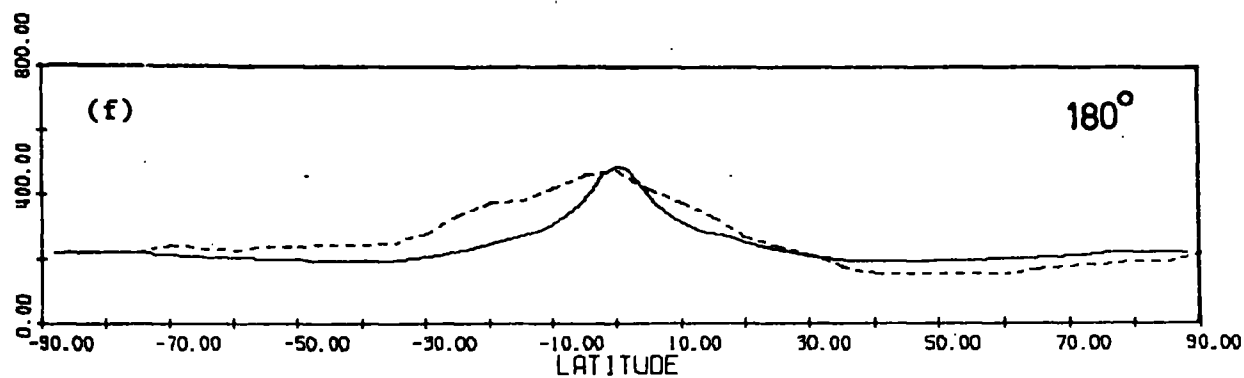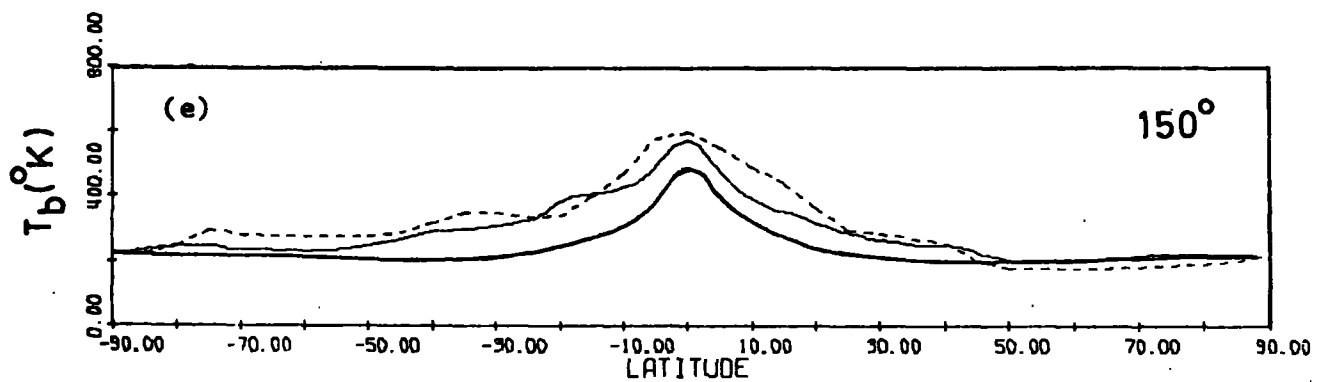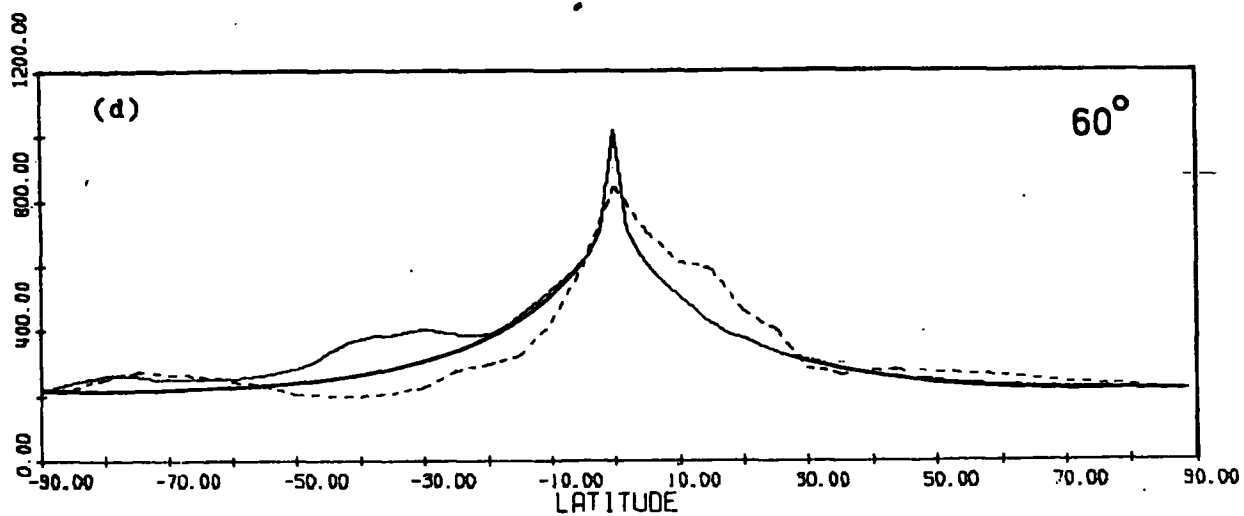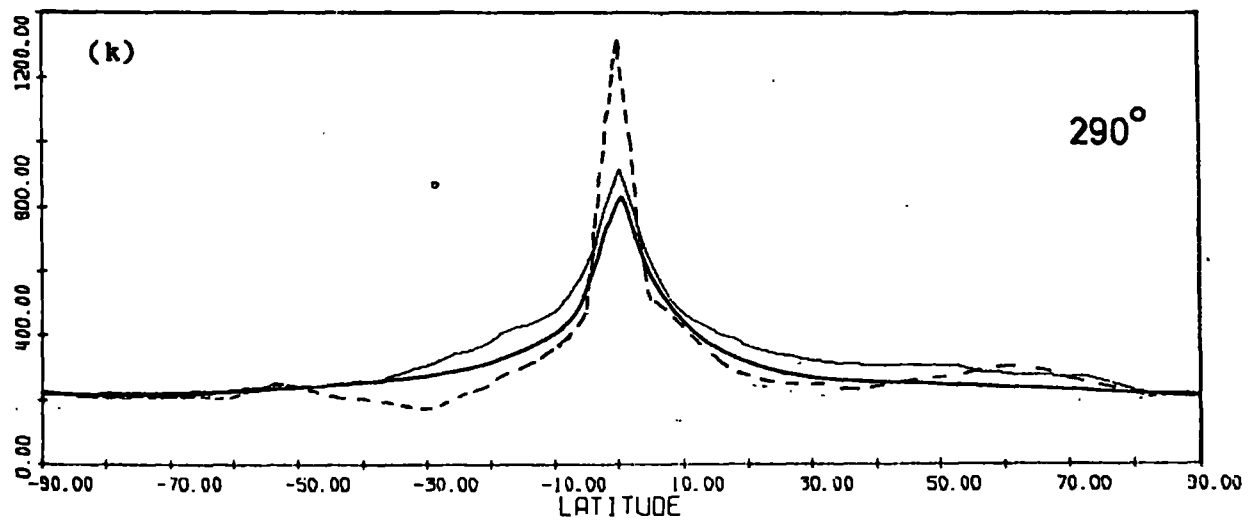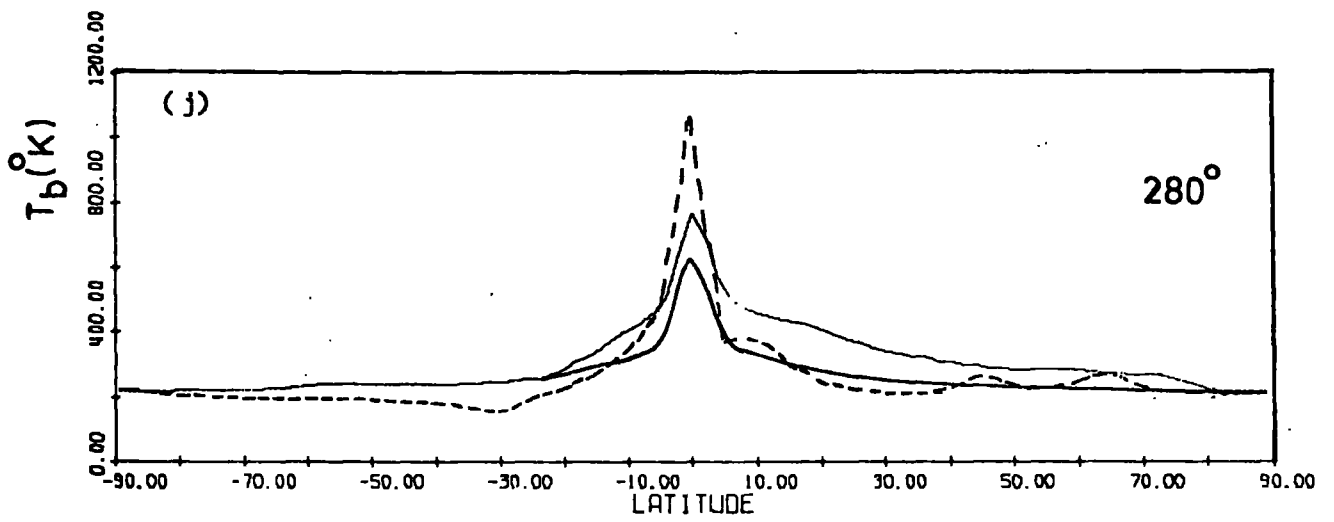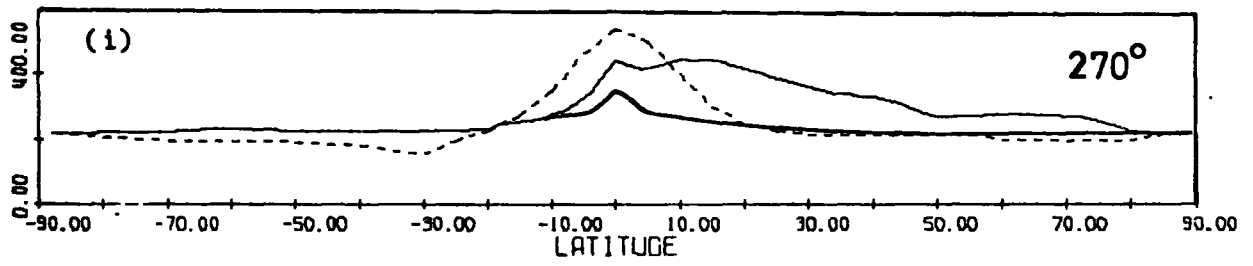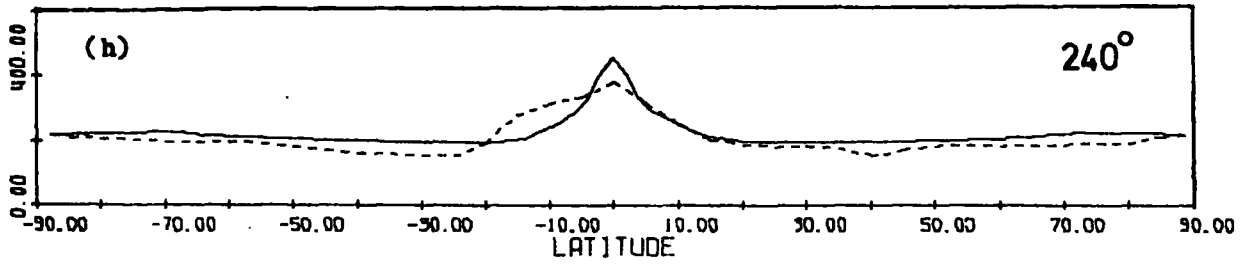
also show how much of the emission is assumed to be coming from the radio spurs. When two solid lines are present on a profile the lower line represents the diffuse galactic continuum emission whereas the upper line is the sum of the diffuse emission and the emission expected from the spurs. Figure 7.16 presents the intensity contour plots for the three spurs as obtained by Spoelstra (1972) and used here to estimate the emission from the spurs at 150 MHz.

The profiles presented are representative cuts for the whole sky map, figure 7.14, excluding the region $150^{\circ} > \ell^{II} > 60^{\circ}$ where the Cygnus complex and a complex centred on $\ell^{II} = 120^{\circ} - 130^{\circ}$ considerably distort the profiles close to the galactic plane. The profiles presented in figure 7.15 will now be discussed in detail.

(a) $\ell^{II} = 30^{\circ}$

For southern latitudes the predicted profile agrees well with the observations. The peak temperature at $b^{II} = 0^{\circ}$ is somewhat higher than the observed galactic plane temperature suggesting that the spiral pattern used in this analysis is perhaps too tightly wound for this longitude. The same is also seen to be true for the $\ell^{II} = 40^{\circ}$, $\ell^{II} = 50^{\circ}$ and, to a lesser extent, the $\ell^{II} = 60^{\circ}$ profiles. The galactic plane profile, figure 7.3, clearly shows this discrepancy for the whole of this longitude range. The North Polar Spur makes a very large contribution to the observed brightness temperature for inter-mediate positive latitudes. The contribution added, assuming the Van deₐLaan model seems unable to account for all the emission. As the fit in this latitude range is good for the southern hemisphere it is likely that the Van deₐLaan model is underestimating the brightness of the North Polar Spur in this region.

(b) $\ell^{II} = 40^{\circ}$

The contribution from the North Polar Spur at this longitude for northerly latitudes brings the theoretical profile into agreement with the
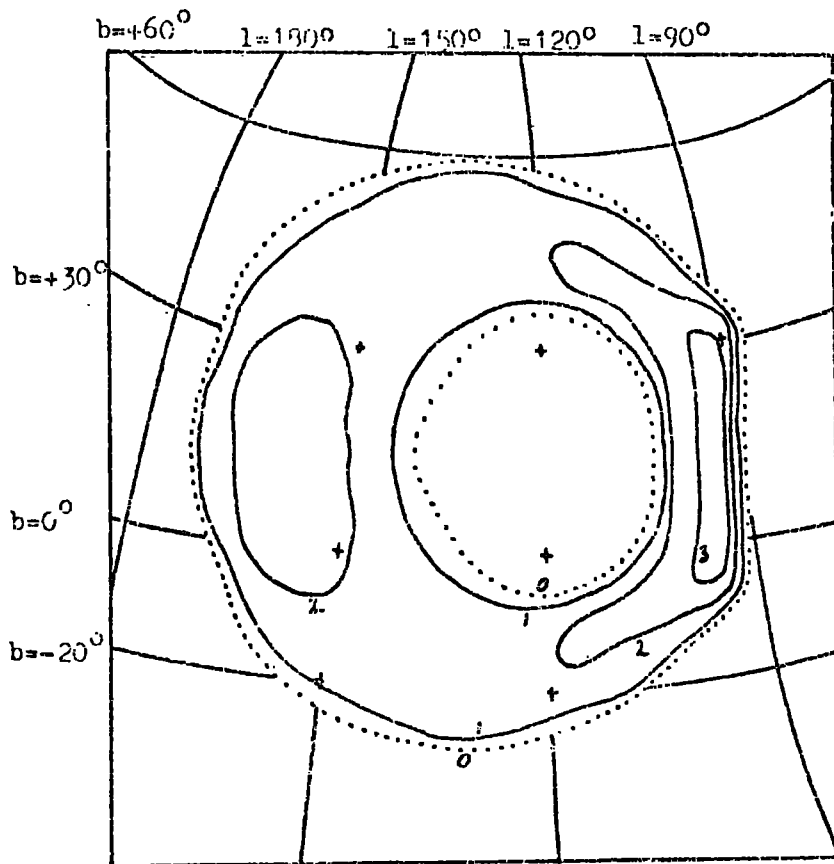
(C)

Figure 7.16:
Intensity contour plots for the radio spurs as presented by
Spoelstra(1972) using the Van de Laan model.
(A) North Polar Spur.
(B) Cetus Arc.
(C) Loop III.

observations. For southerly latitudes the fit is good apart from the observed peak being rather broad for $|b^{II}| < 10^{\circ}$. As the northern hemisphere fits well for $|b^{II}| < 10^{\circ}$ it is probable that this broadening is not due to the diffuse emission but rather due to some spatially localised source or distortion of the plane.

(c) $\ell^{II} = 50^{\circ}$

This profile has contributions from the Cetus arc for southerly latitudes and from the North Polar spur for northern latitudes. Again the added spur emissions do not seem to agree in detail with the spur emission needed for compatability with the observations.

(d) $\ell^{II} = 60^{\circ}$

The agreement for this longitude is rather poor. The calculated profile for negative latitudes even after the subtraction of the contribution assumed from the Cetus Arc is too broad whereas for positive latitudes the predicted distribution is too narrow. Obviously in this region some spur emission is present. As seen from figure 7.16b Spoelstra does not predict any emission from the Cetus Arc for positive latitudes at this longitude. It would appear that the model presented by Spoelstra for the Cetus Arc is too small in angular extent to be consistent with the observations. This is particularly noticeable for southern latitudes where Spoelstra predicts a ridge of emission for $\ell^{II} \approx 60^{\circ}$ while the observations in fact show minima at this longitude and the ridge of emission at approximately $\ell^{II} = 50^{\circ}$.

(e) $\ell^{II} = 150^{\circ}$

After the addition of the spur emissions (Cetus Arc and Loop III) the agreement with the observations is good.

(f) $\ell^{II} = 180^{\circ}$,   (g) $\ell^{II} = 210^{\circ}$ and (h) $\ell^{II} = 240^{\circ}$

The agreement with observation for these longitudes is fair apart from the observed enhanced emission for negative latitudes. This may be due to a distortion of the galactic disc, an effect of the sun not being exactly on the galactic plane or some nearby emission. Such distorting influences as the above are likely to be more pronounced in profiles for the anticentre directions where the lines of sight are relatively short.

(i) $\ell^{\pi} = 270^{\circ}$

Here the emission added for the north polar spur at northern latitudes is much greater than that observed. As seen from the calculated contour plot, figure 14, the emission over a very large range of ℓ^{π} and positive b^{π} is greatly in excess of that observed (see figure 5.1). This extensive excessive emission is clearly due to the addition of the North Polar Spur. This would suggest that Spoestra, using the Van de Laan model, predicts too much emission for this ridge region.

For the remaining profiles, (j) - (o), the predicted emission is slightly broader than the observations for $50^{\circ} > /b^{\pi}/ > 10^{\circ}$ and the predicted spur emissions seem to be at variance with the observations.

Figure 7.17 shows the way in which the emissivity varies along various lines of sight for Model 3D 6. The components of the emissivity from the regular field and the irregular field are plotted.

In the plane about half of the emission is coming from spiral arms and about half comes from each of the field components. Plots are presented for longitudes 330° and 180° for various latitudes. The line of sight distance for $b^{\pi} > 0^{\circ}$ is the line of sight projected onto the plane of the galaxy. For the $\ell^{\pi} = 330^{\circ}$ direction it is clearly seen that the spiral arms only contribute to the emission for $b^{\pi} < 2.5^{\circ}$ whereas for the $\ell^{\pi} = 180^{\circ}$ direction the local arm introduced at 0.5 kpc from the sun still makes a small contribution at $b^{\pi} = 40^{\circ}$. Therefore in general the emission from the arms only affects the predicted

LONGITUDE=180.0 LATITUDE=0.0
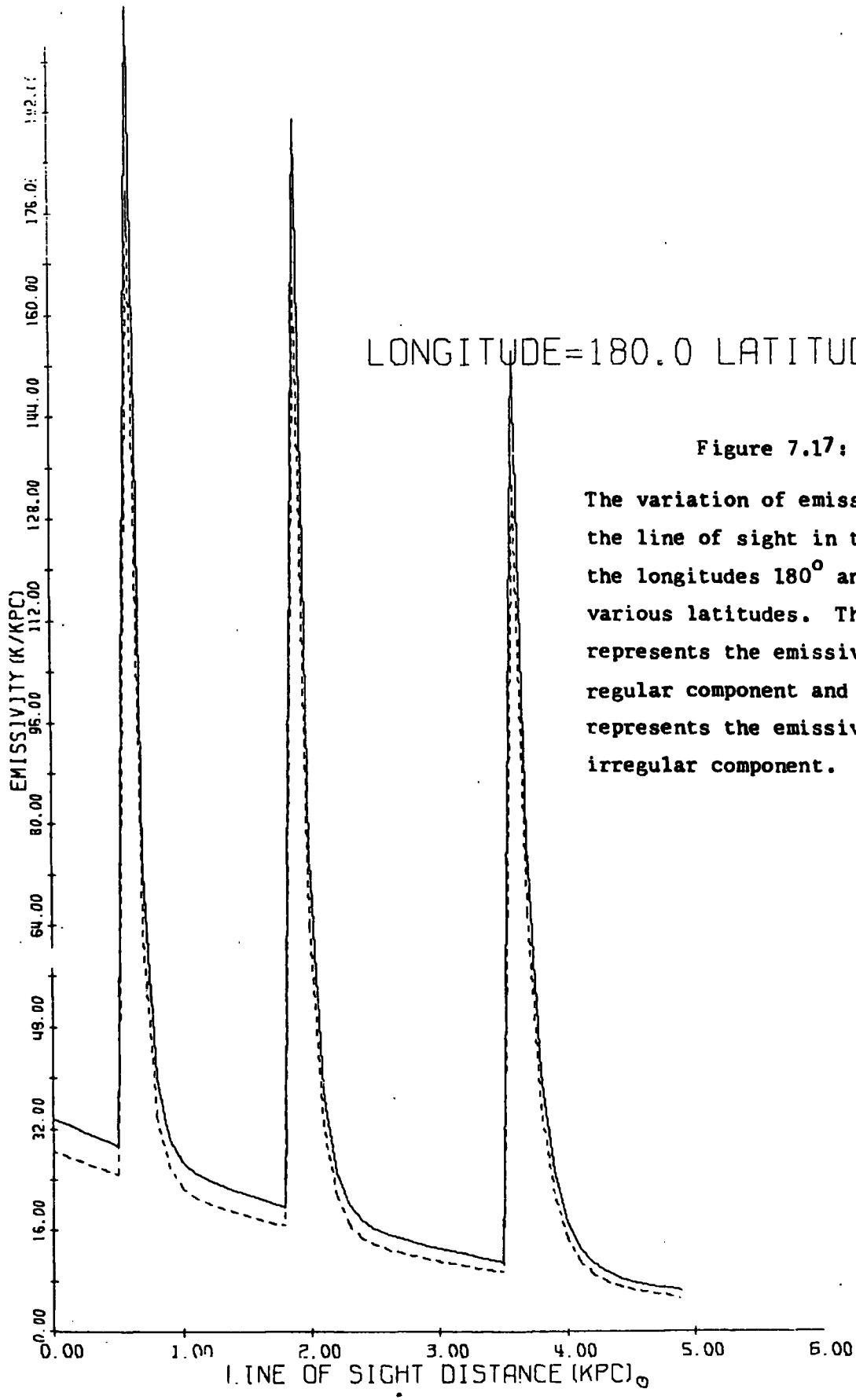
Figure 7.17:

The variation of emissivity along
the line of sight in the plane for
the longitudes 180° and 330° for
various latitudes. The dashed line
represents the emissivity from the
regular component and the solid line
represents the emissivity from the
irregular component.

LONGITUDE=180.0 LATITUDE=10.0

EMISSIVITY (K/KPC)

LINE OF SIGHT DISTANCE (KPC)
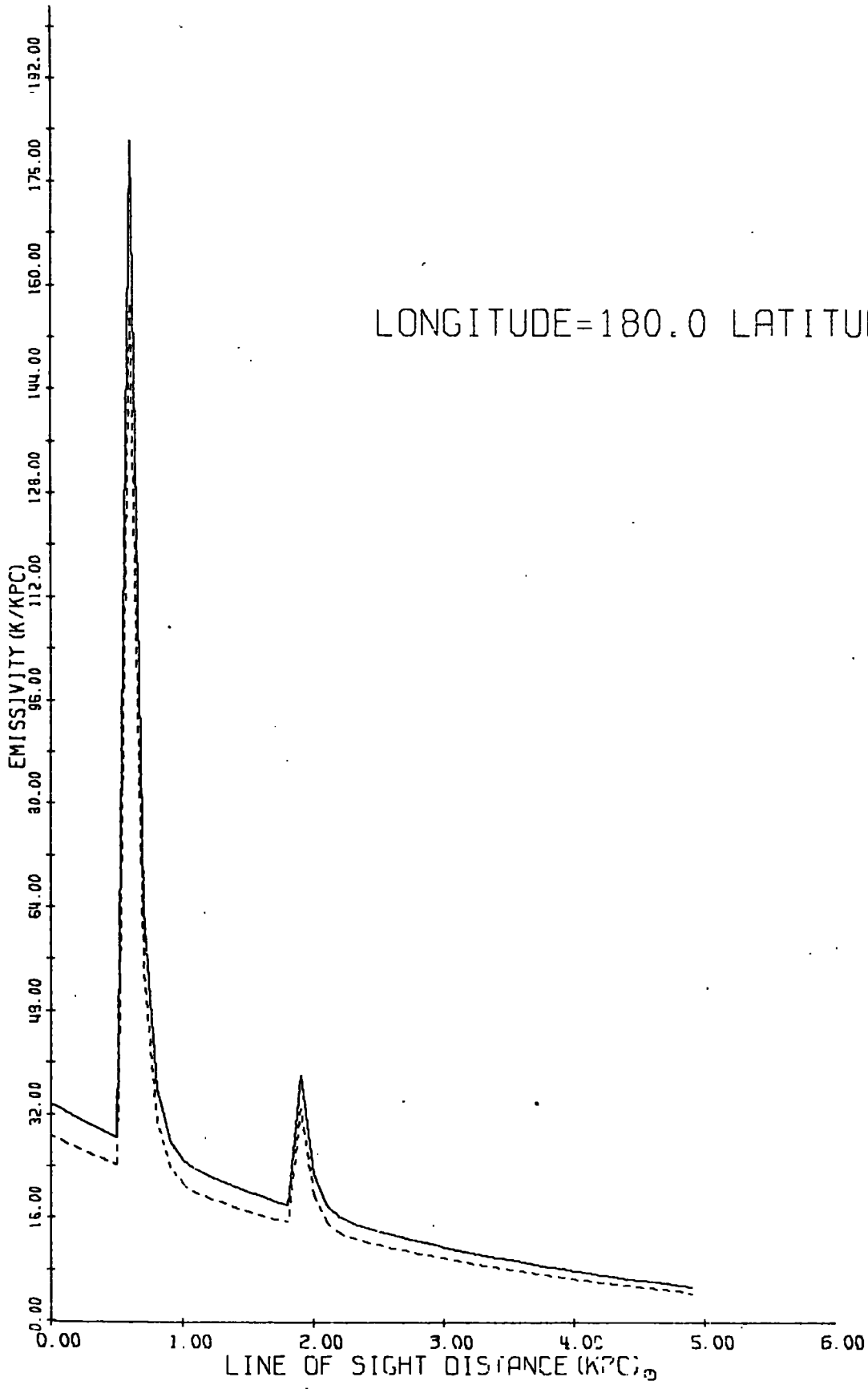
LONGITUDE=180.0 LATITUDE=20.0

LONGITUDE=180.0 LATITUDE=30.0

LONGITUDE=180.0 LATITUDE=40.0

LONGITUDE=330.0 LATITUDE=0.0

EMISSIVITY (K/KPC)

LINE OF SIGHT DISTANCE (KPC)

LONGITUDE=330.0 LATITUDE=10.0

LONGITUDE=330.0 LATITUDE=20.0

LONGITUDE=330.0 LATITUDE=30.0

LONGITUDE=330.0 LATITUDE=40.0

temperature profiles for $|b^{\pi}| < 20^{\circ}$ resulting in the predicted profile being rather insensitive to the form taken for the demodulation of the spiral arms.

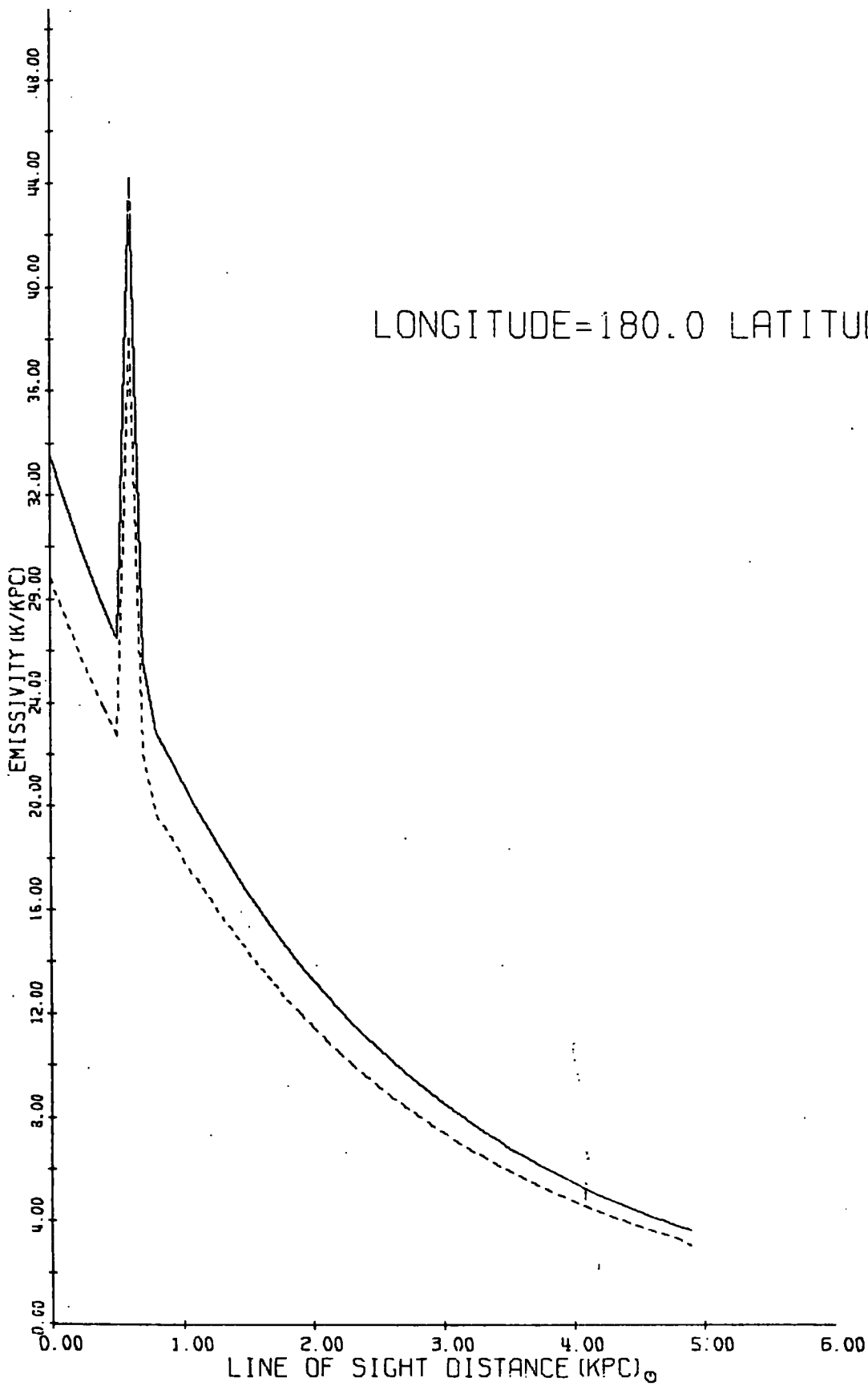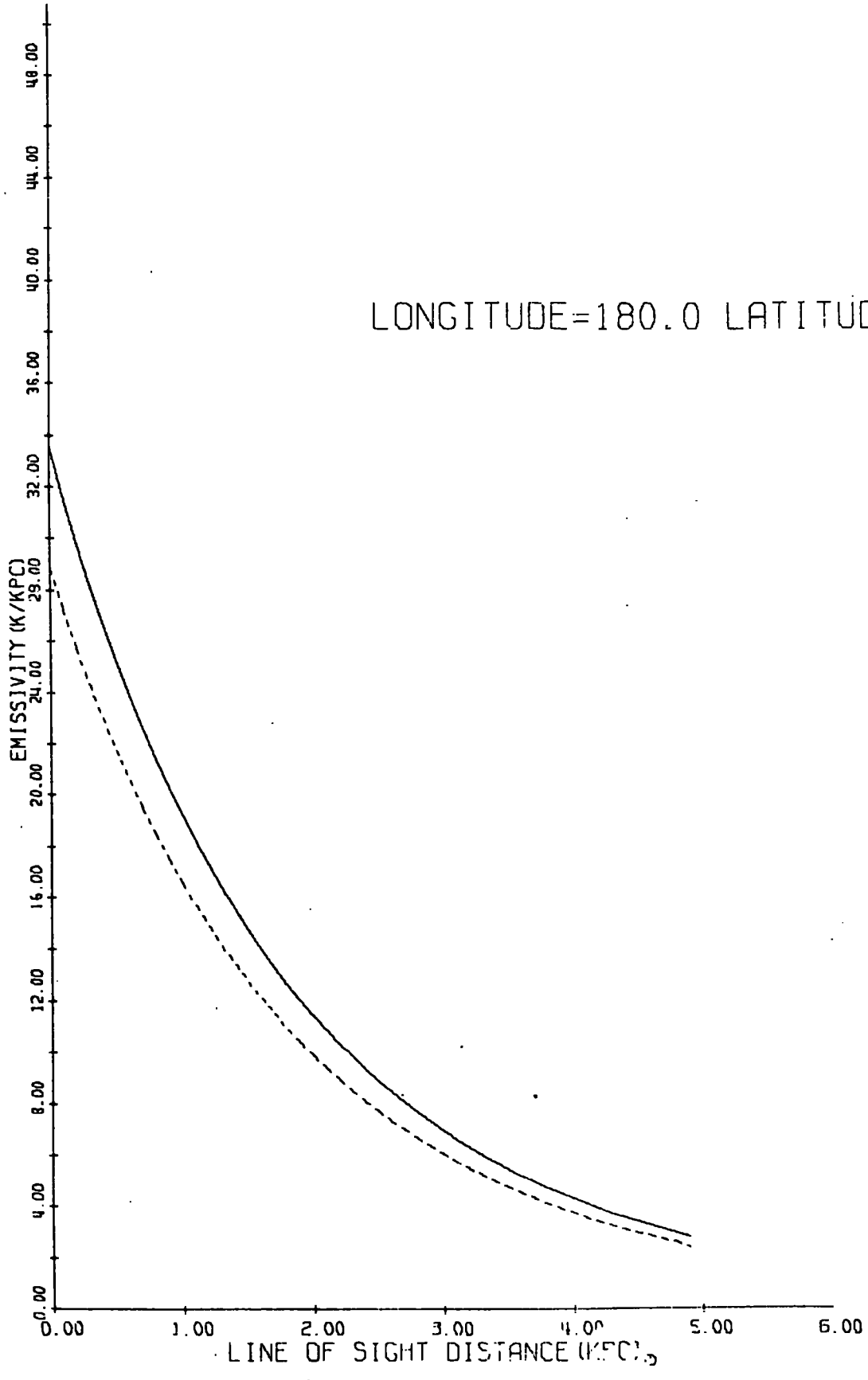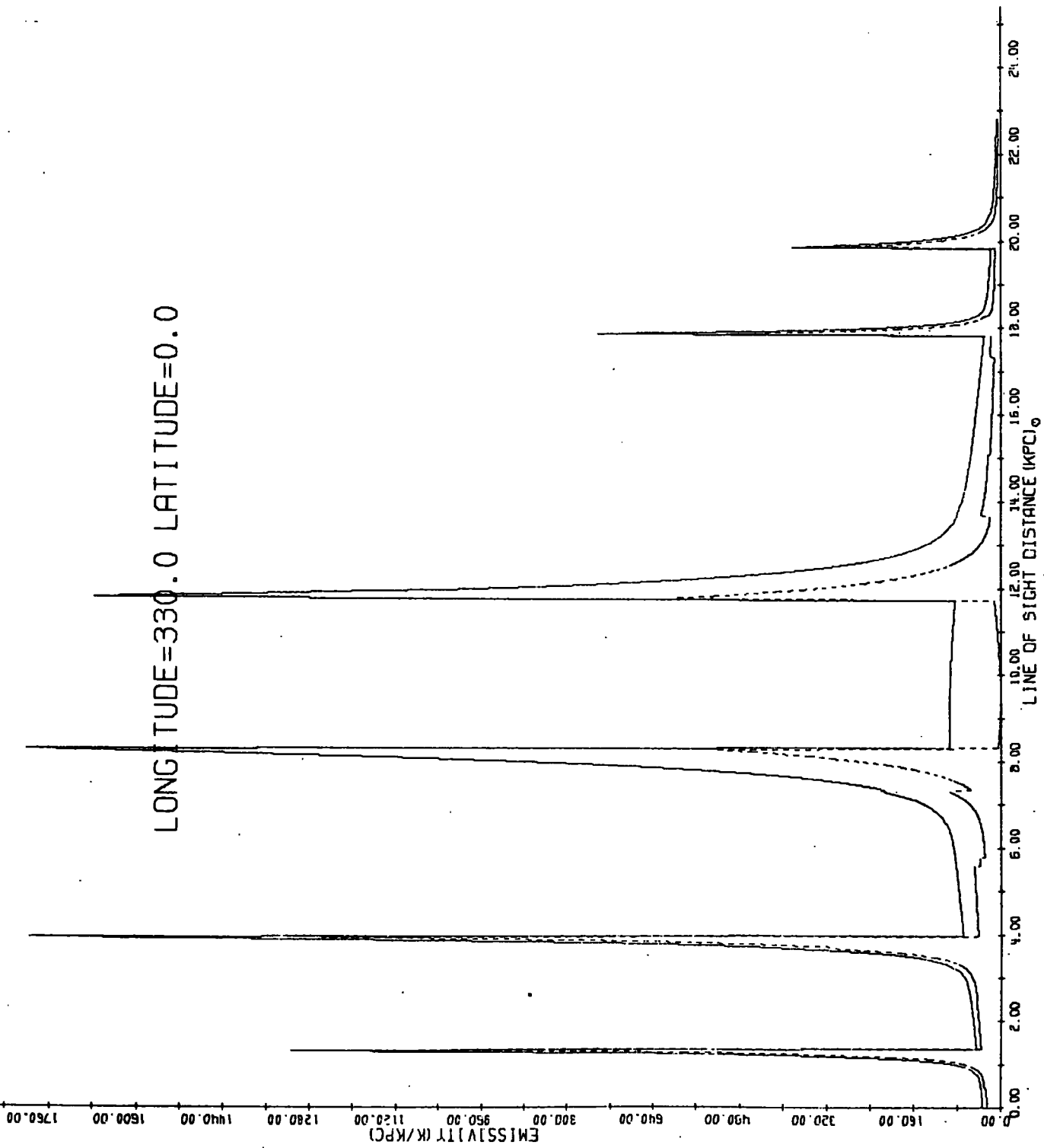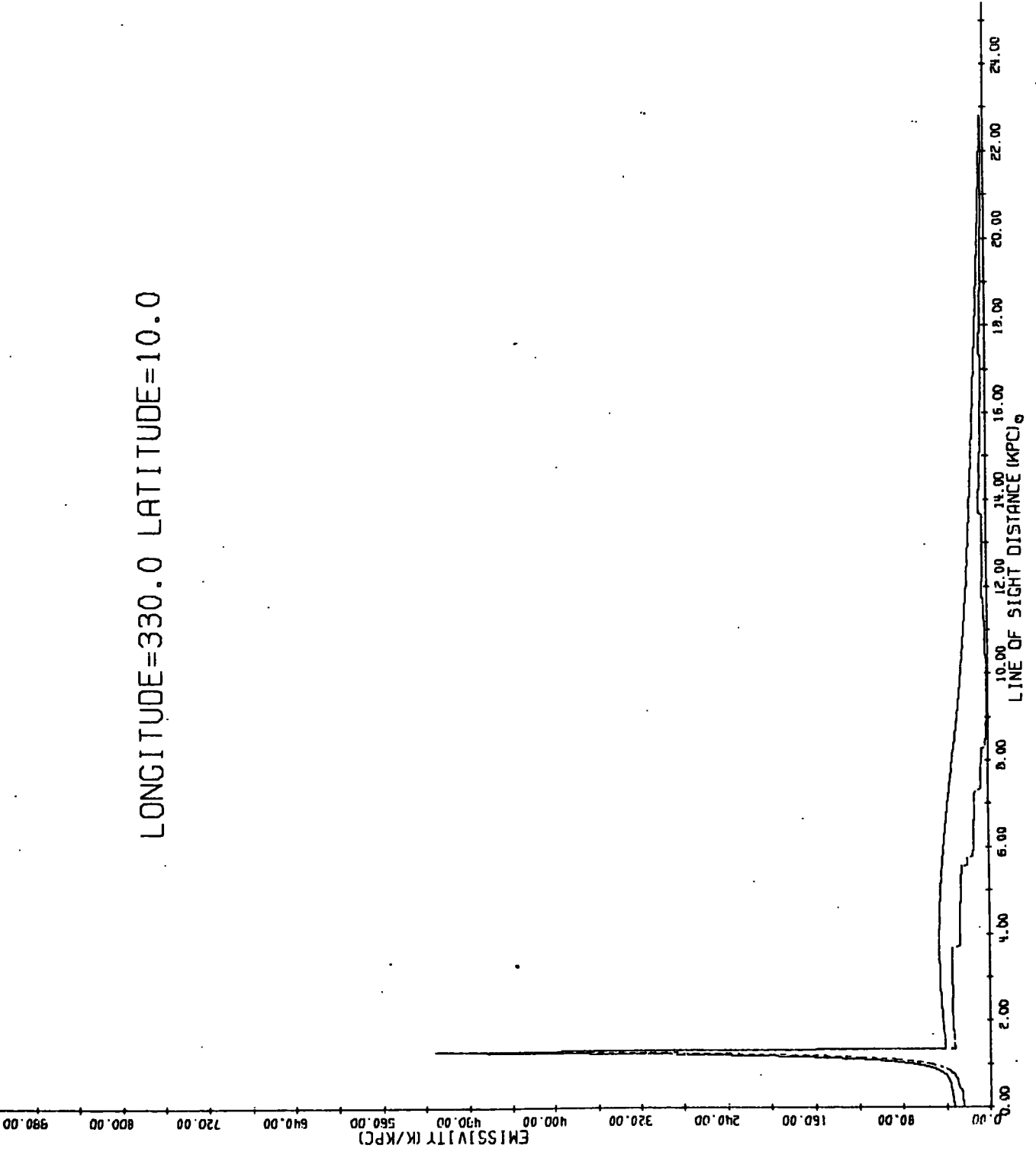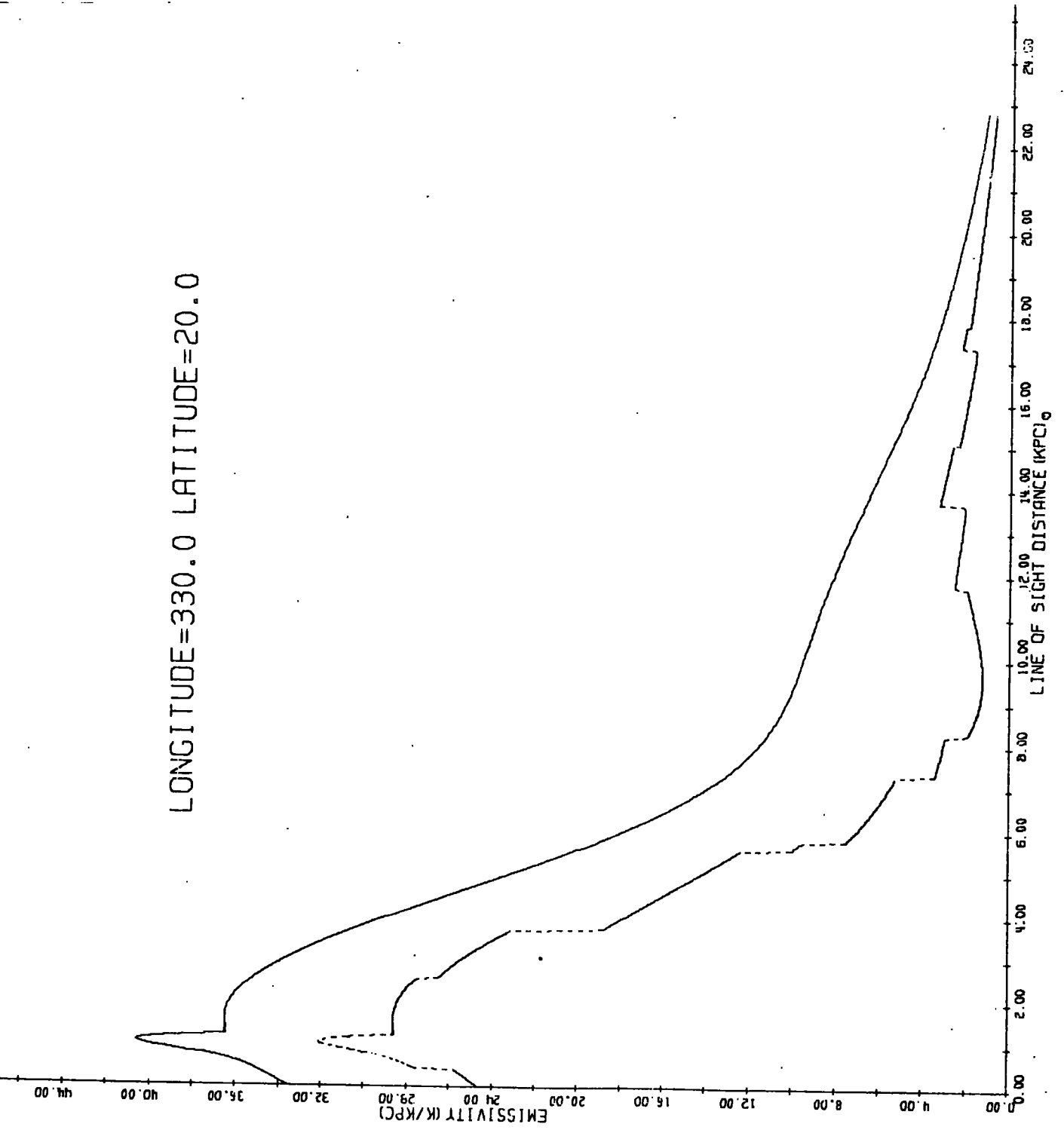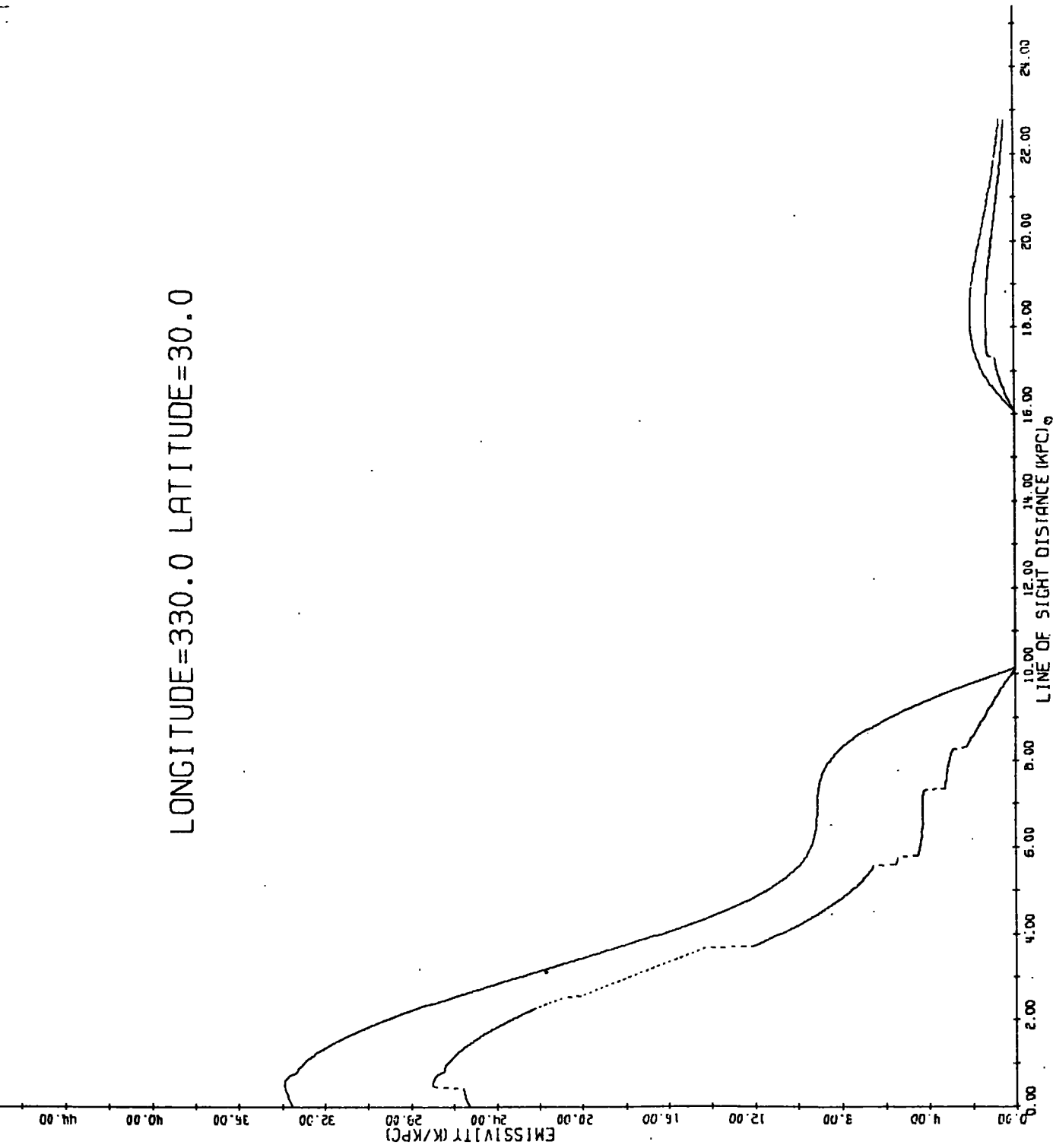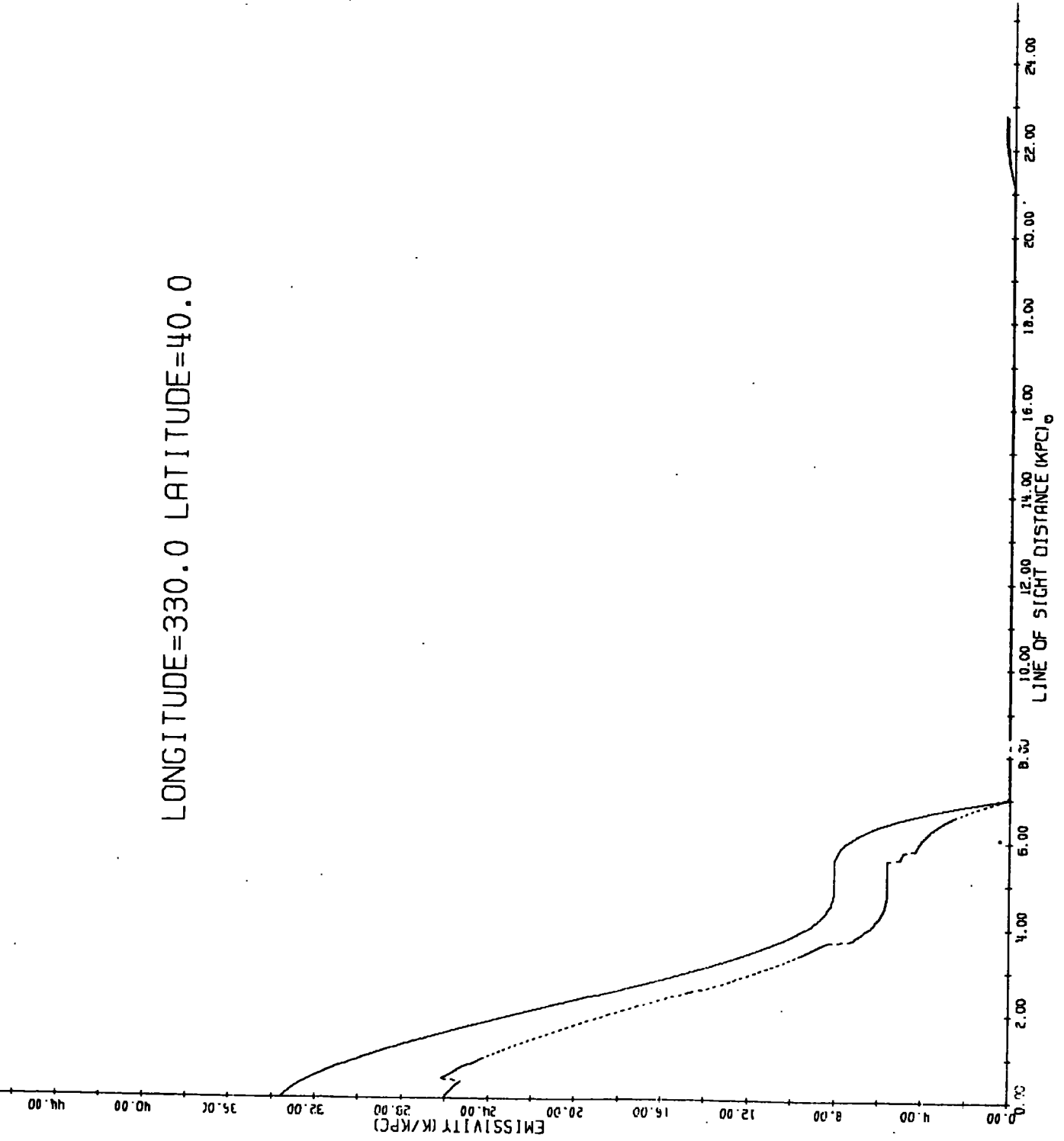Comparison can now be made directly between the predicted emission in front of the H_{II} regions considered by Caswell and the values inferred from observation. Table 7.5 presents the results for the brightness temperatures in front of the nine H_{II} regions. Apart from NGC 1805 and NGC 1848 the calculated brightness temperatures in front of the H_{II} regions are consistently lower than the observed values. The values for NGC 1499 the λ Orion nebula and Barnards Loop are particularly low as the line of sight does not reach into the next arm. This would suggest, from these measurements alone, that the arm introduced at 0.5 kpc away from the sun should have perhaps been closer. Unfortunately if this is done the magnetic field measurements from the rotation measures of pulsars become inconsistent with the predicted line of sight fields from such a model. The lines of sight to several of the nearby pulsars would now extend to and beyond this local arm predicting a greatly increased line of sight magnetic field. (Figure 3.11) The uncertainty in the distance to the pulsars, deduced from their dispersion measures may be sufficient to overcome this disagreement. The distance to a particular pulsar may be overestimated if clouds of thermal electrons denser than the assumed background thermal electron density are present in the line of sight. It should also be born in mind that the Orion arm, not being part of the 'grand design', may in fact be a material arm rather than a density wave feature perhaps making it rather non uniform both in location and in intensity resulting in the expected magnetic field varying along its length. Also presented in Table 7.5 is the brightness temperature observed and calculated for distances beyond the H_{II} regions. Both temperatures have had an extragalactic contribution removed: 50K for the calculated values and a value of 9.8×10^{4}K at

T A B L E   7.5

H_{II} Region	Distance (kpc)	Coordinates		Brightness Temperature in front of H_{II} region		Brightness Temperature beyond H_{II} region	
		ℓ^{II}	b^{II}	Observed	Calculated	Observed	Calculated
NGC 7822	0.85	118°	$0^\circ.85$	$190^\circ K$	$85^\circ K$	$153^\circ K$	$398^\circ K$
NGC 1805	2.2	$134^\circ.5$	$1^\circ.0$	$194^\circ K$	$243^\circ K$	$161^\circ K$	$214^\circ K$
NGC 1848	2.1	$137^\circ.0$	$1^\circ.0$	$185^\circ K$	$207^\circ K$	$161^\circ K$	$253^\circ K$
NGC 1499	0.44	$160^\circ.5$	$-12^\circ.5$	$140^\circ K$	$28^\circ K$	$71^\circ K$	$285^\circ K$
IC 405	0.65	$172^\circ.5$	$-1^\circ.5$	$230^\circ K$	$139^\circ K$	$29^\circ K$	$257^\circ K$
S 249	1.9	$189^\circ.0$	$4^\circ.0$	$262^\circ K$	$204^\circ K$	$0^\circ K$	$142^\circ K$
λ Ori. neb.	0.5	$196^\circ.0$	-12.0	$144^\circ.4 K$	$27.5^\circ K$	$67^\circ K$	$202.5^\circ K$
NGC 2264	0.71	$203^\circ.0$	$+2^\circ.5$	$188^\circ K$	$122^\circ K$	$47^\circ K$	$277^\circ K$
Barnard Loop	0.5	$208^\circ.0$	$-20^\circ.0$	$126^\circ K$	$25^\circ K$	$13^\circ K$	$150^\circ K$

10 MHz (Simon 1977). In all cases excluding NGC 1805 and 1848 the calculated emission is greatly in excess of the Caswell values. Care must be taken in the interpretation of this result as the free-free absorption of the 10 MHz radiation is probably considerable when long lines of sight are considered. This is probably one of the reasons for the emission behind S.249 being inferred to be zero.

In the next chapter the various conclusions that can be reached regarding the distribution of cosmic ray electrons and magnetic field in the galaxy are discussed.

References

Allen R.J., Baldwin J.E. and Sancisi R. 1977 submitted Astronomy and Astrophys.

Anand K.C., Daniel R.R. and Stephens S.A. 1968 Proc. Ind. acad. Sci. 67A 267

Andrew B.H. 1969 M.N.R.A.S. 143 17

Baldwin J.E. 1955a M.N.R.A.S. 115 690-700

Baldwin J.E. 1955b Observatory 75 229

Baldwin J.E. 1967 I.A.U. Symp. No. 31. 337.

Baldwin J.E. 1976 in 'The Structure and Content of the Galaxy and galactic
        gamma rays' ed Fichtel C.E. and Stecker F.W. Goddard Space Flight
        Centre. p. 206.

Bridle A.H. 1967 M.N.R.A.S. 136 219

Bridle A.H. 1968 M.N.R.A.S. 138 251

Bulanov S.V., Dogiel V.A., Syrovatskii S.I. 1975. Cosmic Studies 13 787-791

Bulanov S.V., Syrovatskii S.I., Dogiel V.A. 1976 Astrophys. and Space Sci.
        44 255-266

Burke B.F. 1967 IAU Symp. No. 31. p.361

Dogiel V.A., Bulanov S.V. and Syrovatskii S.I. 1975 14th Int. Cosmic Ray Conf.
        OG2 p.700

Ekers R.D. and Sancisi R. 1977 Astron. Astrophys. 54 973-974.

French D.K. and Osborne J.L. 1976 M.N.R.A.S. 177 569-582.

Ipavich F.M. 1975 Ap. J. 196 107-120

Jackson P.D. and Kellman S.A. 1974 Ap. J. 190 53-58.

Jones B.B. and Finlay E.A. 1974 Aust. J. Phys. 27 687-711

Kruit P.C. vander and Allen R.J. 1976 Ann. Rev. Astr. and Astrophys. 14 417.
        Lin C.C. and Shu F.G. 1967 I.A.U. Symp. No. 31 p.313.

Mills B.Y. 1959 Paris Symp. Radio Astronomy ed R.N. Bracewell,
        Stanford University Press.

Owens A.J. and Jokipii J.R. 1977 Ap. J. 215. 677-684

Parrish A. 1972 Ap. J. 174 33-44

Price R.M. 1974 Astron and Astrophys. 33 33-38

Roger R.S. 1969 Ap. J. 155 831

Shklovskii I.S. 1952 Astron. Zh. 29 418.

Simon A.J.B. 1977 M.N.R.A.S. 180 429-445

Sironi G. 1974 M.N.R.A.S. 166 345

Spoelstra T.A. Th. 1972 Astron. Astrophys. 21 61-64.

Strong A.W. 1977 submitted Astronomy and Astrophys.

Webster A.S. 1974 M.N.R.A.S. <u>166</u> 355

Webster A.S. 1975 M.N.R.A.S. <u>171</u> 243-257

Webster A.S. 1977 Private communication.

Wielebønski R. 1976 Astronomy and Astrophys. <u>48</u> 155-158

CHAPTER 8.

Conclusion

In this the final chapter the various conclusions that can be reached on the distribution of cosmic ray electrons and magnetic field in the galaxy from the models developed in chapters 6 and 7 will be discussed. In the last section several comments on the closed galaxy model will be made.

8.1 Conclusions regarding the distribution of electrons and magnetic field in the plane of the galaxy.

Within the framework of the spiral structure assumed the various two dimensional models have been able to identify some important facts concerning the galactic continuum disc. Of the two extreme models assumed for the electron distribution, Model A in which the distribution is uniform throughout the galaxy was found to give a good fit to the data. Model B, in which the electron density varies as the square of the magnetic field, was found to be untenable as the sun was required to be located in a spiral arm thereby causing difficulties when agreement between the observed and calculated pole temperature was required. The longitude profile predicted from the final two dimensional model, Model A3, agreed with observation when local sources were taken into account for all longitudes except for the region $\ell^{\pi} =$ 30° to 60°. This discrepancy suggests that the spiral form assumed is too tightly wound. The magnetic field required was found to have the strength of its two components, the regular component and the isotropically random component in the ratio 1 : 1.3. This is consistent with previous observations of the magnetic field. (chapter 4). The best fit to the observations for Model A required that the sun should be located in an interarm region as far as the magnetic field strength was concerned. To help reduce the discrepancy between the calculated local

emissivity and that implied from the observation of H II regions a local
arm was introduced at a few hundred parsecs away from the Sun in the
direction of the anticentre. As seen in the last section of Chapter 7
the fit to the observations was still not good. Unfortunately the
observations resulting in the local emissivity estimate are rather liable
to error caused by the H II region not completely filling the beam,
the H II region not being optically thick enough, errors in the distance
assumed for the H II region and, in particular when the temperature
behind the region is considered, the absorption of the low frequency
radiation by free-free absorption. As discussed in Chapter 7 the
agreement with the observations can be improved if the arm is considered
to be closer than 500 pc from the Sun. The problems then encountered
with the implied line of sight fields in comparison with the observed
fields from the observation of pulsars can then be either attributed to
errors in the distances to the pulsars or to irregularities in the
local arm itself. It is therefore clear that at present due to the
above difficulties the disagreement between the derived emissivities and
the observations is perhaps not as serious as it first appears.
Observations of the local, Orion, arm do suggest that the sun is
indeed located near to its inner edge which is consistent with the
requirement of the model to have an arm within 500 pc of the sun in the
anticentre direction. Before moving to the 3 - D structure of the
continuum emission it is worth considering the results for electron
distributions intermediate between Model A and B. If the electron
density was assumed to vary linearly with the magnetic field then the
emissivity from the spiral arms would be greatly increased compared with
that from Model A. This would make the longitude profile considerably
more angular if not resulting in the sun having to be in a spiral arm to
obtain agreement in the plane. It is therefore likely that such a
distribution would run into similar problems as to those encountered by

Model B although not quite so severe.

8.2 Conclusions regarding the distribution of electrons and magnetic field above the plane of the galaxy.

It has been shown in chapter 5 that the spiral arm compression produced by the shocks of the density waves decreases rapidly with the height above the plane. The way in which the demodulation was calculated to vary with Z is consistent with the observed width, in Z of optical spiral arms and with the latitude profiles observed for the continuum emission. The arm emission is shown to contribute only towards the brightness temperature distribution within 5° of the galactic plane. The way in which the emissivity falls with height above the plane was found to be consistent with the continuum observations for two separate models. Model 3D3, in which the emissivity falls linearly with height above the plane and the width of this distribution varies with galactocentric distance, was found to require an extragalactic component of 100^OK at 150 MHZ to obtain agreement with the observations. Such an ad hoc increase in the extragalactic temperature is considered unreasonable in the light of the present observations of an extragalactic component of approximately 50^OK at 150 MHz. To obtain a fit to the observations with an extragalactic contribution of only 50^OK it was found necessary to have the emissivity falling with height in a pseudo exponential manner with the width of this distribution varying with galactocentric distance. The best fit to the high latitude observations requires that the galaxy possesses a thick disc or halo. The parameters of the halo being as follows:- At the sun the emissivity falls in a pseudo exponential manner out to 10.85 kpc such that its equivalent half width, including the disc emission, is 2.75 kpc and its half width to half maximum is 2 kpc. For locations closer to the galactic centre the distribution is narrower, whereas at locations further from the galactic centre the distribution is broader. If a galaxy such as NGC 891, possessed such an emissivity

distribution and was observed edge-on the temperature distribution around the galaxy would not look very dissimilar to that observed for NGC 891. The peculiarity of the emissivity distribution would be hidden by the line of sight effect of the observed brightness temperature.

The brightness temperature expected from the final model for $\ell^{\pi} = 0°, \; b^{\pi} = 0°$ can be determined if for the region inside R = 4 kpc the field is assumed to be that of an interarm region falling to zero at the galactic centre as represented by the $\left[1 - exp \left(-R^2/4 \right) \right]$ term of equation 6.2 and the spiral arms are assumed symmetric on either side of the galactic centre. The value obtained after convolution to a beam shape appropriate to the survey used for the galactic centre region of the Landecker and Wielebinski map is 4200°K. The observed temperature of the galactic centre is approximately 7000°K at 150 MHz. Using the 408 MHz. survey of Green (1974), the galactic centre temperature, after sources have been removed, is found to be 375°K at 408 MHz. Convolving this to the Landecker and Wielebinski survey and converting to 150 MHz. using a spectral index of β = 2.8 the galactic centre temperature is 5700°K without sources and 6700°K with sources. This would suggest that at 150 MHz. approximately 1000 - 1500°K of the observed temperature is contributed from sources at the galactic centre, e.g. Sgr. A, and approximately 5700°K from the diffuse continuum emission. This value of 5700°K is 1500°K higher than the value of 4200°K predicted by the model suggesting that within 4 kpc of the galactic centre there must be regions of high non-thermal emissivity.

8.3. The Spur Emissions.

As indicated in the last section of chapter seven the spur emissions predicted by Spoelstra (1972) on the basis of the Van der Laan model (1962) do not appear to fit the 150 MHz. observations very well. Spoelstra produced his model of the spur emissions for a frequency of 1415 MHz. As the size of the spurs is dominated by

the compression created in the shells, on the Van deALaan model, and
not by the energy loss of the electrons it is to be expected that the
spurs are of comparable size at all frequencies. In fact the ridge
lines observed at 820MHz. by Berkhuijsen (1971) agree with those of
the Landecker and Wielebinski 150MHz. map. The apparent sizes of the
spurs predicted by Spoelstra appear in general, to be rather smaller than
the sizes implied from both the 150 and 820 MHz. observations perhaps
indicating that the distances assumed by Spoelstra for the spurs were
too great.

8.4   The Closed Galaxy Model.

The revised closed galaxy model of Peters and Westergaard (1977a)
will be discussed in the light of the radio continuum observations. In
this model, in contrast to the original closed galaxy model discussed in
section 2.5 of chapter 2, the earth and the cosmic ray sources are
located within the galactic spiral arms. The cosmic rays may drift
rapidly along the arms but drift more slowly out of the arms with a
rigidity dependent lifetime into the galactic disc and surrounding halo.
The galaxy is closed in that nuclei of all energies are retained
indefinitely in the halo until their energy is lost by nuclear
interactions. At the ... earth the cosmic rays are made up of 'young'
particles which have yet to escape from the spiral arm for the first
time and 'old' particles which fill the whole galaxy. The parameters of
the spiral arms are then chosen to agree with observations on nuclear
composition up to 100 Ge V and the isotropy of the flux at rather higher
energies. Up to 100 Ge V the fraction of 'old' particles at the earth
is then less than 20% and in this energy region the model is not
significantly different from the usual leaky box model except in the
power requirement of the cosmic ray sources. At higher energies where
the 'old' particles predominate the predictions of the two models differ
widely with respect to nuclear composition and isotropy. Peters and

Westergaard (1977b) show that their model would give agreement with the observed positron flux. The problems of the positron flux for the original closed galaxy model of Rasmussen and Peters (1975) was pointed out in the last section of chapter 2, French and Osborne (1976).

The required properties of the spiral arms are that they should contain only about 1% of the total gas in the galaxy and that their diameter should be $\sim$ o.24 kpc. Because of the small fraction of the galaxy filled with cosmic rays at the intensity observed at the earth the power requirements of the model are an order of magnitude less than for the conventional leaky box. For the same reason, however, there are great difficulties in accounting for the level of synchrotron radiation from the galaxy. The local emissivity of $\mathcal{E}_{\nu} \approx$ 60K kpc^{-1} at 150 MHz. would be that in such an arm. Outside the arm there are essentially no primary electrons in the closed galaxy model due to their high rate of energy loss compared to nucleons. The intensity of secondary electrons in equilibrium with the flux of 'old' cosmic ray nuclei outside the arm can be no more than a few per cent of the intensity of primary electrons inside. Thus the synchrotron emissivity outside the arm must be very low. The brightness temperature predicted by this model are then $\sim 7^{\circ}$K towards the poles and $\sim 50^{\circ}$K towards the anticentre (assuming three spiral arm beyond the earth in the anticentre direction). These are to be compared with observed values of 170°K and 420°K respectively, after the subtraction of a 50°K extragalactic component. To obtain the required rigidity dependent grammage in escape from the spiral arm a field of $7\,\mu$G is required by the Peters and Westergaard model. This field is much higher than that indicated by pulsar rotation measures but even so would raise the temperatures in the pole and anticentre directions only to 16°K and 111°K. Thus although the model is consistent with the fluxes of cosmic ray electrons at the earth it is not compatible with their distribution throughout the galaxy as implied by the synchrotron emission. It is

important to note that this conclusion is independent of the model
developed in this thesis for the radiation distribution. Stated
simply the observed level of synchrotron radiation in the anticentre
direction requires that the emissivity averaged over the line of sight
is appreciably higher than the local value while the Peters and
Westergaard model would give a very much lower average than the local
value.

References

Berkhuijsen E.M. 1971   Astron and Astrophys. $\underline{14}$ 359 - 386

French D.K. and Osborne J.L. 1976   Nature $\underline{260}$ 372

Green A.J. 1974 Astron and Astrophys. Suppl. $\underline{18}$ 267 - 307

Peters B and Westergaard N.J. 1977a Astrophys Space Sci. $\underline{48}$ 21-46

Peters B and Westergaard N.J. 1977b   Proc. 15th Int. Cosmic Ray
                                        Conf. Vol 1   p. 435.

Rasmussen I.L. and Peters B. 1975 Nature $\underline{256}$ 412

Spoelstra T.A. Th. 1972 Astron and Astrophys. $\underline{21}$ 61 - 84

Van de Laan H. 1962 M.N.R.A.S. $\underline{124}$ 125

APPENDIX I
SYNCHROTRON THEORY

I 1. Basic theory for a monoenergetic electron in a uniform magnetic field.

Synchrotron radiation is emitted by relativistic electrons that are spiralling about magnetic field lines.   An electron of velocity V moving in a field of strength H has a gyration frequency:

$$\nu_g = \frac{e\,H_\perp}{2\pi mc}\left(1 - v^2/c^2\right)^{1/2}$$

I.1

where $H_\perp = H\sin(\Theta)$, Θ being the angle between V and H. As the electron is accelerating continuously it radiates as a dipole which in the frame of the observer has the forward lobe of the radiation pattern compressed into a small cone with its axis along the instantaneous velocity vector.   The
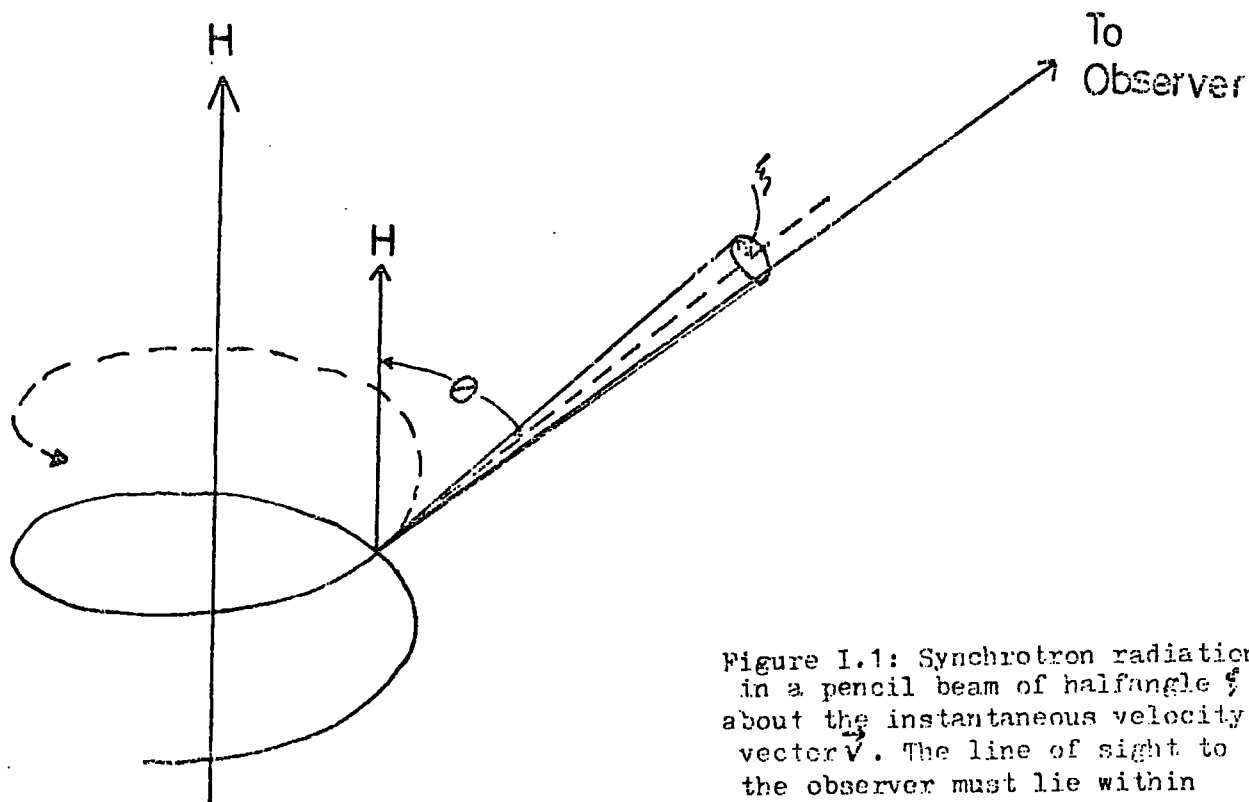

Figure I.1: Synchrotron radiation in a pencil beam of halfangle φ about the instantaneous velocity vector $\vec{V}$. The line of sight to the observer must lie within this cone for an appreciable amount of radiation to be observed.

half-angle of this cone can be approximated by:

$$\zeta = mc^2/E \qquad \text{I.2}$$

For energies of a few Gev. ζ is a few minutes of arc. The velocity

vector V sweeps out a cone of half-angle θ around H. The observer must

be situated within the angle ζ of θ in order that he detects a pulse of

radiation each time the velocity vector sweeps past him, assuming that

the observer is sufficiently distant such that the motion of the electron

parallel to H will not alter the angle between H and the line of sight

from the observer to the electron.

Each pulse of synchrotron radiation is doppler-shifted such that its

gyration frequency,

$$\nu_g' \approx \nu_g /(1 - V\cos^2\theta/c) \approx \nu_g /\sin^2\theta. \qquad 1.3$$

The pulses of the radiation therefore repeat at this frequency and the

observed radiation has a frequency spectrum that is the sum of all the

harmonics of ν_g'. Most of the energy is radiated in those harmonics

which yield frequencies of the order of $(2\pi\Delta t)^{-1}$ where Δt is the

approximate pulse width given by,

$$\Delta t \approx \frac{(1 - V^2/c^2)^{3/2}}{2\pi \, \nu_g} \qquad 1.4$$

at frequencies around

$$\frac{1}{2\pi\Delta t} = \frac{1}{2\pi} \frac{2\pi \nu_g}{(1 - V^2/c^2)^{3/2}} = \frac{e H_\perp}{2\pi mc} \left(\frac{E}{mc^2}\right)^2$$

For $E \gg mc^2$ the harmonics are so closely spaced that the spectrum appears

as a continuum.

A critical frequency is defined as:

$$\nu_c = \frac{3e \, H_\perp}{4\pi \, mc} \cdot \left(\frac{E}{mc^2}\right)^2 = A \, H_\perp E^2 \qquad 1.5$$

where A = 16.08 if $H_\perp$ is measured in μG, E in Gev. and ν_c in MHz.

The power spectrum for the radiating electron is found by summing the

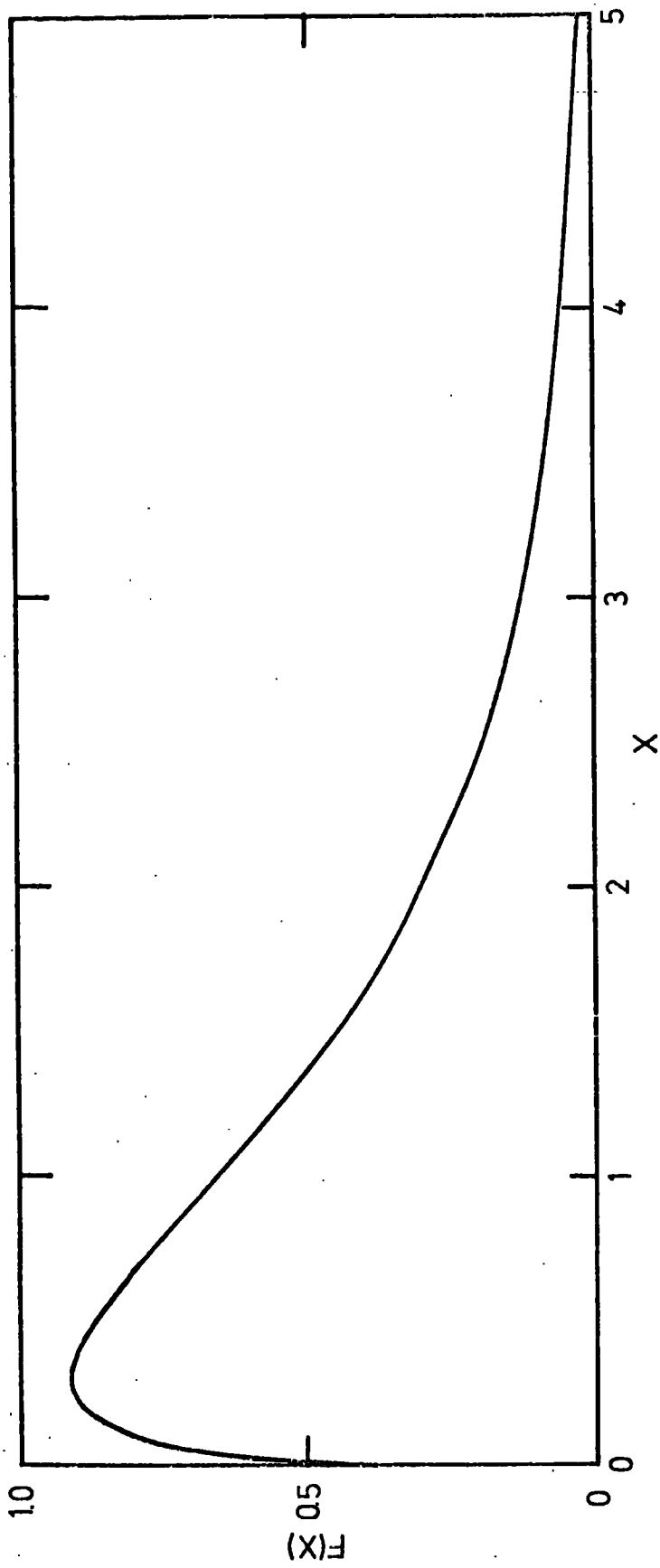emission from the various harmonics by taking the Fourier transform of

Figure I.2

The function F(X) versus X, where X = ν/ν_c

the electric field in the radiation cones. The power emitted by an electron of energy E over all frequencies for all polarisations per steradian may be expressed in terms of $X = \nu/\nu_c$ to be:-

$$P(E,\nu)d\nu = \frac{\sqrt{3}\,e^3}{mc^2 4\pi} H_\perp x \int_x^\infty K_{5/3}(\eta)\,d\eta\,d\nu = BH_\perp F(x)d\nu \qquad \text{I.6}$$

where $B = \sqrt{3}\,e^3/mc^2 4\pi = 1.865 \times 10^{-23}$ c.g.s.

and $K_{5/3}(\eta)$ is a modified Bessel function of the second kind.

The function $F(X) = x \int_x^\infty K_{5/3}(\eta)\,d\eta$

has the form as shown in figure I.2

I. 2. Emission from a power law distribution of electrons in a uniform magnetic field.

For a power law energy distribution of number density of electrons given by

$$n(E) = n_0\, E^{-\gamma}\,dE$$

uniformly distributed in space the volume emissivity $\mathcal{E}_\nu$ (power per unit volume) is given by

$$\int_0^\infty n(E)\,P(E,\nu)\,dE$$

which equals

$$\mathcal{E}_\nu^{total} = \frac{\sqrt{3}\,e^3}{16\pi mc^2} n_0\, H_\perp \left(\frac{3e}{4\pi m^3 c^5} \frac{H_\perp}{\nu}\right)^{\frac{\gamma-1}{2}} 2 \int_0^\infty x^{(\gamma-1)/2} \int_x^\infty K_{5/3}(\eta)\,d\eta\,dx$$

$$= \frac{1}{2} B\, n_0\, H_\perp^{\frac{\gamma+1}{2}} \left(\frac{C}{\nu}\right)^{\frac{\gamma-1}{2}} \int_0^\infty x^{\frac{\gamma-3}{2}} F(x)\,dx \qquad \text{I.7}$$

where $C = \frac{3e}{4\pi m^3 c^5} = 6.23 \times 10^{19}$ c.g.s. and the other symbols have the same meaning as in the previous equations.

$\mathcal{E}_\nu^{total}$ may be evaluated in terms of gamma functions to give

$$\mathcal{E}_\nu^{total} = \frac{B}{2} C^{\frac{\gamma-1}{2}} H_\perp^{\frac{\gamma+1}{2}} \nu^{-(\gamma-1)/2} \alpha(\gamma) \qquad \text{I.8}$$

where

$$\alpha(\gamma) = \int_0^\infty x^{\frac{\gamma-1}{2}} \int_x^\infty K_{5/3}(\eta)\,d\eta\,dx = \frac{\gamma + 7/3}{\gamma + 1} 2^{\frac{\gamma-3}{2}} \Gamma\left(\frac{3\gamma-1}{12}\right) \Gamma\left(\frac{3\gamma+7}{12}\right)$$
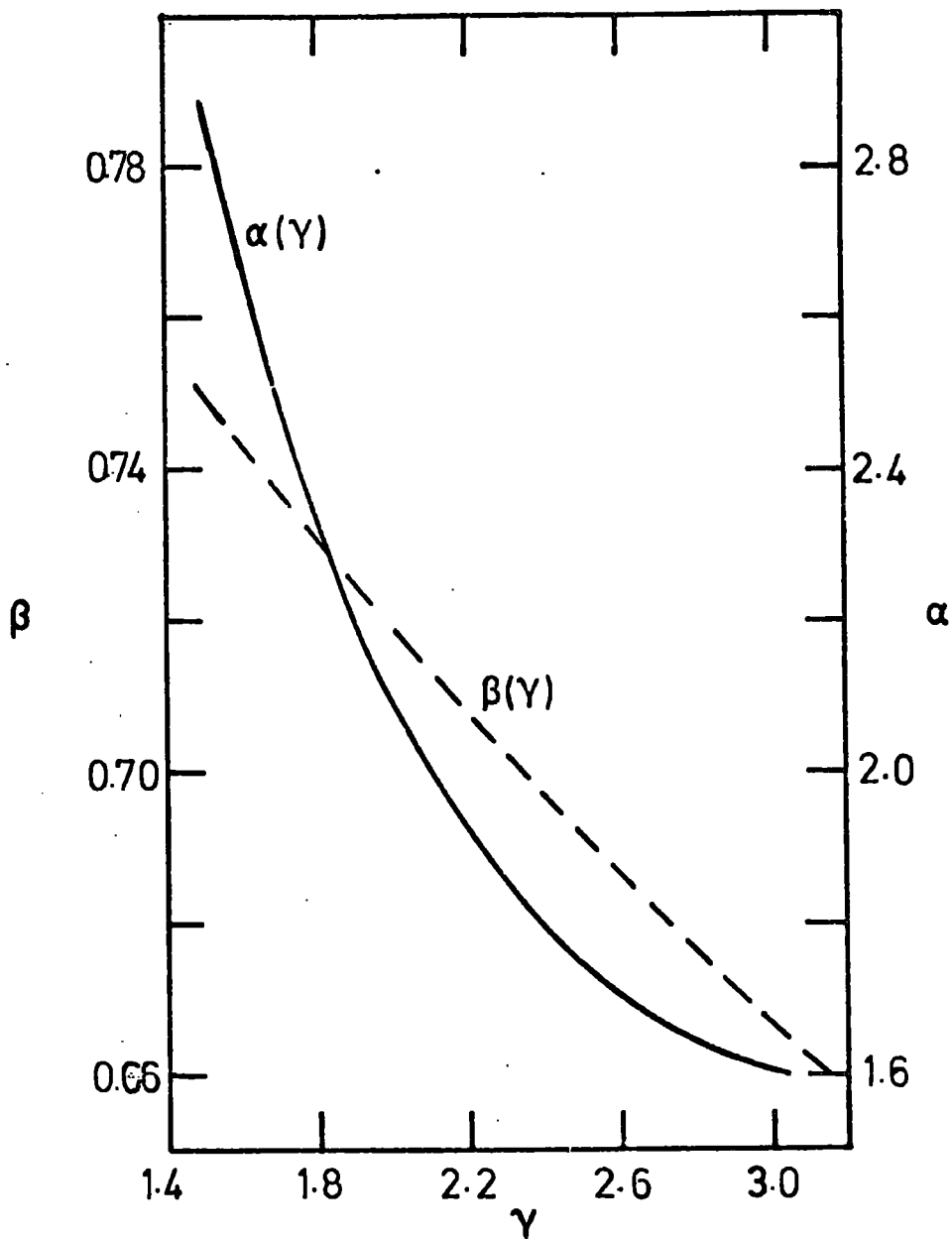
Figure I.3

$\beta(\gamma)$, the reduction factor for $H^{\frac{\gamma+1}{2}}$ for an isotropic magnetic field. $\alpha(\gamma)$, as defined in the text equation I.8.

$\alpha(\gamma)$ is plotted in figure I.3.

Equation I.8 may be expressed in more useful units.

The intensity of radiation at a particular frequency may be written as

$$I(\nu) = \mathcal{E}_\nu \ell$$

where l is the line of sight through the emitting region.

From equation I.8

$$I(\nu) = 3.010 \times 10^{-22} (4.008)^\gamma \alpha(\gamma) \ell I_o H_\perp^{\frac{\gamma+1}{2}} \nu^{-\frac{\gamma-1}{2}} \mu g. \, s^{-1} cm^{-2} H_z^{-1} sr^{-1} \qquad I.9$$

where $l, H_\perp$ and ν are measured in kpc., μG. and MH$_z$. respectively and I_o is the intensity of electrons at 1GeV. measured in $(m^2.s.sr.GeV.)^{-1}$.

The emissivity may also be expressed in terms of brightness temperature per unit length along the line of sight through the emitting region.

Using $T_b = \frac{\lambda^2 I}{2k}$, where k is Boltzmann's constant,

$$\mathcal{E}_\nu = 979.45 (4.008)^\gamma \alpha(\gamma) I_o H_\perp^{\frac{\gamma+1}{2}} \nu^{-\frac{\gamma+3}{2}} \, ^\circ K \, kpc^{-1} \qquad I.10$$

I_o, H and ν are in the same units as used in equation I.9.

Equation I.10 is the form of the equation of synchrotron emission used throughout this thesis. T_b is proportional to $\nu^{-\frac{\gamma+3}{2}}$ and in this thesis $\beta = \frac{\gamma+3}{2}$ is defined as the temperature spectral index.

For a particular value of $H_\perp$, ν and γ it is of interest to know over what range of energies electrons are contributing to the synchrotron emission. For $\gamma = 2.6$ the function $x^{\frac{\gamma-3}{2}} F(x)$ is plotted in figure I.4. To obtain the energy range of electrons contributing 80% of the total emission the value of X_1 and X_2 are found such that the area between $X=0$ and X_1 and the area between X_2 and $X=\infty$ equal 10% of the total area which is proportional to the total emission. For $\gamma = 2.6$ $X_1 = 0.14$ and $X_2 = 2.5$ which correspond respectively to energies of $0.63E_c$ and $2.7E_c$ where E_c is the critical energy corresponding to the critical frequency as defined in equation I.5.
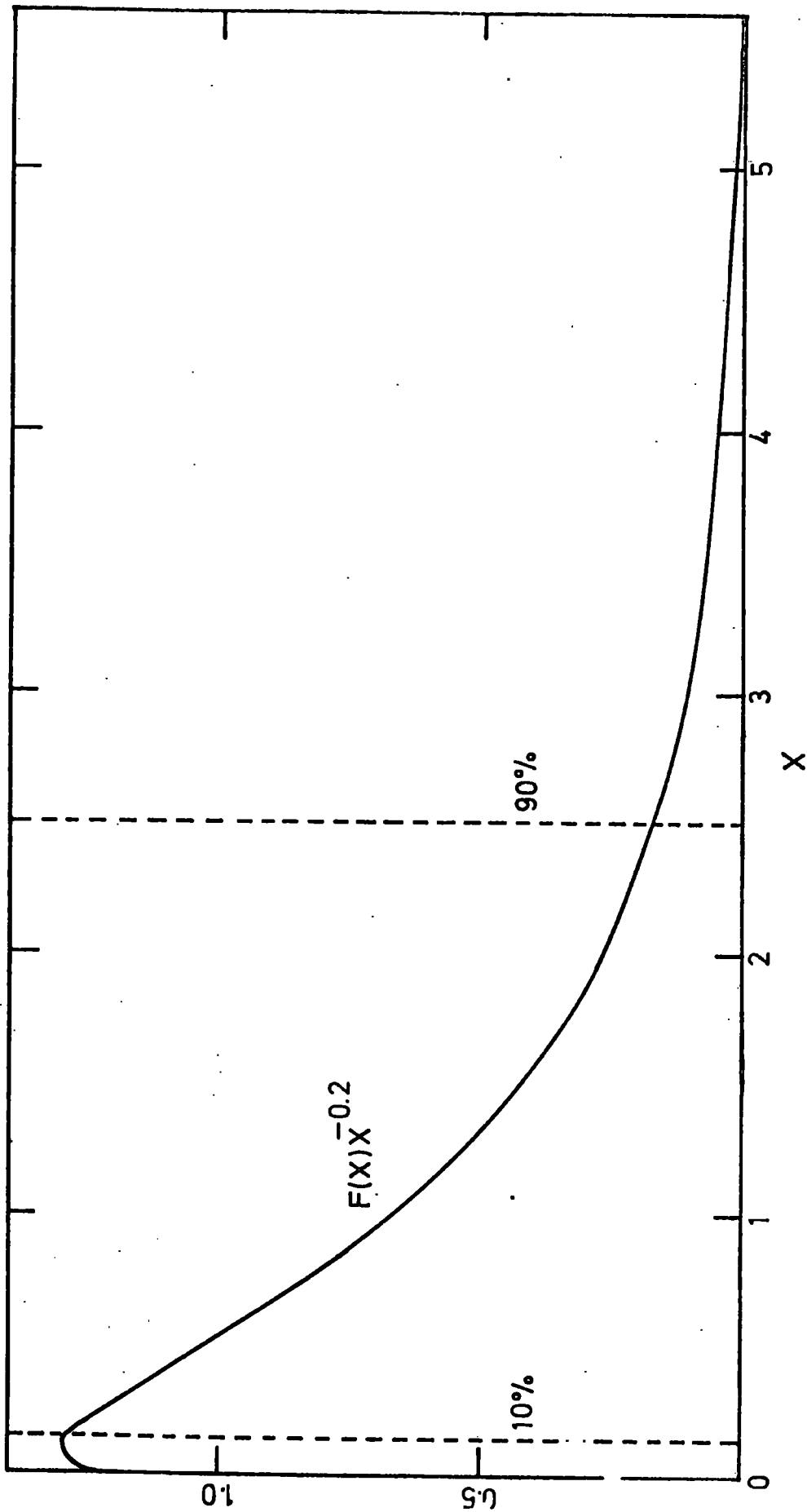
Figure I.4

The function F(X) X $\frac{\mathscr{E}-3}{2}$ versus X showing the X values corresponding to X_1 and X_2 as defined in the text.
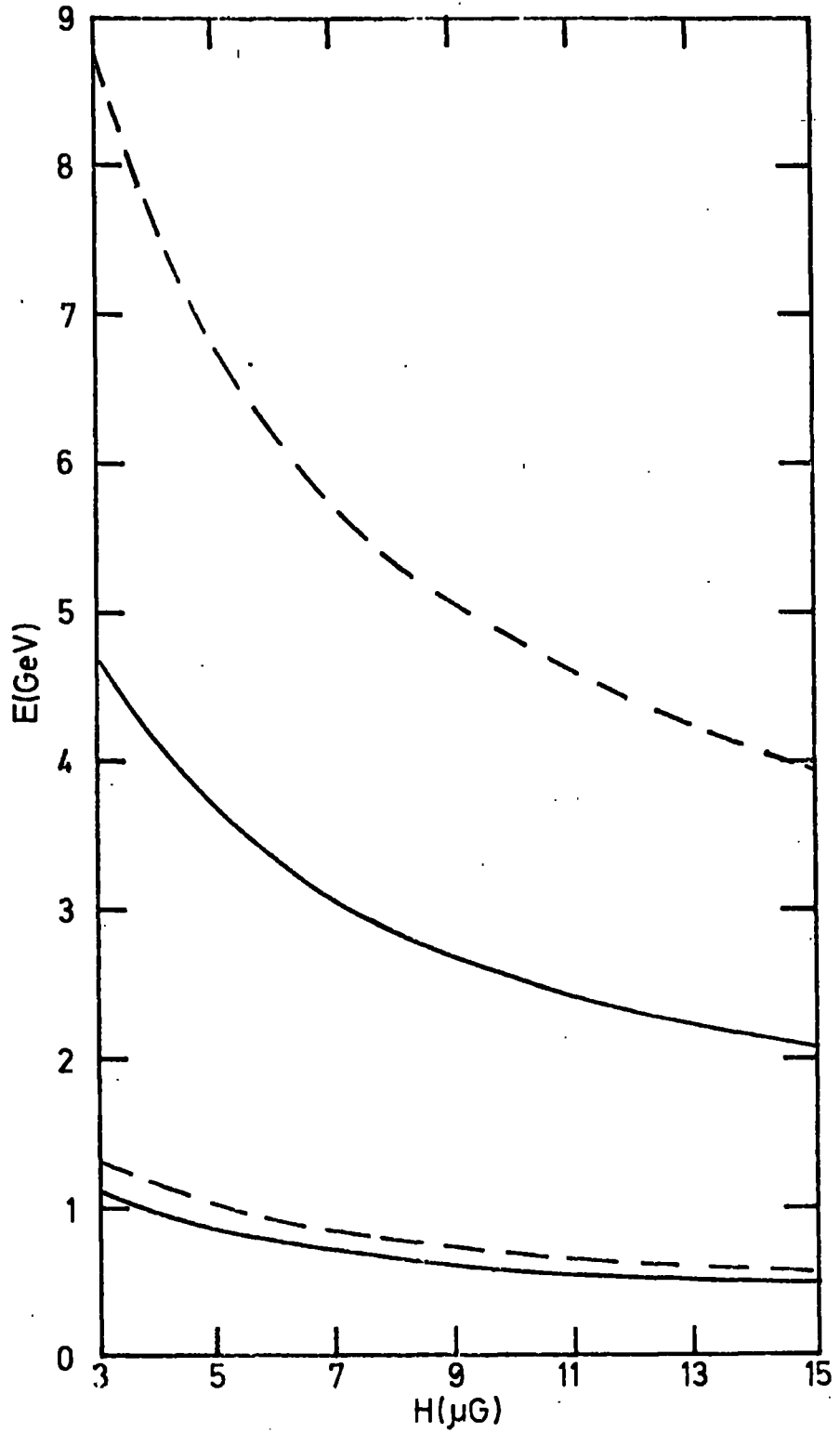
Figure I.5

Energy ranges of electrons contributing 80% to the total emission for various values of the magnetic field — — — corresponds to $\gamma = 1.8$ and ———— corresponds to $\gamma = 2.6$.

Figure I.5 shows the energy range of electrons contributing 80%
to the total emission for various values of the magnetic field
assuming a spectral index γ of 2.6. The corresponding range of
energies is also shown for $\gamma = 1.8$. Both sets of curves are
calculated for a frequency of 150 MHz.

I. 3. Emission in an isotropic magnetic field.

So far the magnetic field H has been assumed to be uniform,
i.e. orientated in a particular direction. If the field is now
considered to be completely isotropic in space the effective magnetic
field H_{eff} must appear in equation I.10 rather than $H_\perp$.

$$H_\perp^{\frac{\gamma+1}{2}} = (H \sin\theta)^{\frac{\gamma+1}{2}}$$

$\sin\theta^{\frac{\gamma+1}{2}}$ must be averaged over all θ.

Therefore H_{eff} $=$ $H^{\frac{\gamma+1}{2}}$ $\dfrac{\int_0^\pi 2\pi \sin\theta \sin\theta^{\frac{\gamma+1}{2}} d\theta}{\int_0^\pi 2\pi \sin\theta \, d\theta}$

$= H^{\frac{\gamma+1}{2}} \pi^{1/2}/2 \dfrac{\Gamma\left(\frac{\gamma+5}{4}\right)}{\Gamma\left(\frac{\gamma+7}{4}\right)} = \beta(\gamma) H^{\frac{\gamma+1}{2}}$

$\beta(\gamma)$ is plotted in figure I.3.

Therefore for an isotropic field equation I.10 becomes;

$$\mathcal{E}_\nu = 979.45 \, (4.00 \times)^{\gamma} \, d(\gamma) \, \beta(\gamma) \, I_o \, H^{\frac{\gamma+1}{2}} \, \nu^{-\frac{\gamma+3}{2}} \, {}^\circ K \, kpc^{-1} \qquad \text{I.11}$$

I. 4. The polarisation of synchrotron radiation.

For an electron radiating in a uniform field the emitted radiation is
in general elliptically polarised with components nearly in and perpendic-
ular to the plane of the electron's orbit. The ellipticity of the
polarisation varies with the position of the observer in relation to the
electron's orbit. The polarisation becomes linear when the observer's
line of sight lies on the surface of the cone swept out by the electron's
instantaneous velocity vector. The rotation of the electric vector around

the polarisation ellipse is in opposite directions for the observer's line of sight lying either inside or outside the instantaneous velocity cone. For synchrotron emission from an ensemble of electrons it can be assumed that there are equal numbers lying within and without this cone and the radiations with different senses of elliptical polarisation cancel resulting in the observed radiation being partially linearly polarised.

For a power law distribution of electrons in a uniform magnetic field the degree of polarisation is dependent only on the electron spectral index and is given by:

$$\pi = \frac{\gamma+1}{\gamma+ 7/3}$$

$$\pi = 0.75 \quad \text{for} \quad \gamma = 3$$

In practise the magnetic field is usually tangled resulting inevitably in a reduction in the degree of polarisation from that given above. Another possibility of decreasing the polarisation is Faraday rotation within the emitting region. The polarisation of an optically thin homogeneous emitter vanishes for those frequencies for which the rotation angle χ for the traversal through the whole region is a multiple of π.

$$\pi = \gamma+1 / \gamma+ \frac{1}{3} \left| \frac{\sin \chi}{\chi} \right| \quad \text{with} \quad \chi \propto \nu^{-2}$$

This results in the radiation being polarised at high frequencies while π drops rather suddenly practically to zero at the polarisation - cutoff frequency which is approximately given by $\chi = \pi$.

General references:

Feltﬁn J.E., Morrison P. 1966 Ap. J. 146 686-707

Moffet A.T. in Stars and Stellar Systems Vol.7 Ch.5

Pacholczyk A.G. Radio Astrophysics Publ. Freeman.

ACKNOWLEDGEMENTS

The Science Research Council is thanked for the provision of a Research Studentship during the period of this work.

I wish to thank Professor A.W. Wolfendale, F.R.S., for making available the facilities of the Physics Department of the University of Durham and in particular Dr. J.L. Osborne, my supervisor, for his guidance and encouragement during the period of research for this thesis.

I would like to thank Dr. J.E. Baldwin, Dr. G. Dickinson, Dr. R. Ellis, Mr. P. Kiraly, Dr. A.J. Owens, Dr. J. Skilling, Dr. A.W. Strong, Professor R.J. Taylor, Dr. M.P. White, Dr. D. Worroll and Professor A.W. Wolfendale with whom I have had useful discussions on various aspects of the work presented in this thesis.

The facilities provided by the Durham University Computer Unit are gratefully acknowledged.

I would like to thank Mrs. Carol Scott, Mrs. Sheila Shippen and Miss Margaret Forster for typing this thesis.

Finally I would like to thank my parents who have encouraged and supported me during the preparation of this thesis.